ASME
SETTING THE STANDARD

FLUIDS ENGINEERING DIVISION
Editor
J. KATZ (2009)
Assistant to the Editor
L. MURPHY (2009)

Associate Editors
M. J. ANDREWS (2009)
S. BALACHANDAR (2008)
A. BESKOK (2008)
S. L. CECCIO (2009)
D. DRIKAKIS (2008)
P. DUPONT (2010)
I. EAMES (2010)
C. HAH (2009)
T. J. HEINDEL (2010)
J. KOMPENHANS (2009)
J. A. LIBURDY (2010)
P. LIGRANI (2008)
R. MITTAL (2009)
T. J. O'HERN (2008)
U. PIOMELLI (2010)
Z. RUSAK (2010)
D. SIGINER (2008)
Y. ZHOU (2008)

PUBLICATIONS COMMITTEE
Chair, B. RAVANI

OFFICERS OF THE ASME
President, THOMAS M. BARLOW
Executive Director, THOMAS G. LOUGHLIN
Treasurer, T. D. PESTORIUS

PUBLISHING STAFF
Managing Director, Publishing
P. DI VIETRO
Manager, Journals
C. MCATEER
Production Coordinator
A. HEWITT

Transactions of the ASME, Journal of Fluids Engineering (ISSN 0098-2202) is published monthly by The American Society of Mechanical Engineers, Three Park Avenue, New York, NY 10016. Periodicals postage paid at New York, NY and additional mailing offices.
POSTMASTER: Send address changes to Transactions of the ASME, Journal of Fluids Engineering, c/o THE AMERICAN SOCIETY OF MECHANICAL ENGINEERS, 22 Law Drive, Box 2300, Fairfield, NJ 07007-2300.
CHANGES OF ADDRESS must be received at Society headquarters seven weeks before they are to be effective. Please send old label and new address.
STATEMENT from By-Laws. The Society shall not be responsible for statements or opinions advanced in papers or ... printed in its publications (B7.1, Par. 3).
COPYRIGHT © 2009 by the American Society of Mechanical Engineers. Authorization to photocopy material for internal or personal use under those circumstances not falling within the fair use provisions of the Copyright Act, contact the Copyright Clearance Center (CCC), 222 Rosewood Drive, Danvers, MA 01923, tel: 978-750-8400, www.copyright.com. Request for special permission or bulk copying should be addressed to Reprints/Permission Department.
Canadian Goods & Services Tax Registration #126148048.

Journal of Fluids Engineering

Published Monthly by ASME

VOLUME 131 • NUMBER 1 • JANUARY 2009

RESEARCH PAPERS

Flows in Complex Systems

Fundamental Issues and Canonical Flows

Multiphase Flows

(Contents continued on inside back cover)

This journal is printed on acid-free paper, which exceeds the ANSI Z39.48-1992 specification for permanence of paper and library materials. ♾™
♻ 85% recycled content, including 10% post-consumer fibers.

Downloaded 03 Jun 2010 to 171.66.16.159. Redistribution subject to ASME license or copyright; see http://www.asme.org/terms/Terms_Use.cfm

(**Contents continued**)

Journal of Fluids Engineering **Volume 131, Number 1** **JANUARY 2009**

TECHNICAL BRIEFS

The ASME Journal of Fluids Engineering is abstracted and indexed in the following:

Applied Science & Technology Index, Chemical Abstracts, Chemical Engineering and Biotechnology Abstracts (Electronic equivalent of Process and Chemical Engineering), Civil Engineering Abstracts, Computer & Information Systems Abstracts, Corrosion Abstracts, Current Contents, Ei EncompassLit, Electronics & Communications Abstracts, Engineered Materials Abstracts, Engineering Index, Environmental Engineering Abstracts, Environmental Science and Pollution Management, Excerpta Medica, Fluidex, Index to Scientific Reviews, INSPEC, International Building Services Abstracts, Mechanical & Transportation Engineering Abstracts, Mechanical Engineering Abstracts, METADEX (The electronic equivalent of Metals Abstracts and Alloys Index), Petroleum Abstracts, Process and Chemical Engineering, Referativnyi Zhurnal, Science Citation Index, SciSearch (The electronic equivalent of Science Citation Index), Shock and Vibration Digest, Solid State and Superconductivity Abstracts, Theoretical Chemical Engineering

Downloaded 03 Jun 2010 to 171.66.16.159. Redistribution subject to ASME license or copyright; see http://www.asme.org/terms/Terms_Use.cfm

A Numerical Investigation into the Effectiveness of Multi-Element Pressure Screen Rotor Foils

Sean Delfel
Pulp and Paper Centre and
Department of Mechanical Engineering,
The University of British Columbia,
2385 East Mall,
Vancouver, BC, V6T 1Z4, Canada

Carl Ollivier-Gooch
Department of Mechanical Engineering,
The University of British Columbia,
2324 Main Mall,
Vancouver BC, V6T 1C4, Canada

James Olson
Pulp and Paper Centre and
Department of Mechanical Engineering,
The University of British Columbia,
2385 East Mall,
Vancouver, BC, V6T 1Z4, Canada

Pressure screening is an efficient way to remove unwanted debris from a pulp stream, which improves the quality of the end product paper. Past work has found that increased foil camber and angle-of-attack improve the performance of pressure screen foil rotors by increasing the magnitude and width of the negative pressure pulse on the screen cylinder while at the same time reducing the magnitude of the positive pressure pulse on the screen cylinder. Too large an angle-of-attack or too much camber leads to separation of the flow over the foil and a loss in rotor performance, however. This study therefore investigates, using computational fluid dynamics, the ability of multi-element rotor foils to delay stall over the foil and improve upon the performance of an existing pressure screen rotor foil. In this study, the effect of foil angle-of-attack, flap angle, the geometry of the trailing edge of the main foil, and the positioning of the flap relative to the main foil were studied. A multi-element foil was developed based on the NACA 8312, a foil used in industrial pressure screen rotors. In general, stall was delayed and a larger angle-of-attack was obtained than the single-element foil, and increased camber was added to the foil by deflecting the flap. Positive pressure pulse on the screen cylinder approached a negligible value with both increasing angle-of-attack and increasing flap angle, while the negative pressure pulse increased in magnitude with both increasing angle-of-attack and flap angle before the foil began to separate and the suction was lost. The x-positioning of the flap was shown to have less of an effect on the foil performance than the y-positioning. All told, the magnitude of the negative pressure pulse was increased by 15% while at the same time eliminating the positive pressure pulse.
[DOI: 10.1115/1.2979002]

1 Introduction

As the most industrial efficient and effective way to remove shives and contaminants from a pulp stream, pressure screens are used in paper making worldwide. Screening has a positive effect on the overall quality of the paper, including its strength, appearance, and optical qualities. Additionally, modern screens are used to separate the fibers in the pulp by length and flexibility (known as "fractionating" the pulp), allowing for long and short fibers to be processed separately and for the production of high value paper. The ability to efficiently filter and fractionate pulp is making pressure screens increasingly important to both mechanical and chemical pulping processes.

A pressure screen is comprised of two major elements, the rotor and the screen cylinder, and it splits a contaminated feed stream into accept and reject streams. The feed stream typically enters the screen tangentially and is passed between the rotor and the screen cylinder. A pressure drop across the screen cylinder allows for sufficiently small particles to pass through small apertures (either slots or holes) in the screen cylinder and on the accept stream. Oversized particles and the fraction of long fibers that are retained by the screen cylinder continue down the length of the screen and leave via the reject stream.

This work is focused upon the performance of the rotor, which has two main functions within the screen. First, it provides a high tangential velocity to the flow, inducing turbulence at the screen plate that helps keep the pulp fluidized. Second, and more important, as the foil passes along the feed side of the screen cylinder it generates a negative pressure pulse that backflushes the apertures, clearing any debris from the apertures that would cause them to plug. This action has a dramatic affect on screen performance, typically measured by three parameters—the fractionation or contamination removal efficiency of the screen; the capacity of the screen, defined as the amount of pulp in the accept stream; and the power consumption of the screen. An ideal screen would maximize efficiency and capacity and at the same time minimize power consumption.

There are two general types of rotors used in screens: solid core and foil rotors. Foil rotors are similar to the airfoils used on the wings of aircraft and allow the flow to circulate around the foil and are typically used in low consistency fine screening. Solid core rotors, on the other hand, consist of elements attached to the outer surface of an inner drum core and allow the flow to only pass over the outer surface of the element. Solid core rotors are usually used earlier in the screening process for higher consistency screening, while foil rotors are used later in the process for fine screening and fractionation. This work will focus on the performance of foil rotors.

In a previous study, Olson et al. [1] found experimentally that the nondimensional power coefficient is independent of Reynolds number, with power coefficient defined as

$$C_{\text{power}} = \frac{\text{power}}{\rho \cdot V_t^3 \cdot D^2} \tag{1}$$

where "power" is the power consumption of the rotor, ρ is the fluid density, V_t is the rotor tip speed, and D is the diameter or the rotor [1]. Reynolds number is based on foil chord length and defined as

Contributed by the Fluids Engineering Division of ASME for publication in the JOURNAL OF FLUIDS ENGINEERING. Manuscript received October 5, 2007; final manuscript received July 6, 2008; published online November 26, 2008. Assoc. Editor: Rajat Mittal.

 Copyright © 2009 by ASME

Downloaded 03 Jun 2010 to 171.66.16.158. Redistribution subject to ASME license or copyright; see http://www.asme.org/terms/Terms_Use.cfm

$$\mathrm{Re} = \frac{\rho V_t c}{\mu} \tag{2}$$

where ρ is the fluid density, V_t is the rotor tip speed, c is the chord length of the foil, and μ is the fluid viscosity. The power consumption of the rotor is therefore proportional to the tip speed of the rotor cubed and a reduction in the rotor velocity would lead to a large reduction in the power required.

Additional studies have shown that increasing the magnitude of the negative pressure pulse generated by the rotor will increase the capacity of the screen, particularly for slotted screen cylinders [2–7]. Pinon et al. [8] and Gonzales [9] found that the nondimensional pressure pulse generated by the rotor is also independent of Reynolds number, with the nondimensional pressure defined by the pressure coefficient

$$C_P = \frac{P}{0.5 \cdot \rho \cdot V_t^2} \tag{3}$$

where P is the pressure, ρ is the fluid density, and V_t is the tip speed of the rotor, implying that the magnitude of the pressure pulse generated by the rotor varies quadratically with the rotor velocity. Since it is desirable to slow the rotor tip speed in order to reduce power consumption, but this will also reduce the magnitude of the pressure pulse, we therefore want to maximize the pulse generated by the foil at a given tip speed. This is the primary goal in pressure screen rotor design.

Gonzales [9] and Feng et al. [10] both studied the effect of a wide range of foil variables on the pressure pulse generated by a foil rotor. They observed that the magnitude of the negative pressure pulse for a given foil would increase with angle-of-attack to a maximum value and would then decrease at higher angles-of-attack (the exception being the NACA 8312 foil, which had a maximum peak magnitude at 0 deg angle-of-attack). Niinimaki [2] made similar observations, showing that increasing foil angle-of-attack improves the capacity of the screen. Additionally, Gonazales [9] and Feng et al. [10] found that the undesirable positive pressure pulse decreased with increasing foil angle-of-attack. They also showed that pressure pulse width and magnitude both increase with increasing foil camber [9,10].

In order to achieve higher angles-of-attack at lower Reynolds numbers, it is common practice in the aerospace field to use multi-element airfoils. Multi-element foils delay stall on the foil by allowing high energy flow on the lower surface of the foil to pass through the slot between the main foil and the flap, reenergizing the boundary layer on the upper surface of the foil. They also have the added affect of increasing the effective camber of the foil as the flap deflection is increased [11].

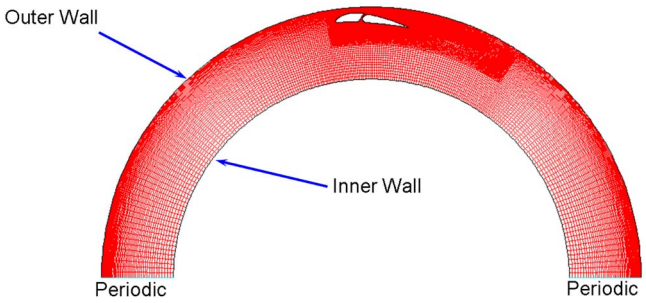

Fig. 1 Computational domain and a typical mesh

Therefore, in an effort to reduce the rotor velocity while maintaining screen performance, the goal of this study is to determine the effectiveness of multi-element pressure screen rotor foils in controlling the magnitude and shape of the negative pressure pulse generated by the foil. The effect of varying the major foil geometry parameters was studied using computational fluid dynamics (CFD). Specifically, the effects of the flap angle, the foil angle-of-attack, the main foil trailing edge geometry, and the positioning of the leading edge of the flap were studied. Validation of the numerical model was obtained using existing experimental data for single-element rotor foils.

2 Numerical Method

The FLUENT 6.1 commercial solver was used to numerically solve the discretized Navier–Stokes equations for this study. The problem is assumed to be isothermal, two dimensional, and steady state, allowing the Navier–Stokes equations to be reduced to the continuity and x- and y-momentum equations. The solver is a second-order finite volume solver: Control volume averages are found for each flow variable and the fluxes at the control volume faces are then found through a second-order spatial interpolation from the control volume center. All cases included in this study were solved at steady state with the SIMPLEC algorithm for pressure-velocity coupling.

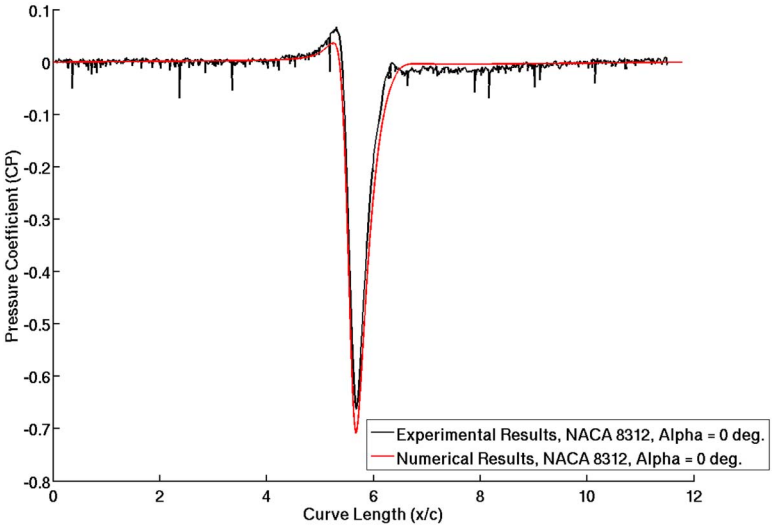

Fig. 2 Experimental and numerical results for pressure traces on the screen cylinder for a NACA 8312 rotor foil at Re=5×10^5, an angle-of-attack of α=0 deg, a chord of c=4 cm, and a gap of g=3 mm

Downloaded 03 Jun 2010 to 171.66.16.158. Redistribution subject to ASME license or copyright; see http://www.asme.org/terms/Terms_Use.cfm

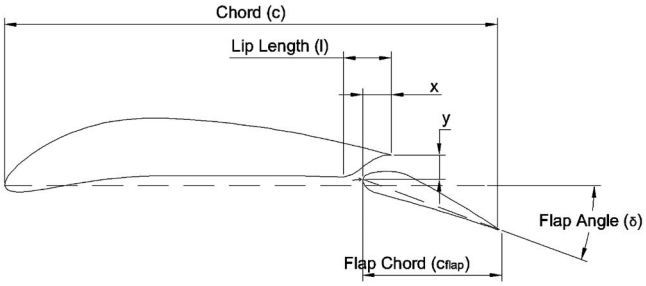

Fig. 3 Multi-element rotor foil with specific foil parameters defined

Turbulence was modeled using the standard k-ε turbulence model with enhanced wall treatment. The k-ε model solves additional transport equations for turbulent kinetic energy k and turbulent dissipation rate ε along with the continuity and momentum equations in order to find closure for the Reynolds stresses. The k-ε model was selected over other available turbulence models as an adequate balance between the accuracy and computation cost and because of a history of its use in screening type problems

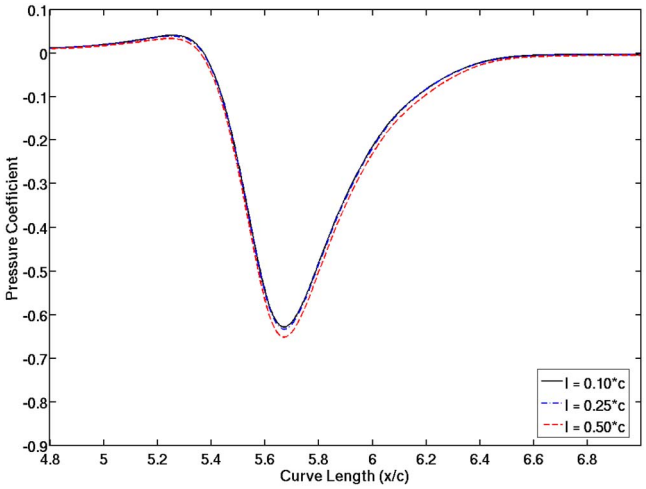

Fig. 5 Pressure traces on the screen cylinder for a multi-element foil with varying main foil trailing edge lip lengths. The foil is at α=0 deg and the flap is at δ=7 deg for all cases.

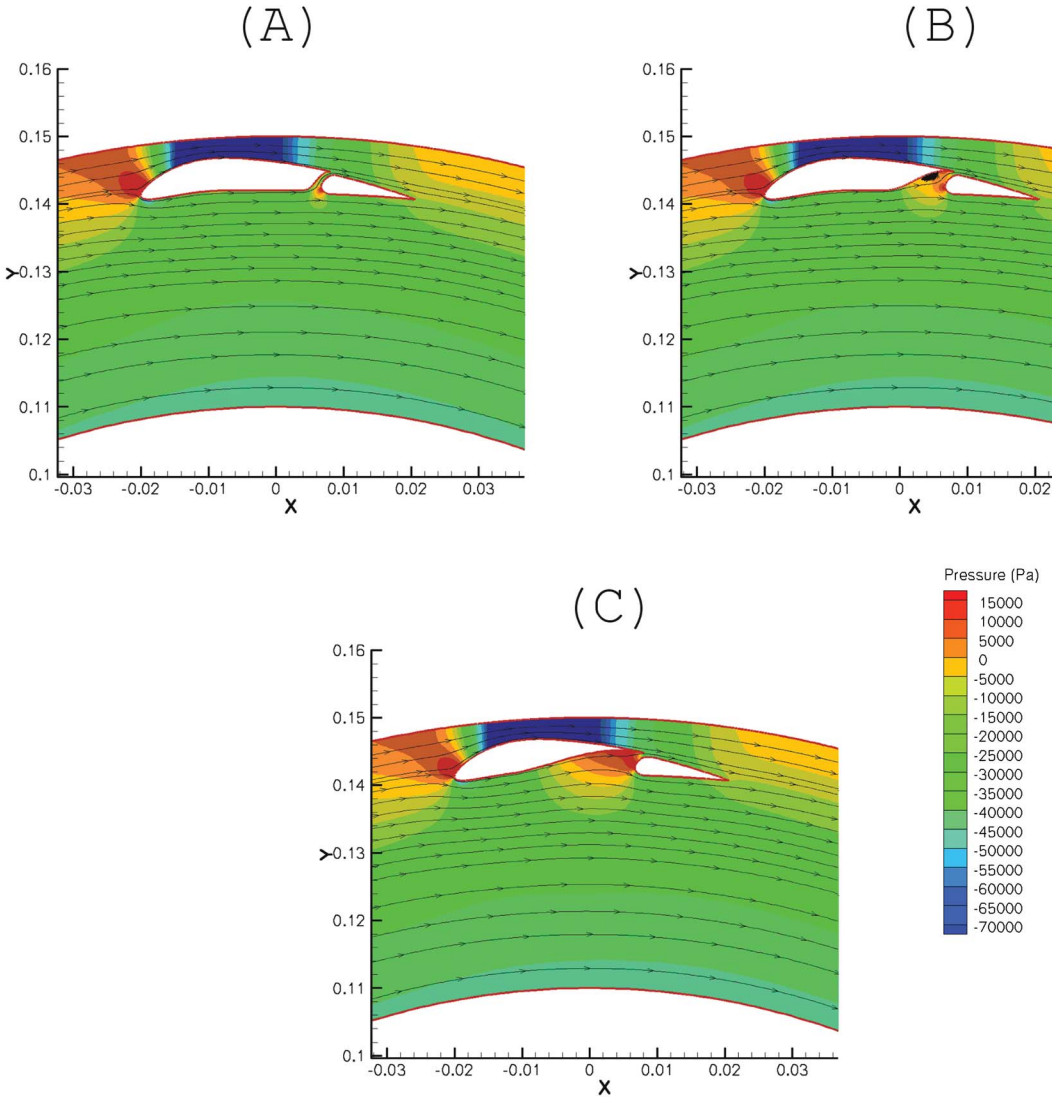

Fig. 4 Pressure contours and streamlines for a multi-element foil with varying main foil trailing edge lip lengths: (*a*) *l*=0.10*c*, (*b*) *l*=0.25*c*, and (*c*) *l*=0.50*c*. The foil is at α=0 deg and the flap is at δ=7 deg for all cases.

Downloaded 03 Jun 2010 to 171.66.16.158. Redistribution subject to ASME license or copyright; see http://www.asme.org/terms/Terms_Use.cfm

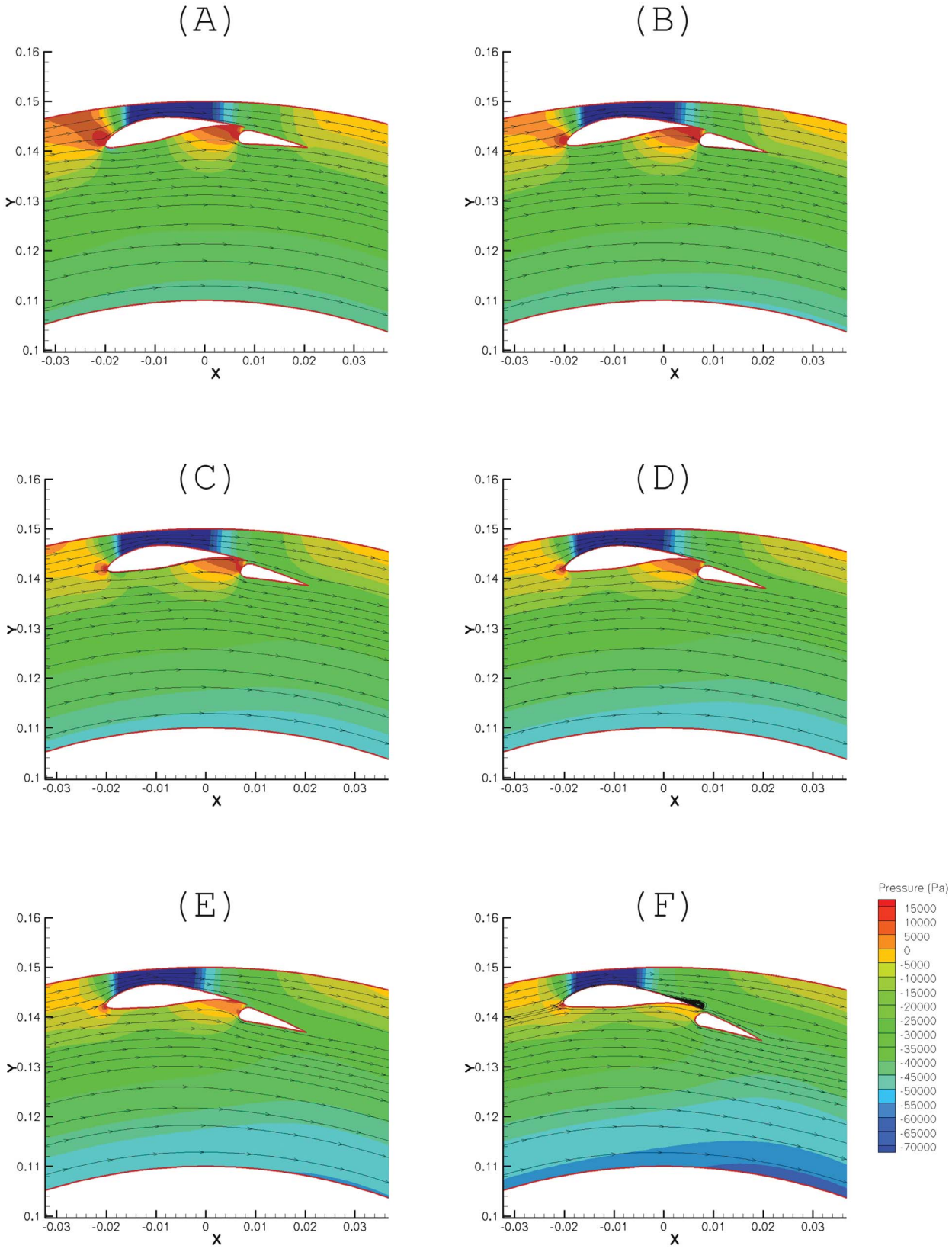

Fig. 6 Pressure contours and streamlines for a multi-element foil at (*a*) α=0 deg, (*b*) α=2 deg, (*c*) α=4 deg, (*d*) α=5 deg, (*e*) α=7 deg, and (*f*) α=10 deg. The flap is at δ=7 deg for all cases.

[10,12]. Following the results of Mahon and Zhang [12], the enhanced wall treatment for the k-ε model was included in the simulations. In essence, with the enhanced wall treatment, the turbulent quantities are computed directly all the way into the viscous sublayer, with the laminar and turbulent laws-of-the-wall being blended in the near-wall region. While being considerably more

Downloaded 03 Jun 2010 to 171.66.16.158. Redistribution subject to ASME license or copyright; see http://www.asme.org/terms/Terms_Use.cfm

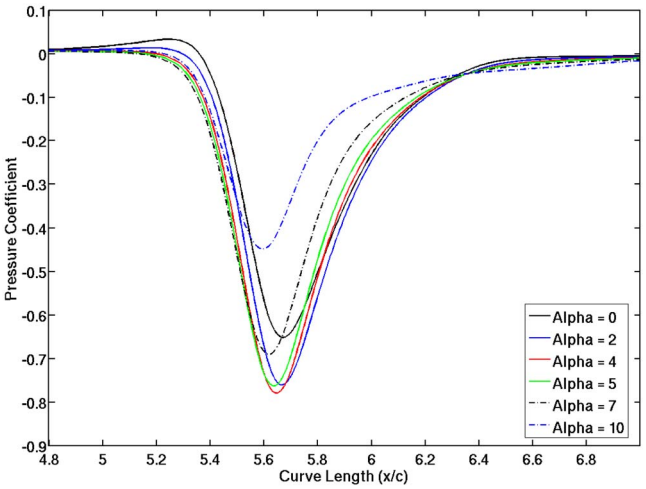

Fig. 7 Pressure traces on the screen cylinder for a multi-element foil at varying angles-of-attack. The flap is at δ =7 deg for all cases.

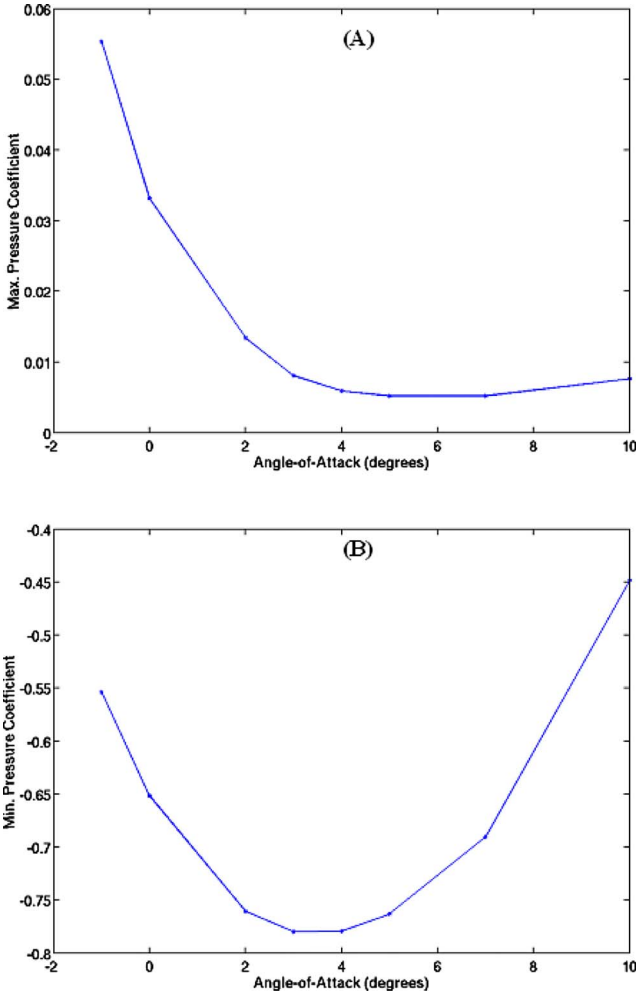

Fig. 8 (*a*) Maximum wall pressure coefficient on the screen cylinder and (*b*) minimum wall pressure coefficient on the screen cylinder versus foil angle-of-attack. The flap is at δ =7 deg for all cases.

expensive computationally, the enhanced wall treatments allowed for substantial improvement in the accuracy of the solution, especially for the pressure field, which is the main focus of this study [13,14].

3 Computational Domain and Mesh Generation

The cross section of a PSV 2100 pressure screen was modeled, as shown in Fig. 1. In all cases, 2D hybrid structured/unstructured multiblock meshes were used, in Cartesian coordinates. A very fine C-mesh was used around the foils in order to obtain acceptable boundary layer and wake resolution. As required by the k-ε turbulence model with enhanced wall treatment, the first mesh cell at the foil surface lies at a nondimensional distance of $y^+ \approx 1$. In order to minimize CPU time, a much coarser structured mesh was used in the far field and an unstructured block was added to smoothly blend the fine C-mesh and the coarse far-field meshes. All meshes were generated using GAMBIT, the commercial preprocessing package for FLUENT.

4 Boundary Conditions

The domain is rotationally periodic in order to simulate a two-bladed rotor. The periodicity of the flow ensures that it is turbulent, even though typical Reynolds numbers are on the order of $\mathrm{Re}=10^5$ based on the foil chord length, as each foil is operating in the wake of the preceding foil. A rotating computational coordinate system moving at the same speed as the foil is assigned to the center of the cylinder because the flow is steady when viewed in this frame. The inner and outer cylinder walls and the foil walls are all set with no-slip boundary conditions. The inner cylinder wall and the foil walls are set with zero angular velocity relative to the spinning computational coordinate system. The outer wall, which represents the screen cylinder, is stationary and is therefore set to zero angular velocity in the absolute coordinate system.

The inner cylinder wall has a radius of $r_{\mathrm{inner}}=0.73r_{\mathrm{outer}}$ and is representative of the core of fluid at the center of the screen moving at the rotor's angular velocity. It is a simplification that greatly reduces computational time by allowing us to remove grid points outside the area of interest. Feng [15] studied the effect of the inner wall diameter in a simulation of a PSV 2100 and found that below an inner wall radius of $r_{\mathrm{inner}}<0.867r_{\mathrm{outer}}$, the effect on measured pressure pulse is negligible. The complex flow through the screen cylinder is not considered here (i.e., $V_{\mathrm{slot}}=0.0$ m/s), which is equivalent to the critical design case of a plugged screen.

There are a number of other assumptions and simplifications that have been made in the study that should be noted: Water, rather than pulp, is used in the simulations (consistency is 0.0%), and the flow in the simulations is two dimensional. Gonzales [9] studied the effect of pulp consistency on the pulse and found that increasing consistency reduced the magnitude of the pulse, but the shape and trends remained unchanged. Also, pulp consistency during screening is generally very low, on the order of 1–2%, and turbulent pulp suspensions in this range have been found to behave as a Newtonian fluid with the same density and viscosity as water. Using water rather than pulp is therefore reasonable for this design problem. Finally, screen rotor foils typically have aspect ratios of 8 or more with a low relative axial, or spanwise, flow velocity, making the two-dimensional assumption a valid representation of a slice of the foil near midspan.

5 Grid Independence and Model Validation

The experimental data collected by Gonzales [9] and Feng et al. [10] for a NACA 8312 foil rotor was used to validate the model. As mentioned previously, in those studies, pressure traces on the screen cylinder were measured for a variety of single-element foils under different operating conditions using the cross-sectional screen (CSS), a laboratory screen that was designed to represent a section of a PSV 2100 pressure screen. For this study, the magnitude of the negative pressure pulse, measured in terms of nondimensional pressure coefficient C_P, as defined in Eq. (2), was used

Downloaded 03 Jun 2010 to 171.66.16.158. Redistribution subject to ASME license or copyright; see http://www.asme.org/terms/Terms_Use.cfm

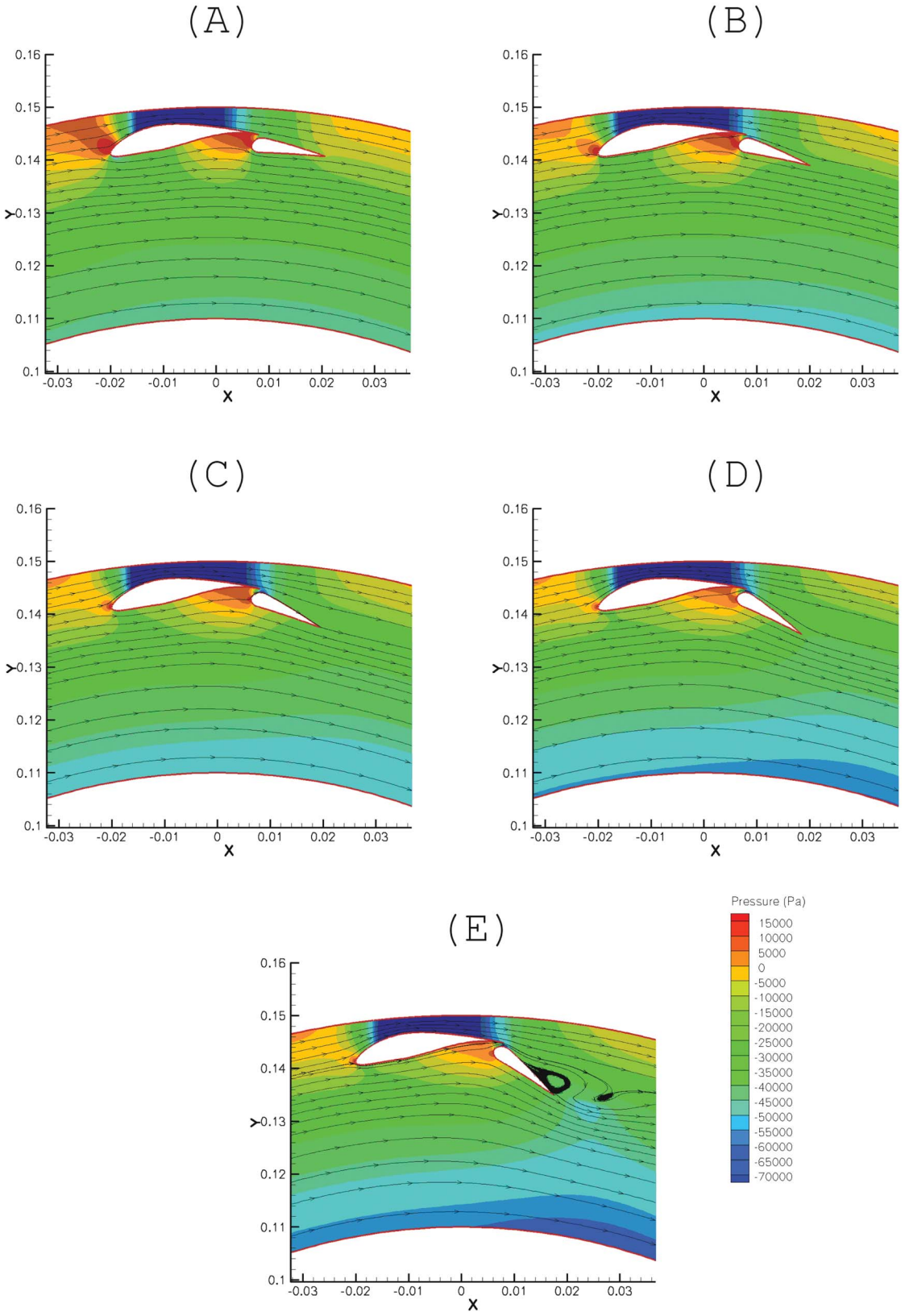

Fig. 9 Pressure contours and streamlines for a multi-element foil at (*a*) δ=7 deg, (*b*) δ=15 deg, (*c*) δ =22 deg, (*d*) δ=29 deg, and (*e*) δ=36 deg. The foil is at α=7 deg for all cases.

to determine both the independence of the solution from the computational grid resolution and the accuracy of the converged solution.

Grid independence studies were conducted for both the single- and multi-element foils used in the study. For the single-element model, five geometrically similar meshes were generated with

Downloaded 03 Jun 2010 to 171.66.16.158. Redistribution subject to ASME license or copyright; see http://www.asme.org/terms/Terms_Use.cfm

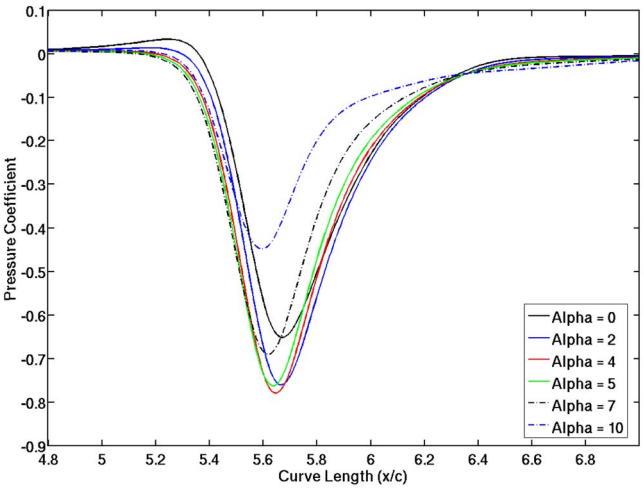

Fig. 10 Pressure traces on the screen cylinder for a multi-element foil at varying flap angles. The foil is at $\alpha=0$ deg for all cases.

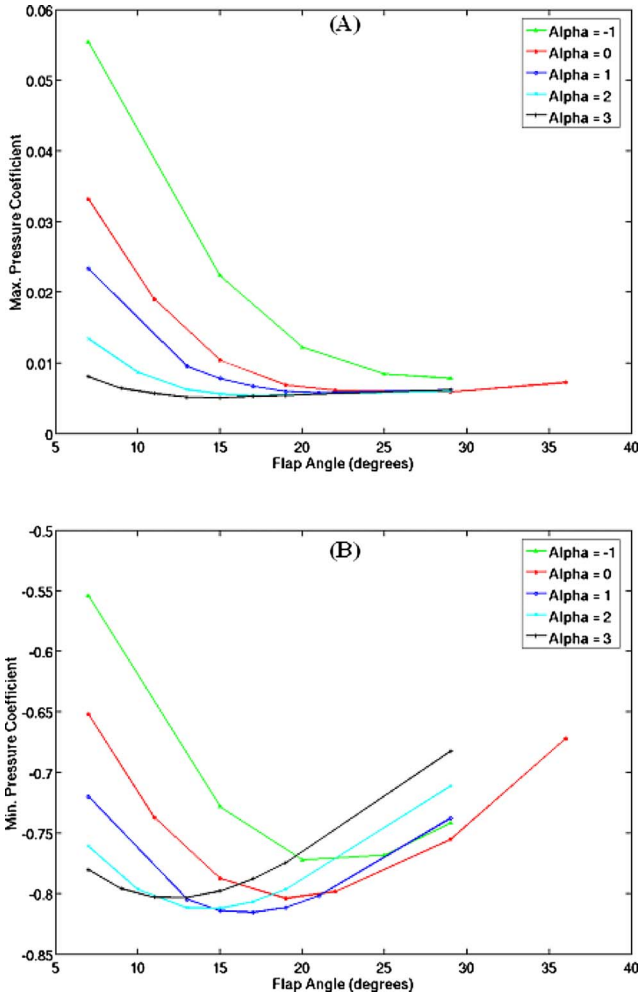

Fig. 11 (*a*) Maximum wall pressure coefficient at the screen cylinder and (*b*) minimum wall pressure coefficient at the screen cylinder versus flap angle for various angles-of-attack

grid resolutions of 65,000–400,000 volumes. The solution was found to be grid independent for meshes larger than 190,000 volumes. For the multi-element model, three geometrically similar grids were studied with grid resolutions between 80,000 volumes and 300,000 volumes. The solution was found to be grid independent for grids larger than 160,000 volumes. By removing excess volumes in the far-field, the grid count for the multi-element model was reduced around 80,000 volumes without effecting grid independence. For the optimized meshes, 58% of the control volumes lie within the foil boundary layer and wake regions of the mesh.

The NACA 8312 was modeled in the PSV 2100 using the numerical model described previously at a Reynolds number of $\mathrm{Re}=5\times10^5$, an angle-of-attack of $\alpha=0$ deg, a chord length of $c=4$ cm, and a gap between the foil and the screen cylinder of $g=3$ mm. These numerical results were compared with experimental results for the same foil, in the same configuration, operating in water with no accept flow [9,10]. Figure 2 shows the experimental and numerical pressure traces along the screen cylinder plotted together. The minimum C_P on the screen cylinder for the foil in these operating conditions was found to be $C_P=-0.708$, which matches the experimental data within 5%.

6 Results and Discussion

A multi-element rotor foil based on a NACA 8312 foil was studied using the aforementioned numerical techniques. The effect of a number of foil parameters on the pressure pulse generated by the foil was studied, including foil angle-of-attack, main foil trailing edge geometry, flap deflection, and the positioning of the flap relative to the main foil.

The NACA 8312 was used as the starting point for our multi-element foil since it generated the strongest negative pressure pulse out of the foils studied by Feng et al. [10]. A smooth-splined slot was placed in the NACA 8312 to create the multi-element foil so that the flap chord was 35% of the total foil chord ($c_{\mathrm{flap}}=0.35c$), as can be seen in Fig. 3. The upper surface was unchanged from the original NACA 8312's profile, and the length of the spline at the trailing edge of the main foil was defined as the trailing edge lip length l. The angle between the chord line of the foil with no flap deflection and the horizontal is referred to as the angle-of-attack (α) of the foil, and the angle between the flap chord line and the undeflected chord is referred to as the flap deflection angle (δ).

6.1 Lip Length. The effect of the main foil trailing edge design is shown in Fig. 4, which shows pressure contours and streamlines for a multi-element foil with varying lip lengths. There is a small separation bubble at the trailing edge of the main foil for the lip length of $l=0.25c$, which is a source of unwanted pressure drag. As can be seen in Fig. 5, which shows the pressure trace along the screen cylinder for each trailing edge geometry, the lip length has a slight effect on the pressure pulse, with the $l=0.50c$ foil having a slightly wider and stronger negative pulse. Because the $l=0.50c$ foil has a slightly stronger pulse and no separation at the lip, this lip length was used for the rest of the study.

6.2 Angle-of-Attack. Figure 6 shows the pressure contours and streamlines as angle-of-attack is varied for a multi-element foil with no flap deflection. The negative pressure pulse between the upper surface of the foil and the screen cylinder widens until an angle-of-attack of $\alpha=4$ deg, an improvement over the single-element NACA 8312, which was shown to lose suction strength at any angle-of-attack greater than $\alpha=0$ deg for these operating conditions. The multi-element foil is able to delay stall relative to the NACA 8312 by allowing the flow from the lower surface of the foil to pass through the slot and re-energize the boundary layer on the upper surface of the foil. Additionally, as the stagnation point at the leading edge of the foil rotates more toward the lower surface of the foil with increasing angle-of-attack, the positive pressure pulse emanating from the stagnation point to the screen

Downloaded 03 Jun 2010 to 171.66.16.158. Redistribution subject to ASME license or copyright; see http://www.asme.org/terms/Terms_Use.cfm

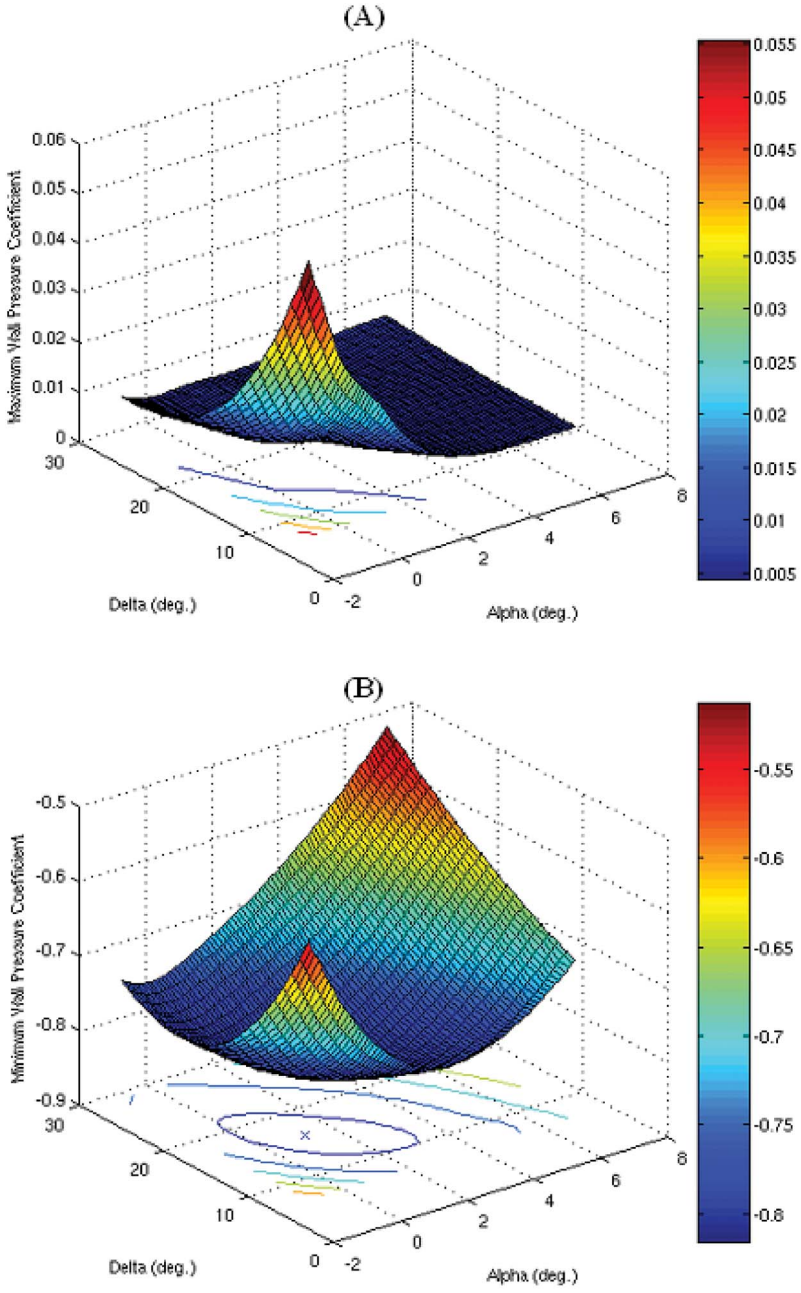

Fig. 12 Surfaces of (*a*) maximum wall pressure coefficient and (*b*) minimum wall pressure coefficient versus foil angle-of-attack and flap angle

cylinder dissipates. After $\alpha=4$ deg, the boundary layer begins to thicken and the negative pressure region starts to shrink. At $\alpha=10$ deg, the main foil has started to stall and the beginnings of a separation bubble can be seen. The results of this flow separation are a reduction in suction and an increase in pressure drag on the foil, as mentioned previously.

A clearer picture of how angle-of-attack affects the pressure on the screen cylinder due to the foil can be seen in Figs. 7 and 8. Figure 7 shows the wall pressure traces for a multi-element foil with constant flap angle at various angles-of-attack, and Fig. 8 shows the peak positive and negative pressures on the wall at each angle-of-attack. The peak negative pressure can be seen at $\alpha=4$ deg with a value of $C_P=-0.78$. Beyond $\alpha=4$ deg, the effect of the flow separation can be seen in an increasing loss in peak suction magnitude and pulse width. The reduction in the positive pressure pulse on the wall due to the stagnation point as the angle-of-attack is increased, as mentioned previously, can also be seen. This phenomenon was also observed by Feng et al. [10] and is believed to be favorable, as a positive pulse would have the effect of pushing unwanted debris through the screen cylinder and reduce the efficiency of the screen.

6.3 Flap Angle. Figure 9 shows the pressure contours and streamlines and Fig. 10 shows the pressure traces on the screen cylinder for a multi-element foil at varying flap angles with a constant angle-of-attack of $\alpha=0$ deg. As can be seen, deflecting the flap, which is effectively an increase in the camber of the foil, causes the pressure pulse to widen and strengthen until $\delta=19$ deg, after which the flow over the flap begins to separate and suction at the screen cylinder diminishes. At $\delta=36$ deg, the flap has stalled fully and the beginnings of vortex shedding can be

Downloaded 03 Jun 2010 to 171.66.16.158. Redistribution subject to ASME license or copyright; see http://www.asme.org/terms/Terms_Use.cfm

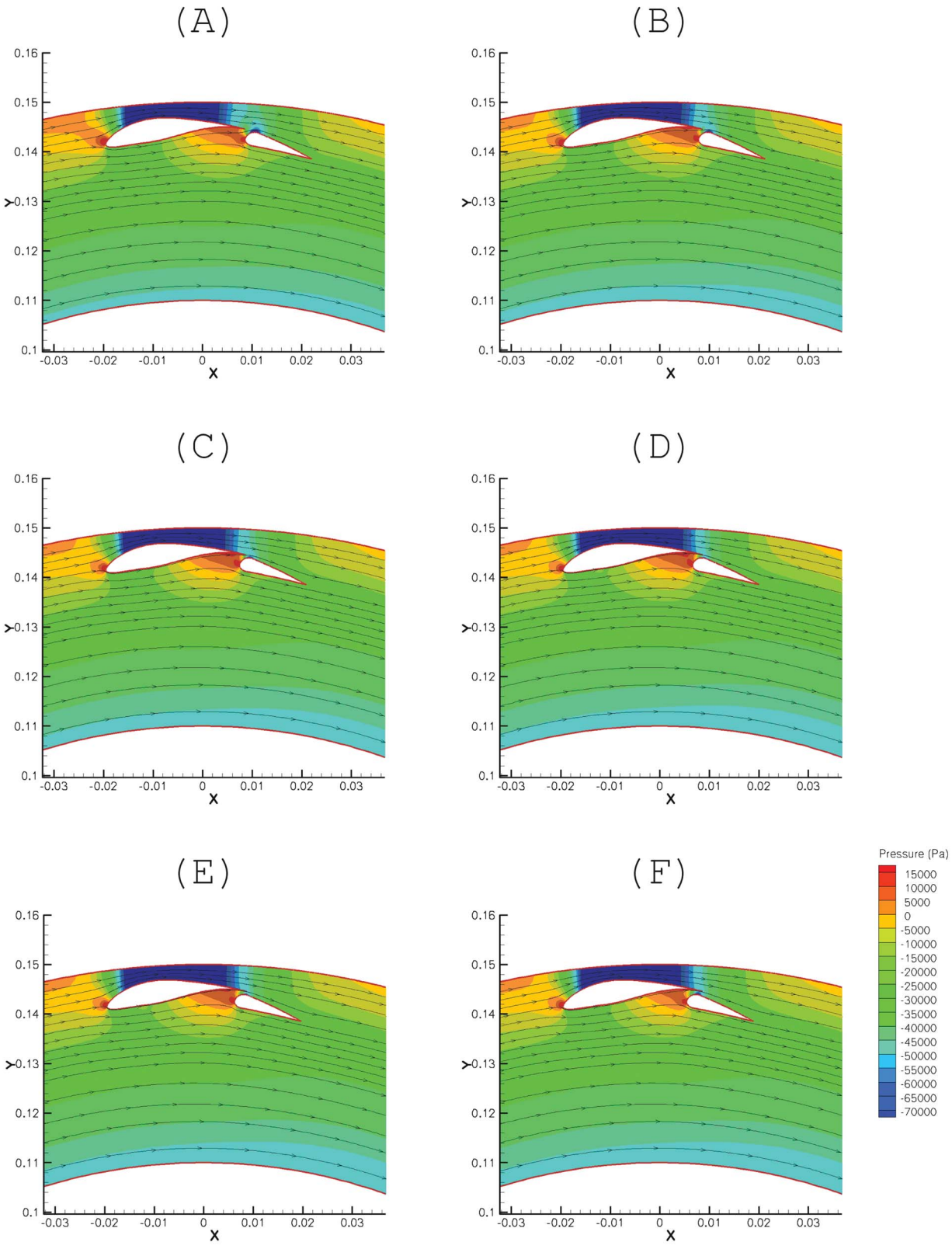

Fig. 13 Pressure contours and streamlines for a multi-element foil with varying *x*-positions for the flap leading edge. The flap leading edge is at (*a*) $x=0.00c$, (*b*) $x=-0.02c$, (*c*) $x=-0.03c$, (*d*) $x=-0.05c$, (*e*) $x=-0.06c$, and (*f*) $x=-0.08c$. In all cases, the flap leading edge is at $y=-0.05c$, $\alpha=1$ deg, and $\delta=15$ deg.

Downloaded 03 Jun 2010 to 171.66.16.158. Redistribution subject to ASME license or copyright; see http://www.asme.org/terms/Terms_Use.cfm

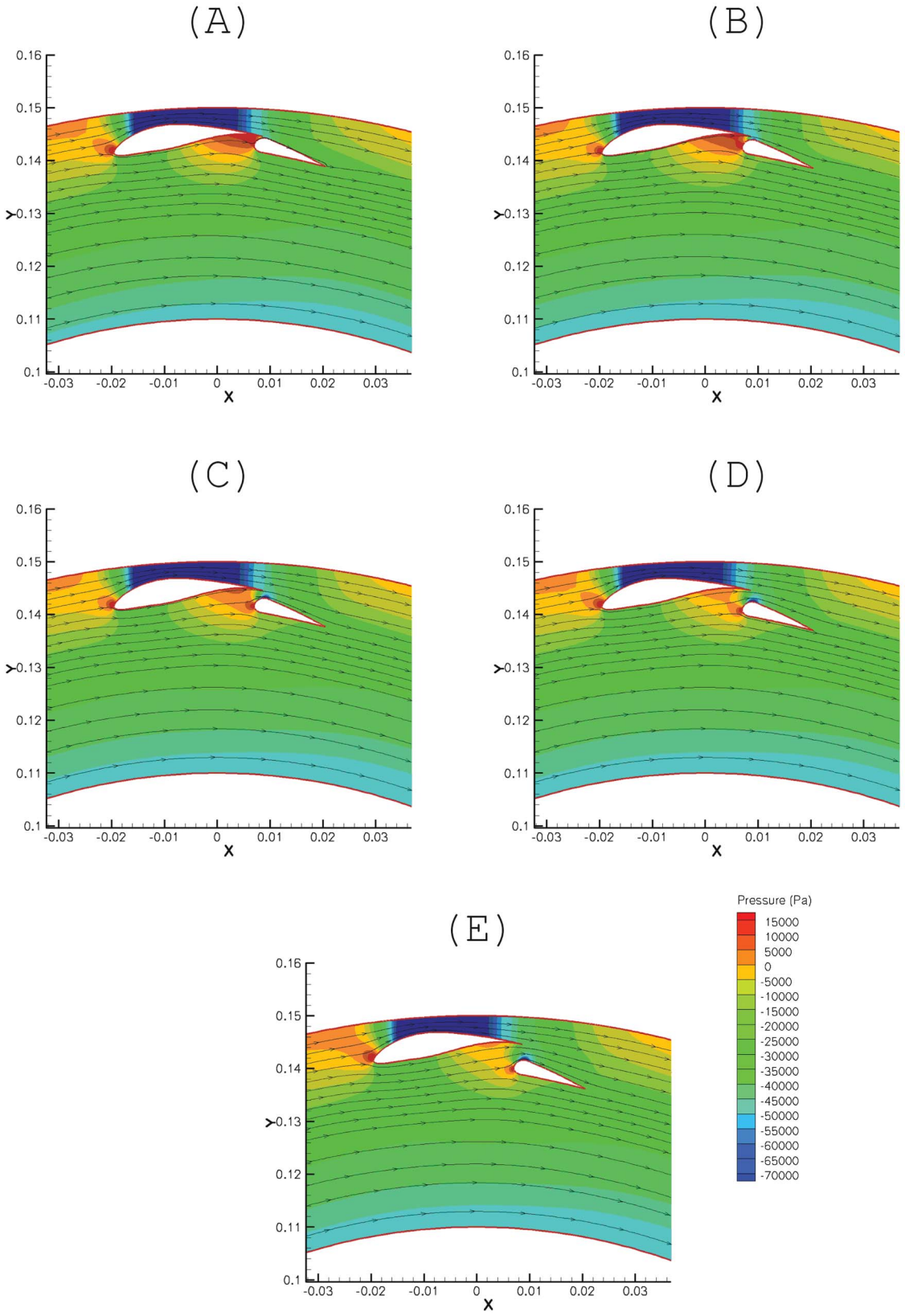

Fig. 14 Pressure contours and streamlines for a multi-element foil with varying *y*-positions for the flap leading edge. The flap leading edge is at (*a*) $y=-0.04c$, (*b*) $y=-0.05c$, (*c*) $y=-0.07c$, (*d*) $y=-0.09c$, and (*e*) $y=-0.11c$. In all cases, the flap leading edge is at $x=0.04c$, $\alpha=1$ deg, and $\delta=15$ deg.

Downloaded 03 Jun 2010 to 171.66.16.158. Redistribution subject to ASME license or copyright; see http://www.asme.org/terms/Terms_Use.cfm

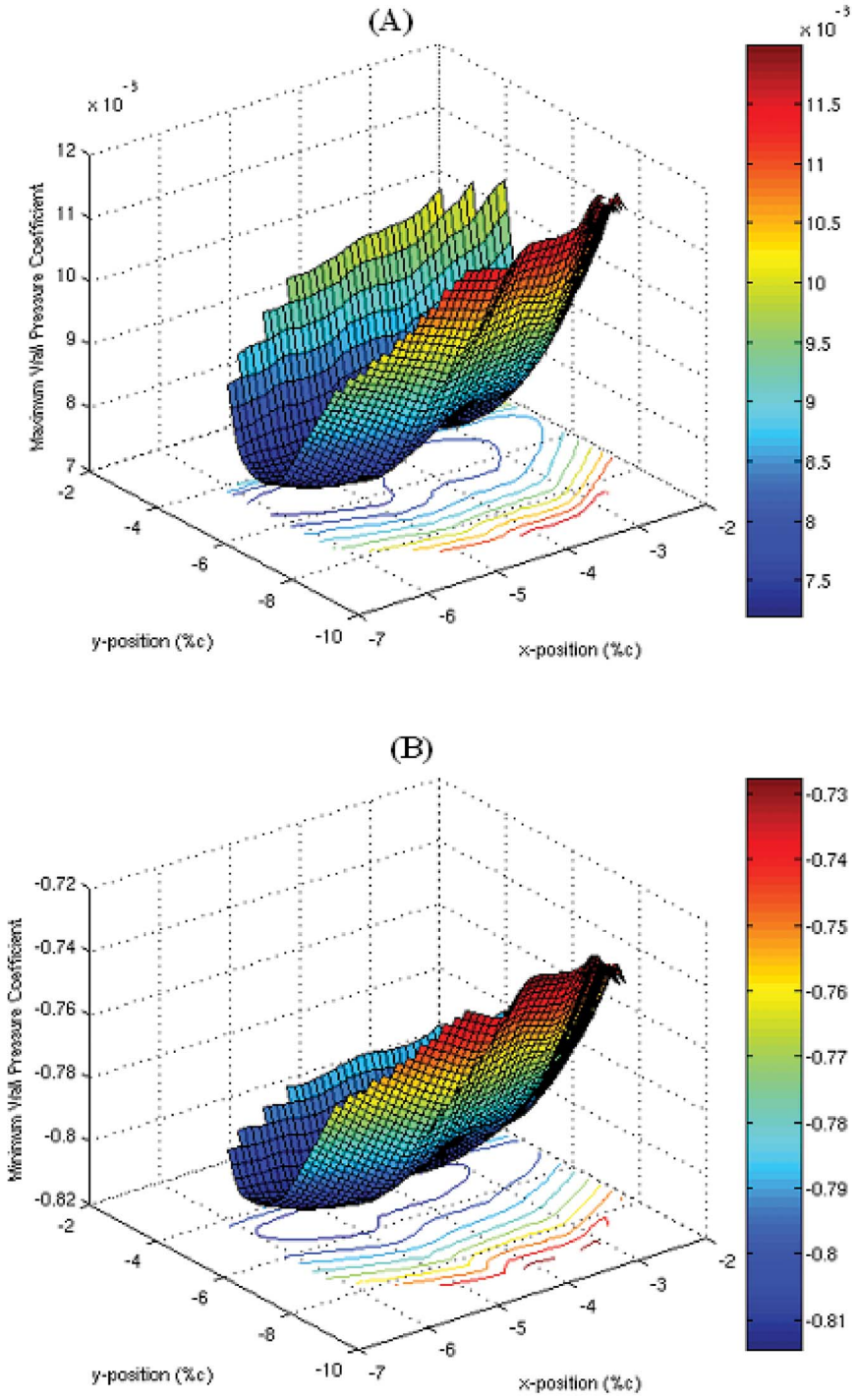

Fig. 15 Surfaces of (*a*) maximum wall pressure coefficient and (*b*) minimum wall pressure coefficient versus flap leading edge *x*- and *y*-positions. The foil is at $\alpha = 1$ deg, and $\delta = 15$ deg for all cases.

seen. Interestingly, increasing the flap angle also has the effect of forcing the stagnation point toward the lower surface of the leading edge of the foil, diminishing the positive pulse on the screen cylinder.

Figure 11 shows the peak positive and negative C_P values on the screen cylinder versus δ for a series of angles-of-attack between $\alpha = -1$ deg and $\alpha = 3$ deg. Varying the flap angle has a similar effect at each of the angles, with a clear optimum existing for minimum C_P and with maximum C_P approaching a negligible value. At lower angles-of-attack, however, the foil is more resistant to stall and the optimal minimum C_P value occurs at higher values of δ.

The α- and δ-sweep data were combined to make surfaces of minimum and maximum C_P values versus both α and δ, as shown in Fig. 12. The surfaces were created from 37 cases using the two-dimensional cubic interpolation functions contained in MATLAB [16]. Minimum C_P is shown to have a strong dependence on flap angle for angles-of-attack at which the flow is fully attached, creating a "troughlike" shape with a clear minimum of $C_P = -0.82$ at $(\alpha, \delta) = (1.2, 16)$. The gradients close to the optimum are

Downloaded 03 Jun 2010 to 171.66.16.158. Redistribution subject to ASME license or copyright; see http://www.asme.org/terms/Terms_Use.cfm

relatively low, however, allowing for flexibility in the foil design. Beyond $\alpha=7$ deg, any deflection of the flap causes the foil to stall and the pressure is not dependent on flap angle. Maximum C_P behaves differently and approaches $C_P=0$ everywhere except at small angles of both α and δ.

6.4 Flap Positioning. The effect of the positioning of the flap foil with respect to the main foil was also studied. There is a special interest in the effect of flap positioning due to the concerns that if the gap between the flap and the main foil is too small, it will become plugged with pulp, shives, or contaminants in the pulp stream. Figures 13 and 14 show the effect of varying the x- and y-position of the leading edge of the flap, respectively, at an angle-of-attack of $\alpha=1$ deg and a flap angle of $\delta=15$ deg. In both cases, the flap leading edge position is measured from the trailing edge of the main foil in percent chord.

As can be seen in Fig. 13, the x-positioning of the flap has little effect on both the negative and positive pulses except for at $x=0.0c$, where the negative pulse diminishes and the positive pulse increases. Figure 14 shows a stronger correlation between the y-position of the flap and both the positive and negative pressure pulses, however. At $y=-0.04c$, the gap between the flap and the main foil is too small and not enough fluid is able to pass through the slot, causing the flap to lose its effect. As the gap is increased to too large of a value, the flap and the main foil lose the ability to interact with each other, causing an increase in positive pulse and a loss of suction.

Once again, surfaces of maximum and minimum C_P were created, this time versus flap foil x- and y-positioning, as shown in Fig. 15. Note that, as previously mentioned, minimum C_P was shown to have a strong dependence on y-position, while the gradients in the x-direction were much smaller. A peak minimum C_P value of $C_P=-0.81$ was found to be at $(x,y)=(-0.050,-0.052)c$. On a typical industrial screen with a chord length on the order of 100 mm, this would correspond to a gap of 2 mm, which, being an order of magnitude larger than the slots in the screen cylinder, is not likely to clog with the debris and fibers being filtered by the screen. Since all maximum C_P are between $C_P=7\times10^{-3}$ and $C_P=1.2\times10^{-2}$, maximum C_P is determined to be close to zero and independent of the flap positioning for this foil configuration.

7 Conclusions

We have studied the ability of multi-element pressure screen rotor foils to provide greater control over the shape and magnitude of the pressure pulses generated by the rotor. Both the negative and positive pressure peaks were shown to have a strong dependence on both angle-of-attack and flap angle. Maximum C_P approached values close to a negligibly small value with increasing α and/or δ. Minimum C_P reached an optimum value with both increasing α and δ before the foil began to separate and suction was lost. The x-positioning of the flap was shown to have little effect on foil performance, while the y-positioning had a large effect on both maximum and minimum C_P values.

In general, the multi-element foil outperformed the single-element NACA 8312 on which it was based. It was able to reach a positive angle-of-attack without stalling, allowing for the positive pressure pulse to be eliminated. Also, the deflection of the flap allowed for a significant increase in the effective camber of the foil, which provided a stronger and wider negative pulse. The minimum negative C_P for the multi-element foil was 15% stronger than that of the single-element NACA 8312. Additionally, the gradients in minimum negative C_P were low near the optimum for the multi-element foil, allowing for flexibility in the design of the foil.

References

[1] Olson, J. A., Turcotte, S., and Gooding, R. W., 2004, "Determination of Power Requirements for Solid Core Pulp Screen Rotors," Nord. Pulp Pap. Res. J., **19**(2), pp. 213–217.

[2] Niinimäki, J., 1999, "Phenomena Affecting the Efficiency of a Pressure Screen," *Proceedings of the Tappi Pulping Conference*, pp. 957–966.

[3] Julien Saint Amand, F., and Perrin, B., 1999, "Fundamentals of Screening: Effect of Rotor Design and Fibre Properties," *Proceedings of the Tappi Pulping Confernce*, pp. 941–955.

[4] Julien Saint Amand, F., and Perrin, B., 2000, "Basic Parameters Affecting Screening Efficiency and Fibre Loss," *Proceedings of the PTS-CTP Deinking Symposium*, pp. 26.1–26.22.

[5] Wakelin, R. F., and Corson, S. R., 1998, "Reject Thickening Behavior of TMP Screening," Pulp Paper Can., **99**(1), pp. 27–30.

[6] Wakelin, R. F., and Corson, S. R., 1995, "TMP Long Fibre Fractionation With Pressure Screens," *Proceedings of the International Mechanical Pulping Conference*, pp. 257–265.

[7] Wakelin, R. F., Blackwell, B. G., and Corson, S. R., 1994, "The influence of Equipment and Process Variables on Mechanical Pulp Fractionation in Pressure Screens," *Proceedings of the Appita Conference*, pp. 611–621.

[8] Pinon, V., Gooding, R. W., and Olson, J. A., 2003, "Measurements of Pressure Pulses From a Solid Core Screen Rotor," Tappi J., **2**(10), pp. 9–12.

[9] Gonzales, J., 2002, "Characterization of Design Parameters for a Free Foil Rotor in a Pressure Screen," M.S. thesis, Department of Mechanical Engineering, University of British Columbia, Vancouver.

[10] Feng, M., Gonzalez, J., Olson, J. A., Ollivier-Gooch, C., and Gooding, R. W., 2005, "Numerical Simulation and Experimental Measurement of Pressure Pulses Produced by a Pulp Screen Foil Rotor," ASME J. Fluids Eng., **127**(2), pp. 347–357.

[11] Abbott, I. H., and Von Doenhoff, A. E., 1949, *Theory of Wing Sections*, McGraw-Hill, New York.

[12] Mahon, S., and Zhang, X., 2005, "Computational Analysis of Pressure and Wake Characteristics of an Aerofoil in Ground Effect," ASME J. Fluids Eng., **127**(2), pp. 290–298.

[13] Pope, S. B., 2000, *Turbulent Flows*, Cambridge, New York.

[14] Fluent, Inc., 2003, FLUENT User's Guide.

[15] Feng, M., 2003, "Numerical Simulation of the Pressure Pulses Produced by a Pressure Screen Foil Rotor," M.S. thesis, Department of Mechanical Engineering, University of British Columbia, Vancouver.

[16] The Mathworks, Inc., 2002, MATLAB Users Guide.

Downloaded 03 Jun 2010 to 171.66.16.158. Redistribution subject to ASME license or copyright; see http://www.asme.org/terms/Terms_Use.cfm

Maximum Drag Reduction Asymptote of Polymeric Fluid Flow in Coiled Tubing

Subhash N. Shah
Stephenson Chair Professor
e-mail: subhash@ou.edu

Yunxu Zhou[1]
Postdoctoral Research Associate
e-mail: YunxuZhou@yahoo.com

Mewbourne School of Petroleum and Geological Engineering,
Well Construction Technology Center,
The University of Oklahoma,
Norman, OK 73019

This study experimentally investigates the drag reduction characteristics of the most commonly used polymer fluids in coiled tubing applications. The flow loop employed consists of 12.7 mm straight and coiled tubing sections. The curvature ratio (a/R, where a and R are the radii of the tubing and the reel drum, respectively) investigated is from 0.01 to 0.076, which covers the typical curvature ratio range encountered in the oil and gas industry applications. Fluids tested include xanthan gum, guar gum, and hydroxypropyl guar at various polymer concentrations. It is found that the drag reduction in coiled tubing is significantly lower than that in straight tubing, probably due to the effect of secondary flow in curved geometry. The onset of drag reduction is also found to be delayed as the curvature ratio was increased. A correlation for the maximum drag reduction (MDR) asymptote in coiled tubing is developed. When the curvature ratio is set to zero, the new correlation reduces to the well-known Virk's MDR asymptote for dilute polymer solutions in straight pipes. A new drag reduction envelope is proposed for the analysis of drag reduction behavior of polymeric fluids in coiled tubing. Application of the new drag reduction envelope is also discussed. [DOI: 10.1115/1.3026578]

Keywords: coiled tubing, drag reduction, polymer fluid, non-Newtonian, stimulation, drilling

Introduction

Frictional pressure in turbulent pipe flow can be drastically reduced by adding small quantities of certain long-chain polymers or surfactants to the solvent, such as water. This phenomenon is called drag reduction. Credit is generally given to Toms [1] for being the first to observe this phenomenon. There have been tremendous studies of drag reduction in a straight pipe. Several authors have provided extensive reviews on this topic, including Lumley [2], Hoyt [3,4], Virk [5], and Berman [6]. Although the drag reduction phenomena have been extensively investigated in recent decades, the underlying mechanisms producing drag reduction are not yet fully understood. Many tentative explanations have been offered to explain the phenomenon, but none of them is entirely convincing. Kostic [7] summarized these theories or hypotheses of drag reduction, which include shear thinning, viscoelasticity, molecular stretching, decreased turbulence production, etc.

In recent years there has been a renewed interest in understanding the mechanisms of drag reduction. In spite of numerous recent studies, a detailed explanation on how minute concentrations of polymer molecules can generate large reductions in turbulent drag still remains a mystery. The development of robust methods for direct numerical simulation (DNS) of viscoelastic turbulent flows has without doubt helped provide better physical understanding. In such simulations, the boundary conditions or governing equations are modified in a controlled manner to elucidate physical patterns.

Housiadas and Beris [8,9] investigated the effects of flow elasticity and inertia in polymer-induced drag reduction through numerical simulations of a turbulent channel flow of dilute polymer solution. In addition, the role of nonconstant viscosity on the modification of the proper wall scaling needed to represent the boundary structure is addressed. Terrapon et al. [10], through Brownian dynamics simulations, reported that polymers experience significant straining around vortices, which results in stretching of polymer molecules. It is postulated that extraction of energy from near-wall vortices by polymer molecules occurs as they are pulled around vortices by upward or downward fluid motion. Dubief et al. [11,12] performed numerical simulations to characterize the action of polymers on turbulence in drag reducing flows. It was found that polymers store and release energy to the flow in a systematic way. As anticipated, the storage of energy occurred around near-wall vortices, while coherent release of energy was observed in the very-near-wall region. The polymer molecules are shown to reduce drag by damping near-wall vortices and to sustain turbulence by providing energy onto the streamwise velocity component in the very-near-wall region. Dimitropoulos et al. [13] investigated the drag reduction in the turbulent boundary layer flow of inhomogeneous polymer solutions using direct numerical simulations. It is found that polymer mixing acts as a relaxation mechanism for drag reduction. The drag reduction, in addition to the elasticity and extensibility of the polymer molecules, depends on the evolution of the near-wall concentration, which enhances an advective transport in the streamwise direction and additive segregation between the wall-layer streaks.

Information in literature on drag reduction in coiled pipes is very scarce. Kelkar and Mashelkar [14] ran tests on aqueous solutions of polyacrylamide through a single coiled tube of 1.25 cm inside diameter and proposed a correlation of reduced friction factor (defined as the ratio of friction factor of polymer solution and friction factor of the purely viscous solvent) as a function of Deborah number. Another relevant research effort was reported by Yokoyama and Tomita [15], who performed tests on dilute aqueous solutions of polyethylene oxide in 360 deg bends with curvature ratios of 0.021, 0.029, and 0.053. It was found that the drag reduction was reduced with increase in curvature ratio.

Recently, Shah and Zhou [16] investigated the drag reduction behavior of polymer fluids in coiled tubing using a full-scale

[1]Now with NOV CTES, 9870 Pozos Lane, Conroe, TX 77303.

Contributed by the Fluids Engineering Division of ASME for publication in the JOURNAL OF FLUIDS ENGINEERING. Manuscript received February 15, 2007; final manuscript received October 11, 2008; published online November 26, 2008. Assoc. Editor: Steven Ceccio. Paper presented at the 2006 ASME International Mechanical Engineering Congress (IMECE2006), Chicago, IL, November 5–10, 2006.

Downloaded 03 Jun 2010 to 171.66.16.158. Redistribution subject to ASME license or copyright; see http://www.asme.org/terms/Terms_Use.cfm

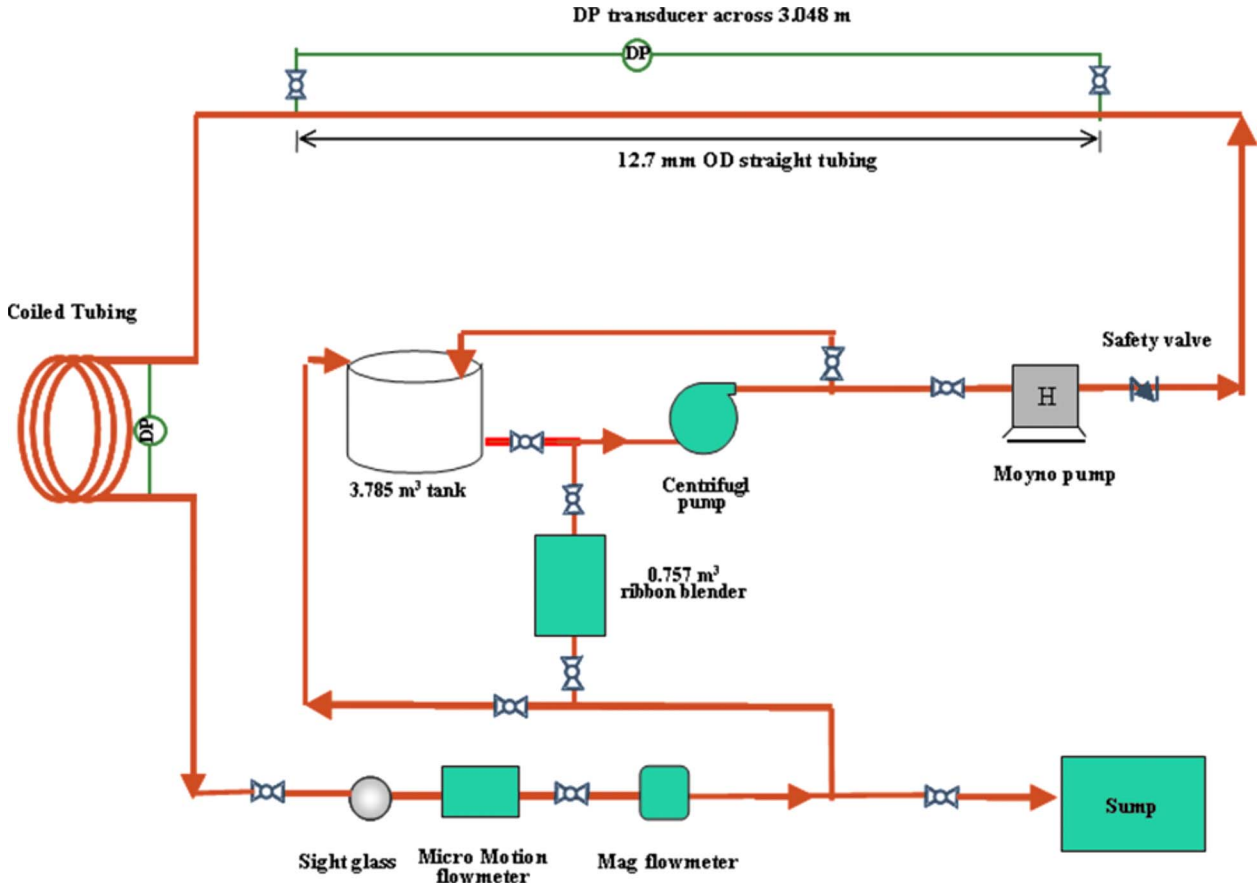

Fig. 1 Schematic of laboratory-scale flow loop

coiled tubing test facility. Interesting and useful observations on the effects of polymer concentration and coiled tubing curvature on drag reduction were provided.

Recent experimental work has indicated that the maximum drag reduction of polymer fluids in coiled tubing is affected by the curvature ratios. The objective of this paper is to present the recent experimental results of drag reduction in coiled tubing and the development of the correlation of the maximum drag reduction asymptote of polymer fluids in coiled tubing.

Experiment

Experimental Setup

Flow Loop. The schematic of the laboratory scale flow loop is shown in Fig. 1. It mainly consists of four coiled tubing reels, one 3.048 m straight tubing (ST) section, fluid mixing and pumping equipment, and data acquisition system.

Coiled Tubing Dimensions. Four coils of 12.7 mm diameter coiled tubing were used in this study. The tubing is 12.7 mm OD and 11.05 mm ID and is made of stainless steel. Their dimensions are given in Table 1. The coils were made by spooling straight stainless steel tubings onto drums with various diameters. Since the tubing diameter is fixed, decreasing the coil diameter (from Coil 1 through Coil 4) increases the curvature ratio. These four coils cover a wide range of curvature ratio from 0.01 to 0.076. The typical range of curvature ratio encountered in the field applications is well within the range of the four coils. The wide curvature ratio range of the present coils helps to investigate the effect of curvature ratio on friction pressure losses in coiled tubing. During flow tests, the four coils can be interchanged through quick connections.

Fluid Mixing and Pumping Equipment. Fluid mixing and storage vessels include a 3.785 m^3 polyethylene storage tank and a 0.757 m^3 ribbon blender. The 3.785 m^3 storage tank serves as a large volume source of test fluid. Pumping is achieved by a Model 6P10 Moyno progressive cavity pump and a Model 5M Deming centrifugal pump. The Moyno pump with its indefinitely variable speed drive can deliver up to approximately 0.53 m^3/min at 4.137 MPa. The centrifugal pump serves to boost the suction of the Moyno pump.

Measurement Instruments and Data Acquisition. A Micro Mo-

Table 1 Dimensions of four 12.7 mm OD coils

No.	Coil diameter (m)	Tubing length (m)	No. of turns	Curvature ratio (a/R)
1	1.100	11.015	3	0.010
2	0.572	5.739	3	0.019
3	0.356	7.090	6	0.031
4	0.146	4.139	7	0.076

Downloaded 03 Jun 2010 to 171.66.16.158. Redistribution subject to ASME license or copyright; see http://www.asme.org/terms/Terms_Use.cfm

Table 2 Power-law model rheological parameters of fluids tested in the 12.7 mm OD flow loop

Fluids	Concentration (kg/m^3)	n	K_p Pa s^n
Xanthan	1.198	0.717	0.0394
	1.797	0.403	0.3616
	2.397	0.365	0.6240
	3.595	0.310	1.4860
Guar	1.198	0.819	0.0092
	2.397	0.619	0.1282
	3.595	0.482	0.5592
HPG	1.198	0.805	0.0171
	2.397	0.598	0.1609
	3.595	0.485	0.6082

tion mass flowmeter (Model CMF050M320NU) was used to measure the flow rate, fluid density and temperature. It measures flow rate in the range 0–0.114 m^3/min, fluid density with accuracy of ± 0.0005 g/cc, and temperature with accuracy of $\pm 1\,^{\circ}C$ or $\pm 0.5\%$ of reading in °C. Honeywell differential pressure transducers (Model STD130) were used for the measurement of frictional pressure losses in a straight tubing section and in coils. Various measurement ranges can be selected between 0 kPa and 689 kPa. The measurement accuracy is $\pm 0.075\%$ of the calibration span. An absolute pressure transducer (Model STG98LC) measures the entry pressure of the system. The flow loop has a working pressure limit of 6.895 MPa.

The data measured by the flowmeters, pressure transducers, as well as pressure gauges were collected and transmitted to a computer, where the data were displayed and saved for later analysis. This task was accomplished by the Fluke Hydra data acquisition system (Model 2625A, Fluke Corporation, Everett, WA). The Fluke Hydra system contains two hydras, each having 21 analog measurement channels. The sample rate is up to 10 samples/s. The Hydra data logger communicates with a host computer via a wireless modem radio link. The wireless tool can allow up to 365.8 m distance between the remote logger and the receiving computer. The data collected are transmitted to a personal computer in the control room and displayed live on computer screen. This helps monitor the test and ensure quality data acquisition.

Fluids Tested. Table 2 shows three polymers, and their concentrations, used in the experiments with the laboratory scale flow loop. A brief description of each fluid is given in the following.

Xanthan. Xanthan gum is a high-molecular-weight biopolymer and is produced by bacterial fermentation of micro-organism *Xanthamonas compestris*. Xanthan gum solutions display remarkable shear-thinning properties. Its major application in drilling fluids is as a suspending agent due to its high viscosity at low shear rate. This shear-thinning property also makes it useful as completion and stimulation fluids. The xanthan polymer used in this study is Xanvis® L of Kelco Oil Field Group (Houston, TX). It is a cream-colored fluid suspension.

Guar and HPG. Guar is a long-chain natural polymer composed of mannose and galactose sugars. Guar gum comes from the endosperm of guar beans. The beans are removed from the bean pod, processed to separate the endosperm from the bean hull and embryo, and ground into a powder. Hydroxypropyl guar (HPG) is obtained by the reaction of propylene oxide with the guar molecules, creating a more temperature stable polymer. It was developed primarily to reduce the residue obtained from guar gum. Guar gum and HPG are the most widely used viscosifiers for water-based fracturing fluids. The guar polymer tested in this study is WG-19 and is a product of Halliburton Energy Services.

Table 2 also shows the rheological parameters when a power-law model ($\tau_w = K_p(8v_m/d)^n$) is used.

Testing Procedure

Fluid Preparation. The fluids were prepared and stored in the 3.785 m^3 polyethylene tank. The mixing procedure recommended by the polymer product supplier was followed. Adequate time was allowed for the gel to hydrate in the mixing tank for proper gelation. Samples of fluid were collected and measured using a Model 35 Fann viscometer to check fluid viscosity.

After the polymer solution was prepared, water was first circulated through the flow loop to conduct a system check. This ensured that the pressure transducer settings and parameter settings of the data acquisition computer were set properly. Water was pumped through both straight and coiled tubings at various flow rates and corresponding pressure drop readings were recorded. The results of water tests were used as the baseline for gel flow data analysis.

Water in the flow loop was then displaced by pumping the test fluid (gel). Once the system was filled with polymer fluid, the drain valve was closed and thus the fluid was pumped in a recirculation mode—from tank to the pump, then through the straight and coiled tubings, and back to the tank. The flow rate was set at a desired value and steady state pressure drop data across straight and coiled tubings were recorded. The flow rate was changed and corresponding pressure drops were recorded. At each flow rate, adequate time was allowed for the flow to achieve a steady state condition. This was confirmed by monitoring the live display of measured flow rate and pressure drop signals.

Fluid samples were collected from the mixing tank at the start of each test. Another sample was collected at the end of the test. The rheology of the samples was evaluated using a Model 35 Fann viscometer. By comparing the samples taken before and after the test, any change in rheology due to polymer degradation and viscous heating can be detected.

After testing with the first coil, the coil was replaced by another coil with a different curvature ratio. A similar test procedure was followed to obtain pressure drop data at various flow rates for all four coils.

Results and Discussion

Drag Reduction and Onset of Drag Reduction. In this study, we followed the original definition of Savins [17] and defined the drag reduction *DR* as follows:

$$DR = 1 - \left(\frac{dp}{dl}\right)_p \Big/ \left(\frac{dp}{dl}\right)_s \tag{1}$$

in which $(dp/dl)_p$ and $(dp/dl)_s$ are the frictional pressure gradients for a polymer solution and the solvent under the same flow conditions, respectively. Assuming that the density of the polymer solution is the same as the density of the solvent (it is a fair assumption for the fluids used in this study), the following equation is applicable:

$$DR = 1 - f_p/f_s \tag{2}$$

in which f_p and f_s are the Fanning friction factors of the polymer solution and the solvent, respectively. *DR* is usually expressed in percentage. The Fanning friction factors, f_p and f_s, can be calculated from Eqs. (3) and (4).

The Fanning friction factor was calculated from the following relationship:

$$f = \frac{\tau_w}{\frac{1}{2}\rho v_m^2} \tag{3}$$

in which the wall shear stress τ_w is calculated from

Downloaded 03 Jun 2010 to 171.66.16.158. Redistribution subject to ASME license or copyright; see http://www.asme.org/terms/Terms_Use.cfm

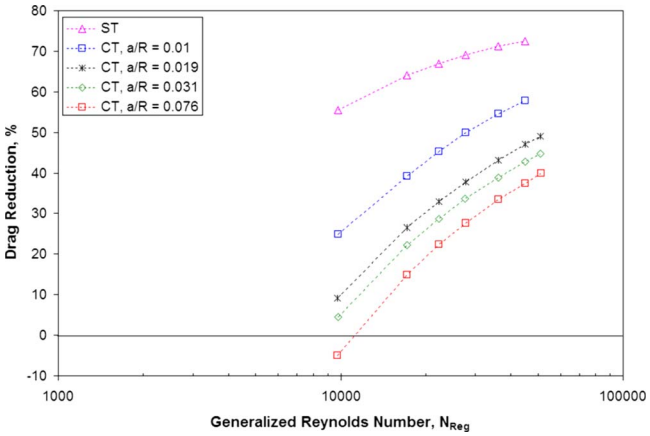

Fig. 2 Drag reduction of 1.198 kg/m^3 HPG in 12.7 mm OD straight and coiled tubing

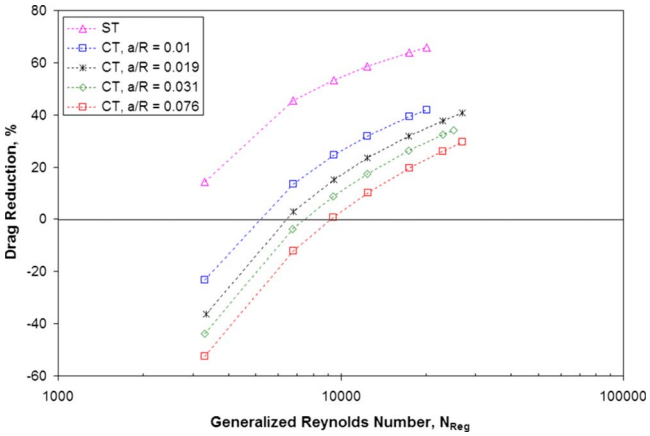

Fig. 4 Drag reduction of 3.595 kg/m^3 HPG in 12.7 mm OD straight and coiled tubing

$$\tau_w = \frac{d\Delta p}{4l} \tag{4}$$

where d is the tubing inside diameter and Δp is the frictional pressure drop over a tubing length of l. Therefore, once the frictional pressure drop for a certain tubing length at a pump rate is obtained from a flow test, the DR can be calculated with the above equations.

Kostic [7] termed the definition given by Eq. (1) as the pressure-drop drag reduction and the definition given by Eq. (2) as the friction factor drag reduction. There has been confusion about these two definitions in the drag reduction literature [4,7]. There could be confusion if the friction factors, f_s and f_p, are calculated at the "same Reynolds number." As pointed out by Kostic, if DR is calculated at the same Reynolds number using Eq. (2), the two definitions will not be the same unless in the case of very dilute polymer solutions with the viscosity of solutions equal to that of the solvent. In this study, we want to stress that the definitions given by Eqs. (1) and (2) are consistent as long as the friction factors, f_s and f_p, are calculated at the "same flow rate."

Figures 2–4 show the plots of drag reduction versus generalized Reynolds number for 1.198 kg/m^3, 2.397 kg/m^3, and 3.595 kg/m^3 (1200 ppm, 2400 ppm, and 3600 ppm) HPG solutions in the four coils and straight section of 12.7 mm diameter. The effect of curvature ratio on drag reduction can be seen clearly. The drag reduction in a straight tubing is significantly higher than in a coiled tubing. The tighter the coil was spooled, the lower the drag reduction in that coil. In literature we found only the results of Yokoyama and Tomita [15] to be comparable with our results. Their results of drag reduction in a coiled tube are shown in Fig. 5. The fluids they used were 1–100 ppm aqueous solutions of polyethylene oxide. They used a single turn (360 deg bend) of copper pipes of 1.4 cm inside diameter. The curvature ratios were a/R=0.021, 0.029, and 0.053 or R/a=47.3, 34.3, and 18.7. Their results show that as curvature ratio (a/R) is increased, the drag reduction is decreased. But, compared to our results, their data are less systematic and quite limited.

Another value that can be derived from plots such as Figs. 2–4 is that they can provide information about the onset of drag reduction. This can be understood better by examining the results of Figs. 3 and 4. The interceptions of the data with the zero-drag reduction line should correspond to the generalized Reynolds number at the onset of drag reduction. Figures 3 and 4 clearly indicate that as curvature ratio increases, the onset of drag reduction is obviously delayed.

In contrast, the drag reduction in a straight tubing has always been present in these tests, even at the lowest flow rate and more concentrated polymer solutions. Therefore, drag reduction in straight tubing occurs much earlier than in coiled tubing. Table 3 summarizes the generalized Reynolds number at the onset of drag reduction for the three types of polymer solutions in a 12.7 mm tubing. In Table 3, the values of critical Reynolds number predicted for the Newtonian laminar-turbulent transition in a coiled

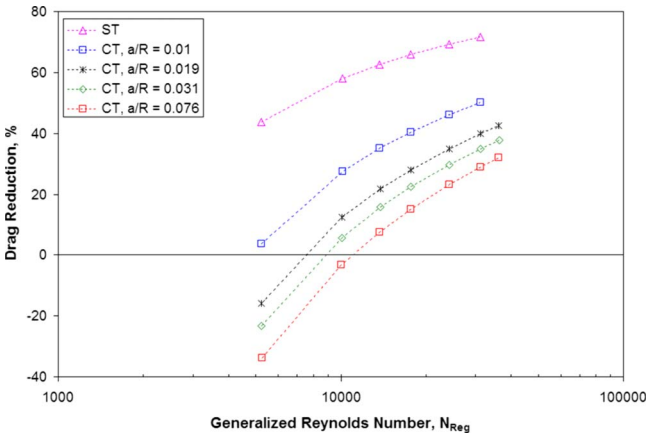

Fig. 3 Drag reduction of 2.397 kg/m^3 HPG in 12.7 mm OD straight and coiled tubing

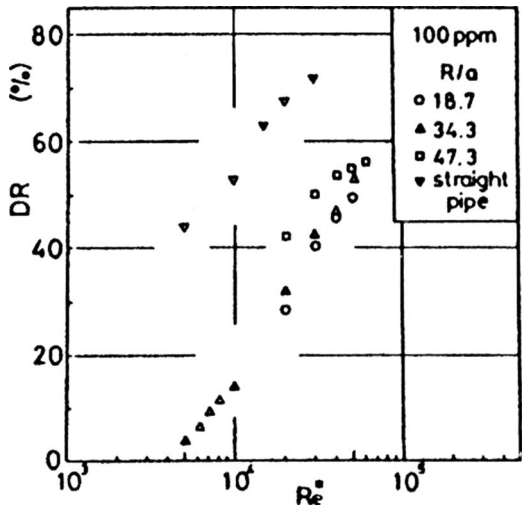

Fig. 5 Effect of curvature ratio on drag reduction studied by Yokoyama and Tomita (Ref. [15])

Downloaded 03 Jun 2010 to 171.66.16.158. Redistribution subject to ASME license or copyright; see http://www.asme.org/terms/Terms_Use.cfm

Table 3 Generalized Reynolds number at onset of drag reduction in a 12.7 mm OD coiled tubing

	Curvature ratio			
Fluid	0.01	0.019	0.031	0.076
2.397 kg/m^3 xanthan	3700	6800	7300	9200
3.595 kg/m^3 xanthan	5800	8000	9300	11,500
2.397 kg/m^3 HPG	4800	7500	9000	11,000
3.595 kg/m^3 HPG	5200	6400	7300	9300
2.397 kg/m^3 guar	4800	7200	8500	10,500
3.595 kg/m^3 guar	4800	7100	8000	10,000
$N_{\mathrm{Re}\,c}$ by Srinivasan et al.[a]	4620	5574	6537	9047

[a]Reference [18].

tubing are also included for comparison. These were calculated using the following correlation of Srinivasan et al. [18] for critical Reynolds number for Newtonian fluids in a coiled pipe:

$$N_{\mathrm{Re}\,c} = 2100\left[1 + 12\left(\frac{a}{R}\right)^{0.5}\right] \tag{5}$$

It can be seen that the generalized Reynolds number at the onset of drag reduction is higher than the critical Reynolds number for Newtonian turbulent flow in coiled tubing (except for 2.397 kg/m^3 (2400 ppm) xanthan in the coil with $a/R=0.01$). Based on the data in Table 3 empirical correlation was obtained for the critical generalized Reynolds number at the onset of drag reduction for the flow of a polymer fluid in a coiled tubing:

$$N^*_{\mathrm{Re}\,g} = c_1 - \frac{c_2}{(a/R)^{0.5}} \tag{6}$$

where $c_1=13{,}172$, $c_2=835.33$, and $a/R=$curvature ratio.

The above correlation for predicting Reynolds number at the onset of drag reduction is compared with the results of tests in the field-size flow loop. The detailed description of the field-size flow loop can be found elsewhere [16,19]. We chose the test data of guar fluids in a 60.33 mm tubing for our analysis, since flow in smaller tubing sizes does not show onset of drag reduction (drag reduction is always present even at low flow rates). Figure 6 shows the plots of drag reduction versus generalized Reynolds number for guar solutions in a 60.33 mm tubing. From the interception of data points with the zero-drag reduction line, the onset Reynolds number for guar fluids in this tubing size is roughly estimated as $N^*_{\mathrm{Re}\,g}=7900$, which is close to 7031, as predicted by Eq. (6). Therefore, Eq. (6) can be used to predict the onset of drag reduction in other coiled tubing sizes.

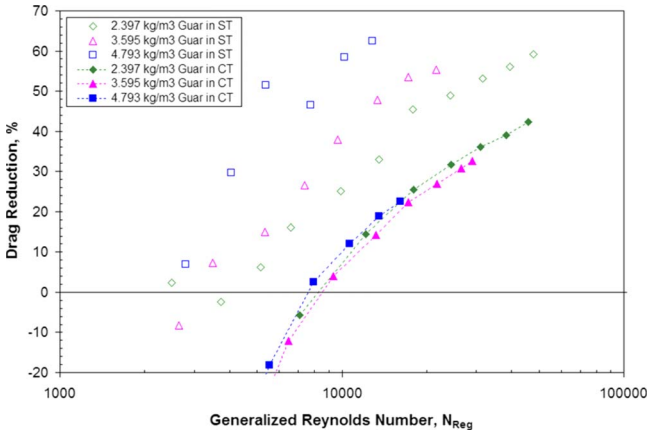

Fig. 6 Drag reduction of guar fluids in 60.33 mm OD straight and coiled tubing ($a/R=0.0185$)

Maximum Drag Reduction Asymptote in Coiled Tubing. For turbulent flow of dilute polymer solutions in straight pipes, Virk et al. [20] proposed an ultimate drag reduction asymptote as given by

$$1/\sqrt{f} = 19.0\log_{10} N_{\mathrm{Re}}\sqrt{f} - 32.4 \tag{7}$$

This correlation is a mean curve of maximum drag reduction data from nine sources with a total of 235 data points. The maximum scatter of the data is $\pm 15\%$. This maximum drag reduction correlation has been referenced by numerous authors in literature on drag reduction or has been used as a reference line for friction pressure analysis of drag-reducing fluids.

Data analysis of friction behavior of polymeric fluids has indicated that the friction factor in straight tubing can be close to or even below the Virk asymptote [19]. The friction factor of more concentrated polymer solutions in straight tubing can be below the Virk asymptote because they are more shear-thinning than the dilute polymer solutions. But, it is evident that the friction factor in coiled tubing never reaches the Virk asymptote. As a matter of fact, the friction factor in coiled tubing is bounded by lines that are functions of the curvature ratio. These bounding lines are called the drag reduction asymptotes in coiled tubing. Virk's asymptote is just a limiting case of the curved tubing asymptotes. In the following, we develop equations for these asymptotes in coiled tubing.

Development of Maximum Drag Reduction Asymptote for Coiled Tubing. First, for each curvature ratio (corresponding to each coil in the laboratory-scale tests), the friction factor data of all fluids at all concentrations were plotted on the same plot as the Fanning friction factor versus generalized Reynolds number. Then, the data points were compared and those data points that showed high friction factor were removed, while those that showed minimum friction factor were kept. This procedure was repeated for other curvature ratios and thus, four data sets of minimum friction factor corresponding to four curvature ratios were obtained. Then, these four data sets were plotted on the Prandtl–Karman coordinates, as shown in Fig. 7.

Clearly, these data sets are straight lines and are curve-fitted with the following equation:

$$\frac{1}{\sqrt{f}} = A\log[N_{\mathrm{Re}\,g}\sqrt{f}] + B \tag{8}$$

The values of correlation constants A and B are given in Table 4.

The correlation constants of the Virk asymptote are also included in Table 4 as a special case with $a/R=0$ for straight tubing. Constants A and B have strong correlations with curvature ratio and are correlated as follows:

Downloaded 03 Jun 2010 to 171.66.16.158. Redistribution subject to ASME license or copyright; see http://www.asme.org/terms/Terms_Use.cfm

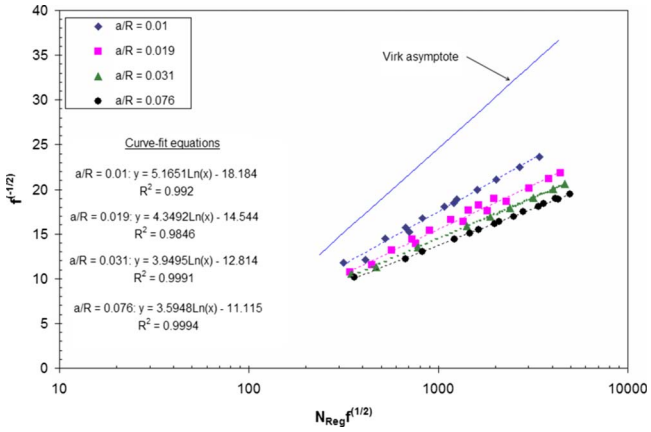

Fig. 7 Friction factors at maximum drag reduction for CT on Prandtl–Karman coordinates, $1/\sqrt{f}$ versus $N_{Re\,g}\sqrt{f}$

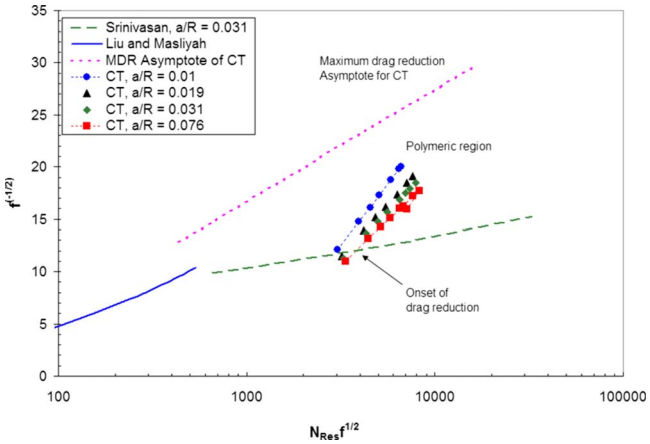

Fig. 8 Drag reduction envelope showing the drag reduction behavior of 3.595 kg/m^3 xanthan in 12.7 mm OD CT

$$A = \left[c_1 + c_2 \left(\frac{a}{R} \right)^{0.5} \right]^{-1} \tag{9}$$

where c_1=0.053109965 and c_2=0.29465004 with correlation coefficient R^2=0.9814.

$$B = \left[c_3 + c_4 \left(\frac{a}{R} \right)^{0.5} \right]^{-1} \tag{10}$$

where c_3=0.0309447 and c_4=0.245746 with correlation coefficient R^2=0.9924. Therefore, the maximum drag reduction asymptotes for coiled tubing can be written as

$$\frac{1}{\sqrt{f}} = \frac{1}{0.05311 + 0.29465 \left(\frac{a}{R} \right)^{0.5}} \log_{10}[N_{Re\,g}\sqrt{f}] + \frac{1}{0.03094 + 0.24575 \left(\frac{a}{R} \right)^{0.5}} \tag{11}$$

When a/R=0, A=18.83 and B=32.32. These values of A and B are very close to Virk's constants of 19.0 and 32.4, respectively, for straight tubing. Therefore, Eq. (11) reduces to the Virk asymptote for straight tubing.

Drag Reduction Envelope for Coiled Tubing. Parallel to the work of Virk [5], we constructed the drag reduction envelope for coiled tubing as follows. Drag reduction in coiled tubing is bounded by three lines—the laminar flow correlation, the maximum drag reduction (MDR) asymptote for coiled tubing (CT), and the zero-drag reduction line which is represented by the correlation of Srinivasan et al. [18] for Newtonian turbulent flow in coiled tubing. For the laminar flow regime, we chose the correlation of Liu and Masliyah [21] based on its performance in predicting the laminar friction factor in coiled tubing [22]. Figure 8 shows an example of drag reduction envelope for coiled tubing. It should be noted that all three bounding lines in the drag reduction envelope are functions of the curvature ratio. This is different from the Virk drag reduction envelope where the bounding lines—Hagen–Poiseuille law, Prandtl–Karman law, and Virk asymptote—are fixed.

Table 4 Correlation constants of the maximum drag reduction asymptotes in CT

a/R	A	B
0	19.0	32.4
0.010	11.893	18.184
0.019	10.014	14.544
0.031	9.094	12.814
0.076	8.277	11.115

Application of CT Drag Reduction Envelope

Effect of Curvature Ratio. As an example, Figs. 9 and 10 show the drag reduction behavior of 1.198 kg/m^3 and 3.595 kg/m^3 HPG fluids on the drag reduction envelope of coiled tubing. Similar drag reduction plots for xanthan fluids in the 12.7 mm tubing system are shown in Figs. 11 and 12. In constructing these envelopes, a curvature ratio of a/R=0.019 was used with the correlation of Srinivasan et al. [18], Liu–Masliyah [21] correlation, and the new MDR asymptote for CT. Several observations can be made based on the results of Figs. 9–12. First, the data exhibit a more or less straight line trend. The slopes of these lines increase slightly with decreasing curvature ratio. The smaller the curvature ratio, the closer the data lines are to the maximum drag reduction asymptote. Second, the intersection points of the data lines with the zero-drag reduction line represent the onset of drag reduction. It can be seen that increasing the curvature ratio delays the onset of drag reduction. Careful observation of Figs. 9 and 10 indicates that the onset points from these plots are consistent with what were shown in Figs. 2 and 4.

Effect of Polymer Concentration on Drag Reduction. Figures 13 and 14 show the effect of polymer concentration on the drag

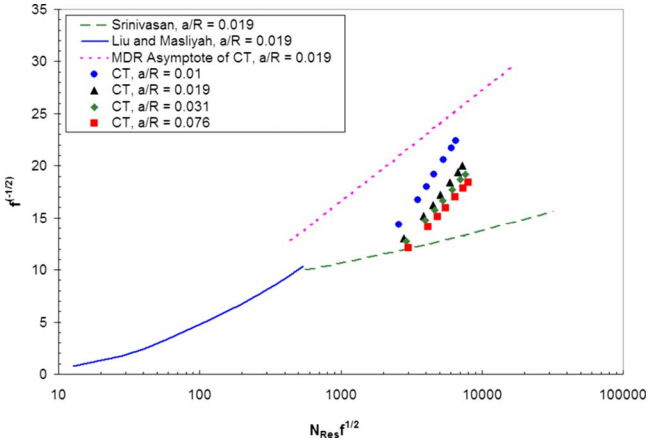

Fig. 9 Effect of curvature ratio on DR of 1.198 kg/m^3 HPG in 12.7 mm OD coiled tubing

Downloaded 03 Jun 2010 to 171.66.16.158. Redistribution subject to ASME license or copyright; see http://www.asme.org/terms/Terms_Use.cfm

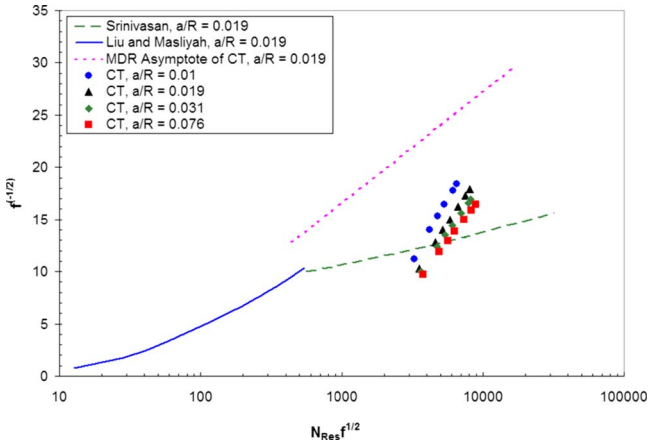

Fig. 10 Effect of curvature ratio on DR of 3.595 kg/m^3 HPG in 12.7 mm OD coiled tubing

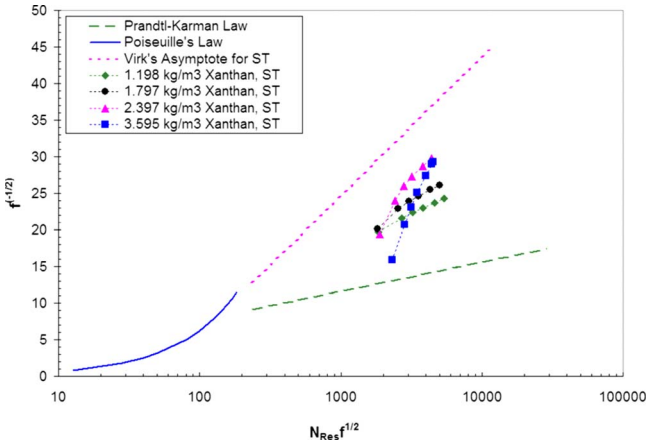

Fig. 13 Effect of xanthan concentration on DR in 12.7 mm OD straight tubing

reduction behavior of xanthan fluids in a straight tubing and a coiled tubing with a curvature ratio of 0.019, respectively. For xanthan fluids in coiled tubing, xanthan concentration has little effect on the slopes of the data lines. We only see a slight decrease in slope in the case of $a/R=0.019$. It can be observed from Fig. 13 that as xanthan polymer concentration increases, the slopes of the data also increase. This is in agreement with Virk's [5] study for drag reduction in a straight pipe. Further decrease in xanthan concentration below 2.397 kg/m^3 reduces the slopes and the vertical position of the data lines of 1.198 kg/m^3 and 1.797 kg/m^3 xanthan solutions. This implies that to minimize the friction factor in straight tubing, xanthan concentration should be higher than 1.797 kg/m^3, whereas for coiled tubing, lower xanthan concentration seems to be more favorable in reducing friction factor. Therefore, the drag reduction envelope can serve as a useful tool in selecting the optimum polymer concentration for drag reduction.

To further illustrate the application of the drag reduction envelope, we can examine the friction results of xanthan fluids tested using the field-size flow loop. Figures 15 and 16 show the results of 1.198 kg/m^3, 2.397 kg/m^3, and 4.793 kg/m^3 (1200 ppm, 2400 ppm, and 4800 ppm) xanthan fluids in 25.4 mm and 60.33 mm coiled tubings, respectively. For 1.198 kg/m^3 (1200 ppm) xanthan in 60.33 mm tubing, the data slope is changed when ($N_{\mathrm{Re},s}f^{1/2}$) is increased. At low flow rate (low $N_{\mathrm{Re},s}f^{1/2}$), the slope is greater, implying that higher drag reduction can be achieved by increasing flow rate. But beyond a certain value of $N_{\mathrm{Re},s}f^{1/2}$, the data points of 1.198 kg/m^3 xanthan fluid turn toward the zero-drag reduction line. This behavior is even more pronounced in the smaller tubing size (25.4 mm). In the case of 25.4 mm coiled tubing, the slope of data points of 1.198 kg/m^3 xanthan fluid approaches almost zero. Therefore, there would be no further gain in drag reduction for 1.198 kg/m^3 xanthan fluid with increased rate. The practical value of the drag

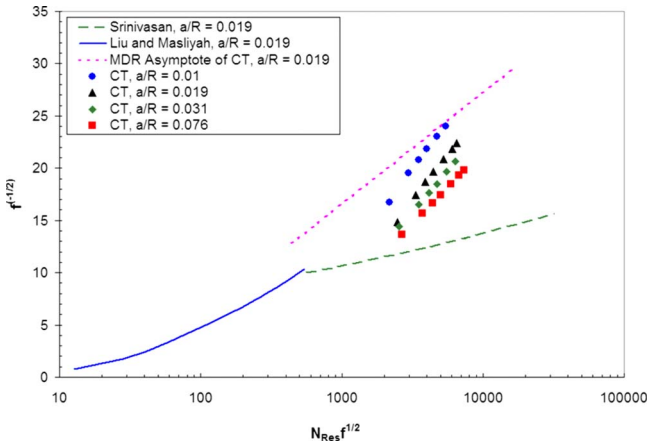

Fig. 11 Effect of curvature ratio on DR of 1.198 kg/m^3 xanthan in 12.7 mm OD coiled tubing

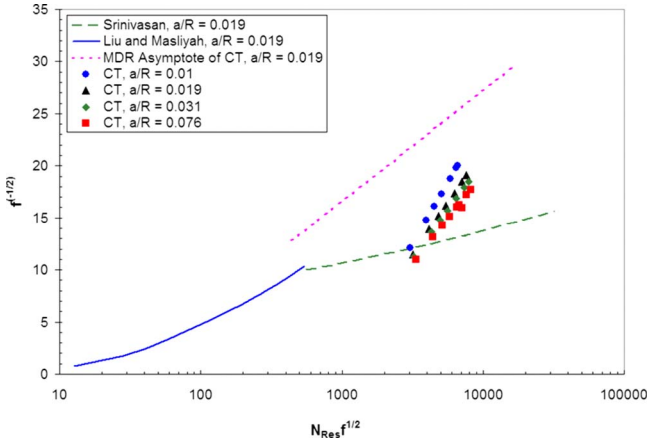

Fig. 12 Effect of curvature ratio on DR of 3.595 kg/m^3 xanthan in 12.7 mm OD coiled tubing

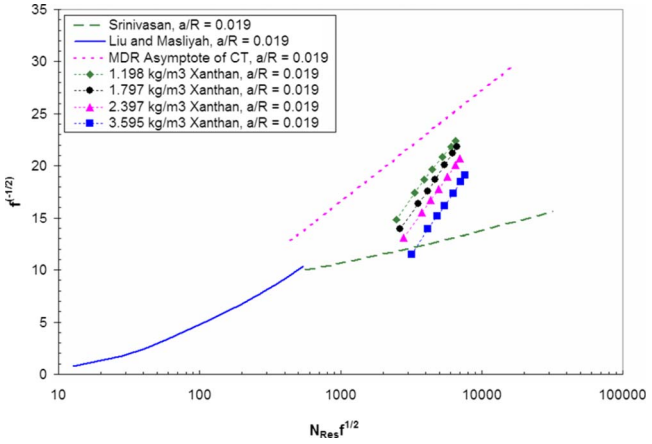

Fig. 14 Effect of xanthan concentration on DR in 12.7 mm OD coiled tubing with curvature ratio $a/R=0.019$

Downloaded 03 Jun 2010 to 171.66.16.158. Redistribution subject to ASME license or copyright; see http://www.asme.org/terms/Terms_Use.cfm

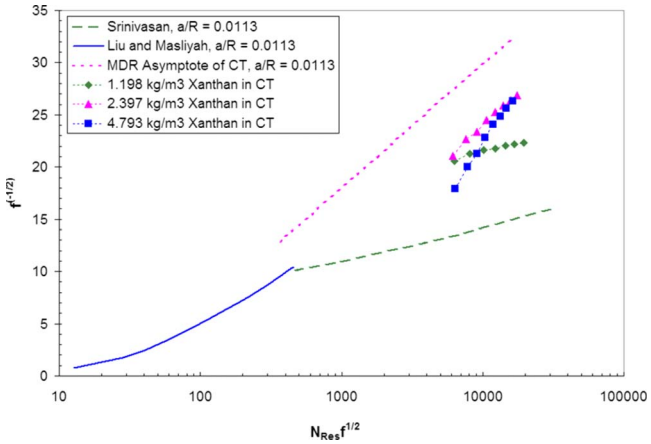

Fig. 15 Effect of xanthan concentration on DR in 25.4 mm OD coiled tubing with curvature ratio a/R=0.0113

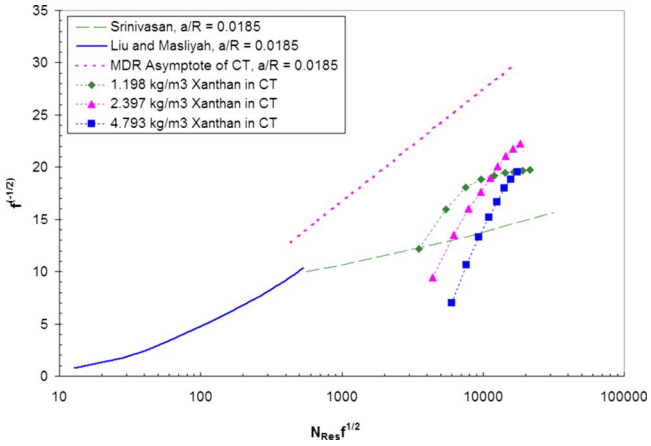

Fig. 16 Effect of xanthan concentration on DR in 60.33 mm OD coiled tubing with curvature ratio a/R=0.0185

reduction analysis in this case is that the maximum drag reduction could not be reached with 1.198 kg/m^3 xanthan fluid. Employing xanthan fluid with higher concentrations should be considered.

Conclusions

The polymer fluids (xanthan, guar, and HPG) tested in this study displayed significant drag reduction properties in both straight and coiled tubings. It was found that the coiled tubing curvature reduces the drag reduction and also delays the onset of drag reduction of polymer fluids in coiled tubing.

Based on the drag reduction data of a 12.7 mm laboratory-scale flow loop, a new correlation of MDR asymptote for polymeric fluids in coiled tubing has been developed. When the curvature ratio is set to zero, this new correlation reduces to Virk's MDR asymptote for dilute polymer solutions in straight pipes. Therefore, this new correlation is more universal than the well-known Virk's MDR asymptote for a straight pipe.

A new drag reduction envelope for polymeric fluid flow in coiled tubing is also proposed. It has been demonstrated with examples that the drag reduction envelope is a useful tool for analyzing the drag reduction behavior of polymer fluids in coiled tubing.

Acknowledgment

The authors would like to gratefully acknowledge the research team (especially Mr. Joe Flenniken) of the Well Construction Technology Center for their help with the experiments. They also wish to thank the members of the joint-industry Coiled Tubing Consortium for their continued support.

Nomenclature

a = radius of tubing
A = correlation constant Eq. (8)
B = correlation constant Eq. (8)
c_1-c_4 = correlation constants
d = inside diameter of tubing
DR = drag reduction Eqs. (1) and (2)
f = Fanning friction factor
f_p = Fanning friction factor of polymer solution
f_s = Fanning friction factor of solvent
K_p = consistency index of power-law fluid from pipe viscometer data
l = tubing length over which Δp is measured
n = flow behavior index of power-law model
N_{Re} = Reynolds number
$N_{\mathrm{Re}\,c}$ = critical Reynolds number
$N_{\mathrm{Re}\,g}$ = generalized Reynolds number
$N^*_{\mathrm{Re}\,g}$ = generalized Reynolds number at onset of drag reduction
$N_{\mathrm{Re}\,s}$ = Reynolds number based on solvent viscosity
Δp = frictional pressure drop over tubing length of l
$(dp/dl)_p$ = frictional pressure gradient of polymer solution
$(dp/dl)_s$ = frictional pressure gradient of solvent
R = radius of curvature of the coiled tubing reel
Re* = Reynolds number based on non-Newtonian viscosity of solution (Ref. [15])
v_m = mean velocity
τ_w = wall shear stress
ρ = fluid density

References

[1] Toms, B. A., 1948, "Some Observations on the Flow of Linear Polymer Solutions Through Straight Tubes at Large Reynolds Numbers," *Proceedings of the First International Congress on Rheology*, North Holland, Amsterdams vol. 2, pp. 135–141.
[2] Lumley, J. L., 1969, "Drag Reduction by Additives," Annu. Rev. Fluid Mech., **1**, pp. 367–384.
[3] Hoyt, J. W., 1972, "The Effect of Additives on Fluid Friction," ASME J. Basic Eng., **94**(2), pp. 258–285.
[4] Hoyt, J. W., 1990, "Drag Reduction by Polymers and Surfactants," *Viscous Drag Reduction in Boundary Layers*, D. M. Bushnell and J. N. Hefner eds., American Institute of Aeronautics and Astronautics, Washington, DC.
[5] Virk, P. S., 1975, "Drag Reduction Fundamentals," AIChE J., **21**(4), pp. 625–656.
[6] Berman, N. S., 1978, "Drag Reduction by Polymers," Annu. Rev. Fluid Mech., **10**, pp. 47–64.
[7] Kostic, M., 1994, "On Turbulent Drag and Heat Transfer Reduction Phenomena and Laminar Heat Transfer Enhancement in Non-Circular Duct Flow of Certain Non-Newtonian Fluids," Int. J. Heat Mass Transfer, **37**(1), pp. 133–147.
[8] Housiadas, K. D., and Beris, A. N., 2003, "Polymer-Induced Drag Reduction: Effects of the Variations in Elasticity and Inertia in Turbulent Viscoelastic Channel Flow," Phys. Fluids, **15**(8), pp. 2369–2384.
[9] Housiadas, K. D., and Beris, A. N., 2004, "Characteristic Scales and Drag Reduction Evaluation in Turbulent Channel Flow of Nonconstant Viscosity Viscoelastic Fluids," Phys. Fluids, **16**(5), pp. 1581–1586.
[10] Terrapon, V. E., Dubief, Y., Moin, P., Shaqfeh, E. S. G., and Lele, S. K., 2004, "Simulated Polymer Stretch in a Turbulent Flow Using Bronian Dynamics," J. Fluid Mech., **504**, pp. 61–71.
[11] Dubief, Y., Terrapon, V. E., White, C. M., Shaqfeh, E. S. G., Moin, P., and Lele, S. K., 2005, "New Answers on the Ineraction between Polymers and Vortices in Turbulent Flows," Flow, Turbul. Combust., **74**, pp. 311–329.
[12] Dubief, Y., White, C. M., Terrapon, V. E., Shaqfeh, E. S. G., Moin, P., and Lele, S. K., 2004, "On the Coherent Drag-Reducing and Turbulence-Enhancing Behavior of Polymers in Wall Flows," J. Fluid Mech., **514**, pp. 271–280.
[13] Dimitropoulos, C. D., Dubief, Y., Shaqfeh, E. S. G., and Moin, P., 2006, "Direct Numerical Simulation of Polymer-Induced Drag Reduction in Turbulent Boundary Layer Flow of Inhomogeneous Polymer Solutions," J. Fluid Mech., **566**, pp. 153–162.
[14] Kelkar, J. V., and Mashelkar, R. A., 1972, "Drag Reduction in Dilute Polymer

Downloaded 03 Jun 2010 to 171.66.16.158. Redistribution subject to ASME license or copyright; see http://www.asme.org/terms/Terms_Use.cfm

Solutions," J. Appl. Polym. Sci., **16**, pp. 3047–3046.
[15] Yokoyama, T., and Tomita, Y., 1986, "Flow of Dilute Polymer Solutions Through Curved Bends," Bull. JSME, **29**(252), pp. 1740–1745.
[16] Shah, S. N., and Zhou, Y., 2003, "An Experimental Study of Drag Reduction of Polymer Solutions in Coiled Tubing," SPEPF, **18**(4), pp. 280–287.
[17] Savins, J. G., 1964, "Drag Reduction Characteristics of Solutions of Macromolecules in Turbulent Pipe Flow," SPEJ, **4**(3), pp. 203–214.
[18] Srinivasan, P. S., Nandapurkar, S. S., and Holland, F. A., 1970, "Friction Factors for Coils," Trans. Inst. Chem. Eng., **48**, pp. T156-T161.
[19] Zhou, Y., 2006, "Theoretical and Experimental Studies of Power-Law Fluid Flow in Coiled Tubing," Ph.D. thesis, University of Oklahoma, Norman, OK.
[20] Virk, P. S., Mickley, H. S., and Smith, K. A., 1970, "The Ultimate Asymptote and Mean Flow Structure in Toms Phenomenon," ASME J. Appl. Mech., **37**, pp. 488–493.
[21] Liu, S., and Masliyah, J. H., 1993, "Axially Invariant Laminar Flow in Helical Pipes With a Finite Pitch," J. Fluid Mech., **251**, pp. 315–353.
[22] Zhou, Y., and Shah, S. N., 2004, "Fluid Flow in Coiled Tubing: A Literature Review and Experimental Investigation," J. Cdn. Pet. Tech., **43**(6), pp. 52–61.

Downloaded 03 Jun 2010 to 171.66.16.158. Redistribution subject to ASME license or copyright; see http://www.asme.org/terms/Terms_Use.cfm

PIV Investigation of Flow Behind Surface Mounted Detached Square Cylinder

P. K. Panigrahi
Department of Mechanical Engineering,
IIT Kanpur,
Kanpur UP 208016, India
e-mail: panig@iitk.ac.in

The flow field behind surface mounted detached square ribs under the approaching flat plate turbulent boundary layer has been experimentally studied using the particle image velocimetry (PIV) (two-component and stereo) technique in both streamwise and cross stream measurement planes. An oil film visualization study has been carried out for correlating the surface flow patterns to the flow structures. The Reynolds number based on the rib height is equal to 11,075. The ratio of the gap height to the square rib size is set equal to 0.2, 0.37, 0.57, and 1.0. The ratio of approaching boundary layer thickness to rib height is equal to 0.2. The mean and rms velocity fields, streamwise and spanwise vorticity fields, velocity gradient and velocity vector fields, turbulent kinetic energy budgets, and stream trace results are reported. The second invariant of the velocity gradient tensor results are presented to distinguish between the rotational and shear contribution of the vorticity field. The recirculation bubbles with a focilike structure are observed behind the detached ribs. These structures are displaced upward, i.e., away from the wall surface with an increase in gap size of the detached cylinder. The size of the recirculation bubble also drops with an increase in the gap size. The stream traces in the cross stream plane show node-saddle patterns, whose near wall concentration is high for a lower gap size detached cylinder. The oil film visualization images show saddle patterns at the meeting point between the flow through the gap and the reattaching shear layer for the lower gap size detached cylinder. The v-velocity magnitude distribution shows greater wall-normal motion across the wake for the detached cylinder of lower gap size. There is a significant near wall velocity fluctuation for the lower gap size detached cylinder. The higher velocity fluctuation due to the near wall flow structures contributes toward an increase in the near wall mixing of a detached cylinder geometry. Overall, the present study clearly demonstrates the flow structures behind detached ribs, which are responsible for effective near wall mixing. The results from this study provide useful understanding for the design of turbulators in various practical applications.
[DOI: 10.1115/1.3026721]

Introduction

The flow around a bluff body placed near a plane wall is of practical significance due to the presence of similar geometrical configurations in many practical applications. Detached cylinders have the potential to act as effective turbulators for the modification of turbulence in various energy devices. The placement of bluff bodies near a plane wall may act toward the modification of near wall mixing, leading to effective heat/mass transfer enhancement. Taniguchi and Miyakoshi [1] experimentally investigated the flow around a circular cylinder placed close to the wall. They observed the formation of Karman vortex streets behind the cylinder, which abruptly get suppressed when the bottom of the cylinder come into contact with the outer region of the boundary layer developing on the bottom wall. Durao et al. [2] reported detailed laser doppler velocimetry (LDV) measurements of a square cylinder placed above a plane wall for a gap to cylinder size range between 0.25 and 0.5. They observed the suppression of regular vortex shedding for a gap to cylinder size ratio less than 0.35. The time averaged separation region length increases due to the proximity of the cylinder from the wall surface. The magnitude of turbulent stresses decreases due to the proximity of the cylinder to the wall. Buresti and Lanciotti [3] carried out experimental investigations of a circular cylinder placed near a plane wall. They reported the critical gap to height ratio for suppression of vortex shedding to drop from 0.4 to 0.3 for a smaller wall boundary layer thickness ($\delta/d=0.1$) compared to larger boundary layer thicknesses ($\delta/d=0.45$ and 1.1).

Liou and Wang [4] studied heat transfer in a developing rectangular duct with a detached square rib array for wall gap to rib height ratio equal to 0.58. The gap size was selected based on earlier results of a detached circular cylinder, at which heat transfer augmentation was most effective. For the detached rib array, a maximum of 40% heat transfer augmentation compared to the attached rib was observed at equal pumping power constraints. The problem of deterioration in heat transfer immediately behind the attached ribs was alleviated for the detached rib configuration.

Bosch et al. [5] studied flow behind a square cylinder near a wall using LDV. They observed suppression of vortex shedding below a critical gap height. This suppression of vortex shedding is not abrupt, and there is a transition range of gap size in which shedding is quasiperiodic in nature. The vortices shed from the bottom side of the cylinder get elongated, vortex trajectories move away from the wall, and the wake becomes oblique in nature. Bailey et al. [6] reported the three dimensional nature of vortex shedding using spanwise surface pressure measurements for a square cylinder near a solid wall as a function of gap size. They observed the relationship between oblique vortex shedding angle and probability of vortex dislocation. The dislocation occurs less frequently for gap heights close to that of vortex suppression and below.

Contributed by the Fluids Engineering Division of ASME for publication in the JOURNAL OF FLUIDS ENGINEERING. Manuscript received July 2, 2007; final manuscript received September 29, 2008; published online November 26, 2008. Assoc. Editor: James A. Liburdy. Paper presented at the 14th International Conference on Nuclear Engineering (ICONE 14) and 2006 ASME Joint U.S.-European Fluids Engineering Summer Meeting (FEDSM 2006), Miami, FL, July 17–20, 2006.

 Copyright © 2009 by ASME

Downloaded 03 Jun 2010 to 171.66.16.158. Redistribution subject to ASME license or copyright; see http://www.asme.org/terms/Terms_Use.cfm

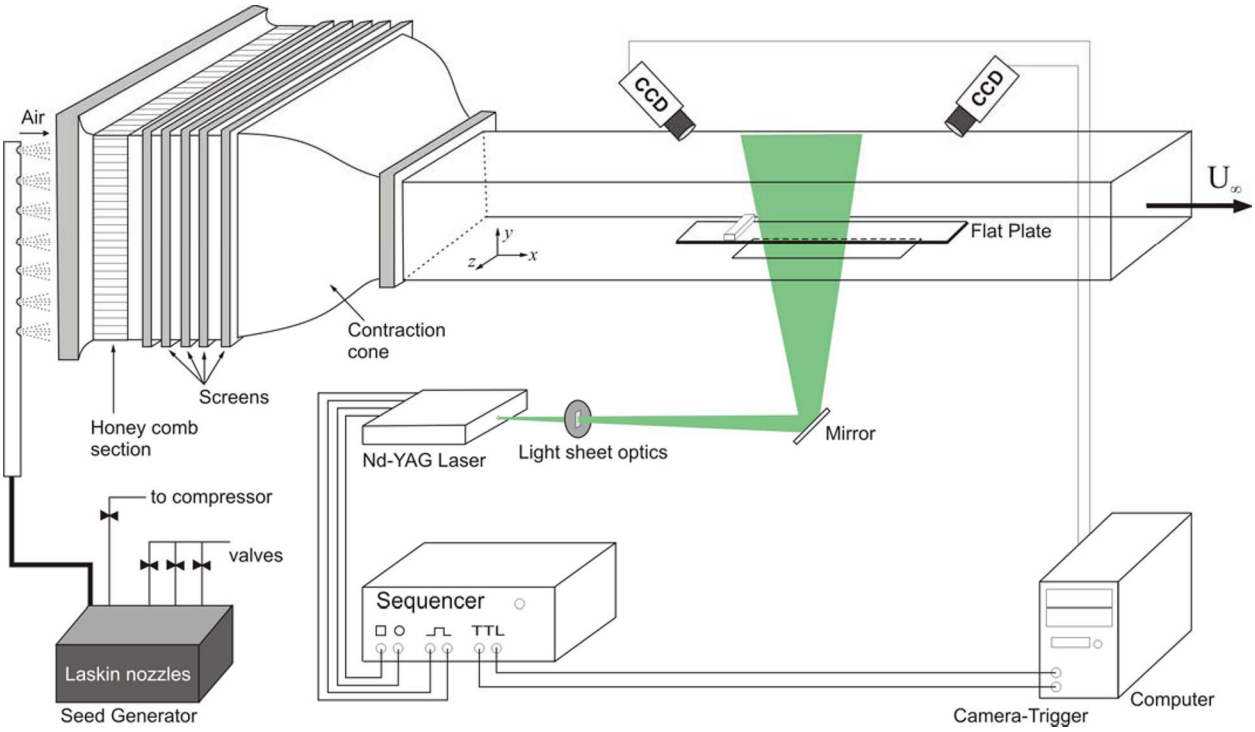

Fig. 1 The schematic of the experimental setup

Liou et al. [7] carried out LDV measurements in a rotating two-pass square duct with detached square ribs. The gap to rib height ratio was set equal to 0.38. They reported that the wall jet emitted from the rib-wall gap effectively removes the rib-duct wall corner vortex for the detached ribs compared to the attached ribs for both rotating and stationary ducts. Their results showed a dominant peak in the bottom rib shear layer due to the interaction with the wall shear layer and a separate frequency peak in the rib top shear layer corresponding to the shedding frequency. Liou et al. [8] also reported local heat transfer, velocity, and wall pressure fluctuations of a rotating two-pass square duct with detached square ribs for gap to height ratio equal to 0.38 using transient liquid crystal thermography, LDV, and pressure transducer measurements. They attributed the overall superior effectiveness of the detached ribs to the combined convection effect of the wall jet and downwash effect of the rib top shear layer. The parameter $(V-U)/U$ characterizing the relative importance of flow downwash and convection correlates to the local Nusselt number. The standard deviation of the local Nusselt number distribution is less for detached ribs compared to the attached rib, indicating greater heat transfer uniformity for the detached rib configuration.

Martinuzzi et al. [9] studied the aerodynamic behavior of a square cylinder located near a wall using surface pressure distribution, LDV, and hot wire anemometry measurements. They identified four different flow regimes based on the nature of flow between the bottom cylinder face and the wall. For gap to height ratio greater than 0.9, back pressure, drag coefficient, and strength of shed vortices are insensitive to the gap height. For the gap to height ratio range between 0.6 and 0.9, the strength of shed vortices and fluctuating lift decrease, while the base pressure increases with a reduction in the ratio of gap to cylinder size. For a gap to height ratio range between 0.3 and 0.6, the flow reattaches intermittently on the bottom face and the shedding of vortices becomes increasingly irregular. For gap to height ratios less than 0.3, the lower shear layer reattaches permanently on the bottom face and periodic fluctuations are completely suppressed.

From the above literature survey, it is evident that most of the earlier investigations on flow past a detached bluff body have primarily concentrated on the nature of vortex shedding. The effectiveness of detached ribs compared to attached ribs for heat transfer enhancement has been established. However, a detailed discussion on flow structures responsible for better effectiveness of detached rib configurations is not available in the literature. The present study reports the detailed flow field behind the detached square cylinder at different gap size to cylinder height ratios. The gap to cylinder height ratio has been set equal to 0.2 (suppressed vortex shedding zone), 0.37 (intermittent vortex shedding zone), 0.57 (regular vortex shedding), and 1.0 (no influence of the gap between the cylinder and the bottom wall). The present study provides a complete characterization of the mean and fluctuating flow fields behind the detached cylinder at different gap heights from the bottom wall. The two component (2C) and stereo particle image velocimetry (PIV) measurements in both streamwise and cross stream planes and surface oil film visualization have been used. The flow structures responsible for superior heat transfer of detached cylinder with smaller gap size are clearly demonstrated.

Description of Experiments

The experiments were carried out in the low turbulence wind tunnel of DLR Goettingen (Fig. 1). The details of the experimental setup have been presented earlier in Panigrahi et al. [10]. The test section is of 0.3×1.5 m^2 cross section and 6.25 m length. The air enters through a contraction section (contraction ratio $=16:1$), settling chamber of 5×1.5 m^2 cross section, honey comb, and series of wire mesh. The average turbulence intensity of the wind tunnel is about 0.05%. A flat plate with a 6:1 elliptical leading edge, 300 mm wide and 1180 mm long, mounted between the sidewalls of the wind tunnel acts as the test model (Fig. 2). The square cylinder of size 15 mm mounted at different gap heights from the flat plate surface acts as the detached cylinder. The experiments have been conducted at freestream velocity equal to 10 m/s, and the corresponding Reynolds number based on rib height is equal to 11,075.

The neodymium doped yttrium aluminum garnet (Nd:YAG) laser system (Quantel, France) with an output energy of

Downloaded 03 Jun 2010 to 171.66.16.158. Redistribution subject to ASME license or copyright; see http://www.asme.org/terms/Terms_Use.cfm

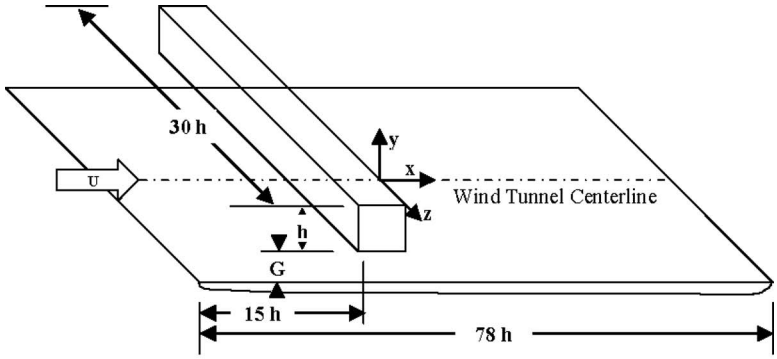

(a)

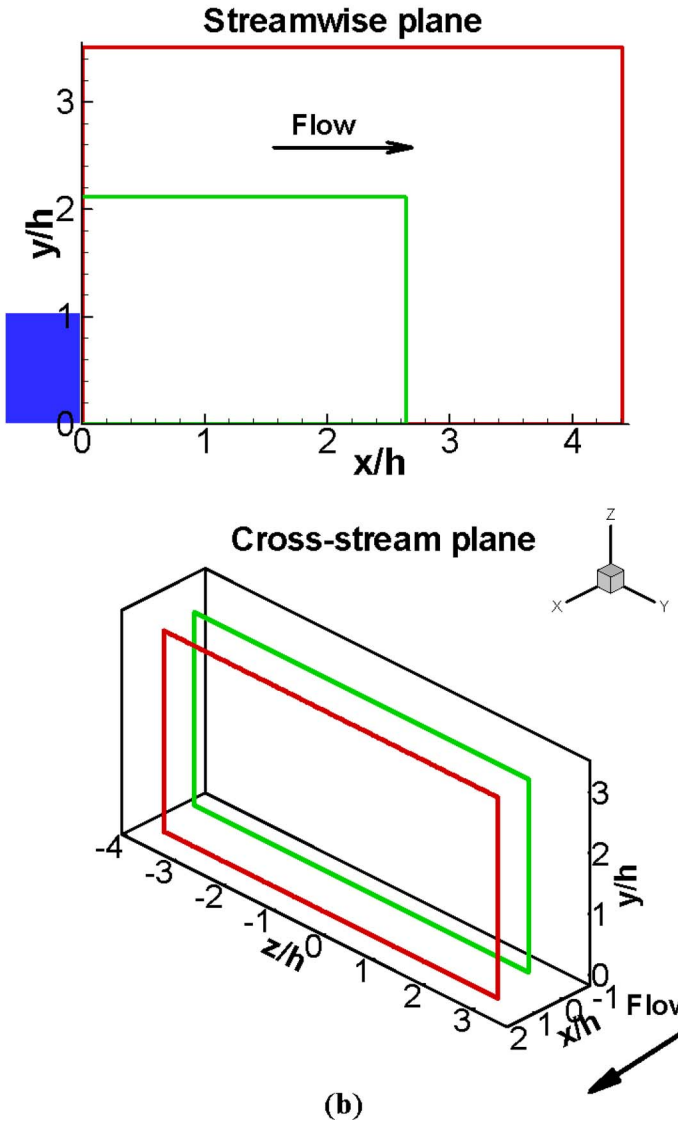

(b)

Fig. 2 (*a*) **The schematic of the detached rib mounted over flat plate and** (*b*) **different measurement zones (streamwise and cross stream planes) for the PIV measurements**

180 mJ/pulse at a wavelength $\lambda = 532$ nm was used as the light source for PIV measurements. One biconcave lens ($f = -150$ mm), one biconvex lens ($f = 300$ mm), one cylindrical lens ($f = 40$ mm), and four mirrors have been used to generate a light sheet of about 1.0–1.5 mm thickness. The synchronization between laser light pulses and the camera is accomplished by transistor-transistor logic (TTL) pulses from the synchronizer (PivTec, GmbH, Germany). Cylindrical lens and mirror positions

Downloaded 03 Jun 2010 to 171.66.16.158. Redistribution subject to ASME license or copyright; see http://www.asme.org/terms/Terms_Use.cfm

are adjusted for controlling the light sheet position and its orientation with respect to the mean flow (streamwise or cross stream). Two PCO Sensicam camera (Kelheim, Germany) of 1280 $\times$1024 pixels with Zeiss (Jena, Germany) makro planar objectives (f-number=2.8, f=100 mm) have been used for image acquisition. A Laskin nozzle has been used to introduce the seeding particles at the entrance of the settling chamber. As tracer particles, diethylhexylsebakat (DEHS) supplied by Palas, Germany was used in the seeding generator.

The laser pulse separation time (range of 60–90 μs) is adjusted to optimize both the maximum cross-correlation value and dynamic range. The absolute value of dynamic range during measurement is typically between 0.5 and 15.5 pixels. The frequency of image pair acquisition is 3.3 Hz. The PIVVIEW software provided by PivTec was used for the PIV data analysis. For the calculation of mean and fluctuating velocity field statistics, 1200 image pairs were acquired at each measurement plane. The raw PIV images are high pass filtered prior to the PIV cross-correlation calculation. The background seen by the two cameras for stereo PIV measurements are different from each other because of different background light contributions due to the angular arrangement of the two cameras. Therefore, an additional background subtraction of each camera image was carried out during the preprocessing stage. Multigrid correlation from an initial interrogation zone size of 64$\times$64 pixels to a final grid size of 16 $\times$16 pixels along with local window shifting and subpixel image deformation (B-spline interpolation) was implemented to improve the dynamic range and accuracy. The Whitaker subpixel correlation peak fit algorithm was used for the fractional displacement estimation. The interrogation zone overlap of 50% was used for improving the number of velocity vectors in the flow field. The spurious vectors calculated based on the local median filtering and maximum displacement differences are less than 1%. The velocity fields from high resolution measurements (0.49 mm) and low resolution measurements (0.82 mm) have been compared using two sets of experiments conducted at different times. There is negligible difference in velocity magnitude between these two experiments, indicating correct implementation of PIV measurement and data analysis procedure. This comparison is not shown here due to space limitation.

Fiesta-fluo tracer mixed with petrol has been used for oil film visualization study. The oil film is applied on the test surface by a roller coating device. The flow was subsequently introduced in the wind tunnel. The resulting surface pattern images on the test surface are captured by a digital camera, which are attributed to the signature of flow structures above the test surface.

The partial derivatives of instantaneous velocities are required for the calculation of turbulent kinetic energy budget terms, vorticity, and the second invariant of the velocity gradient tensor. The uncertainty in the calculation of the partial derivative has two components, i.e., positioning and truncation errors. The positioning error is associated with accuracy in the positioning of the probes. The truncation error depends on the scheme used for finite difference calculation. The positioning error is very small for PIV measurements due to very accurate optical calibration procedure adopted in PIV measurements. The partial derivatives were calculated using Richardson's finite difference formula, with error magnitude of the order of $\Delta\eta^3$, where $\Delta\eta$ is the resolution of the vector field.

Results and Discussions

The effectiveness of detached rib configuration on mixing/heat transfer enhancement can be studied by investigating mean and instantaneous velocities, velocity fluctuation, mean and instantaneous vorticities, and coherent structure distribution in the flow field. The distribution of wall-normal velocity indicates motion of near wall fluid toward the outer flow region and vice versa. The flow structures observed using stream traces from the velocity field in the streamwise and cross stream planes indicate the nature of mean flow motion. Velocity vectors and vorticity distributions demonstrate the interaction between these flow structures. The generation and interaction of coherent structures contribute to fluctuations in the flow field and hence different mixing levels for different detached rib configurations.

The results of the present study are discussed under the following headings: (a) Mean velocity, (b) Stream traces, (c) Velocity fluctuation, (e) Instantaneous velocity, vorticity and velocity gradient, (f) Oil film visualization, (d) Coherent structures, and (g) Turbulent kinetic energy budget. There is specific emphasis on flow structures responsible for effective near wall mixing in detached rib configuration.

Mean Velocity. The mean velocity distribution provides information on bulk motion of fluid, i.e., convection of fluid particles and relative mixing between different regions in the flow field. Figure 3 shows average u- and v-velocity fields normalized by the freestream velocity for different gap to height ratios of the detached square ribs. The strong dependence of the mean velocity field on the gap size is clearly evident in Fig. 3. The flow field behind the detached ribs can be broadly classified into two parts, i.e., flow through the gap and the wake region behind the cylinder. The u-velocity field behind the gap shows a strong correlation to gap size. The velocity distribution immediately behind the gap shows similarity to developing Poiseuille flow. For lower gap size (G/h=0.2), the average u-velocity magnitude of flow through the gap is less compared to that at higher gap height. This may be attributed to the larger pressure drop inside the smaller gap region. The size of the recirculation zone (negative u-velocity region) behind the detached cylinder decreases with increase in gap size (Fig. 3) due to the increase in strength of flow through the gap. This can be attributed to a greater pressure gradient across the wake resulting in higher v-velocity magnitude from the gap region to the recirculation zone for the larger gap size detached cylinder (see Fig. 3).

The nature of the v-velocity distribution, i.e., wall-normal flow component, shows significant dependence on the detached rib geometry. The mean v-velocity in the wake region is negative, i.e., directed toward the wall for G/h equal to 0.2 and 0.37. At G/h =0.2 and 0.37, fluid from the outer mean flow region is transported downward and the fluid from the wall region is carried outward. This is an ideal scheme for generation of cross flow across the wake, which is crucial for enhanced heat transfer and mixing. For G/h=0.57, the negative v-velocity zone is clearly seen immediately behind the cylinder, which is followed by both positive and negative v-velocity zones at both sides of the cylinder centerline. At G/h=1.0, the negative v-velocity zone observed immediately behind the cylinder almost disappears, and two symmetric positive and negative v-velocity zones similar to the characteristic of a regular wake behind a cylinder in freestream are seen. The cross stream mixing region with higher v-velocity magnitude extends further downstream for the low gap size detached cylinder (G/h=0.2 and 0.37) compared to that of the higher gap size (G/h=0.57 and 1.0). In summary, detached rib geometries significantly contribute toward manipulation or modification of the v-velocity field, which is primarily responsible for cross stream mixing.

Stream Traces. Stream traces provide information on fluid particle motion in the flow field. Figure 4 presents the time averaged stream traces in the x-y plane at the centerline (z=0) using the u-v components of velocity. The total velocity magnitude has been superposed on the stream traces. There are two recirculating bubbles at both sides of the cylinder centerline. The total velocity magnitude shows a separating streamline with zero velocity in both upper and lower shear layers at both sides of the cylinder centerline. The streamwise x-location of the merging point between the top and bottom separating streamlines is dependent on the gap size; i.e., it drops from x/h=3.4 to 0.6 with increase in

Downloaded 03 Jun 2010 to 171.66.16.158. Redistribution subject to ASME license or copyright; see http://www.asme.org/terms/Terms_Use.cfm

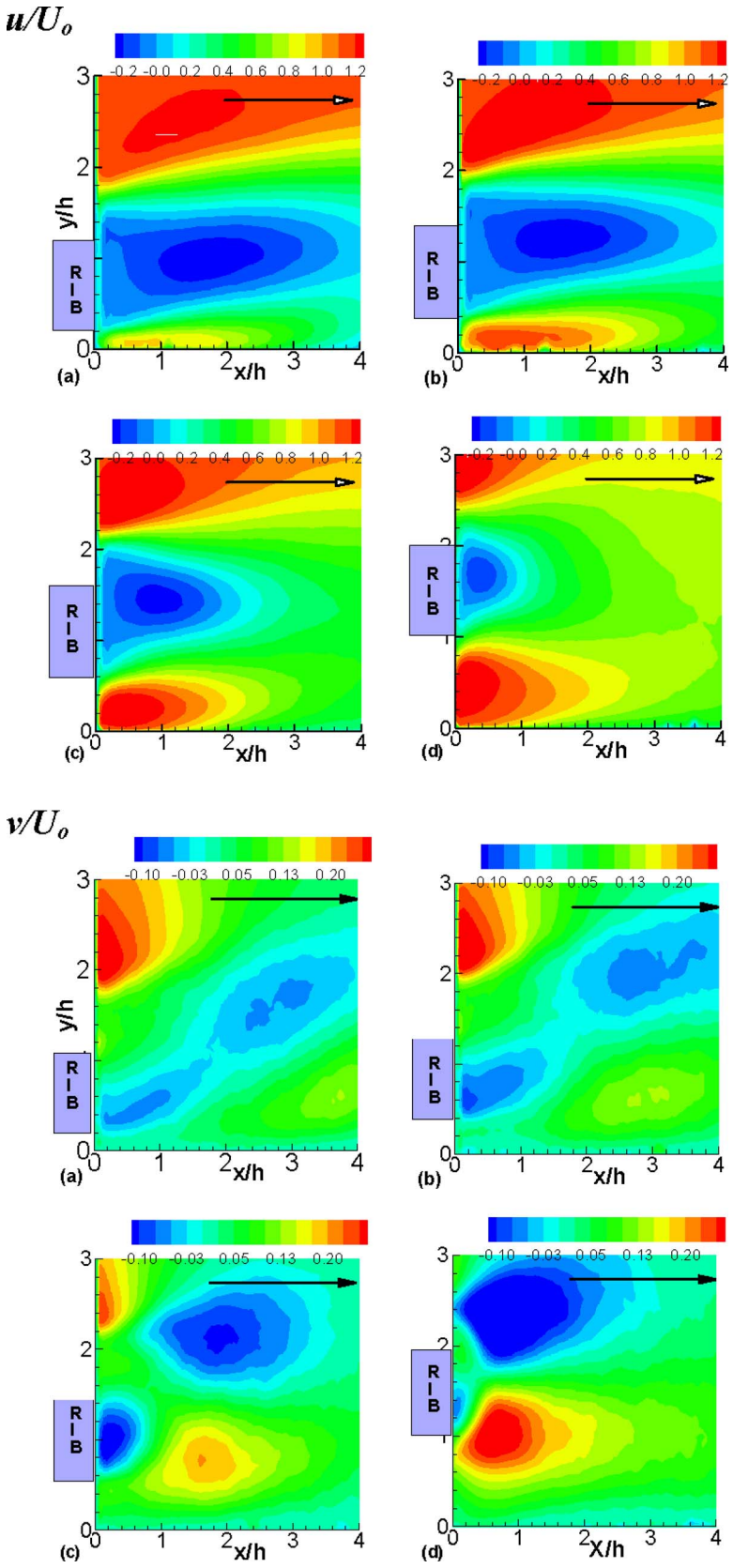

Fig. 3 The normalized *u*-velocity field (top) and *v*-velocity field (bottom) behind detached ribs for gap to rib height ratio: (*a*) *G*/*h*=0.2, (*b*) *G*/*h*=0.37, (*c*) *G*/*h*=0.57, and (*d*) *G*/*h*=1.0

Downloaded 03 Jun 2010 to 171.66.16.158. Redistribution subject to ASME license or copyright; see http://www.asme.org/terms/Terms_Use.cfm

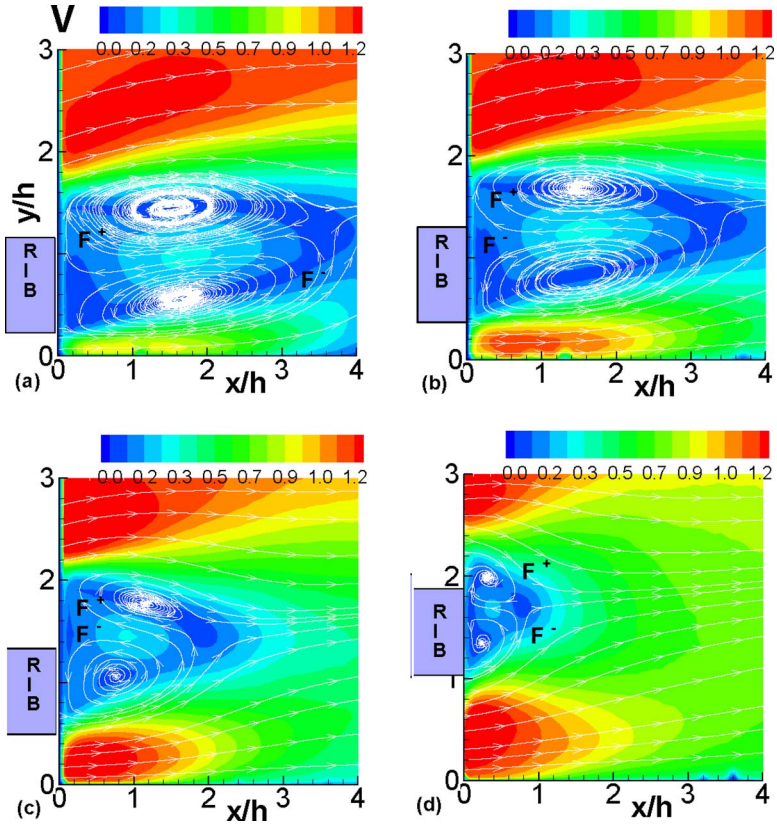

Fig. 4 The time averaged stream traces superposed on the normalized velocity magnitude for detached ribs of gap size to rib height ratio: (*a*) $G/h=0.2$, (*b*) $G/h=0.37$, (*c*) $G/h=0.57$, and (*d*) $G/h=1.0$

gap size from $G/h=0.2$ to 1.0, respectively. There is a corresponding drop in the size of the recirculation zone with increase in gap size (Fig. 3). The recirculating stream trace patterns in Fig. 4 are similar to that of regular foci (F). The direction of rotation (clockwise and anticlockwise) is opposite for the lower and upper recirculating bubbles. The shape and orientation of the recirculating bubble are also a function of the gap size. The core of upper foci (F^+) is located at different y-distances from the cylinder centerline compared to that of lower foci (F^-), and this offset is a function of the gap size. The streamwise (x) location corresponding to the core of foci (F^+ and F^-) also shifts closer to the rib with increase in gap size.

Figure 5 shows the time averaged stream traces using the v-w component of velocity superposed on the u-velocity field at the cross stream (y-z) plane ($x/h=0.5$ and 1.5). The u-velocity field distribution does not show any significant variation in the spanwise (z) direction. This indicates negligible influence of the sidewall because of high aspect ratio of the cylinder and high Reynolds number of the present study. It may be noted that end plates have not been used in the present study to provide optical access for successful near field PIV measurements. The u-velocity field at the central plane ($Z/h=0$) of Fig. 5 correlates well with the u-velocity distribution of Fig. 3, indicating a successful implementation of the stereo PIV technique

Kolar [11] observed that the critical point concept provides qualitative insight into the mechanism of vortex formation process and vortical flows. The critical points are the salient features of a flow pattern, where the streamline slope is indeterminate. The critical points provide valuable insight into the three dimensional nature of the flow. Zhou and Antonia [12] used critical points to explain the turbulent flow patterns in the wake of a circular cylinder. The inter-relationship between critical points in the two orthogonal planes provides possible insight into the three dimensional nature of the flow. All possible flow patterns close to critical points can be derived and classified, where the sectional streamline patterns form saddles, nodes, or foci. Once the position and type of these patterns are known, the rest of the pattern can be deduced qualitatively. The stream traces in cross stream planes show different node-saddle combinations (N-S), which are dependent on gap height (see Fig. 5). The y-location of the node-saddle line is correlated to the location of the recirculation bubbles shown in Fig. 4. One N-S structure is observed at the boundary between the two recirculation zones (Fig. 4), i.e., at about $y/h=0.95$, 1.2, 1.3, and 1.6 for $G/h=0.2$, 0.37, 0.57, and 1.0 respectively ($x/h=0.5$, Fig. 5). The direction of stream traces from these node-saddle locations (N-S^-) are outward for $G/h=0.2$, 0.37, and 0.57. In contrast, the direction of stream traces at the N-S line is inward at $G/h=1.0$. The direction of these stream traces from the v-w component of velocity (Fig. 5) correlates to that of stream traces based on the u-v component of velocity at the corresponding x-plane location ($x/h=0.5$) (Fig. 4). This can be explained based on the location of the $x/h=0.5$ plane with respect to the streamwise extent of the recirculation zone. The $x/h=0.5$ plane is at the downstream side of the recirculation bubble for $G/h=1.0$ contrary to that at $G/h=0.2$, 0.37, and 0.57. A separate node-saddle pattern (N-S^+) is observed at the near wall region for gap to height ratios equal to 0.2, 0.37, and 0.57. The direction of stream traces is toward these node-saddle locations (N-S^+) contrary to that between the recirculation bubbles (N-S^-). The y-location of these node-saddle patterns increases with increase in gap size. At $x/h=1.5$, similar node-saddle combinations are seen as that at $x/h=0.5$ with differences in their y-location. This can be attributed to the different relative location of the cross stream

Downloaded 03 Jun 2010 to 171.66.16.158. Redistribution subject to ASME license or copyright; see http://www.asme.org/terms/Terms_Use.cfm

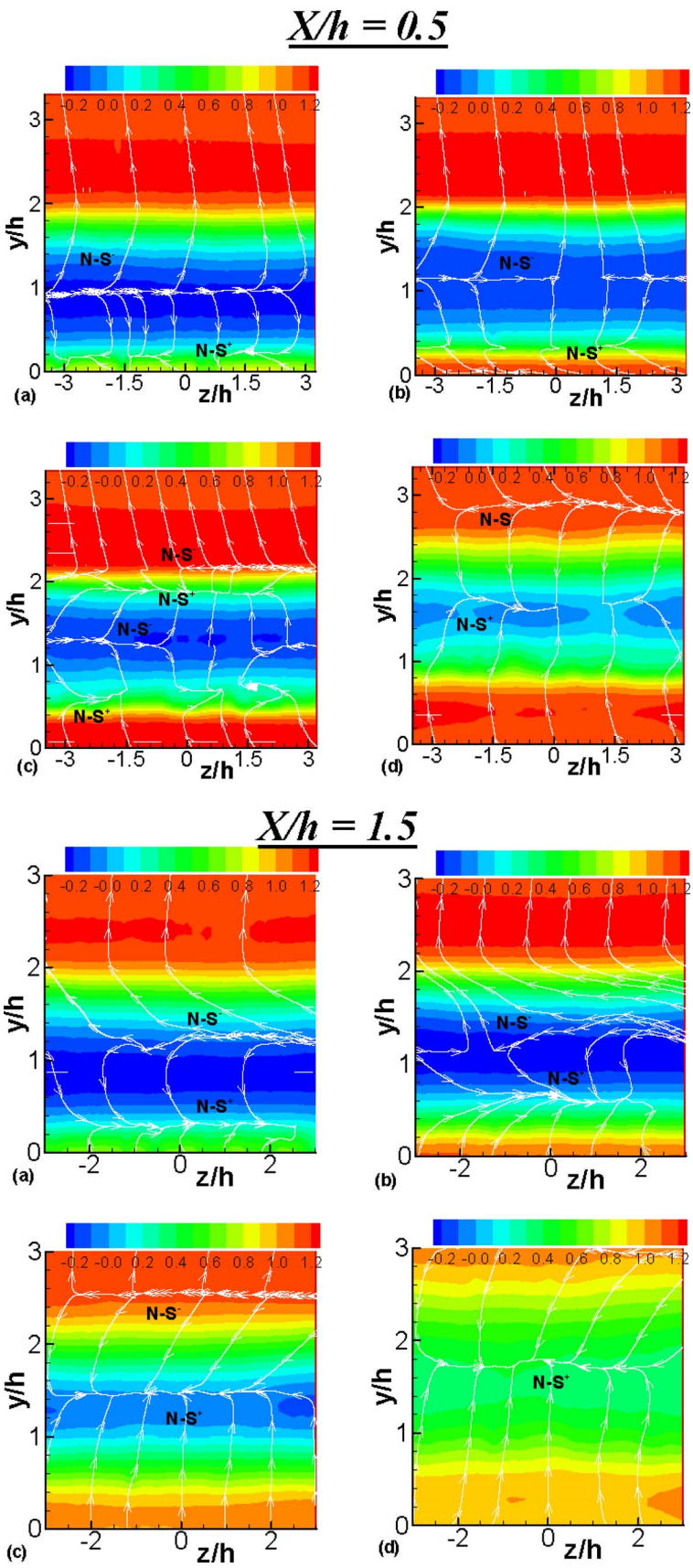

Fig. 5 The stream traces using the *y* and *z* components of velocity (*v*, *w*) superposed on the normalized streamwise (*u*) velocity in the cross stream (*y*-*z*) plane at *x*/*h*=0.5 (top) and *x*/*h*=1.5 (bottom) for detached ribs with gap size to rib height ratio: (*a*) *G*/*h*=0.2, (*b*) *G*/*h*=0.37, (*c*) *G*/*h*=0.57, and (*d*) *G*/*h*=1.0

Downloaded 03 Jun 2010 to 171.66.16.158. Redistribution subject to ASME license or copyright; see http://www.asme.org/terms/Terms_Use.cfm

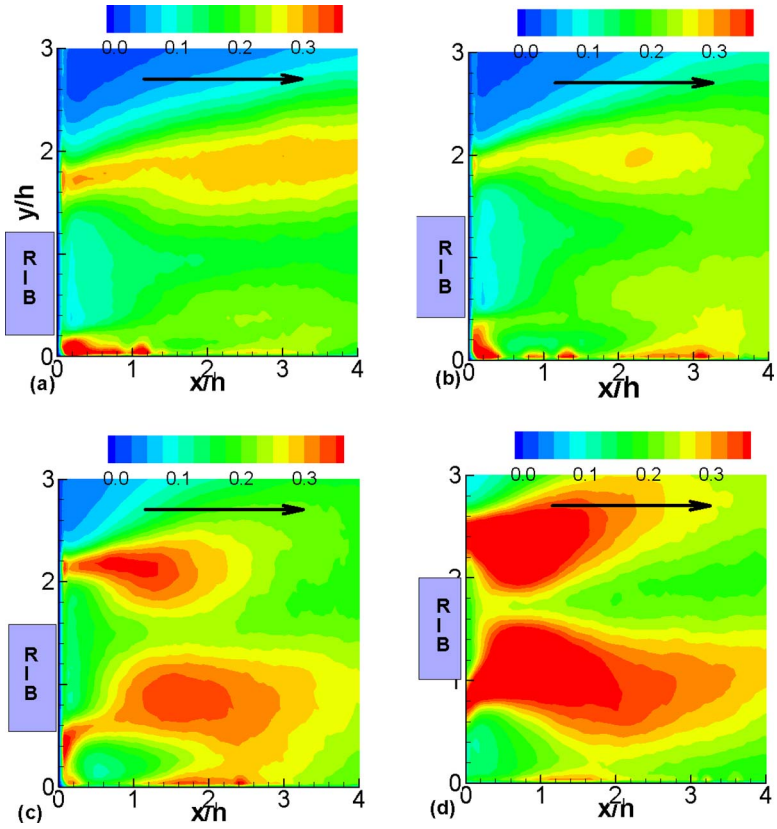

Fig. 6 The normalized u_{rms}/U_o velocity behind the detached ribs in the *x-y* plane for gap size to rib height ratio: (*a*) $G/h=0.2$, (*b*) $G/h=0.37$, (*c*) $G/h=0.57$, and (*d*) $G/h=1.0$

plane (x/h) inside the recirculation zone.

In summary, the streamline patterns show foci- and node-saddle-like flow structures in both streamwise and cross stream planes, respectively. The location, shape, and size of these structures are dependent on the gap size. The presence of these flow structures may be responsible for superior mixing in detached rib configuration.

Velocity Fluctuation. Figure 6 compares the u_{rms} fluctuation field behind different detached rib configurations. The u_{rms} distribution shows greater wall-normal (y) extent for the upper shear layer than that of the lower shear layer for the detached cylinder with $G/h=0.2$ and 0.37. This may be attributed to the wall effect; i.e., the wall limits the transverse growth of the lower shear layer. The u_{rms} distribution of the lower shear layer is concentrated adjacent to the wall surface, indicating greater near wall fluctuation for these detached rib geometries $(G/h=0.2$ and $0.37)$. For higher gap to height ratios $(G/h=0.57$ and $1.0)$, the u_{rms} magnitude in both upper and lower shear layers is higher compared to that of the lower gap size, indicating the presence of strong vortical structures. However, both these high fluctuation zones are located away from the bottom wall and therefore do not contribute to the near wall fluctuation.

Figure 7 compares the normalized u_{rms}, v_{rms}, w_{rms}, and $u_{rms}+v_{rms}+w_{rms}$ fluctuating velocity field in the cross stream $(y\text{-}z)$ plane at the $x/h=0.5$ location. There is negligible variation in the fluctuating velocity field distribution in the spanwise (z) direction, indicating insignificant influence of the sidewall. The high fluctuation intensity (u_{rms} and w_{rms}) zone located near the wall surface for $G/h=0.2$ shifts away from the wall with increase in gap size. The overall fluctuation intensity is higher for the larger gap size $(G/h=0.57$ and $1.0)$ detached cylinder compared to that of the lower gap size. However, the higher gap size is not beneficial for near wall mixing in comparison to the lower gap size because the high fluctuation intensity zone is located away from the wall surface. In summary, the average near-wall fluctuation level of lower gap size detached cylinder is high, resulting in superior near wall mixing.

Instantaneous Velocity, Vorticity, and Velocity Gradient. Figure 8 shows the instantaneous velocity vectors and corresponding instantaneous spanwise vorticity (ω_z) for different detached rib configurations. The velocity vector field clearly demonstrates the nature of flow through the gap. The velocity vectors immediately behind the gap are initially aligned with the wall, but later change their direction outward, i.e., away from the wall. The velocity vector field distribution shows rotational motion of fluid particles in the upper and lower shear layers indicating the presence of vortical structures. The total number and size of vortical structures present inside the shear layer depend on the gap size. The instantaneous vorticity field shows the vorticity contribution of these vortical structures. These vortical structures are deflected upward, leading to their interaction inside the wake region. The vorticity content of the lower shear layer is due to the velocity difference between the wake region and the flow through the gap, while the vorticity content of the upper shear layer is due to the velocity difference between the wake and the freestream. Therefore, the vorticity content inside the upper and lower shear layer region is not identical. As the lower shear layer is close to the wall surface for small gap size $(G/h=0.2$ and $0.37)$ detached cylinder, the instantaneous vorticity is concentrated in the near wall region. The strong instantaneous vorticity region moves away from the bottom wall with increase in gap size. Higher concentration of instantaneous vorticity in the near wall region indicates superior mixing effectiveness of smaller gap size detached cylinder.

For complete information on the rotational component of fluid

Downloaded 03 Jun 2010 to 171.66.16.158. Redistribution subject to ASME license or copyright; see http://www.asme.org/terms/Terms_Use.cfm

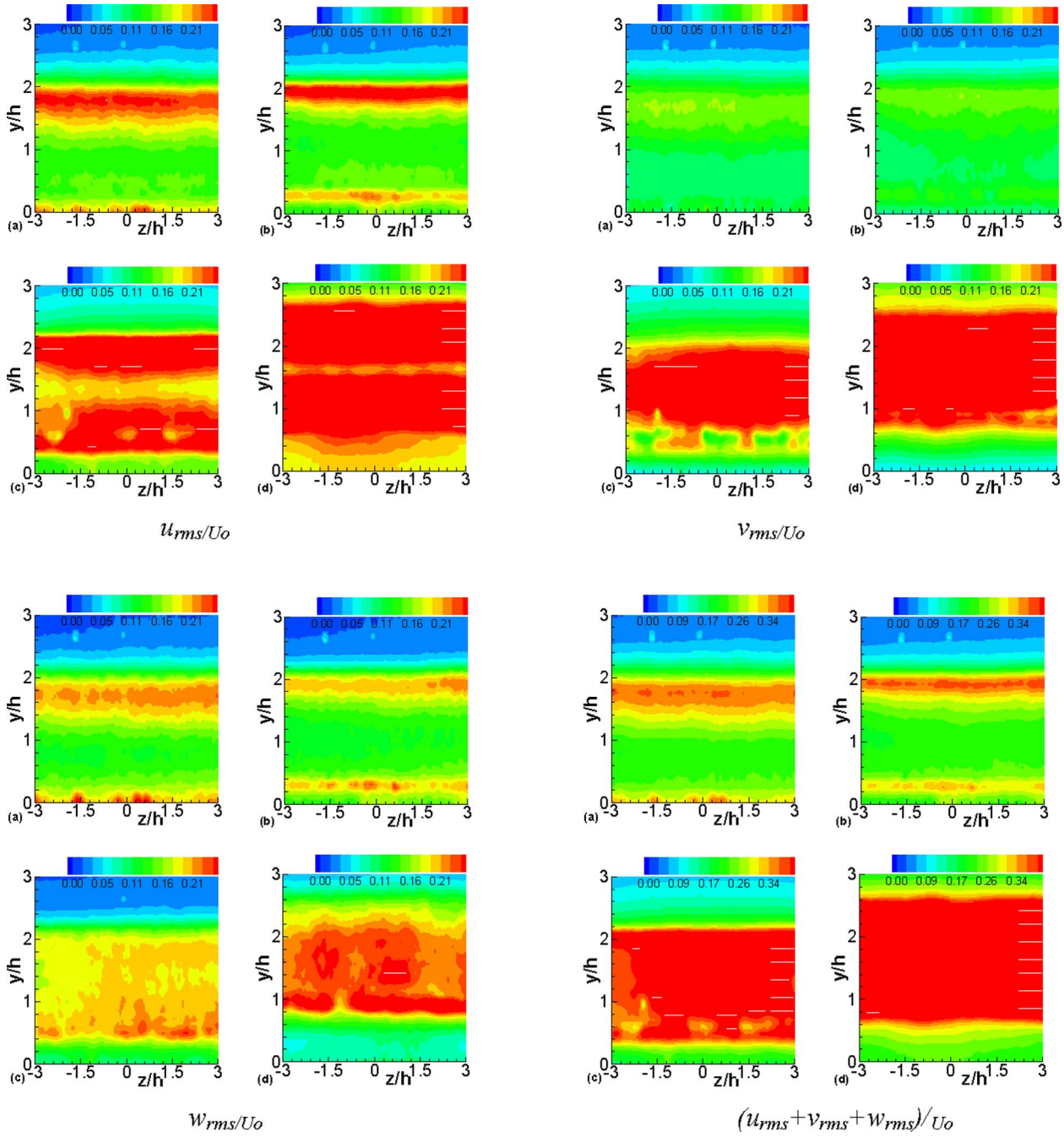

Fig. 7 The normalized u_{rms}, v_{rms}, w_{rms} and total rms velocity behind detached ribs in the cross stream *y-z* plane ($x/h=0.5$) for gap size to rib height ratio: (*a*) $G/h=0.2$, (*b*) $G/h=0.37$, (*c*) $G/h=0.57$, and (*d*) $G/h=1.0$

particle motion, information on all components of vorticity (ω_x, ω_y, and ω_z) is essential. The spanwise vorticity (ω_z) results are presented in Fig. 8. The y-component of vorticity ($\omega_y = \delta u/\delta z - \delta w/\delta x$) cannot be calculated due to the unavailability of instantaneous w-velocity data as a function of the streamwise (x) coordinate from the stereo PIV measurement in the cross stream plane. However, the velocity gradient $\delta u/\delta z$ can be evaluated, which can provide qualitative information about the ω_y vorticity distribution. For complete information about all components of vorticity, the instantaneous streamwise velocity (u), streamwise vorticity (ω_x), and streamwise velocity gradient in the wall-normal ($\delta u/\delta y$) and spanwise ($\delta u/\delta z$) directions are presented in Fig. 9 for different detached rib configurations at the cross stream plane ($x/h=1.5$). The significant magnitude of streamwise vorticity (ω_x) distribution in Fig. 9 indicates appreciable cross stream mixing due to the streamwise vorticity. The ω_x vorticity is primarily concentrated inside the wake region with relatively higher magnitude inside the shear layer region. The spatial averaged magnitude of ω_x vorticity is higher for larger gap size detached cylinder compared to that of the lower gap size. However, the higher vorticity magnitude region is located away from the wall surface for larger gap size detached cylinder. As the near wall vorticity is beneficial for mixing, the smaller gap size detached cylinder is more beneficial than that of larger gap size based on the ω_x vorticity distribution. The $\delta u/\delta y$ velocity gradient distribution indicates the dominant effect of wall-normal gradient of u-velocity on the spanwise vorticity

Downloaded 03 Jun 2010 to 171.66.16.158. Redistribution subject to ASME license or copyright; see http://www.asme.org/terms/Terms_Use.cfm

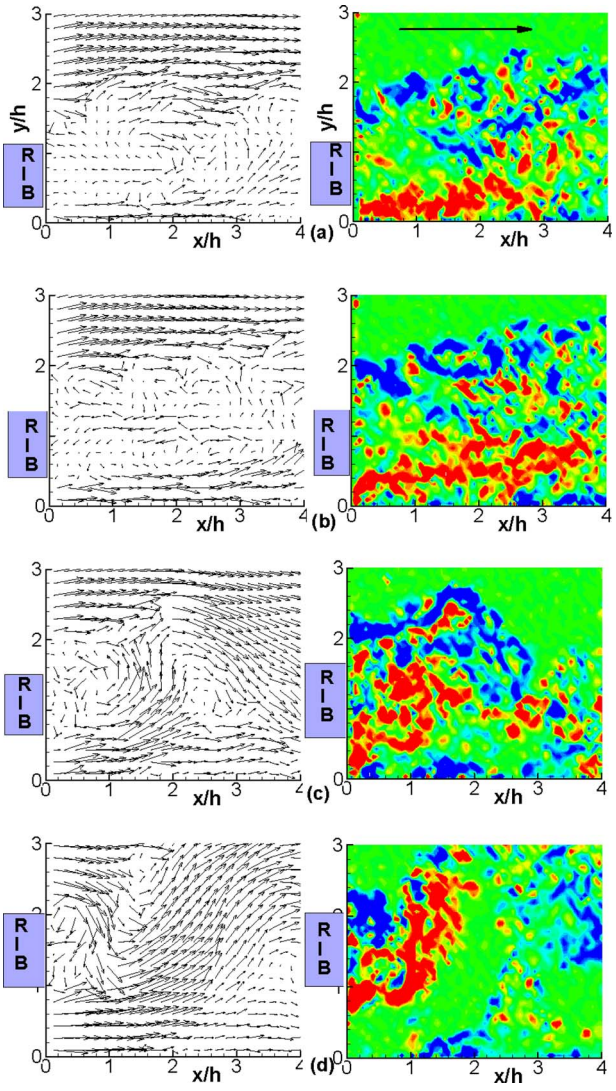

Fig. 8 The instantaneous velocity vector (with three data points skipped in both *x* and *y* directions) and instantaneous vorticity (ω_z) plots behind detached ribs for gap size to rib height ratio: (*a*) $G/h=0.2$, (*b*) $G/h=0.37$, (*c*) $G/h=0.57$, and (*d*) $G/h=1.0$

(ω_z) distribution. The significance of the $\delta u/\delta z$ value inside the shear layer region (Fig. 9) indicates importance of ω_y vorticity distribution. The u-velocity gradient distributions in both streamwise and cross stream planes for different detached rib configurations correlate well with corresponding vorticity distribution.

In summary, combined contribution of all vorticity components (ω_x, ω_y, and ω_z) is high in the near wall region of detached ribs with lower gap size ($G/h=0.2$ and 0.37), indicating superior near wall mixing.

Oil Film Visualization. The surface oil film visualization pictures for different detached rib configurations are presented in Fig. 10. The flow through the gap (see Figs. 3 and 4) is seen as streaklike structures in the near field of detached ribs (Fig. 10). These streaklike structures in the near field region end at a stagnant region, which is seen as a straight line parallel to the rib for the small gap size ($G/h=0.2$ and 0.37) detached cylinder case. The location of this stagnant line (saddle line) shifts downstream with increase in gap size from $G/h=0.2$ to 0.37. This behavior correlates to the streamwise extent of bulk flow through the gap (Fig. 4); i.e., flow through the gap extends further downstream for $G/h=0.37$ compared to that of $G/h=0.2$. At this saddle location, mean streamwise flow through the gap meets the reverse back flow from the reattaching shear layer. The saddle line in Fig. 10 is similar to the reattachment line seen in the visualization images of a surface mounted square rib of Panigrahi et al. [10]. In a reattaching shear layer of surface mounted rib, the shear layer bifurcates at the reattachment point and flows in the opposite direction. However, in a detached rib configuration, the streamwise mean flow through the gap balances the back flow from the reattaching shear layer at the saddle location. At this meeting line, the momentum of flow through the gap is neutralized by the back flow, and the flow gets deflected upward (see Fig. 8). For higher gap size ($G/h=0.57$ and 0.60), the saddle line is not visible compared to that of lower gap size ($G/h=0.2$ and 0.37). This is due to the fact that the reattaching shear layer flow is not strong enough in comparison to the flow through the gap for higher gap sized detached cylinder, resulting in balance between these two flows and a definite saddle point. In summary, the oil film visualization images clearly demonstrate the modification of near wall flow patterns for the lower gap sized detached cylinder.

Coherent Structures. The coherent structures play an important role in understanding entrainment, mixing, drag, heat transfer, and aerodynamic noise generation. The understanding of coherent structures holds the key to turbulence management and control. Therefore, there is a need to identify the large scale vortical regions in turbulent flows. Brown and Roshko [13] showed distinct large scale coherent structures in mixing layer using shadowgraph technique for the first time. Subsequently, many researchers proposed numerous types of coherent structures, i.e., horseshoe vortex, hairpin vortex, vortex rings, burst, ejection, arrowhead vortices, etc., to explain their experimental observations. The vortex structures present in a flow field can interact with each other, leading to either amplification or attenuation of instability modes. Jeong and Hussain [14] outlined different vortex identification schemes, i.e., (a) pressure minimum, (b) closed or spiraling streamlines and pathlines, (c) isovorticity surface, (d) complex eigenvalues of the velocity gradient tensor, and (e) second invariant of the velocity gradient tensor. Calluaud and David [15] used the second invariant of the velocity gradient tensor for the definition of vortex, where large Q values suggest the presence of a vortex and negative values indicate a straining motion. Wang et al. [16] used the Galilean decomposition scheme for visualization of vortices in a channel with periodic ribs. The generation and interaction between the vortex structures of detached rib configuration have been explored in the present section. The coherent structures are identified based on both vorticity and the second invariant of the velocity gradient tensor magnitude. Figure 11 compares the average vorticity field (ω_z) and the second invariant of the velocity gradient tensor (Q_{2D-z}) for different detached rib configurations. The details on their calculation procedure have been described in Panigrahi et al. [10].

The vorticity magnitude indicates the combined influence of both velocity shear and rotational motion of the vortical structures. In contrast, the second invariant of the velocity gradient tensor (Q_{2D-z}) magnitude is primarily influenced by the contribution from the rotational motion of vortical structures. The ω_z vorticity field (Fig. 11) is significant inside both the upper and lower shear layers with opposite signs for all detached rib configurations. The streamwise extent of the high vorticity zone reduces with an increase in gap size, which correlates to the size of the recirculation zone in Figs. 3 and 4. It is mostly assumed that vorticity contributes to the turbulent fluctuation. However, the high vorticity zone of the lower shear layer for smaller gap size ($G/h=0.2$ and 0.37) detached cylinder (Fig. 11) does not correlate to the fluctuation distribution of Fig. 6. This may be explained as

Downloaded 03 Jun 2010 to 171.66.16.158. Redistribution subject to ASME license or copyright; see http://www.asme.org/terms/Terms_Use.cfm

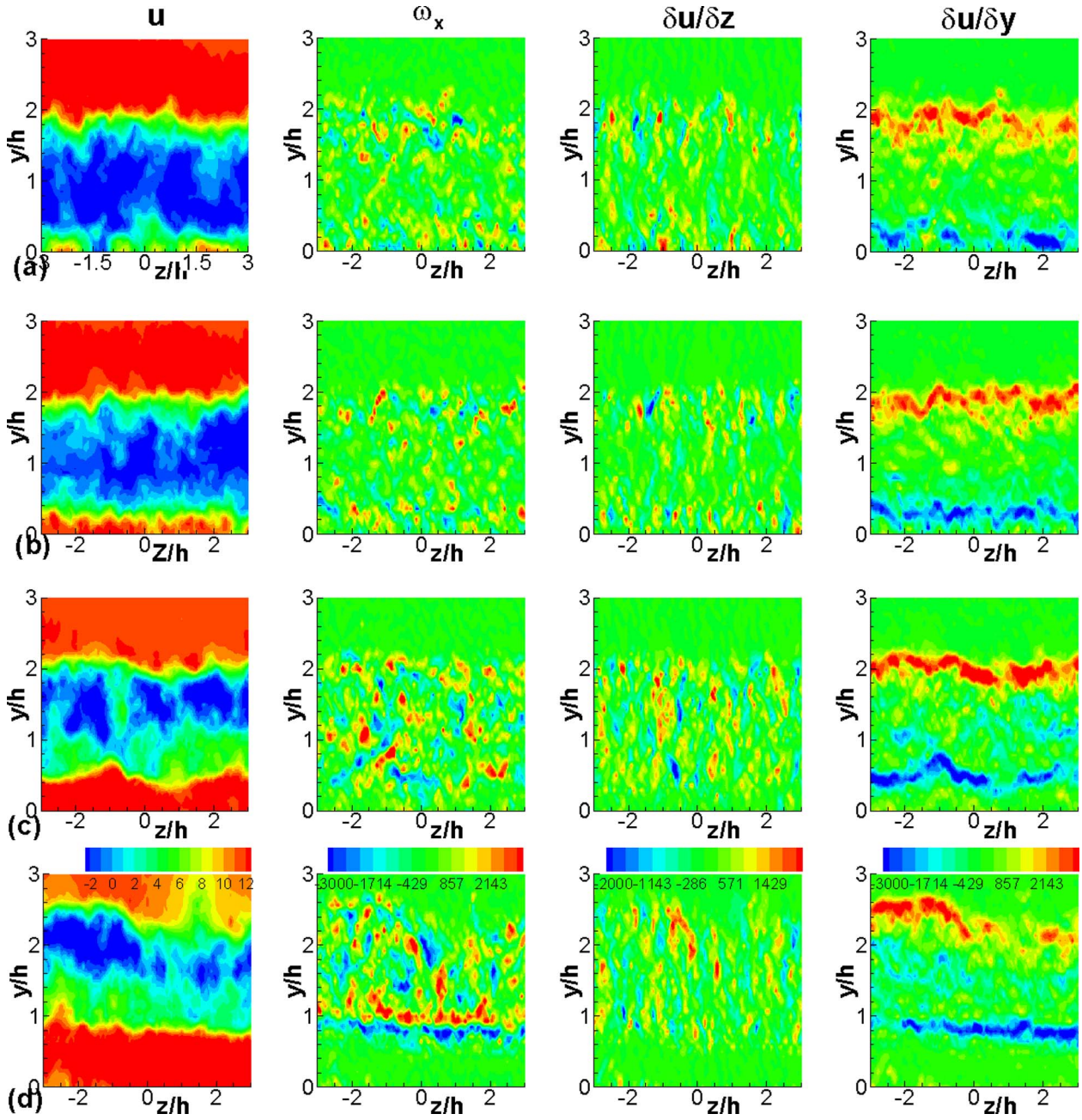

Fig. 9 The instantaneous *u*-velocity, ω_x-vorticity, and velocity gradients ($\delta u/\delta z$ and $\delta u/\delta y$) in the *y-z* plane ($x/h=1.5$) behind detached ribs for gap size to rib height ratio: (*a*) $G/h=0.2$, (*b*) $G/h=0.37$, (*c*) $G/h=0.57$, and (*d*) $G/h=1.0$

follows. Vorticity is due to the combined contribution from shear and rotational motion of the fluid element. The lower value of turbulence in the near wall region for smaller gap size detached cylinder may be attributed to the smaller rotational motion. The vortices generated by the lower shear layer get diffused by the viscous effect of the wall boundary layer. The second invariant of the velocity gradient tensor is small in the near wall region (Fig. 11), indicating lower value of rotational motion in the near wall region for the smaller gap size detached cylinder ($G/h=0.2$, 0.37, and 0.57). This explains the corresponding lower value of turbulent fluctuation in Fig. 6. The Q_{2D-z} distribution shows greater magnitude in the upper shear layer compared to the lower shear layer for the detached ribs with $G/h=0.2$, 0.37, and 0.57, indicating larger rotational contribution of the vortical structures. The vortical structures in the lower shear layer are expected to be diffused and annihilated by the viscous effect in the near wall region. The symmetry of the Q_{2D-z} distribution for higher gap size ($G/h=1$) detached cylinder can be attributed to insignificant wall effect on the vortex shedding. The overall contribution of rotational motion in the near wall region is marginally superior for lower gap size detached cylinder compared to that of higher gap size, indicating better effectiveness of lower gap sized detached ribs for near wall mixing enhancement.

Turbulent Kinetic Energy Budget. The production of turbulent kinetic energy and its transport can explain the fluctuation distribution inside a flow field. The transport mechanism responsible for the distribution of turbulent fluctuation behind different detached rib configurations has been discussed in this section using the budget terms of the turbulent kinetic energy transport equation:

Downloaded 03 Jun 2010 to 171.66.16.158. Redistribution subject to ASME license or copyright; see http://www.asme.org/terms/Terms_Use.cfm

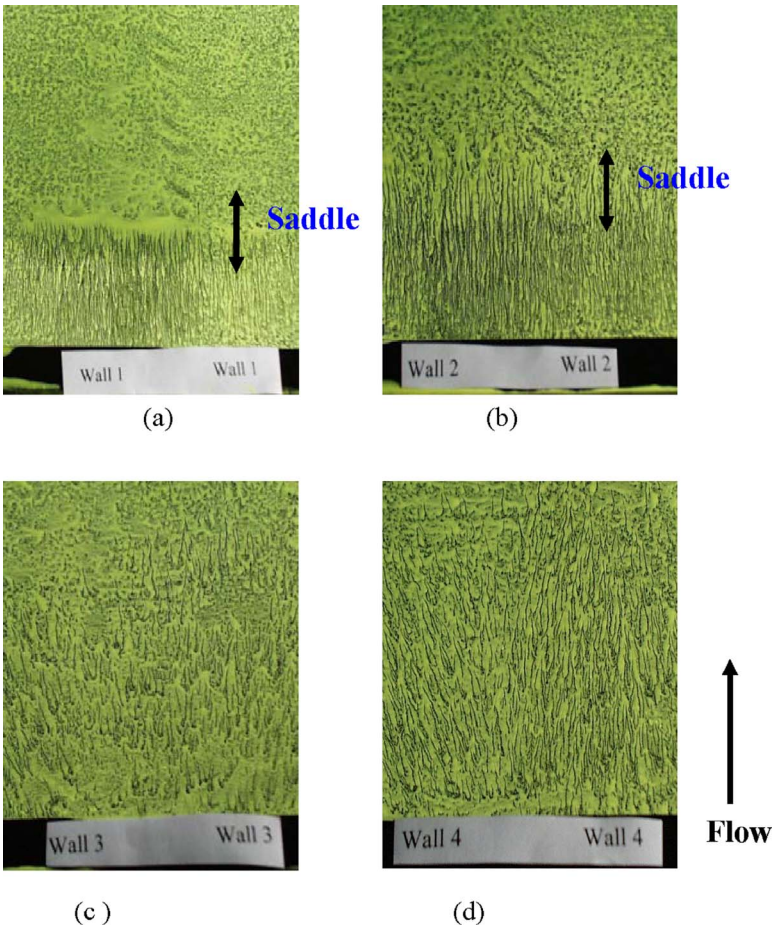

Fig. 10 The oil film visualization pictures of different detached rib configurations for gap size to rib height ratio: (*a*) *G*/*h*=0.2, (*b*) *G*/*h*=0.37, (*c*) *G*/*h*=0.57, and (*d*) *G*/*h*=1.0

$$\frac{\partial K_t}{\partial t} = -U_j\frac{\partial K_t}{\partial x_j} - \langle u_i' u_j' \rangle S_{ij} - \frac{\partial}{\partial x_j}\langle u_i' u_i' u_j' \rangle - \nu\langle s_{ij} s_{ij} \rangle - \frac{\partial}{\partial x_j}\langle 2\nu u_i' s_{ij} \rangle - \frac{\partial}{\partial x}\frac{1}{\rho}\langle u_j' p' \rangle$$

where S_{ij} and s_{ij} are the mean rate of strain and fluctuating rate of strain, respectively, and the turbulent kinetic energy (K_t) is given by

$$K_t = \tfrac{1}{2}\langle u'u' + v'v' + w'w' \rangle$$

The left hand side of the above turbulent kinetic energy transport equation is the rate of change of turbulent kinetic energy, and the right hand side terms are different budget terms responsible for the temporal change in turbulent kinetic energy. The first, second, third, fourth, fifth, and sixth terms of the right hand side are, respectively, advection, production, turbulent diffusion, dissipation, viscous diffusion, and pressure transport. The details of the simplification of the turbulent energy transport equation for the calculation of individual budget terms were presented in Panigrahi et al. [17].

Figure 12 presents the distribution of normalized turbulent kinetic energy and its production. The turbulent kinetic energy production is significant inside both the upper and lower shear layer regions. For the lower gap size case (G/h=0.2, 0.37, and 0.57), the production in the lower shear layer is less than that of the upper shear layer, and correspondingly the turbulent kinetic energy is higher for the upper shear layer. At higher gap size (G/h =1.0), the turbulent production is identical in both the shear layers, indicating minimal wall influence on the turbulent production. The turbulent production is higher for the larger gap size case with corresponding larger value of turbulent kinetic energy compared to that of the lower gap size detached cylinder. The turbulent production immediately behind the gap is smaller than that inside the shear layer. The high turbulent kinetic energy zone extends further downstream compared to that of the turbulent production. The above difference in behavior of turbulent kinetic energy and turbulent production indicates importance of other budget terms, which has been described in the following paragraphs.

The budget terms, i.e., convection, diffusion, dissipation, and pressure transport for different detached rib configurations, are shown in Fig. 13. The influence of gap size on different turbulent kinetic energy budget terms is clearly evident in Fig. 13. The turbulent energy convection distribution shows difference in the relative magnitude inside the two shear layers, which correlates to the turbulent production magnitude shown in Fig. 12. For the lower gap size case, the convection term is concentrated in the near wall region. There is a significant difference in the turbulent diffusion distribution of upper and lower shear layer regions for all gap size cases. This indicates greater influence of turbulent diffusion on turbulent kinetic energy distribution for the detached rib geometries. The dissipation distribution shows higher value in the region where the turbulent production is high. The pressure transport term is primarily high in the upper shear layer region for all detached rib configurations.

The total drag due to the flow past bluff bodies is due to the combined contribution from the pressure difference, momentum difference, and Reynolds stress across the control volume. The

Downloaded 03 Jun 2010 to 171.66.16.158. Redistribution subject to ASME license or copyright; see http://www.asme.org/terms/Terms_Use.cfm

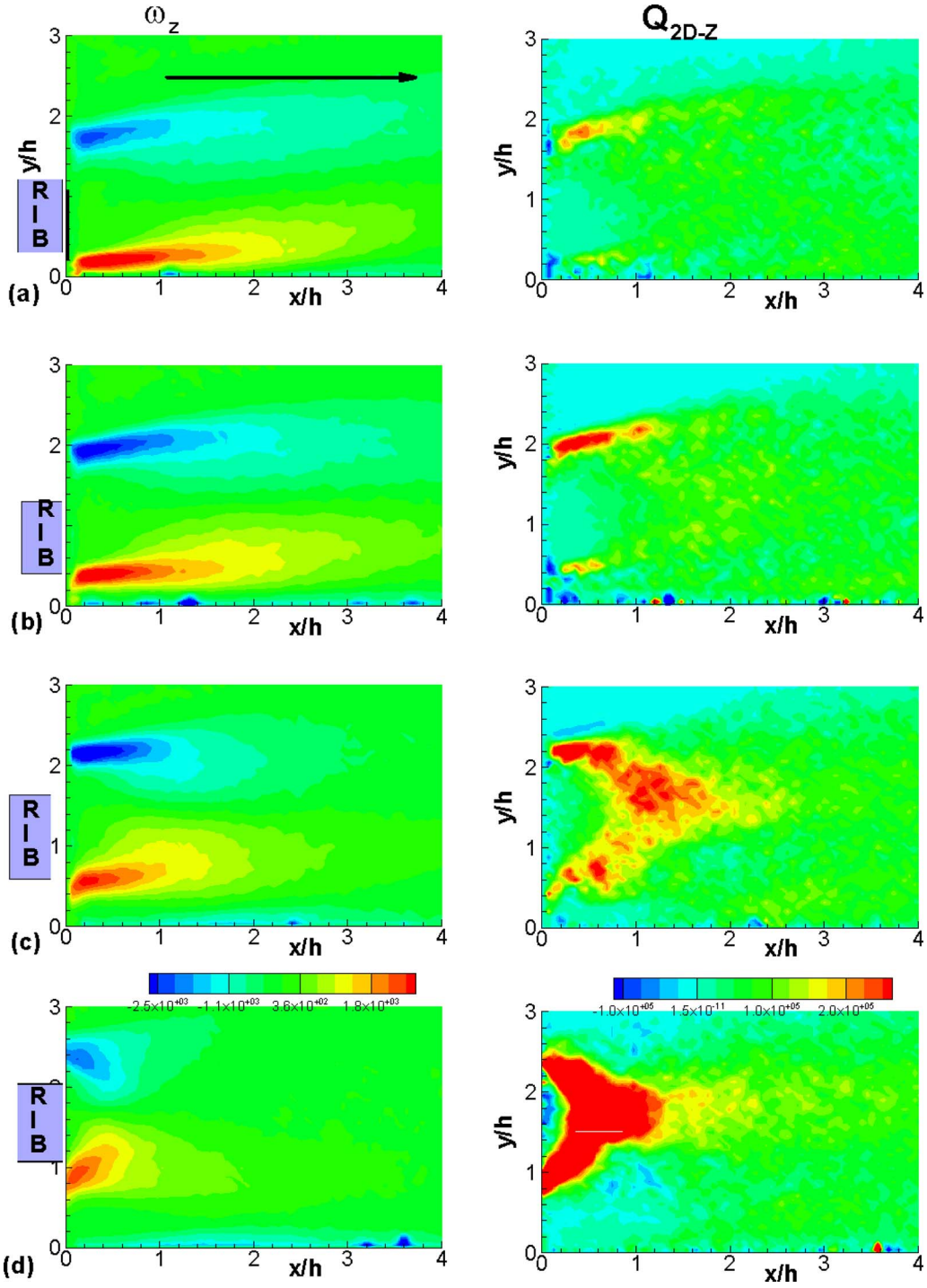

Fig. 11 The average coherent structure evaluation parameters, i.e., vorticity (ω_z) and invariance of the velocity gradient tensor ($Q_{2D\text{-}Z}$) behind detached ribs for gap size to rib height ratio: (*a*) $G/h=0.2$, (*b*) $G/h=0.37$, (*c*) $G/h=0.57$, and (*d*) $G/h=1.0$

higher average turbulent kinetic energy for larger gap size detached cylinder is expected to increase the overall drag compared to the lower gap sized detached cylinder. In addition, the turbulent kinetic energy is higher in the near wall region compared to that away from the wall for the smaller gap sized detached cylinder. Thus, the detached ribs with smaller gap size are expected to be superior from both near wall mixing enhancement and drag penalty point of view.

Summary

The present study has focused on a detailed investigation of the flow field behind detached ribs. Four gap heights to cylinder size ratios have been considered: $G/h=0.2$ (complete suppression of vortex shedding); $G/h=0.37$ and 0.57 (transition zones); and $G/h=1.0$ (freestream flow without wall effect). The Reynolds number based on the rib height is equal to 11075. The objective of

Downloaded 03 Jun 2010 to 171.66.16.158. Redistribution subject to ASME license or copyright; see http://www.asme.org/terms/Terms_Use.cfm

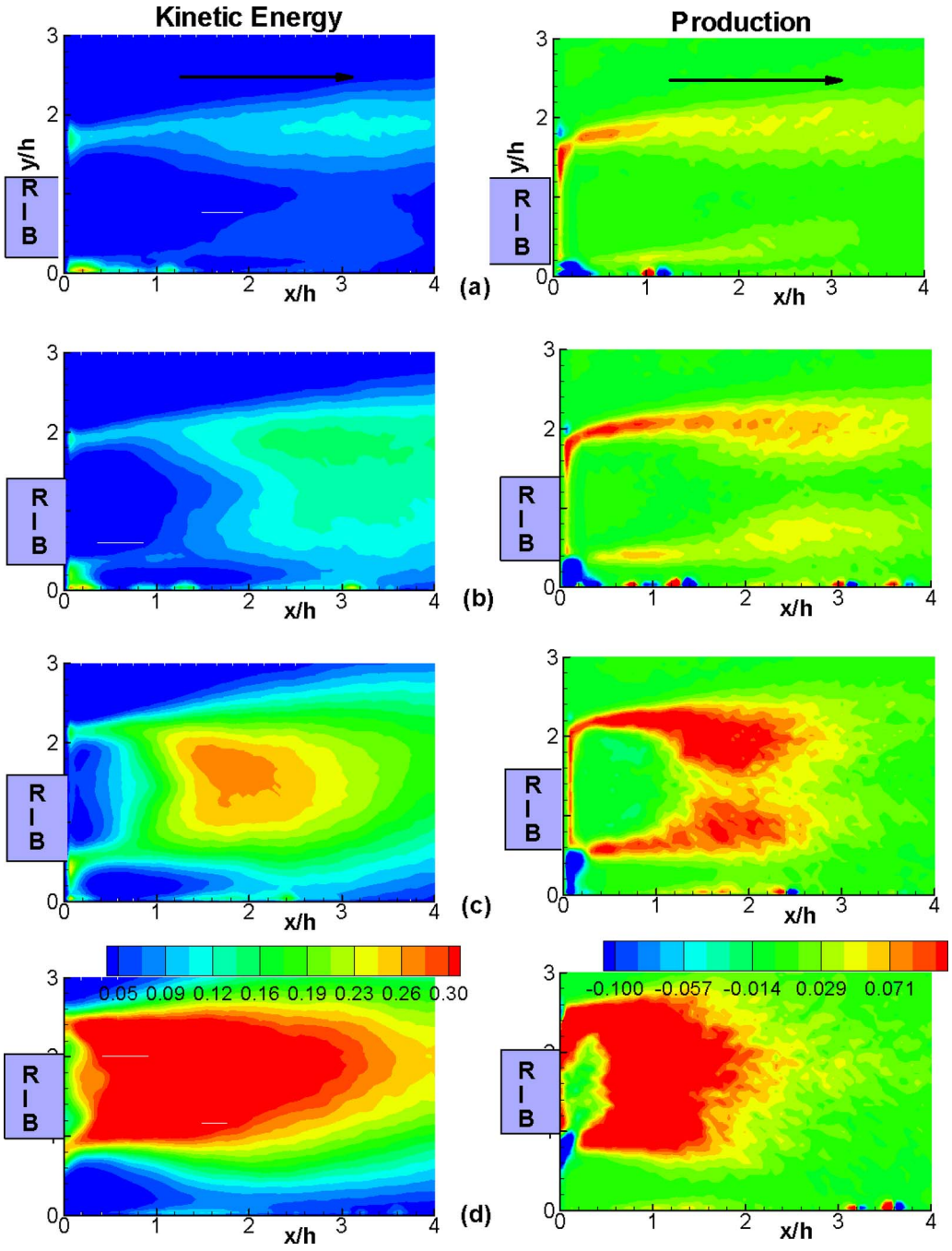

Fig. 12 The normalized total turbulent kinetic energy and the normalized production of turbulent kinetic energy behind detached ribs for gap size to rib height ratio: (*a*) *G*/*h*=0.2, (*b*) *G*/*h*=0.37, (*c*) *G*/*h*=0.57, and (*d*) *G*/*h*=1.0

the present study is more toward a detailed characterization of the flow field with specific interest on the near wall mixing. The 2C PIV, stereo PIV, and oil film visualization measurements have been carried out. The flow structures responsible for the effectiveness of detached rib configurations have been discussed based on velocity, vorticity, velocity gradient, stream traces, turbulent fluctuation intensity, turbulent kinetic energy budget terms, and oil film visualization results. The understanding obtained from this study is expected to benefit the design of turbulators for various practical applications. Some of the salient observations from this study are summarized below.

The detached rib configurations with smaller gap size to cylinder height ratio are beneficial from near wall mixing consideration. The flow structures and the turbulent fluctuation intensity behind the detached ribs are significantly influenced by the size of the gap between the bottom face of the cylinder and the wall surface. The v-velocity results show strong wall-normal motion in the near wall region for detached ribs of small gap size. The instantaneous vorticity is concentrated more in the near wall region for smaller gap size case compared to that of larger gap size. The coherent structure identifiers, i.e., the second invariant of the velocity gradient tensor (Q_{2D}) successfully distinguishes the rotational contribution of the vorticity distribution. The coherent structure distribution is not identical in both the lower and upper shear layer regions. The vortex structures in the lower shear layer

Downloaded 03 Jun 2010 to 171.66.16.158. Redistribution subject to ASME license or copyright; see http://www.asme.org/terms/Terms_Use.cfm

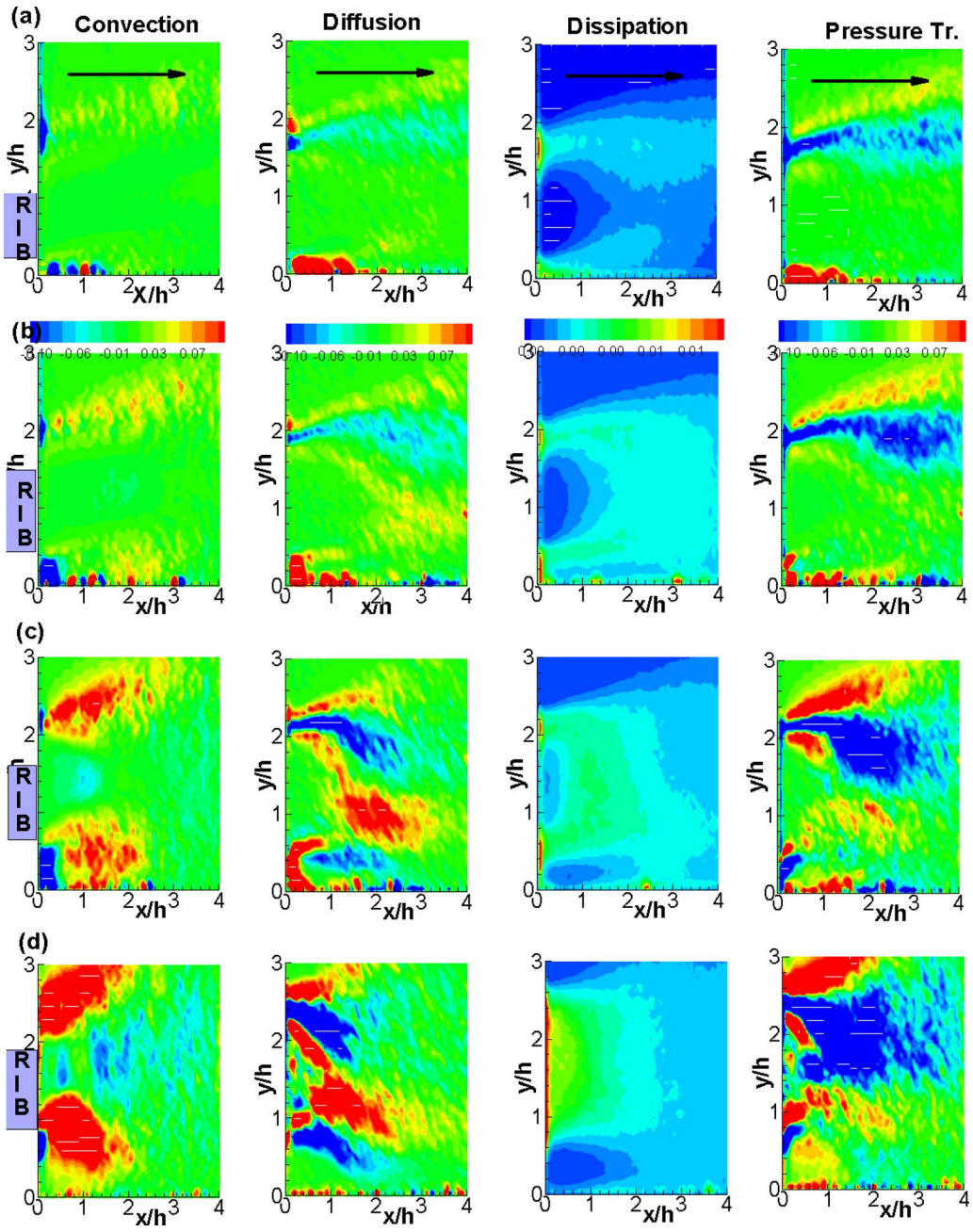

Fig. 13 The normalized turbulent kinetic energy budget terms behind detached ribs for gap size to rib height ratio: (*a*) $G/h=0.2$, (*b*) $G/h=0.37$, (*c*) $G/h=0.57$, and (*d*) $G/h=1.0$

region are influenced by the combined effect of wall boundary layer and flow through the gap. The turbulent kinetic energy distribution in the wake region of the detached ribs is a function of the gap size, and its distribution is influenced by various mechanisms, i.e., convection, diffusion, dissipation, and pressure transport. The stream traces, whose size and shape depends on the gap size, in the streamwise (x-y) plane show recirculation bubble (foci) at both sides of the cylinder centerline. In the cross stream (y-z) plane, node-saddle (N-S) flow patterns are present, whose y-locations are a function of the gap size. Additional node-saddle patterns are observed in the near wall region for detached ribs of smaller gap size.

Acknowledgment

The author gratefully acknowledges the Alexander von Humboldt Foundation (http://www.humboldt-foundation.de) for financial support and Dr. J. Kompenhans of DLR, Germany for hospitality and support.

Nomenclature

x, y, z = spatial coordinates
u, v, w = mean velocity components
u', v', w' = fluctuating velocity components
G = y-separation between the cylinder bottom and flat plate surfaces

Downloaded 03 Jun 2010 to 171.66.16.158. Redistribution subject to ASME license or copyright; see http://www.asme.org/terms/Terms_Use.cfm

h = rib height
V = velocity vector magnitude
Q = second invariant of the velocity gradient tensor
K = turbulent kinetic energy
U_o = freestream velocity
δ = boundary layer thickness
ω = vorticity
rms = root mean square

References

[1] Taniguchi, S., and Miyakoshi, K., 1990, "Fluctuating Fluid Forces Acting on a Circular Cylinder and Interference With a Plane Wall, Effects of Boundary Layer Thickness," Exp. Fluids, **9**, pp. 197–204.

[2] Durao, D. F. G., Gouveiu, P. S. T., and Fereira, J. C. F., 1991, "Velocity Characteristics of the Flow Around a Square Cross Section Cylinder Placed Near a Channel Wall," Exp. Fluids, **11**, pp. 341–350.

[3] Buresti, G., and Lanciotti, A., 1992, "Mean and Fluctuating Forces on a Circular Cylinder in Cross-Flow Near a Plane Surface," J. Wind. Eng. Ind. Aerodyn., **41–44**, pp. 639–650.

[4] Liou, T. M., and Wang, W. B., 1995, "Laser Holographic Interferometry Study of Developing Heat Transfer in a Duct With a Detached Rib Array," Int. J. Heat Mass Transfer, **38**, pp. 91–100.

[5] Bosch, G., Kappler, M., and Rodi, W., 1996, "Experiments on the Flow Past a Square Cylinder Placed Near a Wall," Exp. Therm. Fluid Sci., **13**, pp. 292–305.

[6] Bailey, S. C. C., Martinuzzi, R. J., and Kopp, G. A., 2002, "The Effects of Wall Proximity on Vortex Shedding From a Square Cylinder: Three Dimensional Effects," Phys. Fluids, **14**, pp. 4160–4177.

[7] Liou, T. M., Chen, M. Y., and Chang, K., 2003, "Spectrum Analysis of Fluid Flow in a Rotating Two-Pass Duct With Detached 90° Ribs," Exp. Therm. Fluid Sci., **27**, pp. 313–321.

[8] Liou, T. M., Chen, M. Y., and Wang, Y. M., 2003, "Heat Transfer, Fluid Flow and Pressure Measurements Inside a Rotating Two-Pass Duct With Detached 90-deg Ribs," ASME J. Turbomach., **125**, pp. 565–574.

[9] Martinuzzi, R. J., Bailey, S. C. C., and Kopp, G. A., 2003, "Influence of Wall Proximity on Vortex Shedding From Square Cylinder," Exp. Fluids, **34**, pp. 585–596.

[10] Panigrahi, P. K., Schroeder, A., and Kompenhans, J., 2005, "PIV Investigation of Flow Behind Surface Mounted Permeable Ribs," Exp. Fluids, **40**, pp. 277–300.

[11] Kolar, V., 1991, "On the Critical Points in the Description of Vortical Flows," Acta Mech., **89**, pp. 241–245.

[12] Zhou, Y., and Antonia, R. A., 1994, "Critical Points in a Turbulent Near Wake," J. Fluid Mech., **275**, pp. 59–81.

[13] Brown, G. L., and Roshko, A., 1974, "On Density Effects and Large Structure in Turbulent Mixing Layers," J. Fluid Mech., **64**, pp. 775–816.

[14] Jeong, J., and Hussain, F., 1995, "On the Identification of a Vortex," J. Fluid Mech., **285**, pp. 69–94.

[15] Calluaud, D., and David, L., 2004, "Stereoscopic Particle Velocimetry Measurements of the Flow Around a Surface Mounted Block," Exp. Fluids, **36**, pp. 53–61.

[16] Wang, L., Hejcik, J., and Sunden, B., 2007, "PIV Measurement of Separated Flow in a Square Channel With Streamwise Periodic Ribs on One Wall," ASME J. Fluids Eng., **129**, pp. 834–841.

[17] Panigrahi, P. K., Schroeder, A., and Kompenhans, J., 2008, "Turbulent Structures and Budgets Behind Permeable Ribs," Exp. Therm. Fluid Sci., **32**, pp. 1011–1033.

Downloaded 03 Jun 2010 to 171.66.16.158. Redistribution subject to ASME license or copyright; see http://www.asme.org/terms/Terms_Use.cfm

Pierre Magnier

Vincent Boucinha

Laboratoire de Mécanique et d'Énergétique,
8 Rue Léonard de Vinci,
45072 Orléans, Cedex 02, France

BinJie Dong
GREMI, UMR 6606,
CNRS/Université d'Orléans,
14 Rue d'Issoudun BP 6744,
45072 Orléans, Cedex 02, France

Régine Weber

Annie Leroy-Chesneau

Laboratoire de Mécanique et d'Énergétique,
8 Rue Léonard de Vinci,
45072 Orléans, Cedex 02, France

Dunpin Hong
GREMI, UMR 6606,
CNRS/Université d'Orléans,
14 Rue d'Issoudun BP 6744,
45072 Orléans, Cedex 02, France

Experimental Study of the Flow Induced by a Sinusoidal Dielectric Barrier Discharge Actuator and Its Effects on a Flat Plate Natural Boundary Layer

Since the mid-1990s, electrohydrodynamic actuators have been developed for modifying on subsonic airflows. The principle of plasma action is the use of the direct conversion of electrical energy into kinetic energy in order to act on the flow boundary layer. This paper presents our contribution to such an investigation concerning an electrohydrodynamic actuator consisting of several sinusoidal dielectric barrier discharges. First, the ionic wind induced by this actuator was measured with a pressure sensing probe. The induced flow velocity increased with the applied voltage and frequency. The particle image velocimetry system without external airflow showed the presence of induced swirls, generated by the ion movement in plasma. Then the action of this actuator on a flat plate boundary layer in parallel flow at zero incidence was studied in a subsonic wind tunnel. Experiments were performed for 15 m/s and 22 m/s. They showed that electric discharges (±8 kV, 1 kHz) acting on a laminar flow tripped the laminar-to-turbulent transition. Moreover, higher applied voltages (up to ±12 kV, 1 kHz) were necessary for modifying turbulent boundary layers. [DOI: 10.1115/1.3026722]

Keywords: boundary layer, dielectric barrier discharge, electrohydrodynamics, plasma actuator

1 Introduction

The subsonic flow control can have an important impact on industry. Main objectives are to remove the negative effects of a flow as the reduction of noise or drag decreases, and to improve the positive effects as the lift or fluid mixture increases. It could improve aerodynamic performances of transport vehicles to have higher velocities for lower energy consumption. For example, in the case of military aircrafts, stall angle delay may improve maneuver possibilities. Turbulent boundary layer presents a high velocity gradient on the wall. Then it allows the flow to better resist unfavorable pressure gradients, and thus to not separate from the wall. Thus classical methods of flow control are based on actions on the boundary layer laminar-to-turbulent transition and modifications of the wall friction. Two kinds of action are investigated. Passive methods consist of modifying the wall conditions for promoting transition, such as riblets [1] and vortex generators [2]. Active methods of flow control consist of inducing flow perturbations in the vicinity of the wall, such as moving surface [3], blowing, and suction with periodic excitation [4] among others.

For this purpose, nonthermal plasmas have been studied since the mid-1990s for their use in aerodynamics [5]. Several experimental and numerical investigations have shown the ability of plasma actuators for modifying subsonic airflows. The principle is to use the ionic wind induced by electric discharges [6], with a direct conversion of electrical energy into mechanical energy. The advantages of plasma actuators are no mechanical parts and a short response time. dc corona discharges in steady mode were developed by several authors [7–14] for airflow control. It enabled reductions of flow separation on a NACA 0015 airfoil up to Re =267 K and angles of attack up to 17.5 deg [15]. More efficient actuations were obtained by using different working modes, other electric sources, and/or other geometrical configurations. Indeed, plasma actuators based on dielectric barrier discharge (DBD), supplied by an ac electric source, were developed in Refs. [16–22]. These references used a steady actuation on the flow and significantly acted on airflows, but better effects were achieved with unsteady actuation. Sosa et al. [23] employed a dc corona discharge working in an unsteady mode for delaying the flow separation. By adjusting the applied signal frequency, they acted for Reynolds numbers of up to 333 K. Corke and co-workers [24,25] and Post et al. [26] used ac unsteady DBDs to delay the airfoil stall for Reynolds numbers of up to 584 K. Opaits et al. [27] acted up to 75 m/s on an 8-cm wide airfoil. Plasma actuator placed at the airfoil leading edge has similar effects to leading edge slats, and similar to flaps when it is placed at the trailing edge [25]. A review of the main reported works was done by Moreau [28]. Most authors estimate that the effect of plasma actuators on an airflow is mainly due to the ionic wind, but thermal effects (gas heated by discharges) may also affect the physical properties of the air [29].

However, the plasma-airflow interaction and the effects on boundary layers are not clearly fixed. Therefore, in order to have a better understanding of how to act with plasma on wall-bounded flows, we present in this paper the investigation of a typical natural evolving boundary layer on flat plate and its modifications by an actuator based on multi-DBDs working in steady mode. For this purpose, Velkoff and Ketcham [30] used four successive wires generating corona discharges and shifted the laminar-to-turbulent transition at about 50 m/s. Grundmann and Tropea [31] also delayed transition on a 1.6-m long flat plate at 6 m/s, with two successive DBD actuators. Moreau et al. [32] modified veloc-

Contributed by the Fluids Engineering Division of ASME for publication in the JOURNAL OF FLUIDS ENGINEERING. Manuscript received July 16, 2007; final manuscript received October 9, 2008; published online December 2, 2008. Assoc. Editor: James A. Liburdy.

 Copyright © 2009 by ASME

Downloaded 03 Jun 2010 to 171.66.16.158. Redistribution subject to ASME license or copyright; see http://www.asme.org/terms/Terms_Use.cfm

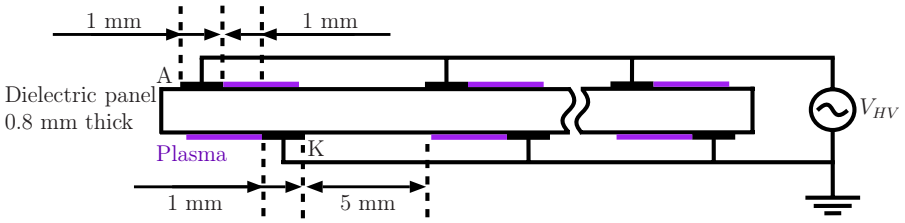

Fig. 1 Actuator with several dielectric barrier discharges

ity profiles and induced a drag reduction on a 30-cm long flat plate with a dc surface corona discharge of up to 25 m/s. Porter et al. [33] used a single DBD for tripping the laminar-to-turbulent transition of a flat plate boundary layer at 4 m/s and 6.5 m/s. Numerical investigations of boundary layer control by electric discharges have shown the ability to strongly modify velocity profiles [34,35]. The investigated plasma actuator in the present study consisted of successive DBDs. The plasma process of this kind of electric discharge was developed by Enloe et al. [19], Van Dyken et al. [36], and Likhanskii et al. [37]. First, the flow induced by this actuator was studied without external flow with the particle image velocimetry (PIV) system for various applied voltages and frequencies. In order to act on laminar then turbulent natural evolving boundary layers, this actuator was then mounted on a 1-m long flat plate and acted at ±8 kV and 1 kHz in various positions. Inlet airflow velocities were 15 m/s and 22 m/s. Velocity profile measurements were performed in numerous positions along the flat plate at zero incidence and evolution of characteristic boundary layer parameters were deduced.

2 Experimental Setup

2.1 Plasma Actuators and Power Supply. The plasma actuator consisted of several dielectric barrier discharges established on a dielectric material ($160\times115\times0.8$ mm^3). The actuator was realized with a printed circuit board (PCB). Each DBD was created between two thin copper electrodes (width of 1 mm, thickness of 35 μm) separated by a dielectric panel in epoxy, see Fig. 1. These electrodes had an asymmetric design with a 1 mm gap between the upper and lower electrodes. The gap between two pairs of electrodes was 5 mm. Measurements with the particle image velocimetry system, shown in Sec. 3.2, were performed with an actuator consisting of 12 successive single DBDs. Induced velocity profiles and action on a flat plate boundary layer were studied with 15 single DBDs. The plasma power consumption was between 7 W and 60 W for the entire actuator (see Table 1). Parametric studies of this kind of actuator geometry were done by Borghi et al. [38], Forte et al. [39] and Magnier et al. [40].

The upper electrodes were connected to an ac power supply, described in Fig. 2. A sound amplifier (Crown®, Xs1200, 0.022–22 kHz, 2.3 kW) magnified the sine waveform delivered by a function generator. Voltage of amplitudes of up to ±20 kV (i.e., 40 kV peak to peak) was obtained with a high voltage transformer (90 V/20 kV, up to 20 kHz). The power supply output voltage was measured with a high voltage probe Tektronix P60115A. Outputs were visualized with a fast digital oscilloscope LeCroy WaveSurfer 454. The lower actuator surface, with electrodes connected to the ground, was covered with a thin layer of Kapton®, in order to inhibit discharges on the grounded side. Plasma actuators worked in steady mode. The typical behavior of the discharge current versus time for a sine high voltage is shown in Fig. 3 (±5 kV, 1 kHz). It shows that the positive discharge consists of successive streamers whereas the negative discharge is more homogeneous.

Table 1 Maximum induced flow velocity for various active powers, 1 mm behind the last electrode

±8 kV	P (W)	U_p (m/s)
0.5 kHz	10.56	1.48
1 kHz	22.99	2.38
2 kHz	42.53	3.06
1 kHz	**P (W)**	**U_p (m/s)**
±6 kV	7.40	1.53
±8 kV	22.99	2.38
±10 kV	38.80	2.95
±12 kV	61.48	3.25

2.2 Flat Plate. In order to investigate modifications of the boundary layer due to the plasma actuator, we used a 1-m long, 300-mm broad, and 30-mm thick flat plate made entirely of polyvinyl chloride (PVC) (Fig. 4). It was divided into three parts, fixed with electrically insulating screws (Nylon®). The flat plate leading edge was a NACA 0015 leading edge (0–30% chord, 60 mm long) since it presents no bubbles at 0 deg for the investigated velocities. The flat plate trailing edge was a NACA 0015 trailing edge (30–100% chord, 140 mm long). Four plasma actuators, each one constituted of 15 single DBDs, were placed in slots separated 13 mm away from the medium part, as described in Fig. 4. The flat plate surface was then quasismooth (the electrode thickness of

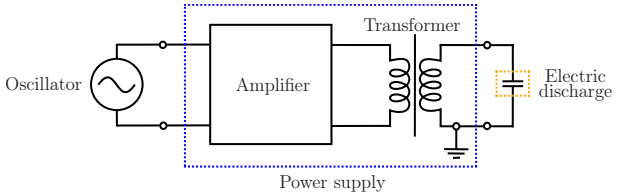

Fig. 2 Power supply for the DBD actuator

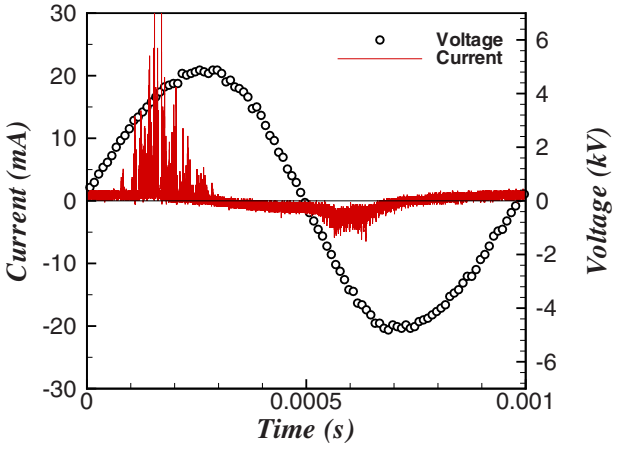

Fig. 3 Voltage and current versus time (±5 kV, 1 kHz)

Downloaded 03 Jun 2010 to 171.66.16.158. Redistribution subject to ASME license or copyright; see http://www.asme.org/terms/Terms_Use.cfm

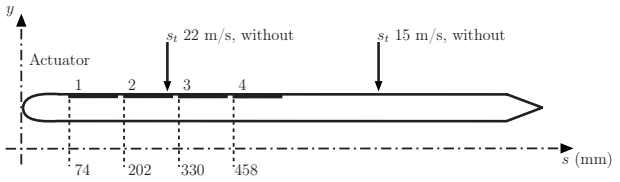

Fig. 4 Schematic of the flat plate with positions of four DBD actuators

35 μm was negligible [41]). All plasma actuators were oriented in order to generate an ionic wind in the same direction as the main flow.

The curvilinear abscissa s is used for determining positions on the flat plate, in order to take into account of the leading edge curvature. The y-axis origin is the flat plate surface, and the s-axis origin is the flat plate leading edge.

2.3 Subsonic Wind Tunnel. Experiments with the flat plate were performed in a subsonic open-circuit wind tunnel with a 2-m long square test section (50×50 cm^2), described in Fig. 5. The nozzle has a section contraction ratio of 1:16. The maximum velocity is about 50 m/s, generated by a 30 kW electric fan. Flow characterization with a hot wire probe indicated that the mean turbulence ratio was 0.4% in the beginning of the test section, without an obstacle, and the flow was bidimensional over 85% of the wind tunnel test section height and width. The 1-m long plate with actuators was placed between two vertical plates (1.5 m $\times$50 cm$\times$15 mm) in order to limit tridimensional effects.

2.4 Flow Measurements

2.4.1 Particle Image Velocimetry System. Flow velocity fields were determined using the PIV system. A laser sheet was generated from a laser beam (wavelength of 532 nm, Nd:Yag laser, Big Sky Laser) using mirrors and lenses, and illuminated smoke particles, which seeded the airflow. A charge coupled device camera PowerView Plus TSI (model 630159) captured images of illuminating particles (2048×2048 pixels^2). Displacement vectors of each particle were then calculated by InSight™ using two successive images recorded for two successive laser pulses (200 mJ each, time delay of 10 μs). The velocity fields presented in this paper are the mean vector fields of 500 pairs of such recorded images.

2.4.2 Pressure Sensing Probe. In order to avoid unwanted electrical arcs, a total pressure probe made of glass was used (external diameter of 0.6 mm, internal diameter of 0.4 mm). The lower vertical measurement position was thus 0.3 mm on the y-axis. In order to have velocity measurements, a static pressure probe was fixed to the glass probe. This pressure measurement system was calibrated with a classical Pitot tube in a subsonic wind tunnel. The error made in pressure measurements is under 0.5% for a probe rotation of $\pm$7.5 deg.

For the induced flow velocity measurements in Sec. 3, the pressure measurement system was connected to a differential low-

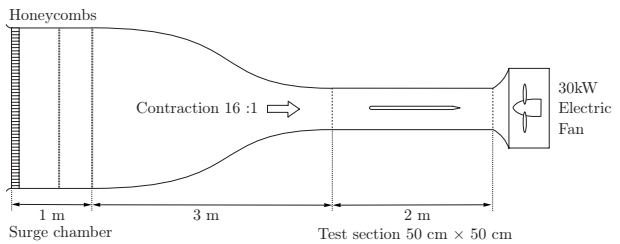

Fig. 5 Subsonic wind tunnel with a square test section of 50 cm$\times$50 cm$\times$2 m

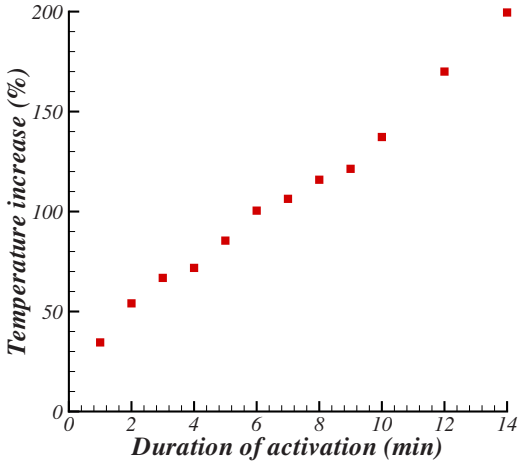

Fig. 6 Actuator temperature increase during its activation duration (initial actuator temperature of 22°C)

pressure transducer Druck™ LPM 9481 with a short pressure brand of 0–20 Pa (output voltage 0–5 V) in order to precisely measure low velocities. For flat plate boundary layer investigations in Sec. 4, the pressure measurement system was connected to a differential pressure transducer Druck™ LPM 9381 with a wider pressure brand of 0–500 Pa (output voltage of 0–5 V). The measurement accuracy of these transducers was 0.1% of the full range. Measurements were acquired on a PC using a 16-bit acquisition card (resolution of the output voltage measured at 8×10^{-5} V, i.e., $\pm$0.008 Pa), over a 1 s interval at a 3 kHz sampling rate. Velocity profiles were obtained from time-averaged pressure measurements.

This velocity measurement system was fixed to a computer controlled two-dimensional traversing system Isel® Automation LF 5 (displacement precision of $\pm$0.02 mm).

2.4.3 Test Procedure. Without external airflow, because of plasma inhibition on the grounded side, an important part of the applied power was dissipated into the dielectric material. The temperature on the actuator surface increased from 22°C to 66°C after an activation duration of 14 min (+200%), as shown in Fig. 6 (measured with a surface thermometer TESTO, from −50°C to 250°C). A test procedure was chosen in order to verify that dielectric surface heating did not produce a notable effect on the flow. It consisted of measuring a velocity profile without activated plasma in a position s, and then velocity profile measurement was performed in the same position with the working actuator. Since the duration of each velocity profile measurement was about 8 min, a velocity profile without discharge was measured and compared with the natural boundary layer after each measurement with plasma. There was no difference between these two profiles without plasma. Therefore dielectric surface heating does not produce a notable effect on the flow.

During these experiments, velocity profiles were measured every 16 mm along the s-axis until the fourth actuator, and every 50 mm downstream. Their heights were measured up to 20 mm in the y-axis.

Temperature in the test section, atmospheric pressure, and relative humidity were recorded for each velocity profile (thermohygrometer Kimo®, HD 100), for determining air density ρ and dynamic viscosity μ.

3 Flow Induced by the Plasma Actuator

First, this actuator was studied without external airflow in order to characterize the flow induced by the successive DBDs.

3.1 Induced Flow Velocity Profiles. The velocity of the induced ionic wind was measured for various voltages (from

Downloaded 03 Jun 2010 to 171.66.16.158. Redistribution subject to ASME license or copyright; see http://www.asme.org/terms/Terms_Use.cfm

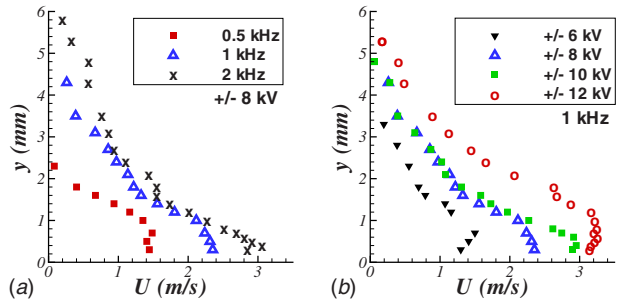

Fig. 7 Induced flow velocity, 1 mm after the last electrode (*a*) for various frequencies (0.5 kHz, 1 kHz, and 2 kHz) and a given applied voltage of ±8 kV, and (*b*) for various high voltages (from ±6 kV to 12 kV) and a given frequency of 1 kHz

±6 kV to ±12 kV) and frequencies (0.5 kHz, 1 kHz, and 2 kHz) of the applied signal. Induced flow velocity profiles, without external airflow, were performed 1 mm behind the last 15th single DBD. Figure 7 shows the measured curves and maximum velocities U_p of induced flow are reported for each case in Table 1.

For a given frequency, the maximum velocity of the plasma-induced flow increased with the voltage amplitude. Indeed, the phenomenon of ionization was more important, therefore more ions moved in the interelectrode space. The momentum transfer with the neutral molecules was more important, and the flow resulting from it was thus faster. Moreover for a given voltage, the velocity was more important when the frequency of the signal increased. Thus to obtain the maximum velocity for this actuator, the frequency and the voltage must be the highest possible voltage according to the power supply limitations.

3.2 Induced Flow Topology. In order to study the induced flow topology on the actuator, measurements with the PIV system were performed without external airflow. The measurement window in Fig. 8 shows the flow streamlines above the last six single DBD (12 couples, gap of 8 mm between two DBD), for 1 kHz and two voltage amplitudes, ±5 and ±12 kV.

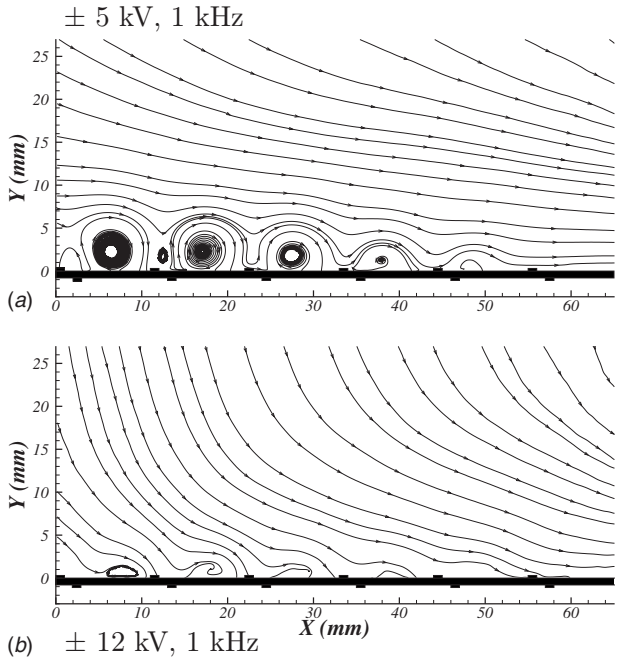

Fig. 8 Flow streamlines induced by the DBD actuator with a frequency of 1 kHz and a voltage of (*a*) ±5 kV and (*b*) ±12 kV

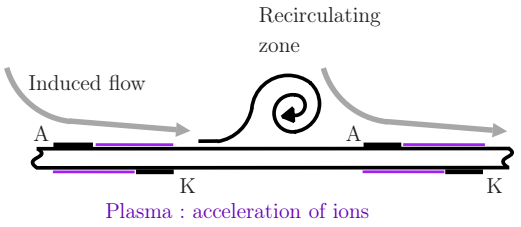

Fig. 9 Schematic of the flow induced by a DBD actuator

This figure shows swirls in space between two pairs of electrodes. The position and the rotation direction of these swirls indicate the way in which the neutral molecules of gas are involved. For each DBD, ions generated by the high voltage move in the interelectrode gap. This movement is very close to the actuator surface (the ion sheath size is up to 50 μm [42]). Some neutral molecules of gas in the direct vicinity of the plasma are thus involved by momentum transfer with ions in the interelectrode space (model of "porous piston" by Likhanskii et al. [37]). These molecules are strongly accelerated near the plasma and induce a flow. It pulls down above the plasma and goes down toward the anode. The global flow movement, resulting from positive and negative half-cycles, is directed from the exposed anode toward the "virtual" cathode (placed on the other side of the dielectric panel). Downstream of the cathode, there is neither more plasma nor ions to keep on involving the flow. Thus its velocity close to the wall decreases due to the wall friction (null velocity). This induced flow downstream of the first DBD is involved toward the wall by the flow induced by the next DBD since the same flow topology is generated by the next plasma, in particular the flow going down toward the anode. Then this could explain the swirl generation between two DBD (Fig. 9).

A part of the flow induced by the first DBD is accelerated by the second one. The flow is then faster downstream this second DBD and is less affected by the flow induced by the next plasma. The size of the swirls is then increasingly reduced along the longitudinal axis. The flow is accelerated after each couple of electrodes, which confirms the observations made by Forte et al. [39].

Moreover, more ionized plasma (generated by the higher applied voltage) induces a faster flow compared with lower applied voltages. The size of swirls for ±12 kV is thus reduced in comparison with ±5 kV.

4 Action of the Plasma Actuator on a Boundary Layer

4.1 Curves and Results. Experiments with external airflow, in the subsonic wind tunnel described in Sec. 2.3, were performed on a 1 m flat plate at zero incidence with four plasma actuators (Fig. 4). Natural boundary layers developed along the plate were modified by one of these actuators working at ±8 kV (i.e., 16 kV peak to peak) and 1 kHz. Time-averaged velocity profiles were measured with the pressure sensing probe without and with the actuator working. Each result presented in this paper was validated by comparison with theoretical curves. The action of the third actuator is not shown here because the results are comprised between the results shown for the second and the fourth ones.

Velocity profiles in three positions (s=155 mm, 187 mm, and 427 mm, which showed different kinds of velocity profiles) for two airflow velocities (15 m/s and 22 m/s), without and with activated actuator 1, are shown in Fig. 10. These curves are compared with the Falkner–Skan solutions (laminar boundary layers) and Prandtl's turbulent solution (law in 1/7). Mean airflow velocity, noted U_∞, was determined from the velocity profile in each position.

We consider the nondimensionalized variables u^+ and y^+ defined by the relations $u^+=u/u_\tau$ and $y^+=yu_\tau/\nu$ with u as the

Downloaded 03 Jun 2010 to 171.66.16.158. Redistribution subject to ASME license or copyright; see http://www.asme.org/terms/Terms_Use.cfm

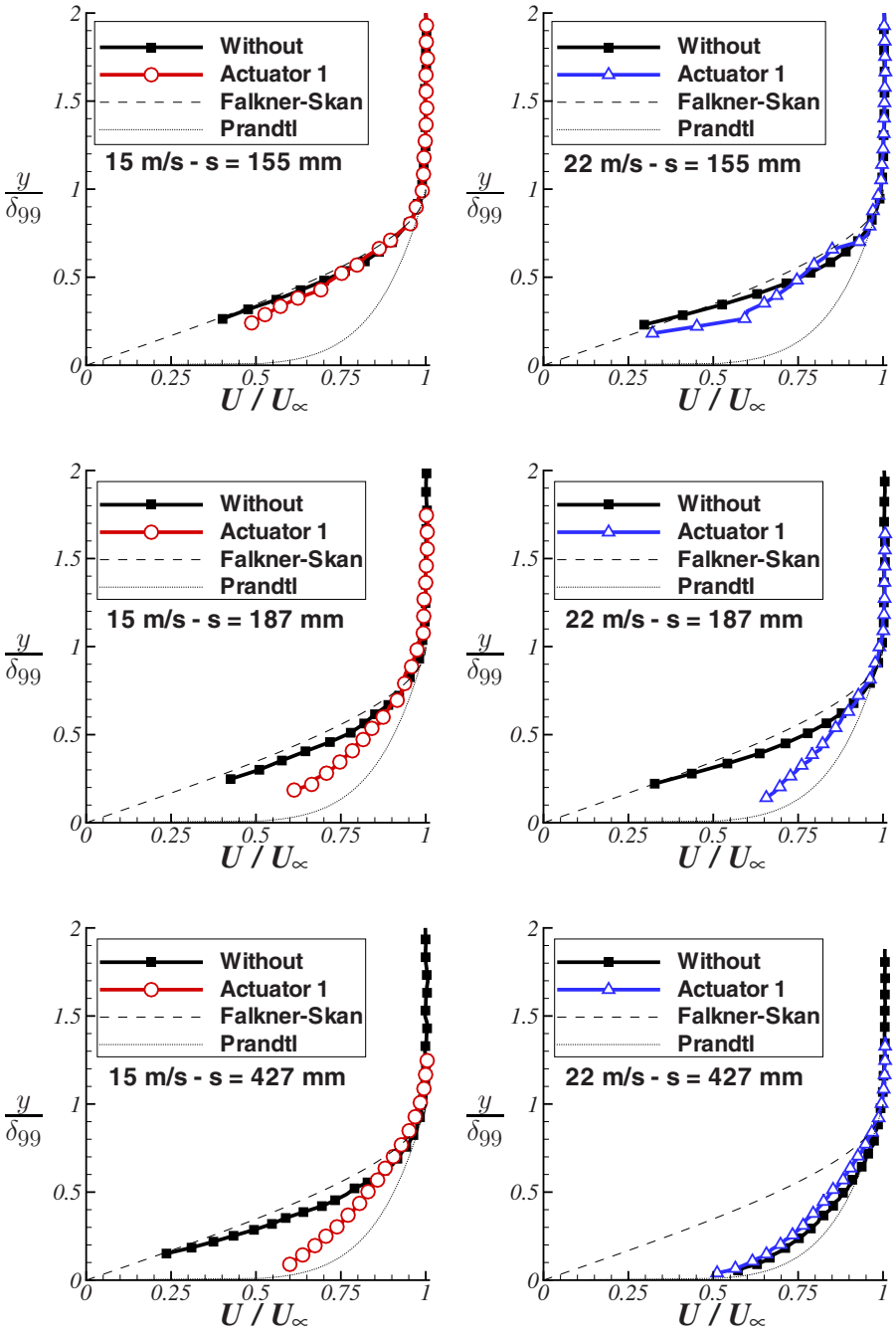

Fig. 10 Nondimensional mean velocity profiles for 15 m/s and 22 m/s, without and with actuator 1 activated (±8 kV, 1 kHz), in *s*=155 mm, 187 mm, and 427 mm

measured velocity at height y. The friction velocity is therefore $u_\tau = \sqrt{(\tau_w/\rho)}$, and the wall shearing-stress is $\tau_w = \mu(\partial u/\partial y)_{y=0}$. The nondimensional mean velocity profiles are plotted on a semilogarithmic scale in Fig. 11, for both velocities and for the three previous positions. These curves are compared with the logarithmic law for turbulent flow [41]: $u^+ = 5.75 \log(y^+) + 5.5$.

From each measured velocity profiles, some characteristic properties were determined as follows:

- the boundary layer thickness δ_{99},
- the displacement thickness $\delta_1 = \int_{y=0}^{\infty}(1 - u/U_\infty)dy$,
- the momentum thickness $\delta_2 = \int_{y=0}^{\infty} u/U_\infty(1 - u/U_\infty)dy$,
- the shape factor $H = \delta_1(s)/\delta_2(s)$,
- and the drag per unit width $D = \rho\int_{y=0}^{\infty} u(U_\infty - u)dy$.

These parameters are plotted along the flat plate in Figs. 12–16, respectively, for each case of actuation. The natural evolving boundary layer parameters are compared with the theoretical laminar evolution (Blasius), and the boundary layer parameters under the action of actuator 1 are compared with the theoretical turbulent evolution (Prandtl). As shown in these figures, the theoretical and experimental curves are similar. But for clearer figures, the theoretical curves are not all plotted. The beginning of the boundary layer turbulent zone s_t is determined for all studied cases by the intersection of the Prandtl turbulent curve with the s-axis on the δ_{99}-graph.

4.2 Effects on a Laminar Boundary Layer. Considering the beginning of the turbulent zone for 15 m/s (s_{t15}=580 mm) in Fig.

Downloaded 03 Jun 2010 to 171.66.16.158. Redistribution subject to ASME license or copyright; see http://www.asme.org/terms/Terms_Use.cfm

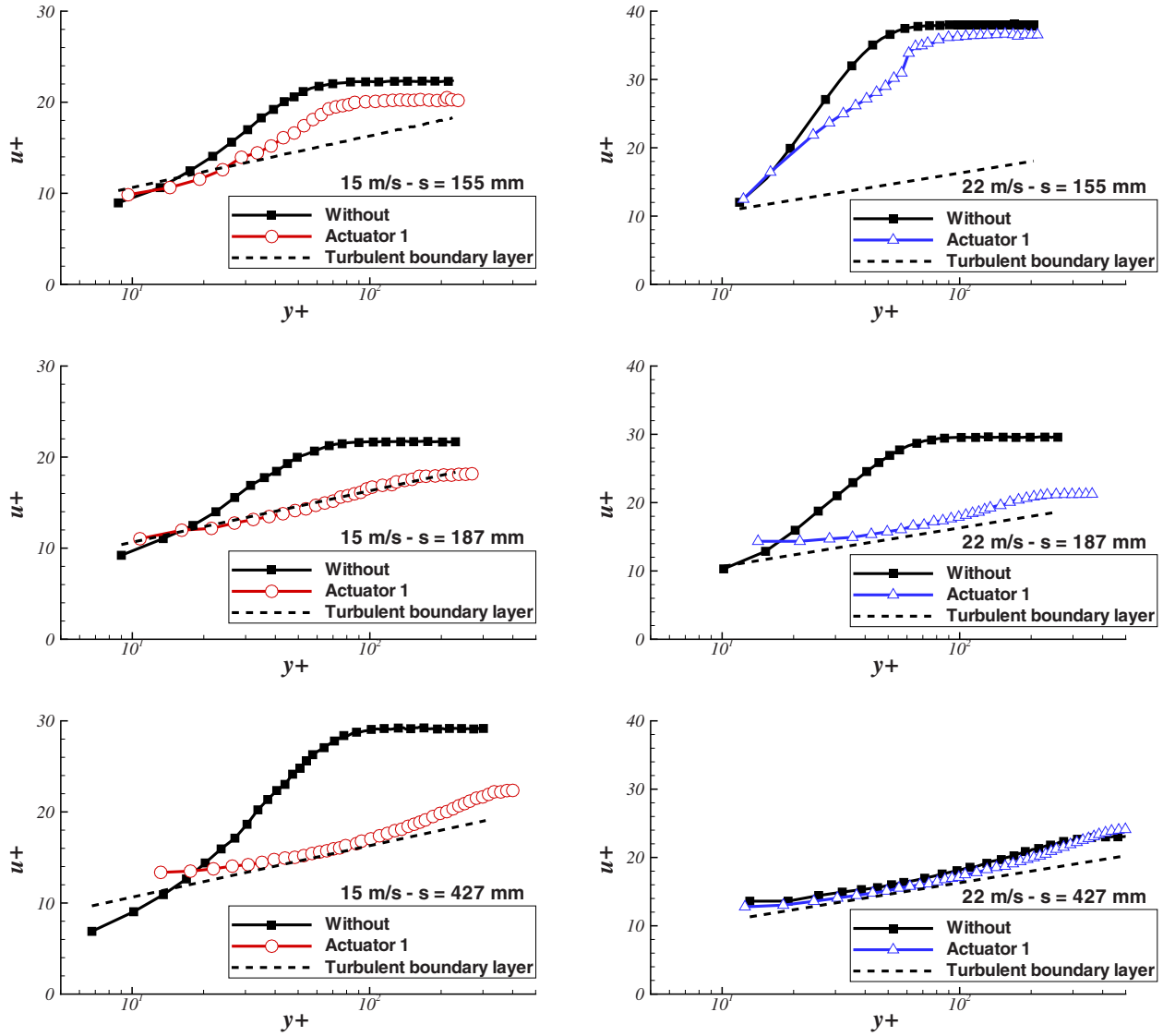

Fig. 11 u^+ **velocity profiles for 15 m/s and 22 m/s, without and with actuator 1 activated (±8 kV, 1 kHz), in** s**=155 mm, 187 mm, and 427 mm**

4, plasma actuators acted on a natural laminar boundary layer. For 22 m/s (s_{t22}=255 mm), the first actuator acted on a laminar boundary layer and the other ones on a turbulent boundary layer.

From Fig. 10, we notice that the boundary layer profiles are modified near to the wall by action of the first actuator in s =155 mm, for both velocities. Then downstream of this position, the velocity gradient on the wall continues to increase along the flat plate, and the forced velocity profiles tend toward the theoretical turbulent solution. We did not notice a clear momentum added by the induced ionic wind on the velocity profiles, as observed for the lower airflow velocity and more powerful discharges by Moreau et al. [32] or Porter et al. [33]. The only visible effect of the plasma actuator on the laminar boundary layer was to make the profiles more turbulent, as shown in Fig. 11. These graphs show that velocity profiles became more turbulent along the plate whereas the natural boundary layer was laminar. Although there was no plasma at position s=427 mm (when actuator 1 was considered), the boundary layer was still turbulent at this position showing that the flow modification was not limited to the place where the actuator was located. Therefore the boundary layer transition was prematurely tripped by the action of the plasma.

The observation of the boundary layer parameters along the flat plate confirms this result. Figures 12–14 show a strong early increase in δ_{99}, δ_1, and δ_2 when actuators are activated. The action of the first actuator on laminar boundary layers for 15 m/s and 22 m/s promoted the transition above this actuator, as shown in Table 2. Moreover the transition was advanced for 15 m/s when the second and fourth actuators were activated. The shape factor H in Fig. 15 strongly decreased above the actuator from the laminar theoretical value (2.59) until the turbulent theoretical value (about 1.4 [41]). This figure clearly shows the beginning of the transition area and the beginning of the boundary layer turbulent zone for each studied case.

Finally, each single DBD of an activated actuator induced an ionic wind, and the effect on a laminar boundary layer was to trip the transition. Each DBD acted as a small turbulator (such as grit paper), which amplified boundary layer instabilities. This succession of disturbances promoted early transition. This remark confirms the experimental results of Porter et al. [33] and the numerical results of Visbal et al. [35]. The main consequence of an earlier turbulent flow on a flat plate was the drag increase, as shown in Fig. 16. Indeed drag was more than tripled (+213%) in s=682 mm for 15 m/s, by action of the first actuator.

4.3 Effects on a Turbulent Boundary Layer. When a plasma actuator acted in a position where the unforced boundary

Downloaded 03 Jun 2010 to 171.66.16.158. Redistribution subject to ASME license or copyright; see http://www.asme.org/terms/Terms_Use.cfm

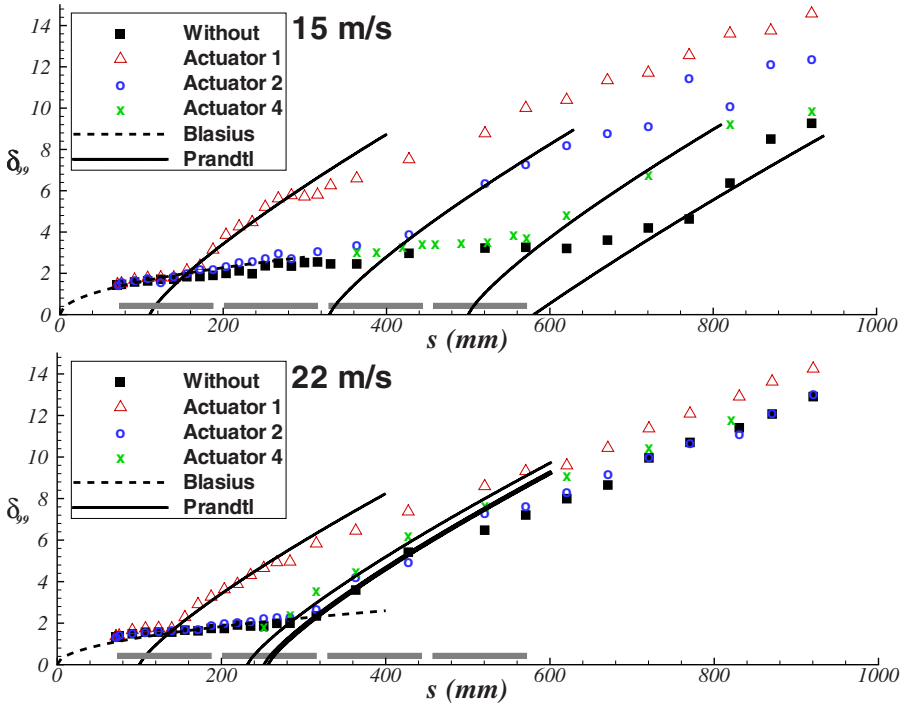

Fig. 12 Boundary layer thickness δ_{99} (mm) along the flat plate for 15 m/s and 22 m/s, for various DBD actuator positions (±8 kV, 1 kHz)

layer was turbulent (s=463 mm), there was no significant effect on the flow for ±8 kV and 1 kHz. For example, boundary layers were not significantly modified above the second plasma actuator when this one was activated. As shown in Fig. 17, nondimensional mean velocity profiles were slightly modified for 22 m/s when the second or the fourth plasma actuator acted on a turbulent flow.

In order to modify a turbulent boundary layer, several high voltages were applied to the actuator, from ±6 kV to ±12 kV and 1 kHz. The boundary layer was mechanically tripped by a turbulator placed in s=100 mm, and the boundary layer for 15

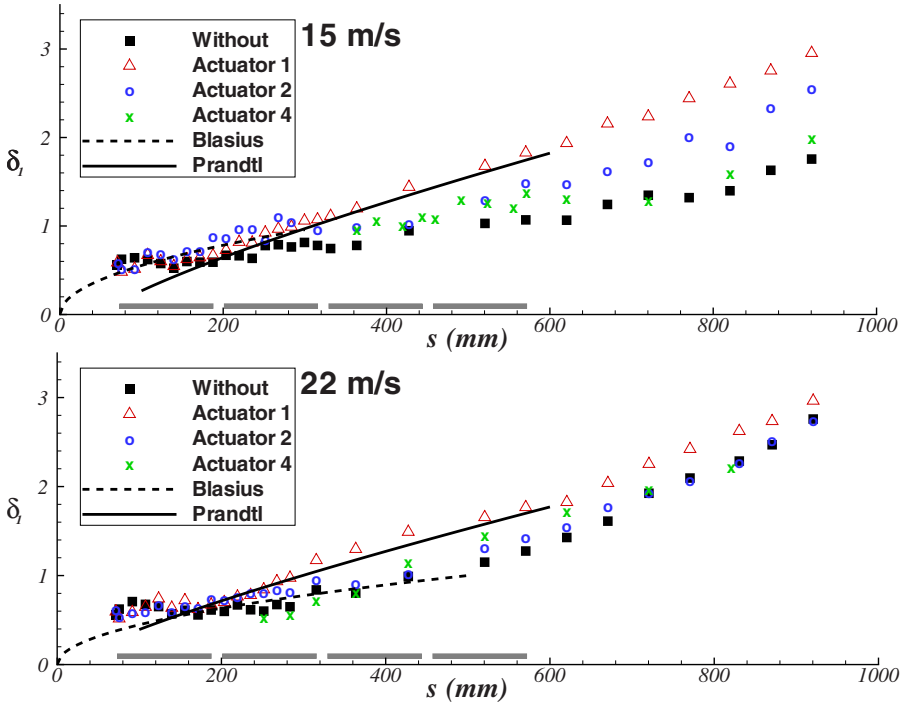

Fig. 13 Displacement thickness δ_1 (mm) along the flat plate for 15 m/s and 22 m/s, for various DBD actuator positions (±8 kV, 1 kHz)

Downloaded 03 Jun 2010 to 171.66.16.158. Redistribution subject to ASME license or copyright; see http://www.asme.org/terms/Terms_Use.cfm

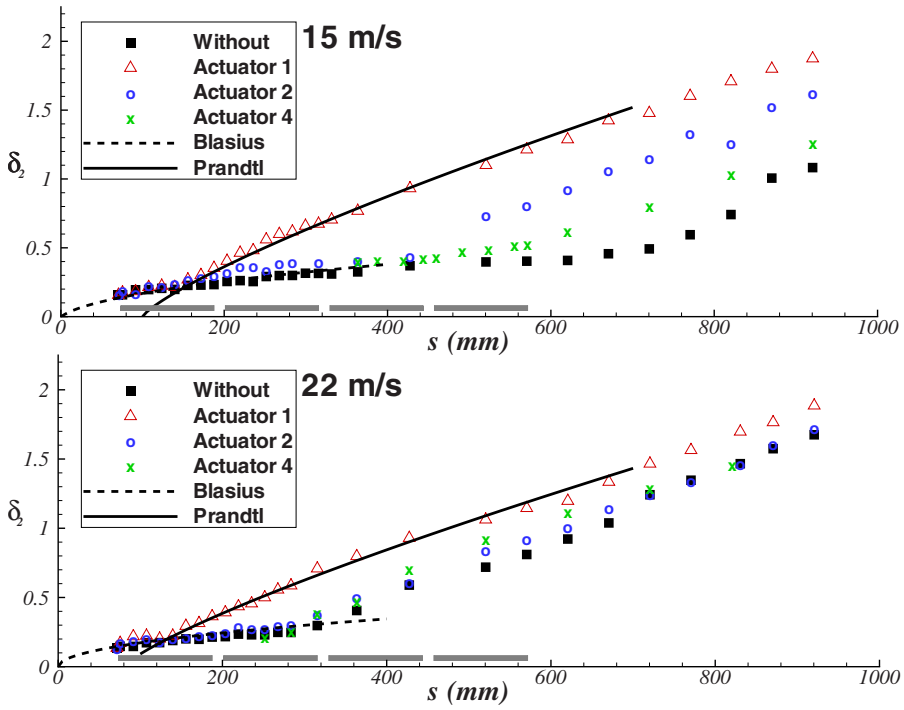

Fig. 14 Momentum thickness δ_2 (mm) along the flat plate for 15 m/s and 22 m/s, for various DBD actuator positions (±8 kV, 1 kHz)

m/s was consequently turbulent above the third actuator. The comparison of velocity profiles measured in $s=446$ mm, 1 mm behind the last pair of electrodes of this actuator (same position as the induced velocity profiles in Sec. 3.1), is shown in Fig. 18. The various boundary layer parameters are reported in Table 3 where the difference in percentage is calculated between the cases without and with a working actuator.

From this experiment, we expected a momentum addition on the velocity profiles related to a decrease in the momentum thickness δ_2, since we increased the actuator active power and then the

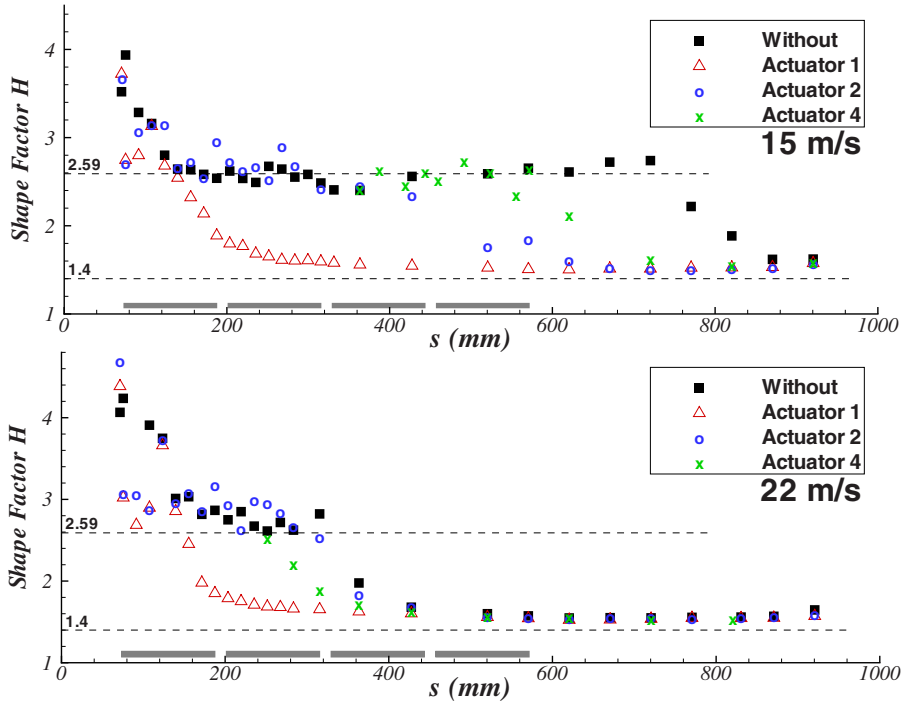

Fig. 15 Shape factor *H* along the flat plate for 15 m/s and 22 m/s, for various DBD actuator positions (±8 kV, 1 kHz)

Downloaded 03 Jun 2010 to 171.66.16.158. Redistribution subject to ASME license or copyright; see http://www.asme.org/terms/Terms_Use.cfm

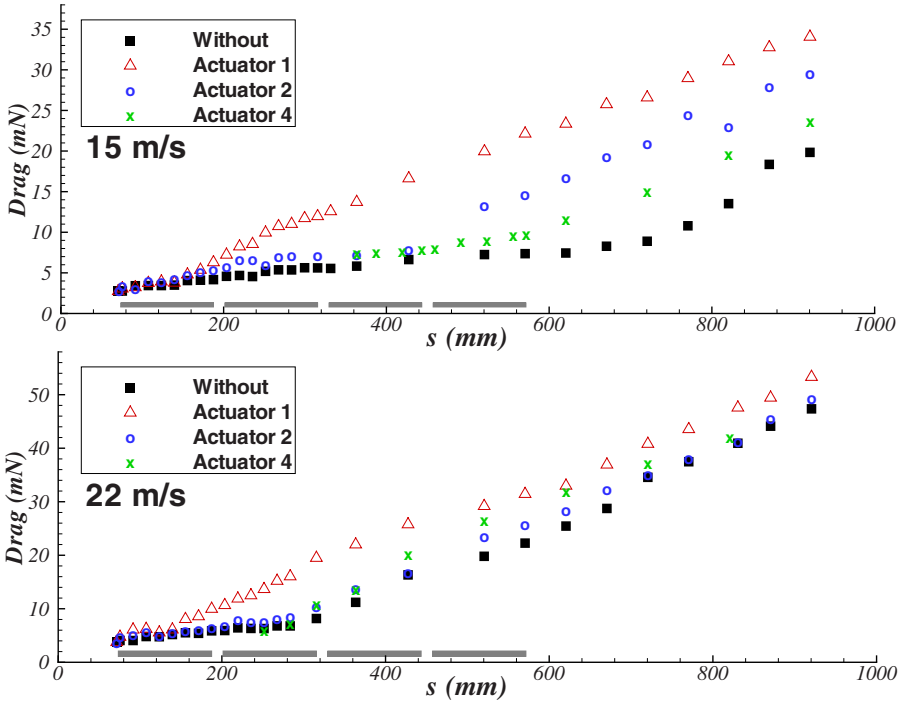

Fig. 16 Drag *D* (mN) along the flat plate for 15 m/s and 22 m/s, for various DBD actuator positions (±8 kV, 1 kHz)

Table 2 Position of the turbulent boundary layer for 15 m/s and 22 m/s, without and with activated actuators 1, 2, or 4 (±8 kV, 1 kHz)

15 m/s	s_t (mm)
Without	580
Actuator 1	110
Actuator 2	330
Actuator 4	500
22 m/s	**s_t (mm)**
Without	255
Actuator 1	100
Actuator 2	250
Actuator 4	240

ionic wind velocity (as shown in Table 1). However we noticed an increase in this parameter, as well as an increase in the boundary layer thickness δ_{99}. The natural turbulent velocity profile was modified in the first millimeter, as shown in Fig. 18, since the plasma induced a momentum addition very close to the wall (Fig. 7). As the values of δ_{99}, δ_1, and δ_2 increased, the effect of plasma actuation was to enhance turbulence in the boundary layer. Moreover, for higher discharge voltages the modified boundary layer was increasingly turbulent. Indeed, as shown in Sec. 3, more ionized plasma induce faster and thicker ionic wind. Therefore the more that the thickness of the plasma influence is large and strong, the more that its action on a velocity profile is important.

Finally, our plasma actuator with a too low momentum addition cannot significantly modify a turbulent boundary layer. A higher voltage of ±12 kV was applied to the actuator but was too important for this actuator configuration. After a few minutes of activation, the powerful plasma generated electric arcs, which damaged the dielectric and occurred a very short actuator lifespan.

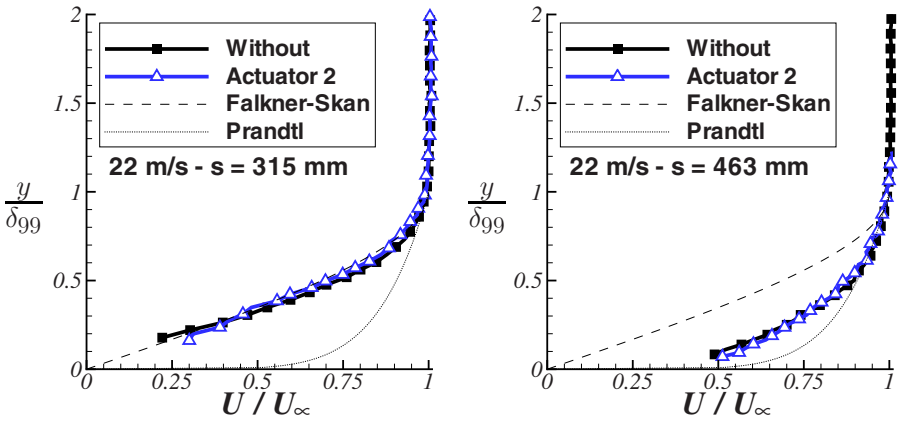

Fig. 17 Velocity profiles for 22 m/s, without and with actuator 2 activated (±8 kV, 1 kHz), in *s*=315 mm and 463 mm

Downloaded 03 Jun 2010 to 171.66.16.158. Redistribution subject to ASME license or copyright; see http://www.asme.org/terms/Terms_Use.cfm

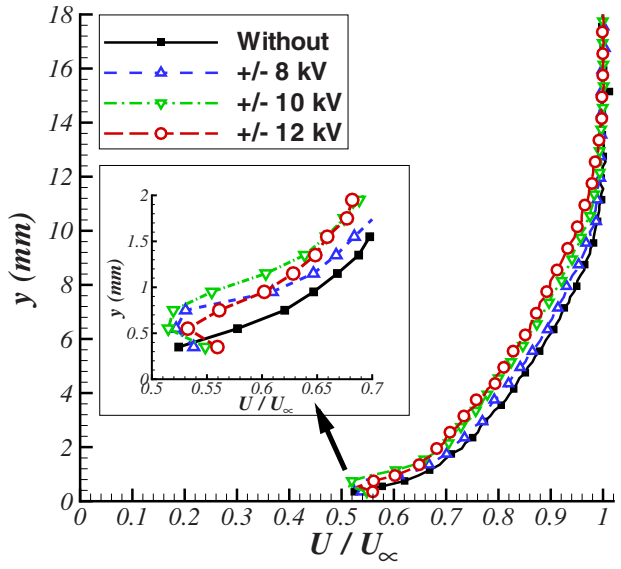

Fig. 18 Velocity profiles in s=446 mm for 15 m/s, with promoted transition, without and with actuator 3 activated (from ±8 kV to ±12 kV, 1 kHz)

5 Conclusion

In the present investigation, a plasma actuator with successive single dielectric barrier discharges was developed. With a pressure sensing probe and PIV visualizations, the ionic wind induced by the actuator was characterized. The higher the frequency and the applied voltage were, the faster was the induced flow downstream of the last pair of electrodes. After each single DBD, the induced velocity increased, and swirls observed between two pairs of electrodes decreased.

Effects of this actuator on a natural evolving boundary layer at zero incidence were studied on a 1-m long flat plate for 15 m/s and 22 m/s. For a moderate applied voltage (±8 kV, 1 kHz), this actuator acted on laminar boundary layers. Flow instabilities were promoted by the ionic wind induced by the DBDs, and the laminar-to-turbulent transition was precociously tripped farther upstream of the unforced case. However, with these applied electric signal conditions, the actuator had no significant effect on turbulent boundary layers.

Higher applied voltages (up to ±12 kV) were applied for modifying turbulent boundary layers. Velocity profiles were modified by the action of the plasma. Thickness and velocity maximum values of the ionic wind are parameters, which are to be considered for an optimization of the actuator effects in the case of turbulent boundary layers.

From these experiments and considering this actuator setup, two kinds of action on wall-bounded subsonic flows can be considered. The first one is to add momentum on the boundary layer. One can thus act everywhere on the surface, whatever the flow regime. However, this type of action requires important applied voltage and power, limiting the lifespan of actuators. The second kind of action is to operate on the laminar-to-transition boundary layer such as in Ref. [15]. In this context, if several actuators are successively mounted along the body surface, boundary layer transition could be tripped everywhere on the surface. Moreover, this last control strategy involves moderate power consumption.

Table 3 Boundary layer parameters in s=446 mm for 15 m/s, with promoted transition, without and with actuator 3 activated (1 kHz and various applied voltages)

	δ_{99}		δ_1		δ_2	
15 m/s	mm	%	mm	%	mm	%
Without	10.45	—	1.52	—	1.17	—
±6 kV	10.73	+2.7	1.54	+1.6	1.18	+1.2
±8 kV	11.59	+10.9	1.71	+12.2	1.28	+9.5
±10 kV	11.89	+13.8	1.94	+27.8	1.43	+22.5
±12 kV	12.92	+23.6	2.05	+35.0	1.54	+31.4

Acknowledgment

This work benefited from the financial support of the research federation EPEE (CNRS/SPI—Orleans University) and the Région Centre in France. Authors would like to thank Stéphane Loyer for his assistance in setting up these experiments.

Nomenclature

A = anode
D = drag
H = shape factor
K = cathode
Re = Reynolds number
s = curvilinear abscissa
s_t = position of the turbulent zone
u = velocity
u^+ = nondimensionalized wall velocity
u_τ = friction velocity
U_p = induced flow maximum velocity
U_∞ = inlet velocity
y = height
y^+ = nondimensionalized wall height
δ_1 = displacement thickness
δ_2 = momentum thickness
δ_{99} = boundary layer thickness
ρ = air density
τ_w = wall shearing-stress
μ = dynamic viscosity
ν = cinematic viscosity

References

[1] Lee, S. J., and Jang, Y. G., 2005, "Control of Flow Around a NACA 0012 Airfoil With a Micro-Ribblet Film," J. Fluids Struct., **20**, pp. 659–672.
[2] Lin, J. C., 2002, "Review of Research on Low-Profile Vortex Generators to Control Boundary-Layer Separation," Prog. Aerosp. Sci., **38**, pp. 389–420.
[3] Modi, V. J., 1997, "Moving Surface Boundary-Layer Control: A Review," J. Fluids Struct., **11**, pp. 627–663.
[4] Greenblatt, D., and Wygnanski, I. J., 2000, "The Control of Separation by Periodic Excitation," Prog. Aerosp. Sci., **36**, pp. 487–545.
[5] Liu C., and Roth, J. R., 1994, "Applications of the One Atmosphere Glow Discharge Plasma to Illumination and Aerodynamic Boundary Layer Control," 36th Annual Meeting APS Division of Plasma Physics, Minneapolis, APS Bulletin, **39**(7), p. 1730.
[6] Robinson, M., 1961, "Movement of Air in the Electric Wind of a Corona Discharge," Trans. Am. Inst. Electr. Eng., **80**, pp. 143–150.
[7] Soetomo, F., 1992, "The Influence of High Voltage Discharge on Flat Plate Drag at Low Reynolds Number Air Flow," M.S. thesis, Iowa State University, Ames.
[8] Artana, G., D'Adamo, J., Desimone, G., and Diprimio, G., 2000, "Air Flow Control With Electrohydrodynamic Actuators," Second International Workshop on Conduction Convection and Breakdown in Fluid, Grenoble, France, pp. 190–194.
[9] Artana, G., Desimone, G., and Touchard, G., 1999, "Study of the Changes in the Flow Around a Cylinder Caused by Electroconvection," *Electrostatics '99*, IOP, Bristol, Philadelphia, pp. 147–152.
[10] Sosa, R., and Artana, G., 2006, "Steady Control of Laminar Separation Over Airfoils With Plasma Sheet Actuators," J. Electrost., **64**, pp. 604–610.
[11] Leger, L., Moreau, E., Artana, G., and Touchard, G., 2001, "Influence of a DC Corona Discharge on the Airflow Along an Inclined Flat Plate," J. Electrost., **51–52**, pp. 300–306.
[12] Leger, L., Moreau, E., and Touchard, G., 2002, "Effect of a DC Corona Electrical Discharge on the Airflow Along a Flat Plate," IEEE Trans. Ind. Appl., **38**(6), pp. 1478–1485.
[13] Leger, L., Moreau, E., and Touchard, G., 2002, "Electrohydrodynamic Airflow Control Along a Flat Plate by a DC Surface Corona Discharge—Velocity Profile and Wall Pressure Measurements," AIAA Paper No. 2002-2833.
[14] Magnier, P., Hong, D., Leroy-Chesneau, A., Pouvesle, J. M., and Hureau, J., 2007, "A DC Corona Discharge on a Flat Plate to Induce Air Movement," J.

Downloaded 03 Jun 2010 to 171.66.16.158. Redistribution subject to ASME license or copyright; see http://www.asme.org/terms/Terms_Use.cfm

Electrost., **65**(10–11), pp. 655–659.
[15] Magnier, P., Hong, D., Leroy-Chesneau, A., Bauchire, J. M., and Hureau, J., 2007, "Control of Separated Flows With the Ionic Wind Generated by a DC Corona Discharge," Exp. Fluids, **42**(5), pp. 815–825.
[16] Roth, J. R., Sherman, D. M., and Wilkinson, S. P., 1998, "Boundary Layer Flow Control With a One Atmosphere Uniform Glow Discharge Surface Plasma," AIAA Paper No. 98-0328.
[17] Roth, J. R., Sin, H., Madhan, R. C. M., and Wilkinson, S. P., 2003, "Flow Re-Attachment and Acceleration by Paraelectric and Peristaltic Electrohydrodynamic (EHD) Effects," AIAA Paper No. 2003-0351.
[18] Roth, J. R., and Dai, X., 2006, "Optimization of the Aerodynamic Plasma Actuator as an Electrohydrodynamic (EHD) Electrical Device," AIAA Paper No. 2006-1203.
[19] Enloe, C. L., McLaughlin, T. E., Van Dyken, R. V., Kachner, K. D., Jumper, E. J., and Corke, T. C., 2003, "Mechanisms and Responses of a Single Dielectric Barrier Plasma," AIAA Paper No. 2003-1021.
[20] Enloe, C. L., McLaughlin, T. E., Van Dyken, R. V., Kachner, K. D., Jumper, E. J., and Corke, T. C., 2004, "Mechanisms and Responses of a Single Dielectric Barrier Plasma Actuator: Geometric Effects," AIAA J., **42**(3), pp. 595–604.
[21] Enloe, C. L., McLaughlin, T. E., Van Dyken, R. V., Kachner, K. D., Jumper, E. J., and Corke, T. C., 2004, "Mechanisms and Responses of a Single Dielectric Barrier Plasma Actuator: Plasma Morphology," AIAA J., **42**(3), pp. 589–594.
[22] Pons, J., Moreau, E., and Touchard, G., 2005, "Asymmetric Surface Dielectric Barrier Discharge in Air at Atmospheric Pressure: Electrical Properties and Induced Airflow Characteristics," J. Phys. D, **38**, pp. 3635–3642.
[23] Sosa, R., Moreau, E., Touchard, G., and Artana, G., 2004, "Stall Control at High Angle of Attack With Periodically Excited EHD Actuators," AIAA Paper No. 2004-2738.
[24] Corke, T. C., and Post, M. L., 2005, "Overview of Plasma Flow Control: Concepts, Optimization and Applications," AIAA Paper No. 2005-0563.
[25] Corke, T. C., Merts, B., and Patel, M. P., 2006, "Plasma Flow Control Optimized Airfoil," AIAA Paper No. 2006-1208.
[26] Post, M. L., Greenwade, S. L., Yan, M. H., Corke, T. C., and Patel, M. P., 2007, "Effects of an Aerodynamic Plasma Actuator on an HSNLF Airfoil," AIAA Paper No. 2007-638.
[27] Opaits, D. F., Roupasov, D. V., Starikovskaia, A. Y., Zavialov, I. N., and Saddoughi, S. G., 2005, "Plasma Control of Boundary Layer Using Low-Temperature Non Equilibrium Plasma of Gas Discharge," AIAA Paper No. 2005-1180.
[28] Moreau, E., 2007, "Airflow Control by Non Thermal Plasma Actuators," J. Phys. D, **40**, pp. 605–636.
[29] Sosa, R., 2007, "Mecanismos de Acople en Actuadores EHD," Ph.D. thesis, University of Buenos Aires, Buenos Aires, Argentina.
[30] Velkoff, H., and Ketcham, J., 1968, "Effect of an Electrostatic Field on Boundary Layer Transition," AIAA J., **16**(7), pp. 1381–1383.
[31] Grundmann, S., and Tropea, C., 2007, "Experimental Transition Delay by Using Glow-Discharge Plasma Actuators," Exp. Fluids, **42**(4), pp. 653–657.
[32] Moreau, E., Léger, L., and Touchard, G., 2006, "Effect of a DC Surface-Corona Discharge on a Flat Plate Boundary Layer for Air Flow Velocity Up to 25 m/s," J. Electrost., **64**(3–4), pp. 215–225.
[33] Porter, C. O., McLaughlin, T. E., Enloe, C. L., Font, G. I., Roney, J., and Baughn, J. W., 2007, "Boundary Layer Control Using a DBD Plasma Actuator," AIAA Paper No. 2007-786.
[34] Vilela Mendes, R., and Dente, J. A., 1998, "Boundary-Layer Control by Electric Fields," ASME J. Fluids Eng., **120**, pp. 626–629.
[35] Visbal, M. R., Gaitonde, D. V., and Roy, S., 2006, "Control of Transitional and Turbulent Flows Using Plasma-Based Actuators," AIAA Paper No. 2006-3230.
[36] Van Dyken, R. V., Enloe, C. L., and McLaughlin, T. E., 2004, "Parametric Investigations of a Single Dielectric Barrier Plasma Actuator," AIAA Paper No. 2004-0846.
[37] Likhanskii, A. V., Schneider, M. N., Macheret, S. O., and Miles, R. B., 2006, "Modeling of Interaction Between Weakly Ionized Near-Surface Plasmas and Gas Flow," AIAA Paper No. 2006-1204.
[38] Borghi, C. A., Carraro, M. R., and Cristofolini, A., 2005, "Plasma and Flow Characterization in a Flat Panel One Atmosphere Uniform Barrier Discharge," AIAA Paper No. 2005-5307.
[39] Forte, M., Jolibois, J., Moreau, E., Touchard, G., and Cazalens, M., 2006, "Optimization of a Dielectric Barrier Discharge Actuator by Stationary and Non-Stationary Measurements of the Induced Flow Velocity—Application to Airflow Control," AIAA Paper No. 2006-2863.
[40] Magnier, P., Dong, B., Hong, D., Bauchire, J. M., Hureau, J., and Pouvesle, J. M., 2006, "Dielectric Barrier Discharge for Airflow Control," Proceedings of the International Symposium on Electrohydrodynamics, Buenos Aires, Argentina, pp. 63–66.
[41] Schlichting, H., 1968, *Boundary-Layer Theory*, 6th ed., McGraw-Hill, New York.
[42] Boeuf, J. P., Lagmich, Y., Unfer, T., Callegari, T., and Pitchford, L. C., 2007, "Electrohydrodynamic Force in Dielectric Barrier Discharge Plasma Actuators," J. Phys. D, **40**, pp. 652–662.

Downloaded 03 Jun 2010 to 171.66.16.158. Redistribution subject to ASME license or copyright; see http://www.asme.org/terms/Terms_Use.cfm

Aero-Acoustic Coupling Inside Large Deep Cavities at Low-Subsonic Speeds

Mouhammad El Hassan
Ph.D.
Laboratoire de Mécanique et d'Énergetique,
Université de Valenciennes,
Le Mont Houy,
Valenciennes 59300, France
e-mail: elhassanmoh@yahoo.fr

Laurent Keirsbulck
Ph.D.

Larbi Labraga
Professor

Université de Valenciennes,
Le Mont Houy,
Valenciennes 59300, France

Aero-acoustic coupling inside a deep cavity is present in many industrial processes. This investigation focuses on the pressure amplitude response, within two deep cavities characterized by their length over depth ratios ($L/H=0.2$ and 0.41), as a function of freestream velocities of a 2×2 m^2 wind tunnel. Convection velocity of instabilities was measured along the shear layer, using velocity cross-correlations. Experiments have shown that in deep cavity for low Mach numbers, oscillations of discrete frequencies can be produced. These oscillations appear when the freestream velocity becomes higher than a minimum value. Oscillations start at $L/\theta_0=10$ and 21 for $L/H=0.2$ and 0.41, respectively. The highest sound pressure level inside a deep cavity is localized at the cavity floor. A quite different behavior of the convection velocity was observed between oscillating and nonoscillating shear-layer modes. The hydrodynamic mode of the cavity shear layer is well predicted by the Rossiter model (1964, "Wind Tunnel Experiments on the Flow Over Rectangular Cavities at Subsonic and Transonic Speeds," Aeronautical Research Council Reports and Memo No. 3438) when measured convection velocity is used and the empirical time delay is neglected. For $L/H=0.2$, only the first Rossiter mode is present. For $L/H=0.41$, both the first and the second modes are detected with the second mode being the strongest. [DOI: 10.1115/1.3026725]

1 Introduction

Turbulent flow over a rectangular cavity may lead to aero-acoustic couplings between the cavity shear-layer oscillations and the acoustic modes of the installation. This phenomenon is studied in this paper for particularly deep and large cavities ($L/H=0.2$ and 0.41).

Large and deep cavity configurations at subsonic velocities can be found in many industrial processes, ranging from windows and sunroofs in automobiles to space between a two-vehicle train or between buildings in civil engineering. The aero-acoustic coupling in these cavities results in resonance of high pressure level as well as strong vibrations and structural fatigue.

In most cavity flows, the incident turbulent boundary layer (TBL) separates at the cavity leading edge. This separation is followed by a roll-up leading to coherent structures into the cavity shear layer. Before their impingement at the cavity downstream corner, these structures are convected from the leading to the trailing edge of the cavity. The number of these shear-layer vortical structures depends on both the TBL thickness (δ_0) and the cavity length (L). The coherent structures of the shear layer impinge on the downstream edge of the cavity generating acoustic disturbances.

The pressure oscillation features inside, and around cavities, have been treated by many authors (Rossiter [1], Tam and Block [2], Rockwell and Knisely [3], Rockwell et al. [4], and others). The Rossiter model [1] was used in most of the publications concerning this phenomenon. In this model, the determination of peak frequency where high distinguished amplitude occurs is important in quantifying pressure variations inside and around the cavity. This frequency depends on the oscillating mode order, the cavity length, and the convection velocity (u_c) of coherent structures in the shear layer.

The number of structures in the cavity shear layer depends on the mode order of cavity oscillation [5,6]. The flow visualizations done by Gharib and Roshko [5] showed that for mode 2 of the oscillation, two wavelengths (or vortical structures) exist along the shear layer of the cavity, while in mode 3 there are three waves (or vortical structures). In our study ($5<L/\theta_0<24$), only the first Rossiter mode is present for $L/H=0.2$. However, modes 1 and 2 are detectable for $L/H=0.41$.

Sarohia [7] defined the minimum cavity length for the onset of oscillations. The determination of this minimum length is based on three flow parameters: U_0 (freestream velocity), δ_0 (thickness of the TBL just upstream from the cavity), and ν (kinematic viscosity of fluid). Rockwell and Knisely [3] showed that the variation in the cavity length leads to multiple peaks in the pressure spectrum. Knisely and Rockwell [8] varied the cavity length for constant U_0. They found a slight amplitude change of the pressure level at the fundamental frequency.

A comparison between two large deep cavities that present the same depth and different lengths under the same flow conditions is made in the present paper.

For shallow cavities, the flow exhibits strong three-dimensionality. The choice of small L/H values leads to a two-dimensional organization of the flow [6]. Therefore, two small geometric aspect ratios ($L/H=0.2$ and 0.41) are studied in this paper.

The present research shows the effects of both acoustic modes and Rossiter-type shear-layer resonances in large deep cavities. This study improves our knowledge of cavity oscillation phenomenon. New aspects are summarized as follows.

1. As proposed by Rossiter [1], the convection velocity was considered in most of the previous studies as an empirical parameter $u_c/U_0=0.57$, where U_0 is the freestream velocity). In the present study, the convection velocity of structures was experimentally obtained from velocity cross-correlations. Convection velocity distribution of structures along cavity shear layer is discussed for both cavity configurations and for different freestream velocities.

Contributed by the Fluids Engineering Division of ASME for publication in the JOURNAL OF FLUIDS ENGINEERING. Manuscript received July 26, 2007; final manuscript received October 8, 2008; published online December 2, 2008. Assoc. Editor: Juergen Kompenhans.

 Copyright © 2009 by ASME

Downloaded 03 Jun 2010 to 171.66.16.158. Redistribution subject to ASME license or copyright; see http://www.asme.org/terms/Terms_Use.cfm

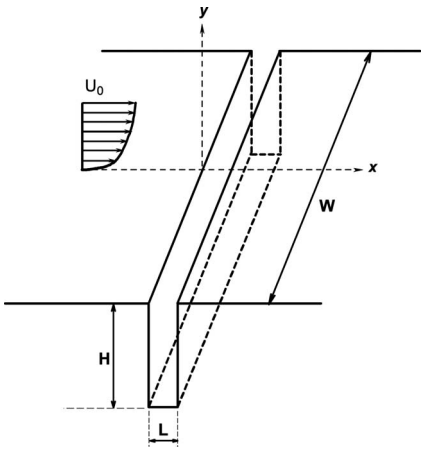

Fig. 1 Three-dimensional view of the cavity

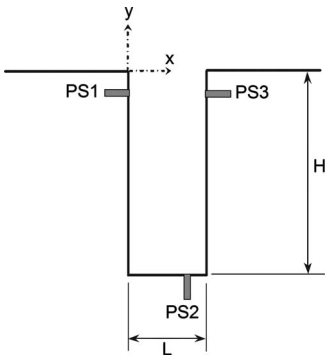

Fig. 2 Kulite sensor positions

2. The incoming TBL characteristics affect the amplitude of events as was shown numerically by Gloerfelt et al. [9] and experimentally by Grace et al. [10] and Camussi et al. [11]. The long and large test section of the present investigation leads to a fully developed turbulent boundary layer, characterized by a large thickness (δ_0). The boundary layer thickness of the present study (90 mm $< \delta_0 <$ 210 mm) is greater than those of all previous studies concerning cavity oscillation phenomenon.
3. East [12] found that for small working section dimensions, the tunnel and the cavity interact acoustically. However, with greater test section dimensions, no interference was discerned. This phenomenon was predicted as highly probable in many previous studies. This has motivated our choice of large test section dimensions.
4. Although the $L/H=0.41$ configuration was previously studied at M=0.8 [6,13], different flow conditions of the present study aim at enlarging database related to this cavity configuration. Indeed, in the present study, Mach numbers are very low and the flow regime is low-subsonic. In addition, convection velocity of structures was measured with different freestream velocities and exhibits a quite different behavior between oscillating and nonoscillating regimes. Moreover, the maximum spectra pressure level was obtained at different cavity walls (leading edge, trailing edge, and the cavity bottom).
5. Particularly deep cavity ($L/H=0.2$) is being studied. El Hassan et al. [14] found that this cavity configuration affects both the incident turbulent boundary layer and the skin friction velocity. The current study aims at showing how this particular deep cavity could affect shear-layer oscillations.

2 Apparatus and Experimental Procedures

2.1 Wind Tunnel and Cavity Model Details. The experimental measurements have been conducted in the closed circuit low speed wind tunnel of the Mechanics and Energetic Laboratory of Valenciennes. The test section is 2×2 m^2 in cross section and 10 m long. The maximum outlet velocity along the centerline of the test section is 60 m/s. The relative turbulence level at 30 m/s is about 0.5%. Pressure measurements were made at freestream velocities covering the range 1–56 m/s. The dimensions of the first cavity configuration were $L=104$ mm in length, $H=520$ mm in depth, and $W=2000$ mm in width. Aspect ratios were $L/H=0.2$ and $L/W=0.052$. The second cavity configuration had the same H and W as the first one, with $L=213$ mm. Its ratios were $L/H=0.41$ and $L/W=0.107$. A three-dimensional view of the cavity is shown in Fig. 1. Each cavity was installed on the lateral wall of the test section, with the leading edge located 8 m downstream from the test section inlet. The boundary layer was characterized just upstream of the cavity leading edge. Hot-wire measurements of velocity profiles at this location showed that for a low velocity ($U_0=2$ m/s) the boundary layer was fully developed. These measurements, at low freestream velocities, show that the boundary layer thickness ($\delta_0=18$ cm) corresponds to that found in a fully developed boundary layer.

2.2 Pressure Measurements. Kulite pressure transducers were employed with a nominal sensitivity of 275 mV/bar. The outputs from the transducers were connected to a multichannel signal conditioner. Data acquisition of pressure signals is accomplished using an analog-to-digital (A/D) board with 12 bit resolution. A gain adjustment was used in order to meet the required voltage input levels of the A/D board. Data were sampled at 6 kHz typically for 180,000 samples from each channel. The acquired pressure signals were low-pass filtered with a cut-off frequency of 3 kHz to avoid aliasing effects. Wall pressure measurements were made by using three flush-mounted kulite sensors. The sensitive region of the probes is a small circle 2.5 mm in diameter. One sensor ($PS1$) was set on the leading edge at $y=-30$ mm. The second sensor ($PS2$) was positioned at the cavity bottom at $x=80$ mm and 130 mm for $L/H=0.2$ and 0.41, respectively. The third sensor ($PS3$) was located on the trailing edge at $y=-30$ mm. The locations of sensors are indicated in Fig. 2.

Figure 3 shows two pressure spectra obtained for $U_0=46$ m/s. This figure confirms that for the two cavity configurations no interesting physical features exist in the present flow at high frequencies. Oscillating modes and their harmonics are detected at low frequencies. Therefore, $f=500$ Hz will be the maximum frequency of interest for all pressure analyses.

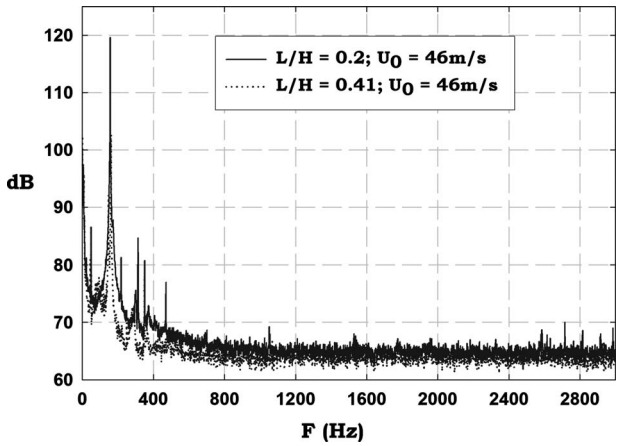

Fig. 3 Pressure spectrum from *PS*3 (kulite sensor at the leading edge)

Downloaded 03 Jun 2010 to 171.66.16.158. Redistribution subject to ASME license or copyright; see http://www.asme.org/terms/Terms_Use.cfm

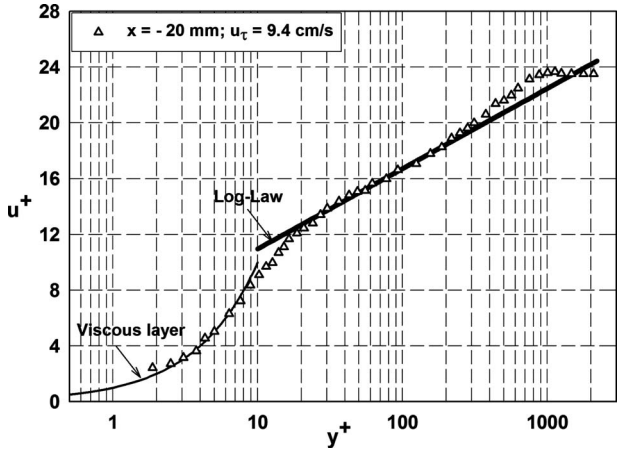

Fig. 4 Mean streamwise velocity profile upstream of the cavity

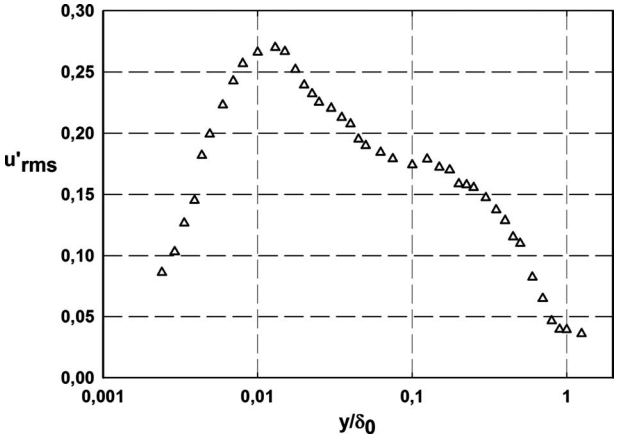

Fig. 5 Streamwise root-mean-square profile upstream of the cavity

2.3 Hot-Wire Measurements. Experiments were carried out using a DANTEC 90C20 constant temperature hot-wire anemometry (CTA) system. The output signal was transferred by an A/D card connected to a PC. The STREAMLINE software supplied by DANTEC was used to acquire and store data. A boundary layer type probe was used for the boundary layer measurements upstream from the cavity. Two single wire probes DANTEC 55P15 were used for cross-correlation measurements in the cavity shear layer. The sensors of both probes consisted of platinum-tungsten wires. Streamwise time-space correlations between velocity signals were performed in order to calculate the convection velocity of structures. These cross-correlation measurements were obtained using two single hot-wire sensors placed in the shear layer at $y=0$ close to the center in the spanwise direction. The space between the two probes was made using a manually controlled mechanism with an accuracy of 10 μm. The longitudinal space between the two hot-wires was then fixed to 8 mm (see Sec. 3.2). A small shift (about 1 mm) of the two hot-wire probes was performed in the spanwise direction in order to avoid a streamwise wake interaction between probes. The relative turbulent level (RTL) was measured along the shear layer for each freestream velocity. In all cases, RTL is below 15% rendering the adopted cross-correlation technique feasible. A traversing system was used to move the probes in the streamwise direction. A traverse grid was defined for each cavity configuration. For each freestream velocity, data are acquired along the shear layer. The signals from the CTA were filtered and amplified to give signals that covered most of the ± 10 V range of the A/D converter.

3 Results

3.1 Incident Turbulent Boundary Layer. Single hot-wire measurements were taken 20 mm upstream from the cavity leading edge in order to lay down the characteristics of the incident boundary layer. Figures 4 and 5, respectively, show the mean streamwise velocity profiles and its root-mean-square turbulent level for $U_0=2$ m/s. These figures illustrate the turbulent and fully developed aspect of the incident boundary layer. The low subsonic velocity (2 m/s) allows measurements in the viscous layer and gives accurate estimation of the skin friction velocity (u_τ). In Fig. 4, u^+ and y^+ are normalized using u_τ. The log-law fits the data well for $30<y^+<300$. Turbulent boundary layer parameters are deduced from the velocity profile. At $U_0=2$ m/s the boundary layer upstream of the cavity had a shape factor $H=\delta_1/\theta_0=1.32$ where $\delta_1=22.5$ mm (displacement thickness) and $\theta_0=17$ mm (momentum thickness). The Reynolds number is $\mathrm{Re}_{\theta_0}=2267$.

3.2 Structure Advection Along the Shear Layer. Structures or instability waves present in the cavity shear layer are convected from the leading to the trailing edge of the cavity with a characteristic convection velocity u_c. To predict the oscillating modes of the cavity shear layer, Rossiter [1] proposed the equation

$$\mathrm{St}=\frac{fL}{U}=\frac{n-\alpha}{M+\dfrac{1}{\kappa}} \tag{1}$$

where n is the cavity mode order, κ is the ratio of the convection velocity of structure over the freestream velocity, and α the lag time between the impact of a structure on the cavity downstream corner and the emission of an acoustic wave. This last parameter was always taken as an empirical value and was adjusted to fit experimental data (as done by Rossiter [1]). At moderate Mach number there is an acoustic time delay $\alpha=0.25$ [15].

The ratio $\kappa=u_c/U_0$ of the Rossiter formula [1] was often considered by authors as empirical and taken as a constant value ($\kappa=0.57$) along the shear layer [16,17].

This part of our study deals with the experimental measurement of the convection velocity of structures at different positions along the cavity shear layer. The convection velocity was obtained from velocity cross-correlations using two single hot-wire sensors.

The two single hot-wire sensor positions were along the constant $y=0$ line of the shear layer. This y position was chosen considering that in shear-layer mode, the vortical structures travel in the streamwise direction along the cavity shear layer and are detected by the first then the second hot-wire sensor. Although the trajectory of the vortical structures could be influenced by the acoustic waves, Gloerfelt et al. [18] asserted that well-aligned vortices are present in the cavity shear layer with a slight growth of vortices when approaching the downstream corner of the cavity. Moreover, Rowley et al. [15] noted that the interaction of the flow inside the cavity with the shear layer is relatively weak. Preliminary measurements were made with different distances (e) between the two hot-wires. Similar distributions (not shown in this paper) of the convection velocity were obtained for $e=4$ mm, 6 mm, 8 mm, and 11 mm. This allowed us to choose a fixed space ($e=8$ mm) for all measurements of the convection velocity along the shear layer for both cavity configurations.

Figure 6 shows three cross-corrrelation plots obtained for three different distances ($e=4$ mm, 6 mm, and 8 mm) between hot-wire probes. These plots have particular peaks at relatively high amplitudes. This reflects a high interdependency between information obtained from the two single hot-wires. Peaks occur with a time

Downloaded 03 Jun 2010 to 171.66.16.158. Redistribution subject to ASME license or copyright; see http://www.asme.org/terms/Terms_Use.cfm

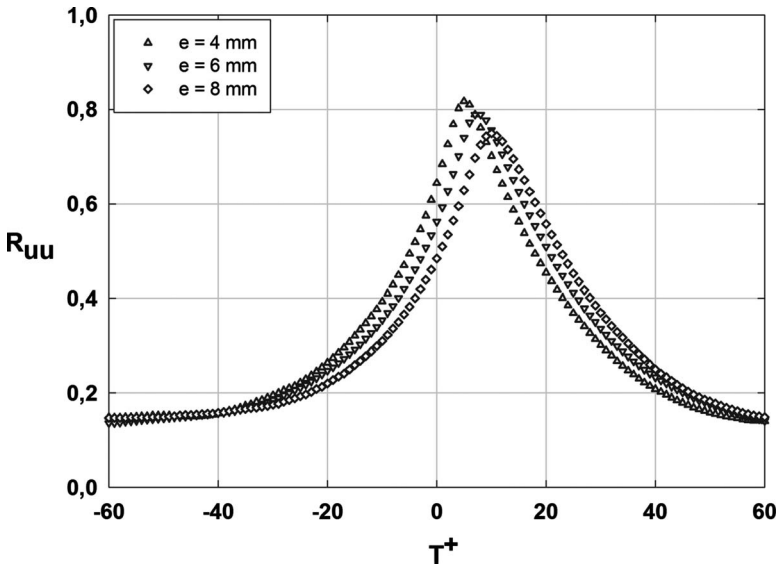

Fig. 6 Velocity cross-correlation obtained from two single hot-wires placed in the cavity shear layer

delay T^+, which represents the time for structures to travel from the first to the second hot-wire in the streamwise direction.

Figures 7 and 8 show the distribution of the convection velocity, normalized by the freestream velocity, plotted against x/L with x being the longitudinal position of the structures along the mixing layer. These figures show a constant coherent structure acceleration in the upstream part of the shear layer with a more pronounced acceleration for higher freestream velocities. In the relaxation region, the convection velocity u_c remains almost constant. In the downstream part of the shear layer, the structures decelerate and the convection velocity decreases.

More physical interpretation could be obtained from measurements of the spreading rate along the shear layer. Indeed, the spreading rate of the shear layer given by the derivation of the momentum thickness in the longitudinal direction is often used to characterize the shear-layer growth. Most researchers found a spreading rate that increases linearly [5,7,19]. Rowley et al. [15] used the vorticity thickness as a measure of the shear-layer thickness. Their data also indicate approximately linear growth of the spreading rate. In our study, the choice of different regions is only based on the behavior of the convection velocity of the structures.

The acceleration of the structures in the shear layer could be related to the "collective interaction mechanism" described by Ho and Huang [20]. At the upstream corner of the cavity, the vorticity must be thin with the presence of small and highly concentrated vortices that emanate from this location. In one part of a period of the wavy shear layer the vortices are drawn together, developing a stronger induced field that causes their rotation around each other and their coalescence into a large vortex [21]. This large vortical structure will have a constant convection speed (region 3 in Figs. 7 and 8) before its deceleration when approaching the downstream corner of the cavity.

Figures 7 and 8 show a quite different behavior with respect to shear-layer oscillations. Indeed, in the upstream part of the shear layer and for $L/H=0.2$, structure acceleration is lower in the nonoscillating case. This could be explained by the fact that the energy level increases with high velocities.

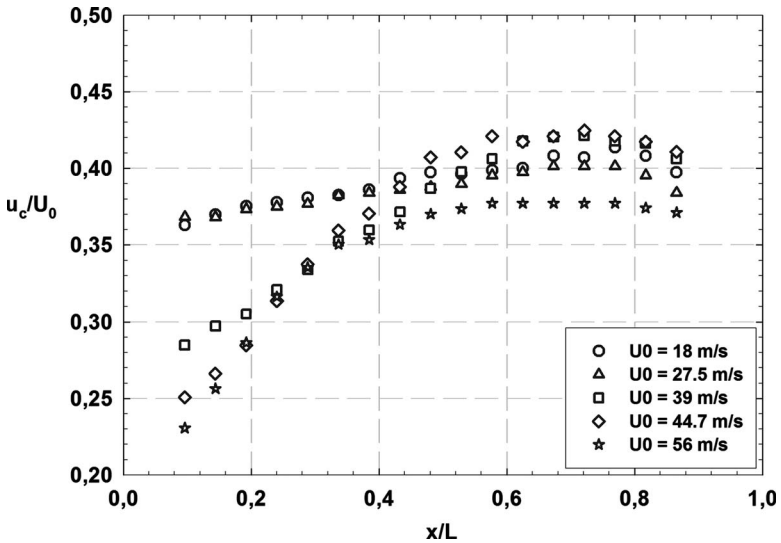

Fig. 7 Convection velocity distribution along the cavity shear layer ($L/H=0.2$)

Downloaded 03 Jun 2010 to 171.66.16.158. Redistribution subject to ASME license or copyright; see http://www.asme.org/terms/Terms_Use.cfm

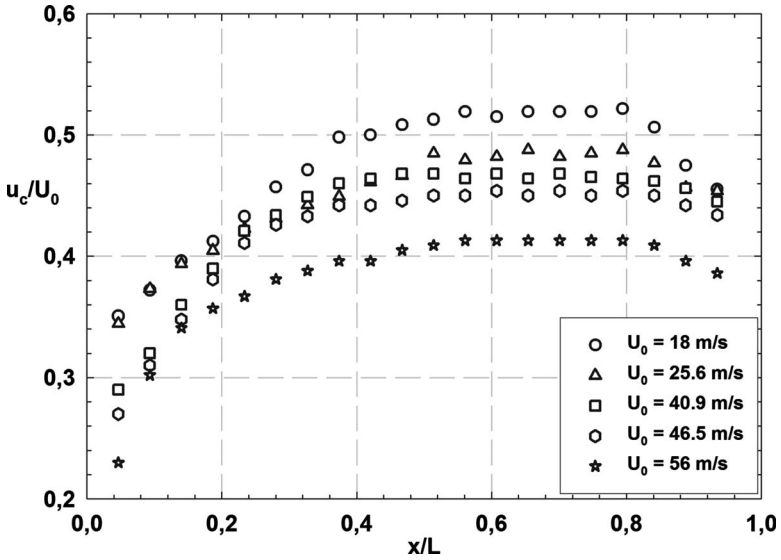

Fig. 8 Convection velocity distribution along the cavity shear layer (L/H =0.41)

The convection time scale (T_c) taken by structures to cross the cavity length was calculated by integrating the convection velocity along the shear layer as shown in Eq. (2). u_c values corresponding to $x/L=0$ and $x/L=1$ were estimated by extrapolation of plots.

$$T_c = \int_0^L \frac{dx}{u_c(x)} \tag{2}$$

Therefore, a mean convection velocity was obtained as the ratio of the cavity length over the time (T_c).

The semi-empirical parameter $\kappa = u_c/U_0$ was thus obtained for different freestream velocities. The results are shown in Fig. 9. It should be stressed that for different freestream velocities, the measured κ is lower than that proposed by Rossiter [1] ($\kappa=0.57$).

The convection velocity obtained for each freestream velocity was used with the Rossiter formula [1] for both $\alpha=0$ and $\alpha=0.25$. This was applied to modes 1 and 2 of cavity oscillations. Accurate determination of peak frequencies from spectrum analysis allowed comparison between our experimental results and those obtained from two analytical models. The results are shown in Figs. 10 and 11. These plots show that the results obtained from Rossiter formula [1] with $\alpha=0$ are in good agreement with our data. Indeed, this value of $\alpha=0$ adequately predicts the modes of the cavity oscillation in both cavity configurations of the present study. While for $\alpha=0.25$, plots depart from our experimental findings. Rossiter [1] suggested that α decreases with L/H. Moreover, Larchevêque et al. [13] proposed that the extension of the Rossiter model [1] to the deep cavity accurately predicts the peak frequency when α is adjusted. From their measurements, these authors found that agreement is achieved for $\alpha=0.038$. The main difference between the two studies is the Mach number value, which was 0.8 while in the present study it is less than 0.17. Chatellier [22] suggested that for low Mach numbers, the feedback due to the interaction of the shear layer with the impingement corner is instantaneous. He considered that the related pa-

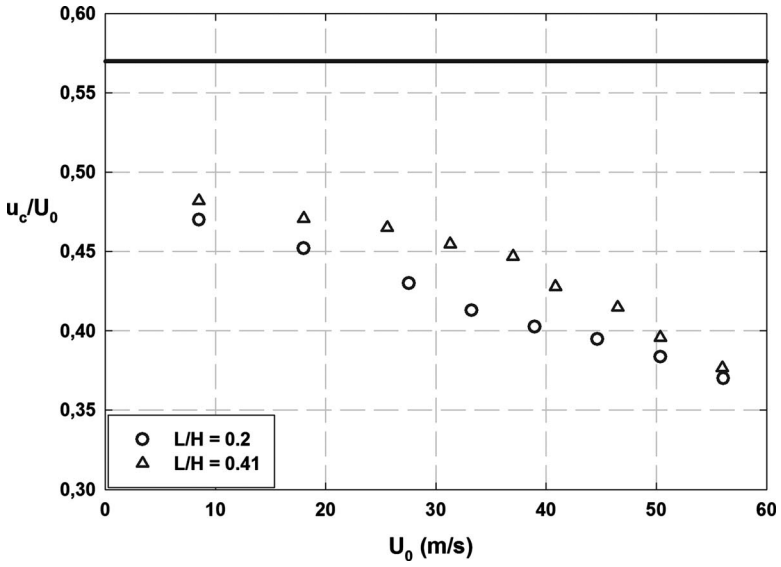

Fig. 9 Mean convection velocity of structures in the cavity shear layer

Downloaded 03 Jun 2010 to 171.66.16.158. Redistribution subject to ASME license or copyright; see http://www.asme.org/terms/Terms_Use.cfm

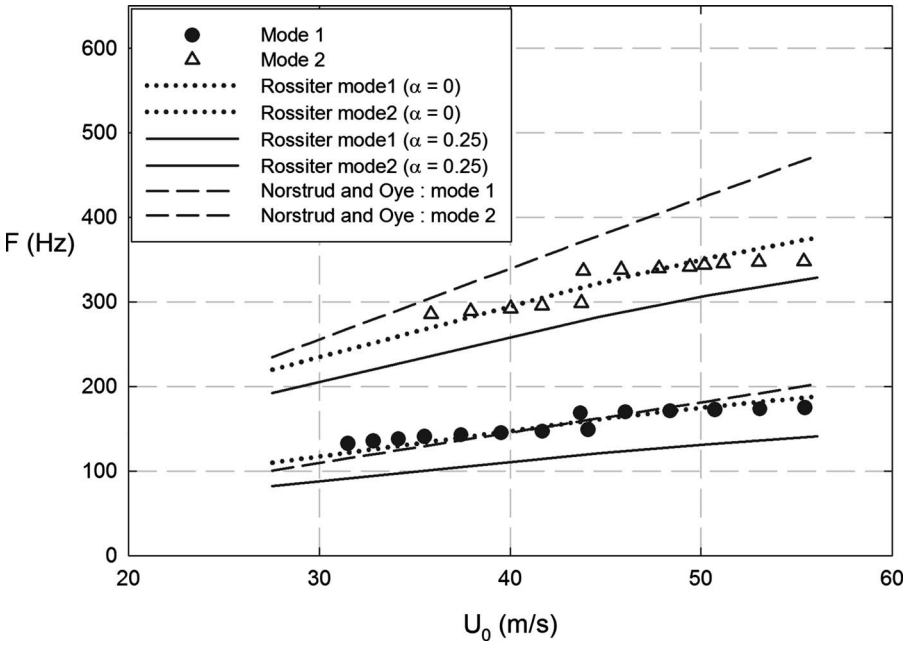

Fig. 10 Oscillating frequencies for $L/H=0.2$

rameter (α) should be negligible. This hypothesis leads to a correct application of the Rossiter formula [1] on his results when adjusting κ.

The correct prediction of oscillation frequencies by the Rossiter formula [1] confirms the existence of a feedback process leading to global instability.

Recently, Nørstrud and Øye [23] proposed a modified Rossiter formula [1] (Eq. (3)) for low Mach numbers by applying the Prandtl–Glauert similarity rule for two-dimensional subsonic flows. Our results are compared with this prediction of shear-layer oscillations (Figs. 10 and 11).

$$\mathrm{St}_{L,\mathrm{M}\leq 0.453} = 0.508(1-\mathrm{M}^2)^{1/2}(m-\alpha); \quad m = 1,2,3 \qquad (3)$$

Figures 10 and 11 show that the Rossiter formula [1] is more appropriate for prediction of both the first and the second oscillating modes of the cavity shear layer. Despite the fact that the first mode could be well predicted by the formula proposed by Nørstrud and Øye [23], experimental results of the second mode deviate from those given by this formula.

3.3 Aero-Acoustic Couplings of Deep Cavity Flow. The purpose of the measurements presented in this section was to

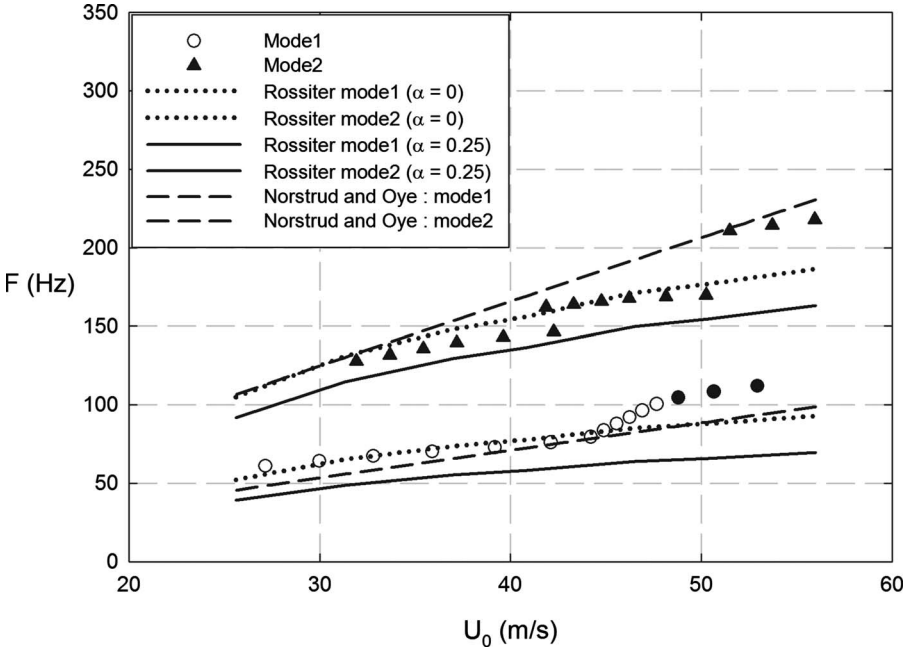

Fig. 11 Oscillating frequencies for $L/H=0.41$

Downloaded 03 Jun 2010 to 171.66.16.158. Redistribution subject to ASME license or copyright; see http://www.asme.org/terms/Terms_Use.cfm

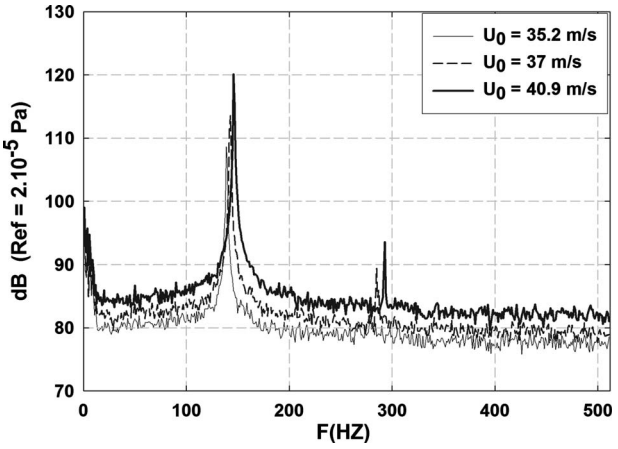

Fig. 12 Pressure spectra for $L/H=0.2$

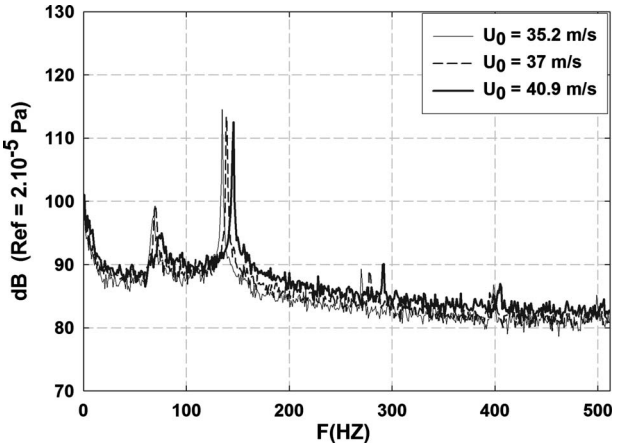

Fig. 13 Pressure spectra for $L/H=0.41$

characterize the flow-acoustic coupling for the two cavity configurations of the present study. The pressure signals are obtained from *PS*3 located at the trailing wall of the cavity (Fig. 2).

Standard 2D representations of pressure spectra are illustrated in Figs. 12 and 13. These 2D plots are useful for a better understanding of the energy content of different modes and their harmonics. Each spectrum has a sharp spectral peak corresponding to a shear-layer oscillation frequency. The most energetic peak corresponds to the first Rossiter mode for $L/H=0.2$ and the second Rossiter mode for $L/H=0.41$. The low energetic peaks in Fig. 12 should be the harmonics of the first oscillating mode.

By increasing the incoming velocity sequentially ($U_0=1.9n-1$; n is an integer covering the range 1–30), a total of 30 spectra were acquired. An interpolation of the pressure spectra was used to build spectrograms that show the pressure amplitude on the plane view of freestream velocity versus frequency.

Figures 14 and 15 represent spectrograms for $L/H=0.2$ and $L/H=0.41$, respectively. It is seen that the pressure sound pressure level (SPL) presents a broadband of increased intensity at low frequencies. This could be explained by reflections of the acoustic waves of the longitudinal modes at the contraction and the rotating propeller of the wind tunnel. As suggested by Bergmann et al. [24], the contraction area and the rotating propeller cannot be seen as a solid wall. Therefore, the spectrum does not show one discrete peak but a rather broadband of increased intensity at the frequencies corresponding to the reflection lengths.

For each U_0, the oscillation is always associated with the presence of a distinct fundamental frequency in the spectrogram. The fundamental frequency was identified as the one that has the highest peak in the power spectrum.

Figures 14 and 15 show that for small freestream velocity $U_0 < U_{0\ \min}$, oscillations are not present in the cavity shear layer. A self-sustained oscillation appears when U_0 reaches $U_{0\ \min}$.

The flow tones produced inside the cavity are due to a flow-acoustic coupling when the instabilities of the shear layer excite acoustic proper modes of the cavity. When the frequencies of hydrodynamic and acoustic phenomena coincide, the excited frequency crosses the acoustic mode and the amplitude of the pressure fluctuations reaches a local maximum.

The cavity depth mode is represented by a quarter wave that forms a standing wave along the cavity with its pressure node at

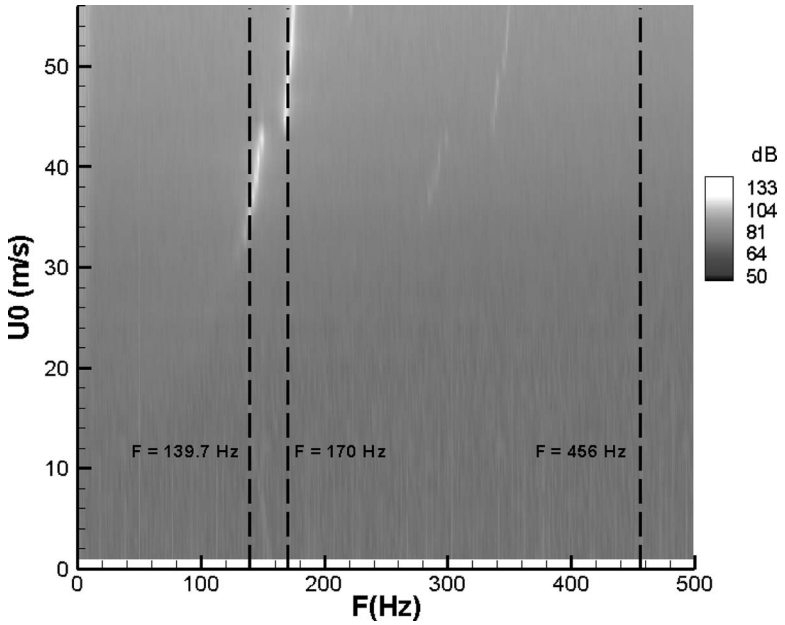

Fig. 14 Spectrogram for $L/H=0.2$

Downloaded 03 Jun 2010 to 171.66.16.158. Redistribution subject to ASME license or copyright; see http://www.asme.org/terms/Terms_Use.cfm

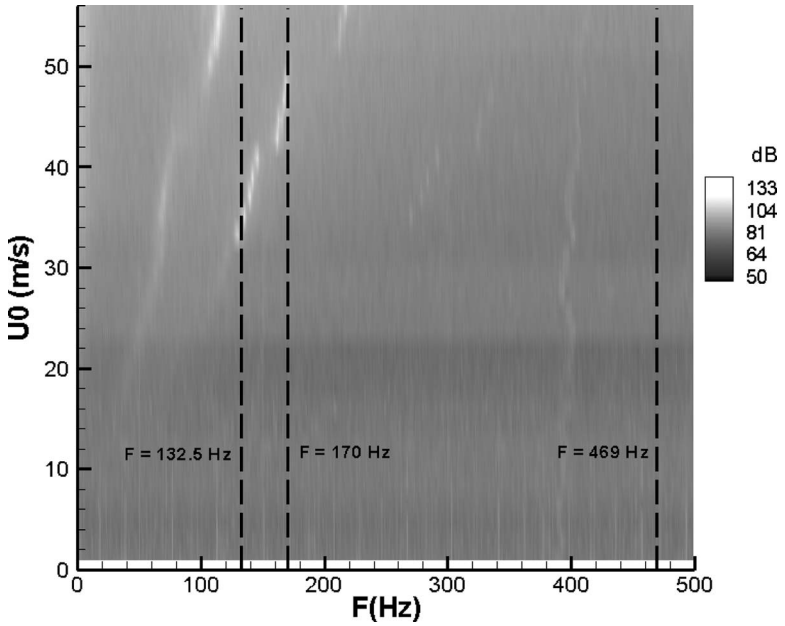

Fig. 15 Spectrogram for $L/H=0.41$

the open end and a pressure antinode at the dead end. These acoustic resonance modes have been computed for the two cavity configurations ($L/H=0.2$ and 0.41), using the numerical method described by Koch [25] and Duan et al. [26]. This method allows computation of Neumann modes, which are the only one present in cavity wind-tunnel tests [1,19], with the cavity located only on one side of the duct. The real and imaginary parts of the dimensionless frequency $K=\omega h/c_0$ are obtained from the computations; with $K/2\pi$ being the Helmholtz number and h the reference length, which in our case is double the channel height ($h=4$ m). The real part of the nondimensional frequency, $\mathrm{Re}(K/2\pi)$, corresponds to the resonant frequency and the imaginary part, $\mathrm{Im}(K/2\pi)$, is a measure for the radiation loss. The cut-on frequencies of the duct are also given by the computations. Relevant acoustic resonances, which correspond to flow-acoustic couplings, are mentioned in Table 1.

The depth mode frequencies could be obtained via East's empirical formula [12]

$$f=\left(\frac{1}{4}+\frac{n}{2}\right)\frac{c_0}{H}\frac{1}{1+0.65\left(\frac{L}{H}\right)^{0.75}} \tag{4}$$

where $c_0=340$ m/s is the sound speed inside the cavity. The depth mode ($n=0$) frequencies of our cavities are about 137 Hz (when $L/H=0.2$) and 123 Hz (when $L/H=0.41$). These results are close to those obtained from the resonance computations (Table 1).

Tam [27] computed the acoustic mode frequencies of a two-dimensional cavity. For $U_0=40$ m/s, depth mode frequencies obtained from Tam's model [27] for $L/H=0.2$ and 0.41 are, respectively, 156 Hz and 260 Hz. These values do not correspond to any flow-acoustic coupling on the spectrograms. Tam [27] studied cavities in a free space. In our case, the cavity is confined in the wind tunnel with acoustically reflecting walls and the cavity can no longer radiate freely in all directions. This could explain the difference between our results and Tam's [27] computational resonances.

Table 1 Neumann cavity resonances

	$L/H=0.2$	$L/H=0.41$
First depth mode frequency (Hz)	139.7	132.5
Second depth mode frequency (Hz)	456	469
Second duct cut-on frequency (Hz)	170	170

Oshkai et al. [28] studied acoustic resonance for shallow cavities. They found that no single model provides a universal fit for all modes of their data and that each of the multiple hydrodynamic modes may be distorted somewhat due to the necessity of lining up with the acoustic resonant modes of the pipe-cavity system.

Figure 14 shows that around $f=139.7$ Hz, the amplitude of the SPL becomes significantly high and a cavity tone occurs accordingly. This is related to the excitation of the first depth mode ($f=139.7$ Hz) by the hydrodynamic oscillating mode of the shear layer. Moreover, a lock-in should exist between the oscillating mode and the second duct cut-on frequency close to $f=170$ Hz. Around this frequency and for a large interval of freestream velocity ($44\ \mathrm{m/s}<U_0<56\ \mathrm{m/s}$), very high amplitudes are discernible.

The second depth modes listed above (Table 1) are highly damped and therefore would not show up in the spectrograms, but the first are weakly damped and seem to be the dominating frequencies in Figs. 14 and 15.

Mode 1 ($n=1$ in the Rossiter formula [1]) of oscillation observed on the spectrogram for $L/H=0.2$ is formed by a succession of two stages (stages I and II) with abrupt jump associated. This jump concerns not only the fundamental frequency but also its harmonic. The frequency jump occurs at $U_0=44$ m/s for $L/H=0.2$. When decreasing the freestream velocity, the jump will occur at the same location. This indicates the absence of hysteresis when the velocity is first increased and then decreased. Rockwell and Knisely [3] showed similar frequency jump with the variation in the freestream velocity. However, these authors noted that the velocity at which the frequency jump occurs was different between the data acquired with increasing and decreasing the freestream velocity. This indicates the occurrence of strong hysteresis in their case.

The role of the frequency jumps is to allow the oscillation of the flow to remain locked-in with an acoustic mode over a wide range of flow velocity [29]. A similar frequency jump is discernible for $L/H=0.41$ at $U_0=41$ m/s and also concerns the lock-in

Downloaded 03 Jun 2010 to 171.66.16.158. Redistribution subject to ASME license or copyright; see http://www.asme.org/terms/Terms_Use.cfm

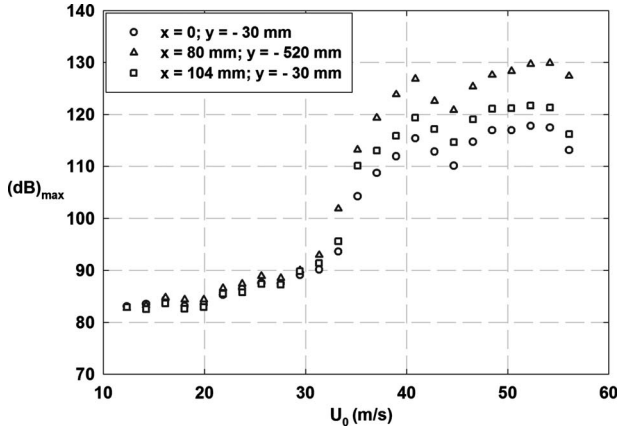

Fig. 16 Maximum pressure level distribution for $L/H=0.2$

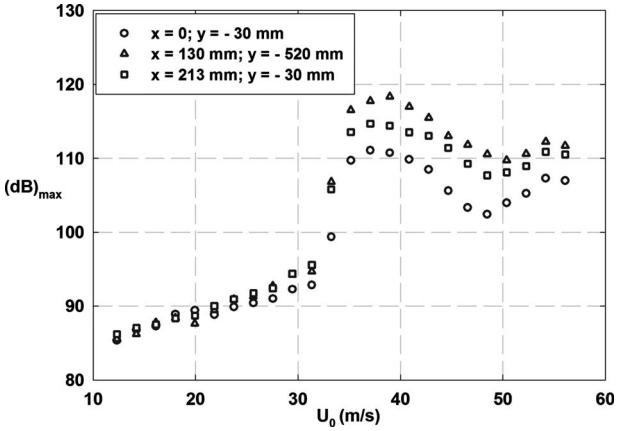

Fig. 17 Maximum pressure level distribution for $L/H=0.41$

between the second Rossiter mode and the second duct cut-off frequency (around $f=170$ Hz).

For $L/H=0.2$, the amplitude evolution of the sound pressure level (Fig. 14) with the freestream velocity shows that the first hydrodynamic mode (mode 1) is dominant for all of Mach numbers where a cavity oscillation occurs. This could confirm that the low energetic peaks are the harmonics of the first mode and not a second Rossiter mode. These harmonics are related to the nonlinear behavior of instabilities [30]. The highly energetic peaks observed for $L/H=0.41$ illustrate the existence of modes 1 and 2 in this configuration. This result confirms that greater cavity length leads to higher hydrodynamic mode order.

For $L/H=0.2$, the freestream velocity when oscillations start is approximately 35 m/s (Fig. 14) while it is around 31 m/s for $L/H=0.41$ (Fig. 15).

Schachenmann and Rockwell [29] defined a minimum normalized cavity length (L/θ_0) value from which cavity flow tones appear. In the present study, both cavity configurations have the same depth and width. Therefore, for greater cavity length ($L=213$ mm), one could expect shear-layer oscillations and cavity flow tones to occur at lower freestream velocity.

For the case of purely hydrodynamic oscillations in the absence of acoustic resonance, the onset of a detectable instability in the cavity shear layer occurred at a minimum L/θ_0 value of 50 following the investigation of Knisely and Rockwell [8]. Gharib and Roshko [5] required $L/\theta_0=80$ as the lower limit below which the cavity oscillations were completely suppressed. In the present study, oscillations start at $L/\theta_0 \approx 10$ and $L/\theta_0 \approx 21$ for $L/H=0.2$ and $L/H=0.41$, respectively. These L/θ_0 values are lower than those predicted by Knisely and Rockwell [8] and Gharib and Roshko [5]. The strong aero-acoustic coupling could explain this large difference. This hypothesis is confirmed by the presence of flow tones.

All these observations indicate that the geometry of both the cavity and the test section, both the laminar or turbulent features of the incoming boundary layer, and the acoustic modes of the cavity model are predominant factors of aero-acoustic coupling presence.

3.4 Maximum Spectra Pressure Level on the Cavity Walls. Comparison between the maximum pressure fluctuation levels of different cavity walls is shown in Figs. 16 and 17. It should be stressed that the measured wall pressure fluctuating signals contain both the hydrodynamic and the acoustic pressure contributions, which cannot be separated [31].

The maximum spectra pressure level (SPL) is obtained from the analysis of the whole data for each location. For $L/H=0.2$ (Fig. 16), this maximum is higher at the cavity bottom than at the downstream corner of the cavity. This could be related to the influence of the acoustic depth mode and its interaction with the hydrodynamic mode, which leads to a more significant resonance. For $L/H=0.41$ configuration, the resonance due to amplification of acoustic mode by the shear-layer oscillation is less important than that of the $L/H=0.2$ configuration.

For the two cavities, maximum SPL is greater at the position near the top of the forward-facing step ($PS2$ location) than that at the leading edge ($PS1$). This observation could be explained by the impingement of the structures of the shear layer near the $PS2$ location and then the increase in the overall fluctuating pressure level. Therefore, the trailing edge is more effective in emitting noise than the leading edge. Camussi et al. [11] found a similar behavior of the pressure fluctuations and SPL distribution with shallow cavities. The influence of the freestream velocity can be observed on all the maximum SPL plots of both configurations. It can be seen that for all measurement locations, the maximum SPL increases with the freestream velocity. A slight increase in the maximum SPL is observed at the transition from nonoscillating to oscillating modes.

4 Conclusion

Experimental characterization of the inside pressure fluctuations at low Mach numbers has been conducted in two deep cavity models. Measurement of the convection velocity of structures, along the cavity shear layer, has been performed using hot-wire cross-correlation. The main conclusions could be summarized as follows.

(a) Instabilities in the shear layer are convected from the leading edge to the trailing edge of the cavity with a nonconstant convection speed (u_c). This convection velocity depends on both the position of structures along the shear layer and the freestream velocity. The behavior of u_c is quite different insofar as the cavity shear layer oscillates or not.

(b) Rossiter formula [1] correctly predicts the hydrodynamic modes of deep cavities with a convection velocity obtained from velocity cross-correlations and with $\alpha=0$ (the modes are pure harmonics). This implies that the generation of acoustic feedback at the downstream corner is instantaneous for low Mach numbers.

(c) The first Rossiter mode exists for $L/H=0.2$ and both the first and the second modes are present for $L/H=0.41$. The pressure amplitudes show a stronger lock-in between hydrodynamic and acoustic resonances for $L/H=0.2$ than $L/H=0.41$. This leads to a more significant maximum SPL in the first configuration.

(d) With an aspect ratio of $L/H=0.2$, oscillations of the shear layer excite acoustic modes of the cavity, leading to a

Downloaded 03 Jun 2010 to 171.66.16.158. Redistribution subject to ASME license or copyright; see http://www.asme.org/terms/Terms_Use.cfm

generation of flow tones. This aero-acoustic coupling is less obvious for $L/H=0.41$. Moreover, as flow velocity is increased, upward jumps in oscillation frequency are observed in the two cavity configurations.

(e) The maximum SPL distributions at different locations on cavity walls highlighted that the SPL maximum magnitude is reached at the cavity bottom and reveals a strong excitation of the depth mode by the shear-layer oscillation at this location.

(f) For $L/H=0.2$, shear-layer oscillations begin at $L/\theta_0 \approx 10$, which is much lower than values found in previous studies. This difference is attributed to both the characteristics of the incident boundary layer as well as the acoustic depth mode of the cavity.

Acknowledgment

The authors are grateful to Werner Koch for performing the resonance computations and for helpful discussions.

Nomenclature

L = cavity length (104 mm and 213 mm)
H = cavity depth (520 mm)
W = cavity width (2000 mm)
U_0 = freestream velocity
$\mathbf{H}$ = shape factor of the incident boundary layer
δ_0 = thickness of the incoming turbulent boundary layer
θ_0 = momentum thickness of the boundary layer just upstream from the cavity
ν = kinematic viscosity of the fluid
u_c = convection velocity of structure along the shear layer
St = Strouhal number
c_0 = sound speed=340 m/s
M = Mach number=U_0/c_0
α = lag time between the impact of a structure on the cavity downstream corner and the emission of an acoustic wave
T^+ = time for structures to travel from the first to the second hot-wire

References

[1] Rossiter, J. E., 1964, "Wind Tunnel Experiments on the Flow Over Rectangular Cavities at Subsonic and Transonic Speeds," Aeronautical Research Council Reports and Memo No. 3438.
[2] Tam, C. K. W., and Block, P. J. W., 1978, "On the Tones and Pressure Oscillations Induced by Flow Over Rectangular Cavities," J. Fluid Mech., **89**(2), pp. 373–399.
[3] Rockwell, D., and Knisely, C., 1980, "Vortex-Edge Interactions: Mechanism for Generating Low Frequency Components," Phys. Fluids, **23**(2), pp. 239–240.
[4] Rockwell, D., Lin, J.-C., Oshkai, P., Reiss, M., and Pollack, M., 2003, "Shallow Cavity Flow Tone Experiments: Onset of Locked-On States," J. Fluids Struct., **17**, pp. 381–414.
[5] Gharib, M., and Roshko, A., 1987, "The Effect of Flow Oscillations on Cavity Drag," J. Fluid Mech., **177**, pp. 501–530.
[6] Forestier, N., Jacquin, L., and Geffroy, P., 2003, "The Mixing Layer Over a Deep Cavity at High-Subsonic Speed," J. Fluid Mech., **475**, pp. 101–145.
[7] Sarohia, V., 1975, "Experimental and Analytical Investigation of Oscillations in Flows Over Cavities," Ph.D. thesis, California Institute of Technology, Pasadena, CA.
[8] Knisely, C., and Rockwell, D., 1982, "Self-Sustained Low-Frequency Components in an Impinging Shear Layer," J. Fluid Mech., **116**, pp. 157–186.
[9] Gloerfelt, X., Bogey, C., and Bailly, C., 2003, "Numerical Evidence of Mode Switching in the Flow-Induced Oscillations by a Cavity," Int. J. Aeroacoust., **2**(2), pp. 193–217.
[10] Grace, S. M., Dewar, W. G., and Wroblewski, D. E., 2004, "Experimental Investigations of the Flow Characteristics Within a Shallow Wall Cavity for Both Laminar and Turbulent Upstream Boundary Layers," Exp. Fluids, **36**, pp. 791–804.
[11] Camussi, R., Guj, G., and Ragni, A., 2006, "Wall Pressure Fluctuations Induced by Turbulent Boundary Layers Over Surface Discontinuities," J. Sound Vib., **294**(1–2), pp. 177–204.
[12] East, L. F., 1966, "Aerodynamically Induced Resonance in Rectangular Cavities," J. Sound Vib., **3**(3), pp. 277–287.
[13] Larchevêque, L., Sagaut, P., Ivan, M., and Labbé, O., 2003, "Large-Eddy Simulation of a Compressible Flow Past a Deep Cavity," Phys. Fluids, **15**(1), pp. 193–210.
[14] El Hassan, M., Keirsbulck, L., and Labraga, L., "Non-Oscillating/Oscillating Shear Layer Over a Large Deep Cavity at Low-Subsonic Speeds," Flow, Turbul. Combust., to be published.
[15] Rowley, C. W., Colonius, T., and Basu, A. J., 2002, "On Self-Sustaining Oscillations in Two-Dimensional Compressible Flow Over Rectangular Cavities," J. Fluid Mech., **455**, pp. 315–346.
[16] Kegerise, M. A., Spina, E. F., Garg, S., and Cattafesta, L. N., 2004, "Mode-Switching and Nonlinear Effects in Compressible Flow Over a Cavity," Phys. Fluids, **16**(3), pp. 678–687.
[17] Hirahara, H., Kawahashi, M., Uddin Khan, M., and Hourigan, K., 2007, "Experimental Investigation of Fluid Dynamic Instability in a Transonic Cavity Flow," Exp. Therm. Fluid Sci., **31**(4), pp. 333–347.
[18] Gloerfelt, X., Bailly, C., and Juvé, D., 2003, "Direct Computation of the Noise Radiated by a Subsonic Cavity Flow and Application of Integral Methods," J. Sound Vib., **266**(1), pp. 119–146.
[19] Cattafesta, L. N., III, Garg, S., Choudhari, M., and Li, F., 1997, "Active Control of Flow-Induced Cavity Resonance," AIAA Paper No. 97-1804.
[20] Ho, C.-M., and Huang, L.-S., 1982, "Subharmonics and Vortex Merging in Mixing Layers," J. Fluid Mech., **119**, pp. 443–473.
[21] Ho, C.-M., and Nosseir, N. S., 1981, "Dynamics of an Impinging Jet. Part 1. The Feedback Phenomenon," J. Fluid Mech., **105**, pp. 119–142.
[22] Chatellier, L., 2002, "Modélisation et contrôle actif des instabilités aéroacoustiques en cavité sous écoulement affleurant," Ph.D. thesis, Université de Poitiers, France.
[23] Nørstrud, H., and Øye, I., 2006, "On Subsonic Flow Over Cavities With Aero Acoustic Applications," *Proceedings of CMFF'06, 13th International Conference on Fluid Flow Technologies*, Budapest, Hungary, Sept. 6–9.
[24] Bergmann, D., Kaiser, U., and Wagner, S., 2003, "Reduction of Low-Frequency Pressure Fluctuations in Wind Tunnels," J. Wind. Eng. Ind. Aerodyn., **91**(4), pp. 543–550.
[25] Koch, W., 2005, "Acoustic Resonances in Rectangular Open Cavities," AIAA J., **43**, pp. 2342–2349.
[26] Duan, Y., Koch, W., Linton, C. M., and McIver, M., 2007, "Complex Resonances and Trapped Modes in Ducted Domains," J. Fluid Mech., **571**, pp. 119–147.
[27] Tam, C. K. W., 1976, "The Acoustic Mode of a Two-Dimensional Rectangular Cavity," J. Sound Vib., **49**, pp. 353–364.
[28] Oshkai, P., Rockwell, D., and Pollack, M., 2005, "Shallow Cavity Flow Tones: Transformation From Large-To Small-Scale Modes," J. Sound Vib., **280**(3–5), pp. 777–813.
[29] Schachenmann, A., and Rockwell, D., 1980, "Self-Sustained Oscillations of Turbulent Pipe Flow Terminated by an Axisymmetric Cavity," J. Sound Vib., **73**(1), pp. 61–72.
[30] Ricot, D., Maillard, V., and Bailly, C., 2002, "Numerical Simulation of Unsteady Cavity Flow Using Lattice Boltzmann Method," *8th AIAA/CEAS AeroAcoustics Conference*, pp. 2002–2532, AIAA Paper No. 2002-2532.
[31] Williams, J. F., 1992, "Modern Methods in Analytical Acoustics Lecture Notes," J. Acoust. Soc. Am., **92**(5), pp. 313–354.

Downloaded 03 Jun 2010 to 171.66.16.158. Redistribution subject to ASME license or copyright; see http://www.asme.org/terms/Terms_Use.cfm

Dynamic Analysis of a Slender Body of Revolution Berthing to a Wall

Q. X. Wang
School of Mathematics,
University of Birmingham Edgbaston,
Birmingham B15 2TT, UK

S. K. Tan
Maritime Research Centre,
Nanyang Technological University,
50 Nanyang Avenue,
Singapore 630798, The Republic of Singapore

A slender body of revolution berthing to a wall is studied by extending the classical slender body theory. This topic is of practical importance for a ship berthing to a quay wall. The flow problem is solved analytically using the method of matched asymptotic expansions. The lateral force and yaw moment on the body are obtained in a closed form too. The translation and yawing of the body are modeled using the second Newton law and coupled with the flow induced. Numerical analyses are performed for the dynamic lateral translation and yawing of a slender spheroid, while its horizontal translation parallel to the wall is prescribed at zero speed, constant speed, and time varying speed, respectively. The analysis reveals the interesting dynamic features of the translation and yawing of the body in terms of the forward speed and starting angle of yaw of the body.
[DOI: 10.1115/1.3026727]

Keywords: ship berthing, slender body theory, matched asymptotic expansions, conformal mapping, dynamic motion, potential flow theory

1 Introduction

A ship berthing to a quay wall is an interesting phenomenon. When a steady ship is pushed by tugboats toward a quay wall, the ship experiences a large repellence due to the wall. In contrast, when a ship berths to a wall with a forward velocity parallel to the wall, the ship experiences a large attraction due to the wall and accelerates toward the wall. Even in a well-executed berthing, a large ship possesses enormous kinetic energy that can seriously damage the berthing structure as well as the ship itself [1].

The empirical formulas based on the added mass approximations are widely used for a rough estimation of the kinematic energy of a berthing ship, but this approach is invalid when the ship is near the quay wall [2]. Tuck and Newman [3], Yeung and co-workers [4,5] and Cohen and Beck [1] analyzed a slender body moving at a constant speed near a wall using the slender body theory, assuming that the clearance between the body and wall is comparable to the body length. Tuck and Newman [3] studied the close interaction of two ships using the gap flow model by assuming that the clearance between them is small compared with ship drafts. This is similar to a wing in extreme effect [6]. Chen and Liu [7] simulated the transient flow of a ship approaching a wall at constant speed based on the Reynolds-averaged Navier–Stokes equations, for the case where the clearance is not small.

This paper deals with the dynamic motion of the body at the last stage of berthing when the clearance between the ship and wall is small. This work is based on the potential flow theory, since it provides a good approximation for high Reynolds number flows. We assume that the Froude number is small and the free surface can be treated as "rigid," since a ship usually moves slowly as it is berthing [4,5]. A ship berthing to a quay wall can thus be approximated by a slender body, consisting of the wet surface of the ship and its image to the water surface, berthing to a wall. Other applications of this topic includes a submarine moving close to the seabed, a missile skimming over the sea surface, and high-speed trains moving in very close proximity to the ground.

Contributed by the Fluids Engineering Division of ASME for publication in the JOURNAL OF FLUIDS ENGINEERING. Manuscript received August 10, 2007; final manuscript received September 1, 2008; published online December 2, 2008. Assoc. Editor: Dimitris Drikakis.

Owing to the difficult mathematical treatment for arbitrary shaped bodies, we only consider a slender body of revolution. First, the analytical flow solution is obtained for the body in unsteady translation and yawing near a wall, by extending the work for the steady translation of the body parallel to a wall by Wang [8]. The formulas for the lateral force and yawing moment acting on the body are then obtained using the control volume approach. The translation and yawing of the body are further modeled using the second Newton law and coupled with the flow induced. Last, numerical analyses are performed for a slender spheroid pushed to a wall by a constant force and the dynamic lateral motion and yaw of the body with prescribed horizontal velocities near a wall.

2 Mathematical Modeling

Consider the dynamic motion of a slender body of revolution near a flat wall of infinite extent, as shown in Fig. 1. A Cartesian coordinate system O-xyz fixed to the body is defined, with its origin located at the gravity center of the body, the x-axis being opposite to the horizontal moving direction of the body, the y-axis is along the contrary direction of the gravity, and the O-zx plane at the plane of symmetry. Denote the body length as L, horizontal velocity component as $U(t)$, angle of yaw as $\alpha^*(t)$, and lateral distance of the body center to the wall as $h_0(t)$. The body surface can be expressed as

$$r = \sqrt{y^2 + (z + \alpha^* x)^2} = a(x), \quad -L/2 \le x \le L/2 \tag{1}$$

where $r=a(x)$ is the radius of the cross section of the body, which is a smooth function required to vanish at the nose and to vary slowly along the body.

We assume that the radius and the angle of yaw of the body, and the clearance beneath the body are the same order small quantities, as compared with its length.

$$a(x),\ h_0,\ \alpha^*(t) = O(\varepsilon) \tag{2a}$$

or

$$(a(x), h_0(t), \alpha^*(t)) = \varepsilon(A(x), H_0(t), \alpha(t)) \tag{2b}$$

with $A(x)$, $H_0(t)$, and $\alpha(t)=O(1)$, where ε is chosen as the ratio of the maximum radius of the body to the length of the body.

We further assume that the fluid is inviscid and incompressible, and the flow is irrotational. A disturbance velocity potential

 Copyright © 2009 by ASME

Downloaded 03 Jun 2010 to 171.66.16.158. Redistribution subject to ASME license or copyright; see http://www.asme.org/terms/Terms_Use.cfm

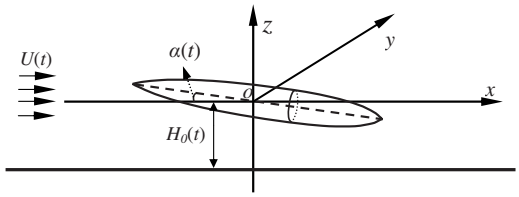

Fig. 1 A slender body of revolution at an angle of yaw in a dynamic motion near a wall

$\varphi(x,y,z,t)$ thus exists in the fluid domain, bounded by the body and wall, and satisfies the Laplace equation in the fluid domain, as follows:

$$\varphi_{xx} + \varphi_{yy} + \varphi_{zz} = 0 \tag{3a}$$

subjected to the following boundary conditions. φ vanishes at infinity and satisfies the impermeable boundary conditions on the wall and body surface:

$$\varphi_z = 0, \quad \text{on} \quad z = -h_0 \tag{3b}$$

$$-\varphi_n = Ua_x + w_c \sin\theta + O(\varepsilon\varphi) \quad \text{as} \quad r = a(x) + O(\varepsilon^2) \tag{3c}$$

where

$$w_c = h_{0t} - x\alpha_t^* - U\alpha^* \tag{4a}$$

$$r = \sqrt{y^2 + (z + \alpha^* x)^2}, \quad \theta = \arctan\left(\frac{z + \alpha^* x}{y}\right) \tag{4b}$$

and $\boldsymbol{n}$ in Eq. (3c) is the unit outward normal vector of the fluid domain on the body surface.

The above assumptions appear reasonable for flow problems of large ships in berthing, with the high Reynolds numbers [8,9]. In addition, we assume that the Froude number in the problem is small, since a ship usually moves slowly as it is berthing. As the Froude number $F_r = U/\sqrt{gL} \to 0$, where g is the gravitational acceleration, the dynamic condition on the free surface becomes $z = 0$ (cf. Appendix). Consequently the free surface can be approximately as rigid [4,5]. A ship berthing to a quay wall can thus be approximated by a slender body, consisting of the wet surface of the ship and its image to the water surface, berthing to a wall.

3 Analytical Flow Solution

We first consider the flow in the outer region far away from the body, where $x,y,z = O(1)$. In the outer region, the flow disturbance can be regarded as the repulsion of the fluid due to the body and its reflected image to the wall $z=0$. Both of them shrink to the line segment of $|x| \le L/2$ and $y=z=0$, as observed from the outer region. The velocity potential in outer region φ^o can thus be expressed by the line source along the segment.

$$\varphi^0(x,y,z,t) = \varepsilon^2 \int_{-L/2}^{L/2} \frac{F(\xi)d\xi}{\sqrt{(x-\xi)^2 + y^2 + z^2}} + o(\varepsilon^2) \tag{5}$$

where $4\pi F(\xi)$ is the strength of the line source. $F(\xi)$ can be obtained, as follows, using the Van Dyke matching principle [10]:

$$F(x) = U(t)A(x)A_x(x) \tag{6}$$

We next consider the flow in the inner region, where $x = O(1)$, and y, $z = O(\varepsilon)$. Introduce the inner variables

$$x = x, \quad Y = y/\varepsilon, \quad Z = (z + \alpha^* x)/\varepsilon \tag{7}$$

The inner limit of the outer expansion $(\phi^o)^i$ can be obtained from Eq. (5).

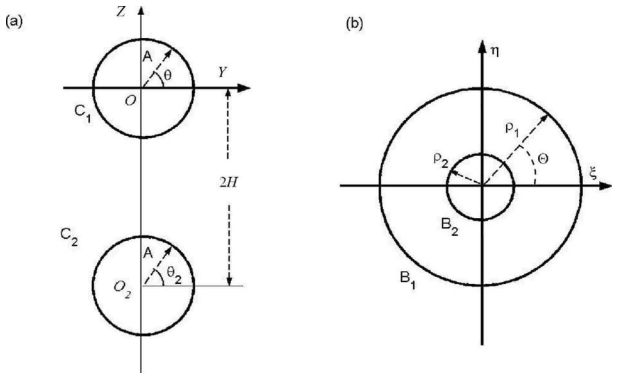

Fig. 2 The conformal mapping of (*a*) the domain outside two circles C_1 and C_2 in the cross-flow plane $Q = Y + iZ$ to (*b*) the domain between two concentric circles B_1 and B_2 in the plane $\varsigma = \rho e^{i\Theta}$

$$(\phi^o)^i = \varepsilon^2 G(x) - \varepsilon^2 F(x)\ln(Y^2 + Z^2) + o(\varepsilon^2)$$
$$G(x) = \int_{-L/2}^{L/2} F_\xi(\xi)\ln|2\xi - 2x|d\xi \tag{8}$$

The inner expansion of the velocity potential φ^i can be conjectured from the inner limit of the outer expansion of Eq. (7) as follows:

$$\varphi^i = \varepsilon^2 G(x) - 2\varepsilon^2 \ln \varepsilon F(x) + \varepsilon^2 \phi(x,Y,Z,t) + o(\varepsilon^2) \tag{9}$$

where $\phi(x,Y,Z,t)$ satisfies the Neumann boundary value problem of the two-dimensional Laplace equation in the cross-flow plane.

$$\phi_{YY} + \phi_{ZZ} = 0 \tag{10a}$$

$$-\phi_n = A_x(x)U(t) + W_c(t)\sin\theta \quad \text{on} \quad \sqrt{Y^2 + Z^2} = A(x) \tag{10b}$$

$$\phi_Z = 0 \quad \text{on} \quad Z = -H(x,t) \tag{10c}$$

where

$$W_c = H_{0t}(t) - \alpha U(t) - \alpha_t(t)x \tag{11a}$$

$$H(x,t) = H_0(t) - \alpha(t)x \tag{11b}$$

It can be noticed from Eq. (10) that ϕ can be regarded as the 2D velocity potential induced by the double circular cylinders at the radius of $A(x)$, expanding (contracting) at the velocity of $U(t)A_x(x)$, departing from (approaching) each other at the velocity of $W_c(t)$, in a symmetrical manner.

To solve the boundary value problem of Eq. (10), we introduce a linear fractional conformal mapping between the cross-flow plane of $Q = Y + iZ$ and the mapped plane of $\varsigma = \rho e^{i\Theta}$.

$$Q = iC\frac{\varsigma + C}{\varsigma - C} - iC\coth\beta \quad \text{with} \quad C = \sqrt{H^2 - A^2}$$
$$\beta = \operatorname{arcsinh}(C/A) \tag{12}$$

It maps the domain outside two circles C_1, $|Q| = A$, and C_2, $|Q - 2H\ i| = A$, in the cross-flow plane Q, to the domain between two concentric circles B_1, $|\zeta| = \rho_1$, and B_2, $|\zeta| = \rho_2$, in the mapped plane ς, as sketched in Fig. 2. ρ_1 and ρ_2 are

$$\rho_1 = Ce^{\beta}, \quad \rho_2 = Ce^{-\beta} \tag{13}$$

The conformal mapping also transforms the line $C_0, Z = -H$, in the cross-flow plane Q, to the circle B_0, $|\varsigma| = C$, in the mapped plane ζ.

To simplify problem (10), we then introduce

Downloaded 03 Jun 2010 to 171.66.16.158. Redistribution subject to ASME license or copyright; see http://www.asme.org/terms/Terms_Use.cfm

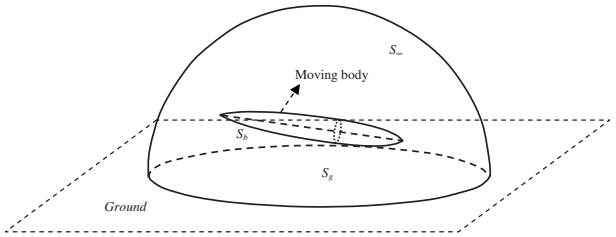

Fig. 3 The control volume, for a slender body moving near a wall, surrounded by the body surface S_b, the wall S_w, and the upper half of a large sphere surface S_∞ in far field

$$\varphi = F \ln \rho - 2F \ln|\varsigma - C| + \Phi \tag{14}$$

The boundary problem of Φ is

$$\Phi_{\xi\xi} + \Phi_{\eta\eta} = 0 \tag{15a}$$

$$\frac{\partial \Phi}{\partial \rho} = W_c \sum_{n=1}^{\infty} n \frac{\cos(n\Theta)}{e^{(n+1)\beta}} \quad \text{on} \quad B_1 \tag{15b}$$

$$\frac{\partial \Phi}{\partial \rho} = W_c \sum_{n=1}^{\infty} n \frac{\cos(n\Theta)}{e^{(n-1)\beta}} \quad \text{on} \quad B_2 \tag{15c}$$

We further assume that the solution of Eq. (15) takes the form of $\Phi = \Sigma_{n=1}^{\infty}(a_n\rho^n + b_n\rho^{-n})\cos(n\Theta)$. Determining its coefficients with Eqs. (15*b*) and (15*c*), and substituting it into Eq. (14), we obtain

$$\phi = F \ln\left(\frac{\rho}{\rho^2 - 2\rho\cos\Theta + C^2}\right) - CW_c \sum_{n=1}^{\infty} \frac{\cos(n\Theta)}{\sinh(n\beta)}\left(\left(\frac{\rho}{\rho_1}\right)^n + \left(\frac{\rho_2}{\rho}\right)^n\right) \tag{16}$$

The series in Eq. (16) converges absolutely in the whole cross-flow domain, corresponding to $\rho_2 \le \rho \le C$ and $0 \le \Theta \le 2\pi$. More details of the solution (16) are referenced [11].

4 Dynamic Analysis

The hydrodynamic force $\boldsymbol{f}$ and moment $\boldsymbol{m_0}$ acting on a body moving in an irrotational flow can be expressed as follows, by using the control volume approach [12]:

$$\frac{\boldsymbol{f}}{\rho_f} = -\frac{d}{dt}\int_{S_b} \varphi \boldsymbol{n} dS - \int_{S_c}\left(\varphi_n \nabla\varphi - \boldsymbol{n}\frac{1}{2}\nabla\varphi\cdot\nabla\varphi\right)dS \tag{17a}$$

$$\frac{\boldsymbol{m}_0}{\rho_f} = -\frac{d}{dt}\int_{S_b} \varphi(\boldsymbol{R}_0 \times \boldsymbol{n})dS - \int_{S_c} \boldsymbol{R}_0\left(\varphi_n \nabla\varphi - \boldsymbol{n}\frac{1}{2}\nabla\varphi\cdot\nabla\varphi\right)dS \tag{17b}$$

where S_b is the body surface, S_c is a fixed control surface exterior to S_b, and $\boldsymbol{n}$ is the unit outward normal vector of the control volume on the control surfaces. d/dt is the material time derivative, $\boldsymbol{m}_0$ is the moment to the initial body center at $t=0$, and $\boldsymbol{R}_0$ is the vector of a point on the control surfaces from the initial body center.

S_c is chosen consisting of the fixed ground S_g and the upper half of a large spherical surface S_∞ in the far field, cut by each other, as shown in Fig. 3. The asymptotic behaviors of φ in the far field can be estimated from Eqs. (5) and (6).

$$\varphi \to O\left(\frac{\varepsilon^2}{r^2}\right), \quad |\nabla\phi| \to O\left(\frac{\varepsilon^2}{r^3}\right)$$
$$\varphi_n \to O\left(\frac{\varepsilon^2}{r^3}\right) \quad \text{as} \quad r = \sqrt{x^2+y^2+z^2} \to \infty \tag{18}$$

Since the surface area of S_∞ is proportional to r^2, the contribution to the second integrals in Eqs. (17*a*) and (17) from S_∞ will vanish as r tends to infinity. Noticing further that $\varphi_n = 0$ on the ground S_g, we obtain

$$\frac{\boldsymbol{f}}{\rho_f} = -\frac{d}{dt}\int_{S_b} \phi \boldsymbol{n} dS - \frac{\boldsymbol{k}}{2}\int_{S_g} \nabla\varphi\cdot\nabla\varphi dS \tag{19}$$

where $\boldsymbol{k}$ is the unit vector along the z-axis.

Using the slenderness assumption and inner expansion of Eq. (9), the vertical force f_z can be given as follows from Eq. (19):

$$\frac{f_z}{\rho_f \varepsilon^3} = \int_{-L/2}^{L/2} (J_{1t}(x,t) - J_2(x,t))dx + O(\varepsilon) \tag{20}$$

where $J_1(x,t)$ and $J_2(x,t)$ as follows:

$$J_1(x,t) = \oint_{C_1} \phi \sin\theta dl \tag{21a}$$

$$J_2(x,t) = \frac{1}{2}\oint_{C_g} (\phi_Y^2 + \phi_Z^2)dl \tag{21b}$$

In a similar way, using the slenderness assumption, Eq. (17*b*) can be simplified as

$$\frac{\boldsymbol{m}_0}{\rho_f \varepsilon^3} = -U t \boldsymbol{j}\int_{-L/2}^{L/2}(J_2 - J_{1t})dx + \boldsymbol{j}\int_{-L/2}^{L/2}[((U+U_t t)J_1 - xJ_{1t} + xJ_2)]dx + O(\varepsilon) \tag{22}$$

Considering that the body moves at the velocity $-U\boldsymbol{i}$, the yawing moment m_y to the y-axis can be given as

$$\frac{m_y}{\rho_f \varepsilon^3} = \int_{-L/2}^{L/2}((U+U_t t)J_1(x,t) - xJ_{1t}(x,t) + xJ_2(x,t))dx + O(\varepsilon) \tag{23}$$

$J_1(x,t)$ and $J_2(x,t)$ of Eq. (21) can be integrated analytically with the following results:

$$J_1 = 2\pi F(H-C) - 4\pi C^2 W_c \sum_{n=1}^{\infty}(n\coth(n\beta)e^{-2n\beta}) \tag{24a}$$

$$J_2 = \frac{\pi}{C}\left(F^2 - 2AFW_c e^{-\beta} + 2C^2 W_c^2 \sum_{n=1}^{\infty} c_n(c_n - c_{n+1})\right)$$
$$c_n = \frac{2ne^{-2n\beta}}{1-e^{-2n\beta}} \tag{24b}$$

Similar integrations are calculated in Ref. [8]. J_{1t} needed in Eqs. (20) and (23) can be obtained from Eq. (24*a*), as follows:

$$J_{1t}(x,t) = 2\pi[F_t(H-C) + F(H_t - C_t)] - 4\pi C\sum_{n=1}^{\infty}\{n[(2C_t W_c + CW_{ct} - 2nCW_c\beta_t)\coth(n\beta) - nCW_c\beta_t \operatorname{csch}^2(n\beta)]e^{-2n\beta}\} \tag{25}$$

C_t, W_{ct}, and β_t needed in Eq. (25) can be obtained from Eqs. (12) and (13)

Downloaded 03 Jun 2010 to 171.66.16.158. Redistribution subject to ASME license or copyright; see http://www.asme.org/terms/Terms_Use.cfm

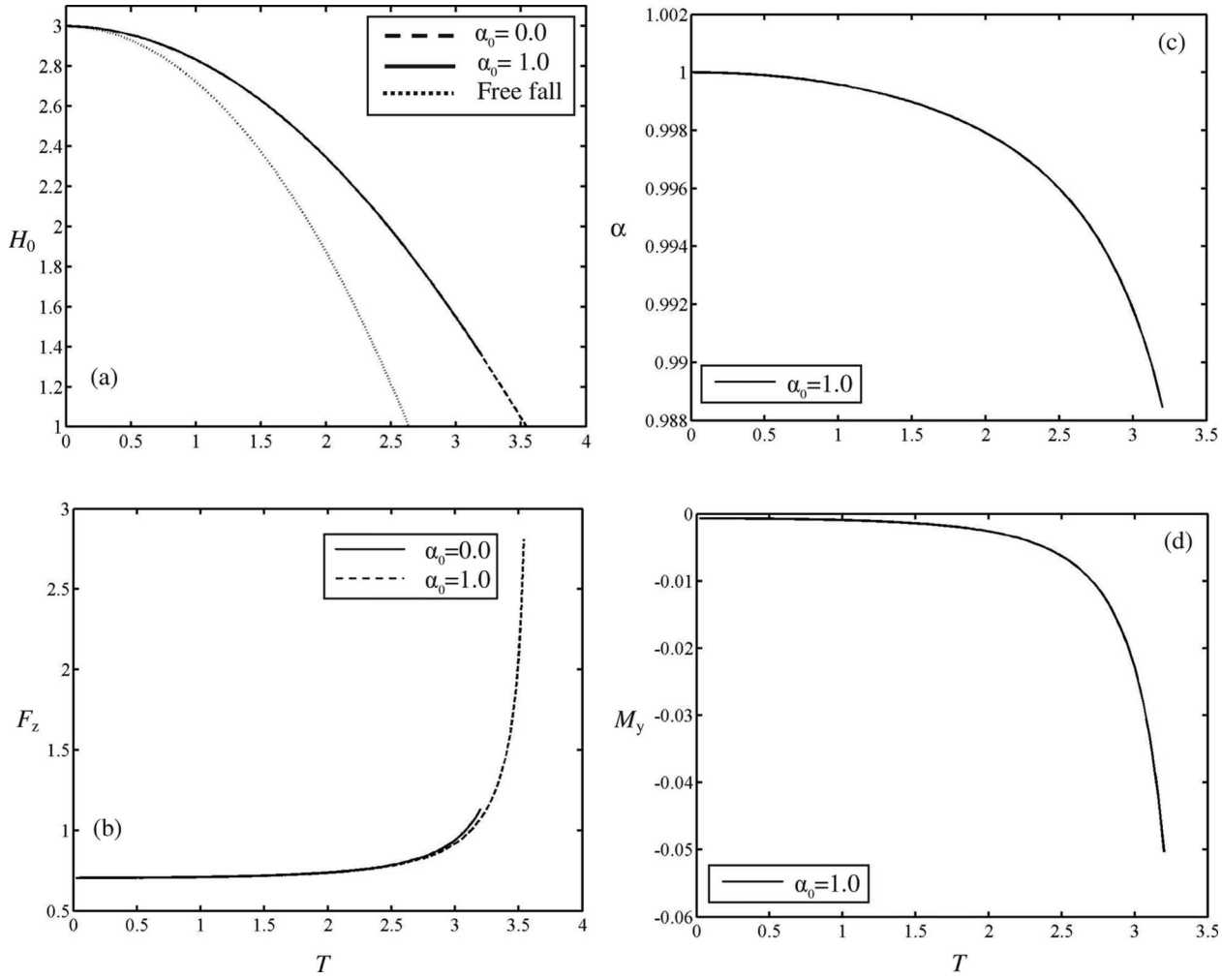

Fig. 4 A slender spheroid falls to a wall at $\rho_s/\rho_f=1.05$. (*a*) The lateral distance of the body center to the wall H_0, (*b*) the lateral force F_z, (*c*) the angle of yaw α, and (*d*) the yawing moment M_y versus time.

$$C_t = \frac{HH_t}{C}, \quad W_{ct} = H_{0tt} - \alpha_t U - \alpha U_t - x\alpha_{tt}, \quad \beta_t = \frac{C_t}{A \cdot \cosh \beta} \tag{26}$$

The three series in Eqs. (24) and (25) are convergent absolutely.

The body is assumed in a prescribed horizontal translation, parallel to the wall, and its dynamic lateral translation and dynamic yawing are governed by Newton's second law

$$mh_{0tt} = f_z + f_g, \quad I_{yy}\alpha^*_{tt} = m_y \tag{27}$$

where f_g is the z-component of the gravity force acting on the body, and m and I_{yy} are the mass of the body and initial moment of the body to the y-axis, respectively.

5 Numerical Analysis

The dynamic motion of a slender body of revolution near a wall, modeled in Sec. 3, is calculated using MATLAB. The three series in Eqs. (24) and (25) converge rapidly, since their terms decay exponentially. The three series are summed at a very high accuracy, with the series truncated when the terms are at $O(10^{-8})$, since the CPU time needed is minimal. The integrations of the lateral force of Eq. (20) and yawing moment of Eq. (23) are performed using the recursive adaptive Simpson quadrature. The time integrations of Eq. (27) are performed using the Euler–Cauchy method.

The calculations are performed for a slender spheroid, with the results shown in dimensionless lateral force F_z, yawing moment M_y, and time T.

$$F_z = \frac{f_z}{\rho V_{\text{ref}}^2 L^2 \varepsilon^3}, \quad M_y = \frac{m_y}{\rho V_{\text{ref}}^2 L^3 \varepsilon^3}, \quad T = \frac{V_{\text{ref}} t}{L} \tag{28}$$

The reference velocity V_{ref} is chosen as

$$V_{\text{ref}} = U(0) \quad \text{as} \quad U(0) \neq 0 \quad \text{and} \quad V_{\text{ref}} = \sqrt{gL} \quad \text{as} \quad U(0) = 0 \tag{29}$$

The simulations start as the lateral distance of the body center to the wall $H_0=3.0$, since the wall effects are small when the body is farther away from the wall.

We first consider the case where a slender spheroid falls down to a wall, under the gravity, buoyancy, and hydrodynamic loads. The body density ρ_s is assumed to be constant and is chosen at $\rho_s/\rho_f=1.05$. This problem is equivalent to the body being pushed toward the wall by a force at the magnitude of $(\rho_s-\rho_f)\cdot g\cdot V_{\text{ol}}$, where V_{ol} is the volume of the body, like a ship pushed by tugboats to a quay wall.

Figures 4(*a*) and 4(*b*) show the time histories of the height of the body center to the wall H_0 and the lateral force F_z on the body, as the starting inclined angle at $\alpha_0=0.0$ (dashed line) and $\alpha_0=1.0$ (solid line). We also depict H_0 for the body in a free fall without the hydrodynamic load (dotted line), for comparison. One

Downloaded 03 Jun 2010 to 171.66.16.158. Redistribution subject to ASME license or copyright; see http://www.asme.org/terms/Terms_Use.cfm

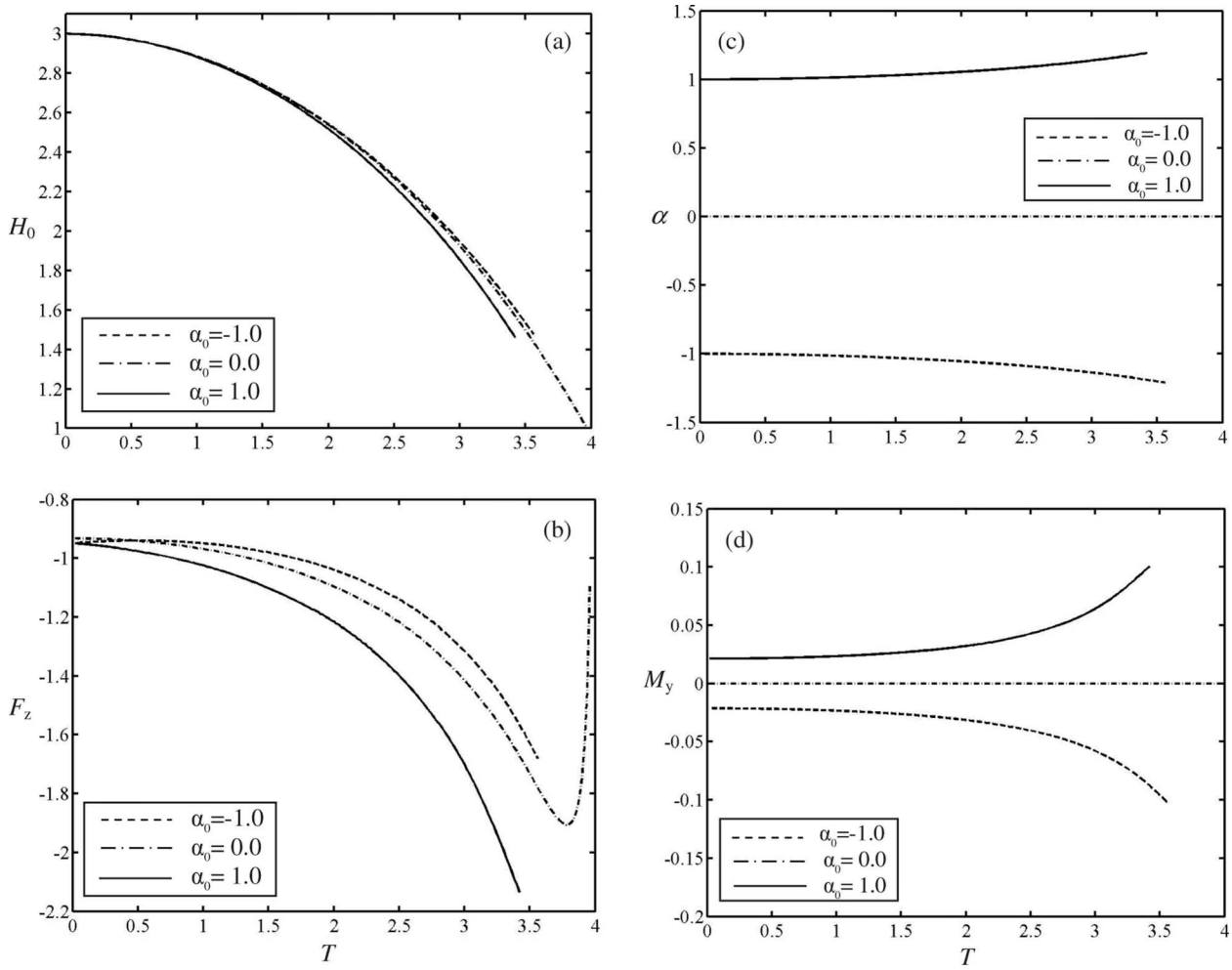

Fig. 5 Dynamic motion of a slender spheroid at constant horizontal velocity $U=1.0$. (*a*) The lateral distance of the body center to the wall H_0, (*b*) the lateral force F_z, (*c*) the angle of yaw α, and (*d*) the yawing moment M_y versus time.

can see that the falling body is repelled by the wall. The repulsion is prominent and increases rapidly with time at the end of the fall (Fig. 4(*b*)). Compared with the free fall, the body is slowed down apparently, and its moment of impact to the wall is reduced by about 29% by the hydrodynamic load. Unlike a body moving in an unbounded inviscid fluid where the added mass is a constant, the added mass in this case increases with time and increases rapidly at the end of the fall. This is because a stagnation point occurs at the wall beneath the falling body, and a high-pressure region is thus formed over there. The body is repelled by the high-pressure region, when it is close to the wall. Similar phenomena were observed for a sphere falling to a wall by Milne-Thomson [13], and a two-dimensional flat plate falling to a wall by Yih [14]. When the body starts to fall at $\alpha_0=1.0$ (solid line), the repulsion is slightly larger than that for $\alpha_0=0.0$ (dashed line); H_0 versus time is nearly the same as that at $\alpha_0=0.0$, except that the body impacts the wall earlier.

Figures 4(*c*) and 4(*d*) show the time histories of the inclined angle α of the body and yawing moment M_y on the body. The yawing moment is small and in the contrary direction of the inclined angle, and its amplitude increases rapidly at the end of the fall (Fig. 4(*d*)). This is because the repulsion on the lower half of the body closer to the wall is larger than that on the upper half. Here the lower half and upper half of the body are divided along the middle cross section of the body. The magnitude of the inclined angle thus reduces with time (Fig. 4(*c*)), and the yawing is stable.

We then consider the dynamic motion of a slender spheroid at a prescribed constant horizontal velocity. It is assumed that the body density is constant and is equal to the fluid density. Figures 5(*a*) and 5(*b*) show the time histories of H_0 and F_z, as the starting angles of yaw at $\alpha_0=-1.0$, 0.0, and 1.0. As $\alpha_0=0$ (dashed-dotted line), attraction acts on the body, and hence the body accelerates to the wall. This is because the flow moves faster and the pressure is lower beneath the body than that above it, due to the constraining effect of the wall. Shortly before the body impacts the wall, the attraction first increases rapidly and then decreases rapidly, reaching its maximum value as the minimum clearance beneath the body being around $0.2R_m$, where R_m is the maximum radius of the spheroid.

The attraction is larger and the body approaches the wall faster at $\alpha_0=1.0$ (solid line) than that at $\alpha_0=0$ (dashed-dotted line). In contrast, the attraction is smaller and the body approaches the wall slower at $\alpha_0=-1.0$ (dashed line) than that at $\alpha_0=0$. As interpreted at the end of Sec. 2, the kinetic effects of the angle of yaw is the approach of (departure from) the cross section of the body to the wall as the angle of yaw is positive (negative). The dynamic effect of the approach of the body to the wall is thus enhanced at a positive angle of yaw, and vice versa, at a negative angle of yaw.

Figures 5(*c*) and 5(*d*) show the angle of yaw α and yawing moment M_y versus time, for this case. At $\alpha_0=1.0$ (solid line), the yawing moment is positive and increases with time as the body accelerates to the wall, and the angle of yaw thus increases with

Downloaded 03 Jun 2010 to 171.66.16.158. Redistribution subject to ASME license or copyright; see http://www.asme.org/terms/Terms_Use.cfm

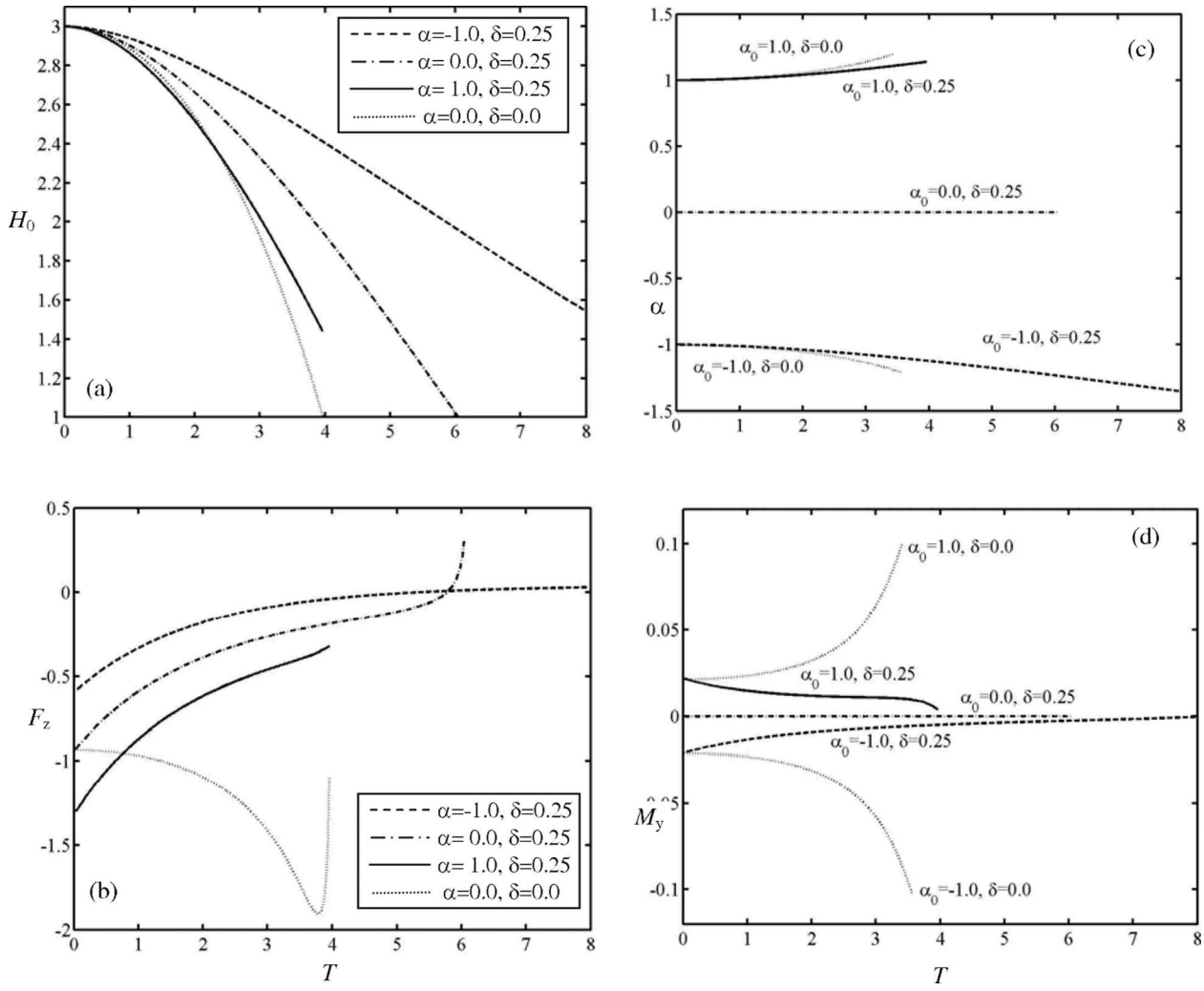

Fig. 6 Dynamic motion of a slender spheroid at the horizontal velocity of $U=\exp(-\delta T)$ and $\delta=0.25$, compared with that at constant horizontal velocity $U=1.0$ ($\delta=0.0$). (*a*) The lateral distance of the body center to the wall H_0, (*b*) the lateral force F_z, (*c*) the angle of yaw α, and (*d*) the yawing moment M_y versus time.

time. This is as expected, since the attraction on the rear half of the body closer to the wall is larger than that on the fore half. In contrast, the yawing moment is negative and decreases with time at $\alpha_0=-1.0$ (dashed line), and hence the angle of yaw decreases with time. The yawing for this case is thus unstable.

Last, we analyze the dynamic motion of a slender spheroid at a prescribed horizontal velocity decreasing with time, $U=\exp(-dT)$ and $\delta=0.25$. Figures 6(*a*) and 6(*b*) show the time histories of H_0 and F_z, at $\alpha_0=-1.0$, 0.0, and 1.0. We also depict the results for the body at $U=1.0$ ($\delta=0.0$) and $\alpha_0=0.0$ for comparison (dotted line). As $\delta=0.25$ and $\alpha_0=0.0$ (dashed-dotted line), F_z starts as an attraction, but its magnitude decreases with time, while the body decelerates horizontally and accelerates to the wall. The lateral force becomes repulsion, shortly before it impacts the wall. As noticed in the last two cases, the body experiences repulsion when it falls to a wall, whereas it experiences attraction when it is predominantly in the horizontal translation. In this case, the attraction effect reduces when the body decelerates horizontally, and the repulsion effect increases when the body accelerates toward the wall. The attraction on the body thus reduces with time and becomes repulsion shortly before it impacts the wall.

The dynamic features versus the starting angle of yaw shown in Fig. 6 are analogous to the last case at a constant horizontal velocity. The attraction is again larger and the body thus falls faster at $\alpha_0=1.0$ (solid line) than that at $\alpha_0=0.0$ (dash-dot line). In contrast, the attraction is smaller and the body falls slower at $\alpha_0=-1.0$ (dashed line) than that at $\alpha_0=0$. The varying amplitudes of F_z and H_0 versus α_0, in this case, are much larger than that at a constant horizontal velocity.

Figures 6(*c*) and 6(*d*) show the time histories of the angle of yaw α and yawing moment M_y for this case. The corresponding results at a constant horizontal velocity are also depicted in the figures for comparison. Similar to the case at a constant horizontal velocity, the yawing moment is positive at $\alpha_0=1.0$, and hence the angle of yaw increases with time, and vice versa, at $\alpha_0=-1.0$. As the result, the yawing is unstable for this case too. The magnitude of the yawing moment decreases with time, when the body decelerates horizontally.

6 Summary

The flow past a slender body of revolution berthing to a wall is obtained analytically by using the method of matched asymptotic expansions. The lateral force and yawing moment acting on the body are obtained, in terms of the integrals along the body length. The translation and yawing of the body are modeled using the second Newton law and coupled with the flow induced. Numerical analyses are performed for the dynamic lateral translation perpendicular to the wall and yawing of a slender spheroid, while its

Downloaded 03 Jun 2010 to 171.66.16.158. Redistribution subject to ASME license or copyright; see http://www.asme.org/terms/Terms_Use.cfm

horizontal translation parallel to the wall is prescribed at zero speed, constant speed, and time varying speed, respectively. The following dynamic features are observed.

When a steady slender spheroid is pushed by an external force or falls to a wall, it experiences a repulsion force due to the wall. The repulsion is prominent and increases rapidly in the short period just before the body impacts the wall. The body is slowed down apparently by this cushion effect, and its moment of impact is reduced significantly. As the body is inclined, the yawing moment on the body is in the contrary direction of its inclined angle, and the yawing of the body is thus stable.

When a slender spheroid berths to a wall with a forward velocity parallel to the wall, the body experiences an attraction due to the wall and accelerates to the wall. When the body decelerates forwardly and/or accelerates laterally to the wall, the attraction decreases rapidly. As the body is with a negative angle of yaw (fore end closer to the wall), the attraction is smaller and the body thus approaches the wall slower than that at zero angle of yaw, and vice versa, as the body with a positive angle of yaw. The yawing moment on the body is in the direction of its angle of yaw, and the yawing of the body is thus unstable. The yawing moment reduces when the body decelerates horizontally and/or accelerates to the wall.

Appendix: The Dynamic Condition on the Free Surface at Low Froude Number

Considering a body moving on a free surface, we discuss the limit format of the dynamic condition on the free surface as $F_r \rightarrow 0$. The dynamic pressure on the free surface is [15]

$$\frac{d\varphi}{dt} = \frac{1}{2}|\nabla\varphi|^2 - gz \tag{A1}$$

We choose the length L and the speed U of the body as the reference length and reference speed. The normalized dynamic condition on the free surface is

$$\frac{d\bar{\varphi}}{d\bar{t}} = \frac{1}{2}|\bar{\nabla}\bar{\phi}|^2 + \frac{\bar{z}}{F_r^2} \tag{A2}$$

where $\bar{\nabla} = \nabla/L$, $\bar{z} = z/L$, $\bar{t} = t/L/U$, $\bar{\varphi} = \varphi/LU$, and $F_r = U/\sqrt{gL}$.

As the Froude number $F_r = U/\sqrt{gL} \rightarrow 0$, the dynamic condition on the free surface becomes $\bar{z} = 0$.

References

[1] Cohen, S. B., and Beck, R. F., 1983, "Experimental and Theoretical Hydrodynamic Forces on a Mathematical Model in Confined Water," J. Ship Res., **27**, pp. 75–89.

[2] Huang, E. T., Davis, D. A., Kim, C. H., and Chen, H. C., 1998, "Measurement of Transient Flow Induced by a Berthing Barge in the Towing Tank," Proceedings of the 25th American Towing Tank Conference, University of Iowa, Iowa City.

[3] Tuck, E. O., and Newman, J. N., 1974, "Hydrodynamic Interactions Between Ships," Proceedings of the Tenth Symposium on Naval Hydrodynamics, Cambridge, MA, Office of Naval Research, Washington, DC, pp. 35–70.

[4] Yeung, R. W., and Hwang, W. Y., 1977, "Nearfield Hydrodynamics and Interactions of Ships in Shallow Water," J. Hydronaut., **11**(4), pp. 128–135.

[5] Yeung, R. W., and Tan, W. T., 1980, "Hydrodynamic Interactions of Ships With Fixed Obstacles," J. Ship Res., **24**(1), pp. 50–59.

[6] Wang, Q. X., 1991, "Flow Around an Unsteady Wing Close to a Curved Ground," J. Fluid Mech., **226**, pp. 175–187.

[7] Chen, H. C., and Liu, T. J., 1999, "Turbulent Flow Induced by Full-Scale Ship in Harbor," J. Eng. Mech., **125**(7), pp. 827–835.

[8] Wang, Q. X., 2005, "Analyses of a Slender Body Moving Near a Curved Ground," Phys. Fluids, **17**, p. 097102.

[9] Wang, Q. X., 2007, "An Analytical Solution for Two Slender Bodies of Revolution Translating in Very Close Proximity," J. Fluid Mech., **582**, pp. 223–251.

[10] Van Dyke, M. D., 1975, *Perturbation Methods in Fluid Mechanics*, 2nd ed., Parabolic, Stanford, CA.

[11] Wang, Q. X., 2004, "Interaction of Two Circular Cylinders in Inviscid Fluid," Phys. Fluids, **16**(12), pp. 4412–4425.

[12] Newman, J. N., 1980, *Marine Hydrodynamics*, 3rd ed., MIT Press, Cambridge, MA.

[13] Milne-Thomson, L. M., 1968, *Theoretical Hydrodynamics*, MacMillan, London.

[14] Yih, C. S., 1974, "Fluid Mechanics of Colliding Plates," Phys. Fluids, **17**, pp. 1936–1940.

[15] Wang, Q. X., 2005, "Unstructured MEL Modelling of Unsteady Nonlinear Ship Waves," J. Comput. Phys., **210**(1), pp. 368–385.

Downloaded 03 Jun 2010 to 171.66.16.158. Redistribution subject to ASME license or copyright; see http://www.asme.org/terms/Terms_Use.cfm

Aerodynamic Characteristics of Asymmetric Bluff Bodies

J. C. Hu

Y. Zhou[1]
e-mail: mmyzhou@polyu.edu.hk

Department of Mechanical Engineering,
Hong Kong Polytechnic University,
Hung Hom, Kowloon, Hong Kong, China

The wake of asymmetric bluff bodies was experimentally measured using particle imaging velocimetry, laser Doppler anemometry, load cell, hotwire, and flow visualization techniques at Re=2600–8500 based on the freestream velocity and the characteristic height of the bluff bodies. Asymmetry is produced by rounding some corners of a square cylinder and leaving others unrounded. It is found that, with increasing corner radius, the flow reversal region is expanded, and the vortex formation length is prolonged. Accordingly, the vortex shedding frequency increases and the base pressure rises, resulting in a reduction in the mean drag as well as the fluctuating drag and lift. It is further found that, while the asymmetric cross section of the cylinder causes the wake centerline to shift toward the sharp corner side of the bluff body, the wake remains globally symmetric about the shifted centerline. The near wake of asymmetric bluff bodies is characterized in detail, including the Reynolds stresses, characteristic velocity, and length scale, and is further compared with that of the symmetric ones. [DOI: 10.1115/1.2979229]

1 Introduction

When a bluff body is subjected to a cross-flow, vortex shedding from the body induces structural vibration, which is a destructive source to the structure. As such, various methods have been devised to control the undesired effects of vortex shedding [1]. As a passive technique to alleviate vortex-excited vibrations, corner modification on a square or rectangular prism has received considerable attention [2–5] in literature. Tamura et al. [6] and Tamura and Miyagi [7] investigated numerically and experimentally aerodynamic forces on a chamfered or rounded cylinder and observed a decrease in the wake width as well as the mean drag coefficient, C_d, as compared with a square cylinder. Zheng and Dalton [8] studied numerically the corner effect in an oscillatory flow and observed vortex separation at irregular high frequency modes when Keulegan–Carpenter number was larger than 3 for a rounded square cylinder. The calculated drag and inertia coefficients were in good agreement with the measurements of Bearman et al. [9]. Dalton and Zheng [10] numerically investigated uniform flow past square and diamond cylinders, with and without corner modifications at Re=250 and 1000, and subsequently suggested that the rounded corners of the bluff bodies yielded a noticeable decrease in drag and lift coefficients. Based on phase-locked particle imaging velocimetry (PIV) and laser Doppler anemometry (LDA) measurements, Hu et al. [11] showed a remarkable effect of the corner radius on the near-wake structure.

Previous investigations largely focus on the bluff bodies of symmetric cross section. In engineering, bluff bodies of asymmetric cross section are frequently seen, such as many modern-looking high-rise buildings designed asymmetrically for the sake of aesthetics. However, the impact of asymmetry on aerodynamic forces imposing on the structures and the wake has not been well documented. A number of questions have yet to be answered such as how the asymmetry would alter the vortex shedding frequency, as compared with a symmetric body (e.g., a circular cylinder). These issues are of fundamental interest, motivating the present investigation. It is also fundamentally and practically interesting to understand how the asymmetry would affect the development of the near wake. Furthermore, there is a need to develop an experimental database for numerical modeling.

In this work, the asymmetry is produced by rounding some corners of a square cylinder, leaving the others squared. Aerodynamic forces on the asymmetric body are measured using load cells, whereas the near wake is documented using hotwire, LDA, and PIV. The measurements are further compared with those associated with symmetric bodies.

2 Experimental Details

Experiments were conducted in a closed-circuit wind tunnel with a test section of 2.4 m(length)×0.6 m(height)×0.6 m(width). The wind speed in the test section is up to 50 m/s and the longitudinal turbulence intensity is less than 0.4%, see Ref. [12] for more details of the tunnel. Three cylinders of the same characteristic height d=12.7 mm but different cross-sectional geometry with respect to the freestream were investigated. Their upper side corner radii, r, are 2 mm, 3 mm, and 6 mm, as shown in Fig. 1(*a*), corresponding to r/d=0.157, 0.236, and 0.472, respectively. For the purpose of systematic documentation of the asymmetric effects, five symmetric cylinders of the same height were also examined: one square cylinder (r/d=0), one circular cylinder (r/d=0.5), and three with the leading corners rounded by r/d=0.157, 0.236, and 0.472, respectively, with the trailing corners squared. The asymmetric geometry was simply produced by rotating the symmetric geometry by 90 deg about its axis (Fig. 1(*a*)). Note that the leading corners play a predominant role in the behavior of streamlines and hence flow separation and base pressure [11]. Therefore, the investigation is focused on the leading corners instead of the trailing, and a difference in the trailing corner is expected to produce a negligibly small effect on the flow. The cylinder was mounted horizontally in the midplane, 0.2 m downstream from the exit plane of the contraction, and spanned the full width of the test section, resulting in an aspect ratio of 47 and a blockage of about 2.1%. Experiments were conducted at the freestream velocities U_∞=3 m/s, 7 m/s, and 10 m/s, and the corresponding Re (Re($\equiv U_\infty d/\nu$), where ν was the kinematic viscosity of the fluid) were 2600, 6000, and 8500, respectively.

2.1 Fluid Force Measurement. A three-component quartz piezoelectric load cell (Kistler Model 9251A) was used to measure the fluid forces on the cylinder. The load cell, characterized by excellent dynamic response, high resolution, and stiffness, was clamped with a spanwise preload of around 30 kN between two polished stainless steel plates. One of the steel plates was clamped on a frame that was fixed on the ground floor to isolate the low

[1]Corresponding author.

Contributed by the Fluids Engineering Division of ASME for publication in the JOURNAL OF FLUIDS ENGINEERING. Manuscript received October 9, 2007; final manuscript received July 12, 2008; published online December 11, 2008. Assoc. Editor: Juergen Kompenhans.

 Copyright © 2009 by ASME

Downloaded 03 Jun 2010 to 171.66.16.158. Redistribution subject to ASME license or copyright; see http://www.asme.org/terms/Terms_Use.cfm

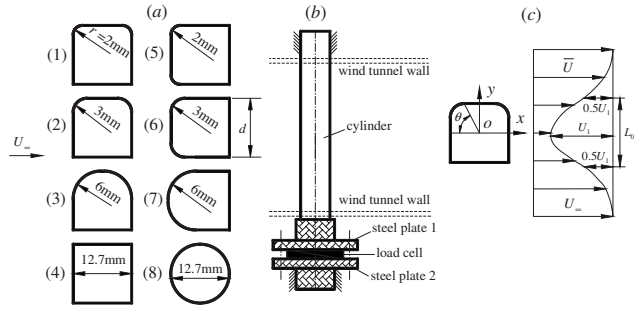

Fig. 1 Experimental details. (*a*) Cross-sectional geometry of cylinders. Asymmetric cylinders: (1) $r/d=0.157$, (2) 0.236, (3) 0.472. Symmetric cylinders: (4) $r/d=0$, (5) 0.157, (6) 0.236, (7) 0.472, (8) 0.5. (*b*) Installation of cylinder and load cell (top view). (*c*) Coordinate system (x,y) and definitions of θ, U_1, and L_0.

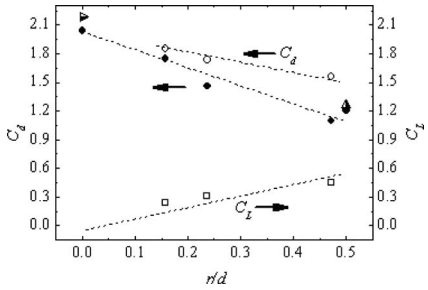

Fig. 2 Dependence of C_d and C_L on r/d (at Re=6000). Open symbols: asymmetric cylinders; solid symbols: symmetric cylinders. Previous data of symmetric cylinders: ▶: Norberg [13], Re=13000; Δ: Bokaian and Geoola [14], Re=5900. The dashed lines denote the best fit curves to the data.

frequency vibration of the wind tunnel. The other was fixed tightly with one end of the cylinder. The other end of the cylinder was mounted on a frame that was also fixed on the ground. Figure 1(*b*) shows schematically the arrangement of the load cell, steel plates, and the cylinder. The natural frequency (f_n) of the installed model was 15.0 Hz for the square cylinder and changed very slightly for other cross sections. On the other hand, the minimum frequency of vortex shedding exceeded 30 Hz for present experimental conditions, thus avoiding a possible synchronization with f_n. The electrostatic charge generated by the load cell was converted to a voltage and amplified with charge amplifiers (Kistler Model 5011). The load cell was calibrated by applying longitudinal and lateral forces, ranging from 0.196 N to 9.6 N, in the midspan of the cylinder. The lateral calibration forces were generated by hanging dead weights of given mass directly on the cylinder, whereas the longitudinal forces were produced by the dead weights with the help of a pulley. The relationship between the forces and the electric voltages was found to be linear and repeatable in both directions. Assuming a uniform wind load distribution along the cylinder, the load cell can measure simultaneously the two force components on the cylinder, including the time-averaged drag (C_d) and lift (C_L), and their root mean square values, C_d' and C_L'. The resolution of the load cell is 10 mN for the range of 0–10 N, and the experimental uncertainty is estimated to be 5%. A single hotwire (tungsten wire of 5 μm in diameter), operated at an overheating ratio of 1.8 on a constant temperature circuit, was placed at $x/d=2$ and $y/d=\pm 1.5$ to measure the dominant vortex shedding frequency, f_s, in the wake. The coordinate system is defined in Fig. 1(*c*), with the origin located at the cylinder center. Coordinates x and y are along the freestream and lateral directions, respectively. The instantaneous velocity components in the x and y directions are designated by U and V, and the corresponding fluctuating velocities are designated by u and v, respectively. The signals from the load cell and the single hotwire were simultaneously measured and then digitized at a sampling rate of 3500 Hz per channel using a 12 bit analog to digital (A/D) converter (16 channels). The duration for each record was 20 s. Force measurement was conducted at $U_\infty=7$ m/s and 10 m/s.

2.2 PIV Measurement. A Dantec standard PIV2100 system was used to measure the near wake. Digital particle images were taken by a charge coupled device (CCD) camera (HiSense type 13, gain×4, double frames, 1280×1024 pixels), synchronized with the flow field illumination using Dantec FlowMap Processor (PIV2100) when capturing images. A wide-angle lens was used, covering a flow field of 140×110 mm^2 in the (x,y) plane, i.e., $x/d=0.5$–11.5 and $y/d=-4.0$–4.0. The flow was seeded by paraffin oil smoke, the typical particle size of which was around 1 μm in diameter. The flow was illuminated by two identical New Wave standard pulsed laser sources with a wavelength of 532 nm and a maximum individual energy output of 120 mJ. The time interval to capture two sequential images was 50 μs. The longitudinal and lateral image magnifications were almost identical, about 0.11 mm/pixel. Each laser pulse lasted for 10 ns, during which a particle only traveled 0.15 mm (1.4 pixels or $0.0118d$) at $U_\infty=3$ m/s. An optical filter was used to allow only the green light (wavelength of 532 nm) to pass. The PIV data analysis is conducted using Dantec software, FLOWMANAGER. The interrogation area of the data is 32 pixels×32 pixels ($\approx0.21d\times0.21d$) with 25% overlap both longitudinally and laterally. Erroneous vectors may be reduced with interrogation areas partially overlapped. The ensuing in-plane velocity vector field consists of 53 ×42 vectors (2226 vectors in total). The percentage of erroneous vectors in raw data is estimated to be less than 1%. The uncertainties are estimated to be 3% for the mean velocities and 5% for the corresponding rms values.

2.3 LDA Measurement. A two-component LDA, i.e., Dantec Model 58N40 with an enhanced flow velocity analyser (FVA) signal processor (BSA F60) and operated on the backscatter mode, was used to measure $\bar{U}$, $\bar{V}$, $\overline{u^2}$, and $\overline{v^2}$ in the near wake. In this paper, overbar denotes time-averaging. Velocity measurements were performed in the (x,y) plane from $y/d=-5$ to 5 across the wake at $x/d=5$. Two laser beams lie in the y-z plane to measure the lateral velocity $(\bar{V}+v)$ and two in the x-z plane to measure the streamwise velocity $(\bar{U}+u)$. The measurement volume, formed by the four laser beams, is an ellipsoid, with its longest axis along the z direction, i.e., along the cylinder span. Given a properly aligned two-component LDA system, the probe can only sense u and v, that is, the u and v measurements are insensitive to the w component. In order to enhance the signal to noise ratio, the flow field was seeded by smoke generated from paraffin oil. The typical validation rate was about 95% and the sampling rate was about 2000 samples/s. At each measurement station, 10,000 valid samples were acquired. The measuring volume has a minor axis of 1.18 mm and a major axis of 2.48 mm. Experimental uncertainties for LDA measurement are estimated to be within 1% for $\bar{U}$ and $\bar{V}$ and 3% for $\overline{u^2}$ and $\overline{v^2}$.

3 Aerodynamic Forces

The cross-sectional geometry of cylinders may affect aerodynamic forces on the cylinders. Figures 2 and 3 present the dependence on r/d of C_d and C_L and C_d' and C_L', respectively, at Re =6000. At $r/d=0$, C_d is 2.03, in agreement with Norberg's [13] report (2.21) at Re=13,000; at $r/d=0.5$, C_d is 1.20, conforming to previous measurements, e.g., 1.25 at Re=5900 by Bokaian and Geoola [14] and 1.30 at Re=22,000 by Igarashi [15]. C_d' is 0.35 at $r/d=0$, close to Alam's [16] measurement (0.29) at Re=47,000,

Downloaded 03 Jun 2010 to 171.66.16.158. Redistribution subject to ASME license or copyright; see http://www.asme.org/terms/Terms_Use.cfm

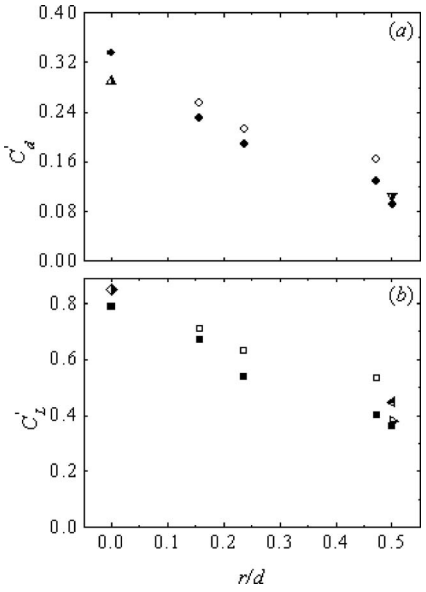

Fig. 3 Dependence of C_d' (*a*) and C_L' (*b*) at Re=6000. Open symbols: asymmetric cylinders; solid symbols: symmetric cylinders. Previous data of symmetric cylinders: Δ: Alam [16], Re=47,000; ▽: West and Apelt [17], Re=56,000; ◈: Dalton and Zheng [10], Re=1000; ◅: Mittal and Balanchandar [18], Re =3900; and ▻: Schewe [19], Re=44,000.

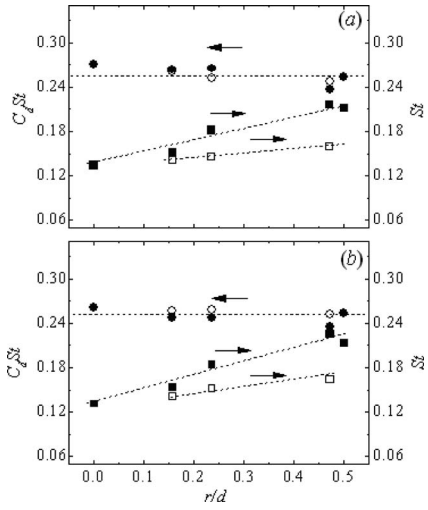

Fig. 4 Dependence of St (□,■) and C_d St (○,●) on corner radius: (*a*) Re=6000 and (*b*) 8500. Open symbols stand for the asymmetric cylinders and solid symbols represent the symmetric cylinders. The dashed lines denote the best fit curves to the data.

and 0.09 at $r/d=0.5$, deviating slightly from West and Apelt's [17] measurement (0.13) at Re=56,000. Meanwhile, C_L' is 0.81 at $r/d=0$, in good agreement with Dalton and Zheng's [10] numerical prediction (0.85) at Re=1000, 0.36 at $r/d=0.5$, close to 0.45 numerically obtained at Re=3900 by Mittal and Balanchandar [18], and 0.38 at Re=44,000 by Schewe [19]. The slight deviation in C_d, C_d', and C_L' between the present data and those in literature might arise from different experimental conditions such as Re, turbulent intensity, cylinder aspect ratio, and end effects [17,20,21]. The comparison provides a validation of the present measurement.

C_d decreases almost linearly from $r/d=0$ to 0.5 (Fig. 2) by about 20% for asymmetric cylinders and 40% for symmetric ones. On the other hand, C_L increases approximately linearly from zero at $r/d=0$ to about 0.4 at $r/d=0.472$, for asymmetric cylinders, but remains to be approximately zero for symmetric cylinders (not shown). Meanwhile, C_d' and C_L' drop by about 50% and 30%, respectively, for asymmetric cylinders (Fig. 3) and by 70% and 40%, respectively, for symmetric cylinders. C_d, C_L, C_d', and C_L' at Re=8500 (not shown) behave similar to those at Re=6000.

Apparently, aerodynamic forces are linked closely with the variation in the cross-sectional geometry of the bluff bodies. The sharp leading corner deflects streamlines more than the rounded corner, resulting in an earlier flow separation. For example, the flow separation angle, calculated from the leading stagnation point, is 45 deg for $r/d=0$ (a square cylinder) and increases with increasing r/d, reaching about 80 deg at $r/d=0.5$ (a circular cylinder), as illustrated in Figs. 11 and 12 of Hu et al. [11]. It is plausible that a postponed flow separation should correspond to a shorter fluid accumulation period for vortex shedding and hence a smaller strength of vortices, i.e., a higher St and smaller C_d, C_d', and C_L'. For the same token, if only one side of a square cylinder is rounded, C_d, C_d', and C_L' drop considerably, albeit to a lesser extent, compared with a cylinder with its two leading corners rounded at the same r/d. As expected, C_L (Fig. 2) on an asymmetric cylinder is nonzero since the separated shear layer deflects more with respect to the *x*-direction at the sharp edge side than at the rounded side, generating a net positive lateral force. A larger r/d on one side of an asymmetric cylinder means a larger difference in the separation angle of the two shear layers, resulting in a larger C_L in magnitude. Consequently, C_L on asymmetric cylinders increases with r/d.

It is well known that C_d is inversely related to the base pressure, and a larger C_d corresponds to a lower C_{pb} (larger in magnitude but negative in sign), or vice versa [22]. Thus, asymmetric cylinder would cause the base pressure to rise, compared with that behind a square cylinder. Lyn et al. [23] proposed that C_d/Γ_0 was approximately constant in the subcritical flow regime for bluff bodies of different cross sections, where Γ_0 was the total circulation. This was supported by the experimental data of Hu et al. [11]. Hu et al. further noted that the ratio of drag to circulation was around 0.25 for symmetric cylinders at Re=2600 (see their Table 1). The relation between C_d and Γ_0 is expected to hold for asymmetric bluff bodies, as would be verified in Sec. 4.2. It may be inferred that as r/d increases, Γ_0 decreases along with C_d, signaling weakened vortex shedding from asymmetric cylinders.

It is noted that as r/d increases, the dominant peaks in the power spectra of the drag and lift signals become broader and less pronounced, conforming to the attenuated forces and weakened vortex shedding.

4 Vortex Shedding Frequency

4.1 Strouhal Number. The Strouhal number, $St=f_s d/U_\infty$, measured by a hotwire is identical to that determined by the force signals. St depends on the corner radius for both asymmetric and symmetric square cylinders (Fig. 4). At Re=6000 (Fig. 4(*a*)), St are 0.134 for a square cylinder ($r/d=0$), which is in conformity with the data in literature [13,24], and 0.211 for a circular cylinder ($r/d=0.5$), in favorable agreement with the well-known range [25]. The flow behind each asymmetric cylinder is characterized by only one dominant frequency across the wake. As r/d increases from 0 to 0.5, St increase almost linearly with r/d by about 25% for the asymmetric cylinder and 60% for the symmetric. The observation is consistent with previous reports [7,11]. Given the same r/d, the asymmetric cylinder, with only one of its leading corners rounded, leads to a lower St and higher C_d, C_d', and C_L' than the symmetric, as discussed earlier. St at Re=2600 (not shown) and 8500 (Fig. 4(*b*)) are roughly equal to that at Re

Downloaded 03 Jun 2010 to 171.66.16.158. Redistribution subject to ASME license or copyright; see http://www.asme.org/terms/Terms_Use.cfm

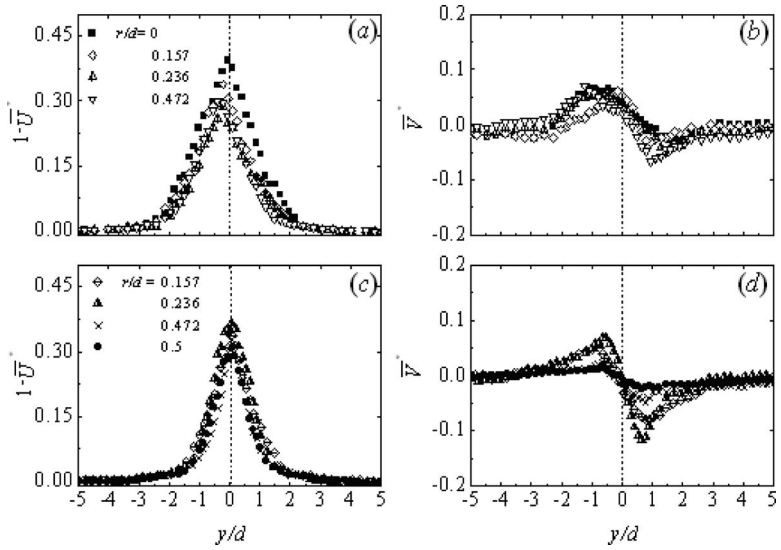

Fig. 5 LDA-measured cross-flow distributions at $x/d=5$ and Re=2600. Asymmetric cylinders: (*a*) $1-\bar{U}^*$ and (*b*) $\bar{V}^*$. Symmetric cylinders: (*c*) $1-\bar{U}^*$ and (*d*) $\bar{V}^*$. The dashed lines denote $y/d=0$.

=6000, regardless of the cross-sectional geometry of cylinders, indicating a negligible Reynolds number effect on St for Re =2600–8500.

4.2 Interrelation of C_d and St. The product of C_d and St is shown in Fig. 4, along with St. In contrast with C_d (Fig. 2), St climbs with increasing r/d. Interestingly, C_d St remains to be a constant, about 0.25, irrespective of the cross-sectional geometry of cylinders and the Reynolds number. This observation is consistent with reports in literature. Schewe and Larsen [26] experimentally observed that, although the Reynolds number in the range of $4\times10^4-2\times10^6$ had a significant effect on the flow around a bridge-deck cross-sectional structure, the Strouhal number times the mean drag coefficient was roughly 0.13. A similar result was obtained by Ahlborn et al. [27], who examined the relationship between St, C_d, and Re of a circular cylinder wake based on mass, momentum, and energy conservations and subsequently concluded that C_d scaled inversely with St, particularly in the crisis region.

Bearman [28] reported that C_{dp} St varied roughly linearly with the base pressure parameter k $(1.0<k=U_s/U_\infty=(1-C_{pb})^{0.5}<1.5)$, where C_{dp} was pressure drag coefficient and U_s was the velocity just outside the boundary layer at the separation point. Griffin [29] extended the range of k up to 2. When the vortex formation of a flow is controlled by splitter plates or base bleeding of low velocity air, the base pressure increases, resulting in a smaller C_{dp} times St (in the range of 0.05–0.20) and $k<1.35$. As $k>1.48$, the flow is usually in the critical and supercritical regimes, or a large confinement flow, or a smooth cylinder in a highly turbulent flow, or a cylinder vibrating in the lock-on range [29]. Under such extreme circumstances, the base pressure becomes significantly lower, compared with flows in the subcritical regime, thus yielding a larger C_{dp} St(=0.26–0.50). Therefore, $1.0<k<2.0$ encompasses essentially the entire range of flow conditions over which vortex shedding occurs from a bluff body. In the subcritical regime, k approximately varies between 1.35 and 1.48 (see Table 1 of Roshko [27] and Fig. 5.44 of Zdravkovich [25]), irrespective of the geometry of the bluff bodies. Accordingly, $C_{pb}=-0.8$ to -1.2 and C_{dp} St$\approx0.23\pm0.02$ (see Fig. 14 of Bearman [28] and Fig. 6 of Griffin [29]). This value is very close to the present estimate of C_d St, which is reasonable in view of a small difference (<5% for the present Re range, see Fig. 4.15 of Zdravkovich [25]) between the pressure drag and total drag.

If using Roshko's [27] formula to estimate Γ_0, viz.,

$$\Gamma_0=\frac{U_s^2T_s}{2U_\infty d}=\frac{1}{2\ \mathrm{St}}\left(\frac{U_s}{U_\infty}\right)^2 \tag{1}$$

where T_s is the shedding period $(=1/f_s)$, then the ratio of C_d to Γ_0 is

$$\frac{C_d}{\Gamma_0}=\frac{C_d}{\frac{1}{2\ \mathrm{St}}\left(\frac{U_s}{U_\infty}\right)^2}=\frac{C_d\ \mathrm{St}}{\frac{1}{2}\left(\frac{U_s}{U_\infty}\right)^2}=\frac{C_d\ \mathrm{St}}{0.5(1-C_{pb})} \tag{2}$$

Note that C_{pb} is in the range of -0.8 to -1.2 for the square prisms in the subcritical flow regime, implying that C_d St$/0.5(1-C_{pb})\approx C_d$ St with a maximum difference of $\pm10\%$ between C_d/Γ_0 and C_d St. Thus, the invariance of C_d St in the subcritical regime can explain the constancy of C_d/Γ_0 proposed by Lyn et al. [23], as mentioned in Sec. 3.

5 Characteristics of Near Wake

5.1 LDA-Measured Cross-Flow Velocity Distributions. The streamwise and lateral velocities are measured across the wake at $x/d=5$, where the vortex formation is completed [12], using LDA. Figures 5 and 6 display the cross-flow distributions of streamwise mean velocity deficit, $1-\bar{U}^*$, lateral mean velocity $\bar{V}^*$, and Reynolds stresses $\overline{u^{2*}}$, $\overline{v^{2*}}$, and $\overline{uv}^*$ at Re=2600. The asterisk denotes normalization by U_∞ and/or d in this paper. A number of observations can be made. First, for all the cylinders, be symmetric or asymmetric in cross section, the distributions of $1-\bar{U}^*$, $\overline{u^{2*}}$, and $\overline{v^{2*}}$ are nearly symmetric about the wake centerline, while those of $\bar{V}^*$ and $\overline{uv}^*$ are approximately antisymmetric. Here, the centerline is defined by the maximum of $1-\bar{U}^*$. The centerline coincides with $y/d=0$ for symmetric cylinders but shifts laterally toward the side with square corners for the asymmetric cylinders, occurring at $y/d=-0.15$, -0.24, -0.30 for $r/d=0.157$, 0.236, 0.472, respectively, apparently caused by the asymmetric cross section. Second, $\overline{u^{2*}}$ and $\overline{v^{2*}}$ display a twin peak and a single peak about the centerline, respectively, arising from the presence of the Karman vortex street. Third, the cross-flow distributions of $1-\bar{U}^*$, $\bar{V}^*$, $\overline{u^{2*}}$,

Downloaded 03 Jun 2010 to 171.66.16.158. Redistribution subject to ASME license or copyright; see http://www.asme.org/terms/Terms_Use.cfm

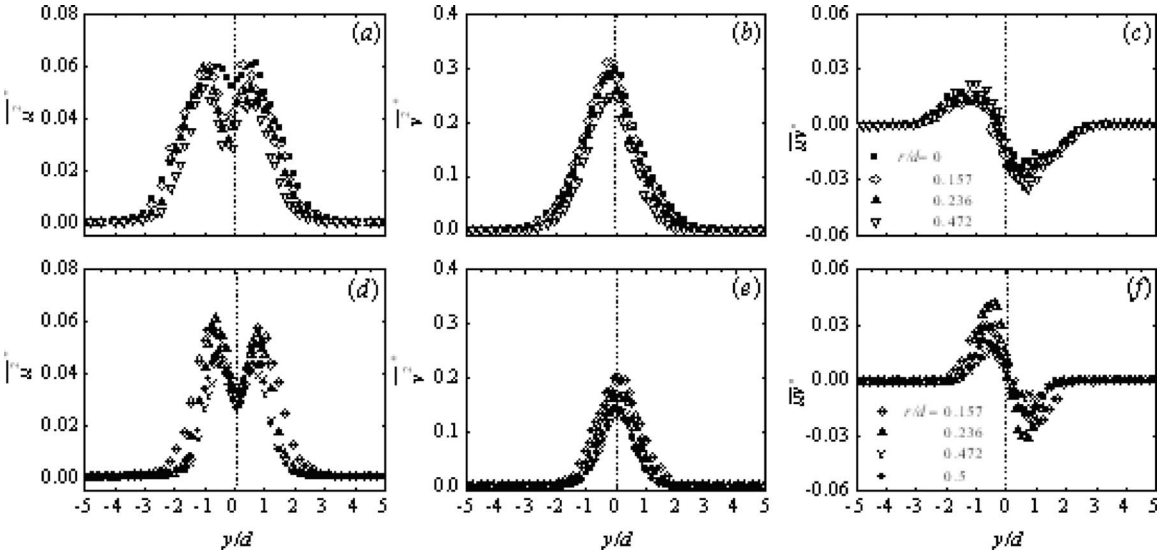

Fig. 6 LDA-measured cross-flow distributions at $x/d=5$ and Re=2600. Asymmetric cylinders: (*a*) $\overline{u^2}$, (*b*) $\overline{v^2}$, and (*c*) $\overline{uv}^*$. Symmetric cylinders: (*d*) $\overline{u^2}$, (*e*) $\overline{v^2}$, and (*f*) $\overline{uv}^*$. The dashed lines denote $y/d=0$.

$\overline{v^2}^*$, and $\overline{uv}^*$ are almost identical for the cylinders of the same leading corner radius. For example, the distributions for the cylinders of $r/d=0$ at the leading corners but $r/d\neq 0$ at the trailing corners are roughly the same as those of the square cylinder (not shown). The results indicate that the trailing corner radius is less influential than the leading corner radius since the leading corners determine the flow separation angle and hence vortex shedding. Finally, the maxima of $\bar{V}^*$, $\overline{u^2}^*$, $\overline{v^2}^*$, and $\overline{uv}^*$ diminish with increasing r/d. So does the distance between the two peaks in the distributions of $\bar{V}^*$ and $\overline{u^2}^*$.

The cross-sectional geometry influences the streamwise mean velocity distribution and the wake width. As shown in Fig. 7, the maximum mean streamwise velocity deficit, U_1^*, and the mean velocity half-width, L_0^* (defined in Fig. 1(*c*)), are r-dependent; with increasing r/d, both U_1^* and L_0^* decrease, consistent with the observations of Tamura and Miyagi [7] and Hu et al. [11]. The asymmetric cylinder produces larger U_1^* and L_0^* than the symmetric at the same r/d. This is reasonable since the sharp corner leads to a larger deflection of the incident fluid with respect to the x-direction, as compared with a rounded corner, resulting in a larger wake width and a larger velocity deficit. The correspondence between a small r/d and a large wake width is also reflected in the $\overline{u^2}^*$ and $\overline{v^2}^*$ distributions. The spread of $\overline{u^2}^*$ is largest at $r/d=0$ (square cylinder) and shrinks as r/d increases (Figs. 6(*a*) and 6(*d*)). Similar behaviors are observed for $\overline{v^2}^*$ (Figs. 6(*b*) and 6(*e*)).

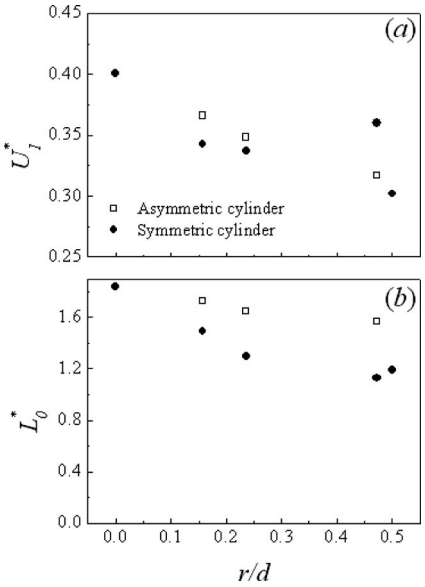

Fig. 7 Dependence of (*a*) maximum mean velocity deficit, U_1^* and (*b*) mean velocity wake half-width, L_0^*, on corner radius. Re=2600 and $x/d=5$.

5.2 PIV-Measured Mean and Fluctuating Velocities. In order to characterize the flow field, 400 sets of PIV-captured instantaneous velocity vectors are averaged for each wake. It has been confirmed that the maximum differences are within 3% in the mean and 5% in the fluctuating velocities if averaging is performed between 200 and 400 PIV images. Figure 8 presents a comparison between the averaged PIV data extracted at $x/d=5$ in the wake of the asymmetric cylinder at $r/d=0.157$ and those measured using LDA with an effective sample size of 10,000. Evidently, the two sets of data collapse reasonably well. The PIV-measured mean velocity is slightly larger than LDA measurements, whereas the PIV-measured root mean square values, i.e., $u_{\rm rms}^*$ and $v_{\rm rms}^*$, of U and V appear smaller. The maximum departure is 8% at the centerline, which is ascribed to not only a difference in the sample size but also a possible deviation in the real x/d, to which $u_{\rm rms}^*$ and $v_{\rm rms}^*$ are sensitive in the near wake, between the measurements. The reasonable agreement between the two techniques provides a validation for the mean and fluctuating flow fields based on 400 PIV images.

5.2.1 Mean Velocities. Figure 9 presents the isocontours of $\bar{U}^*$ at Re=2600 for all the cylinders. The dashed straight line indicates the centerline, as determined by the minimum $\bar{U}^*$. While coinciding with $y/d=0$ for symmetric cylinders, the centerline shifts away from $y/d=0$ toward the sharp corner side for asymmetric cylinders, reinforcing earlier observation from the LDA data. The shift, Δh, is $-0.15d$, $-0.24d$, and $-0.30d$ for $r/d=0.157$, 0.236, 0.472, respectively. An empirical correlation between r/d and $\Delta h/d$ may be given by $\Delta h/d=-1.3762(r/d)^2+1.2965(r/d)-0.0036$ for $0<r/d\leq 0.472$, with a least square deviation of 0.99.

Downloaded 03 Jun 2010 to 171.66.16.158. Redistribution subject to ASME license or copyright; see http://www.asme.org/terms/Terms_Use.cfm

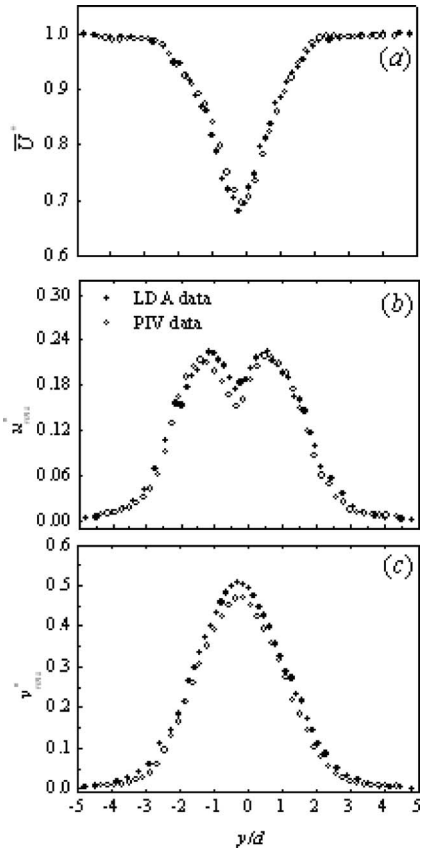

Fig. 8 Comparison between LDA and PIV measurements at $x/d=5$ in the wake of the asymmetric cylinder ($r/d=0.157$, Re $=2600$): (*a*) $\bar{U}^*$, (*b*) u^*_{rms}, and (*c*) v^*_{rms}

The isocontours of $\bar{U}^*$ are approximately symmetric, irrespective of the cross-sectional geometry of the cylinder, about the centerline. The contour of $\bar{U}^*=0$ encloses the recirculation region, which is stretched for increasing r/d. The recirculation region length (Fig. 10), l_c^*, defined from the cylinder center to the farthest position of $\bar{U}^*=0$, is 1.01 for $r/d=0$, close to the report of Lyn et al. [23] (1.3) at Re=21,400. At $r/d=0.5$, l_c^* is 2.52, in good agreement with previous reports, e.g., 2.4 by Konstantinidis et al. [30] at Re=2750 and 2.59 by Hu et al. [11] measured using LDA at Re=2600. Note that l_c^* is shorter for an asymmetric cylinder than the symmetric at the same r/d, which is expected in view of the lower base pressure for an asymmetric cylinder (Sec. 3). For the symmetric cylinders, l_c^* at $r/d=0.5$ is considerably smaller than at $r/d=0.472$, which does not follow the trend of the l_c^* dependence on r/d. An explanation will be provided in Sec. 5.2.2. The stretched l_c^* for a larger r/d is accompanied by a smaller velocity gradient $\partial\bar{U}^*/\partial x$ or a slower recovery of velocity deficit $(1-\bar{U}^*)$, as corroborated by PIV data (not shown), suggesting again a higher base pressure. This stretch further implies that the freestream fluid is less rapidly entrained into the wake due to the increasing base pressure. The observation is consistent with the decreasing C_d, C'_d, and C'_L for a larger r/d (Figs. 2 and 3). For the same reason, the maximum magnitude of $\bar{V}^*$ (not shown) occurs further downstream with increasing r/d. However, at the same r/d this maximum occurs in closer proximity to the cylinder for the asymmetric cylinder than for the symmetric. Furthermore, the lateral spacing between the $\bar{V}^*$ peaks of opposite sign shrinks with increasing r/d, suggesting a narrowing wake, internally consistent with the observation on L_0^* (Fig. 7(*b*)) at $x/d=5$ and also with Tamura and Miyagi's [7] report.

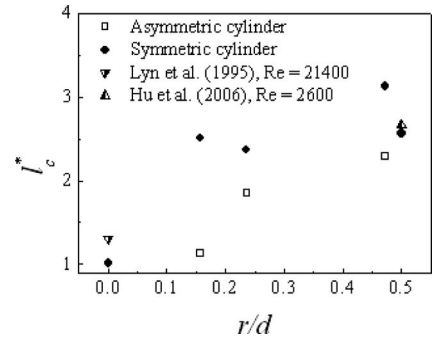

Fig. 10 Dependence of the wake recirculation region length, l_c^*, on corner radius at Re=2600

5.2.2 Fluctuating Velocities. The isocontours of u_{rms} (Fig. 11)

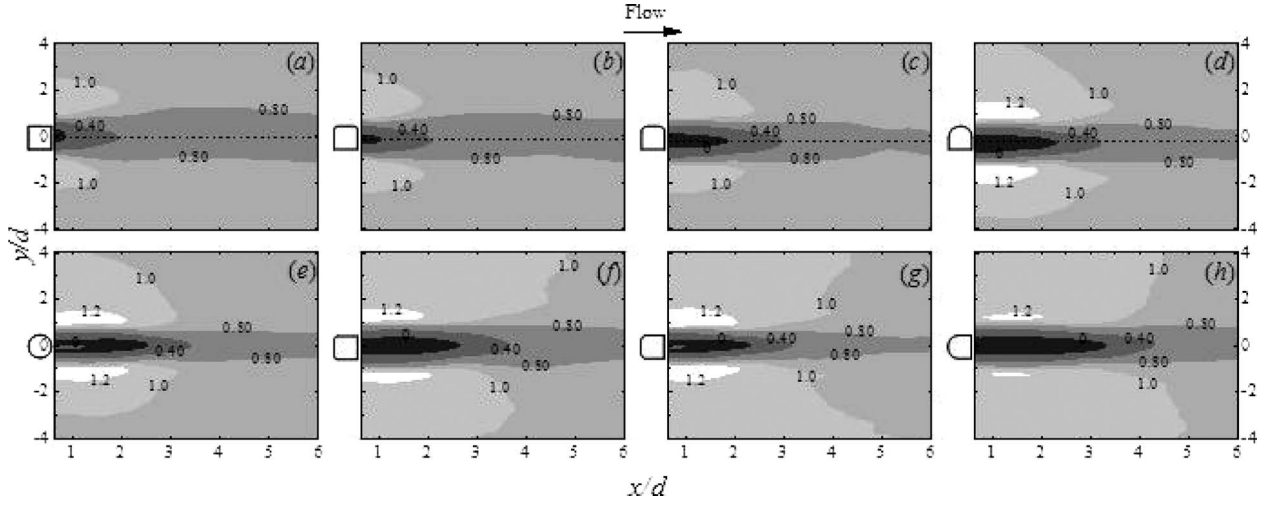

Fig. 9 PIV-measured isocontours of $\bar{U}^*$ at Re=2600. Asymmetric cylinders: (*b*) $r/d=0.157$, (*c*) 0.236, (*d*) 0.472. Symmetric cylinders: (*a*) $r/d=0$ (square cylinder), (*e*) 0.5 (circular cylinder), (*f*) 0.157, (*g*) 0.236, (*h*) 0.472. Cutoff value $\bar{U}^*=0$, contour increment=0.4. The dashed lines denote the wake centerline.

Downloaded 03 Jun 2010 to 171.66.16.158. Redistribution subject to ASME license or copyright; see http://www.asme.org/terms/Terms_Use.cfm

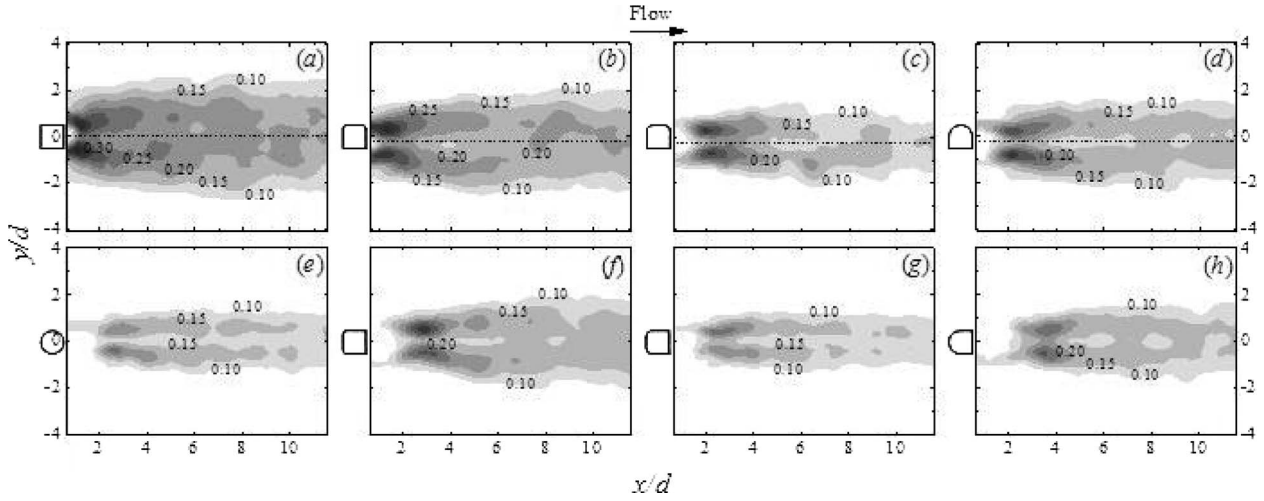

Fig. 11 PIV-measured isocontours of u^*_{rms} at Re=2600. Asymmetric cylinders: (*b*) r/d=0.157, (*c*) 0.236, (*d*) 0.472. Symmetric cylinders: (*a*) r/d=0 (square cylinder), (*e*) 0.5 (circular cylinder), (*f*) 0.157, (*g*) 0.236, (*h*) 0.472. Cutoff value u^*_{rms}=0.1, contour increment=0.05. The dashed lines denote the wake centerline.

and v_{rms} (Fig. 12) display approximate symmetry about the centerline. As r/d increases, the peaks in u_{rms} and v_{rms} occur further downstream from the cylinder. In general, the asymmetric cylinder corresponds to a larger u_{rms} or v_{rms} peak value than the symmetric, and the streamwise position of the maximum u_{rms} or v_{rms} also occurs nearer the cylinder, behaving similar to the maximum $\bar{V}^*$. This observation suggests that increasing the leading corner radius impairs vortex shedding, and this impairment is more significant if both leading corners of a cylinder are rounded instead of only one.

The distance from the cylinder center to the position of the maximum u_{rms} on the centerline is usually defined as the vortex formation length [31], l_f. Figure 13 presents the dependence of l_f on the cross section of the cylinders, extracted from the contours of u_{rms} along the shifted centerline. At r/d=0, l^*_f is 1.26, close to 1.3 and 1.1 measured using LDA by Lyn et al. [23] at Re =21,400 and Hu et al. [11] at Re=2600, respectively. At r/d =0.5, l^*_f is 2.81, showing a small departure from the report of Hu et al. [11] (2.66) at Re=2600. Apparently, l_f increases with r/d. An asymmetric cylinder produces a shorter l_f than the symmetric at the same r/d. This is reasonable since the base pressure, shear layer velocity, and l_f are strongly coupled [32], that is, an increased base pressure corresponds to a decreased shear layer velocity and force coefficients, C_d, C'_d, and C'_L, and a prolonged vortex formation length. Therefore, an increase in r/d corresponds to a stretched l_f.

The lateral spacing, l_{uy}, between the two peaks of the u_{rms} contours may provide a measure of the wake width [33,34]. This width (Fig. 14) is unique for each wake, in contrast with L_0, which depends on the downstream distance from the cylinder. As r/d increases, l_{uy} reduces for both asymmetric and symmetric cylinders, conforming to the observation from L_0 (Fig. 7(*b*)) and the lateral spacing between the two $\bar{V}^*$ peaks. The asymmetric cylinder corresponds to a larger l_{uy} and hence a wider wake than the symmetric at the same r/d.

It is pertinent to comment on the observation of the shorter l_c (Fig. 10) and l_f (Fig. 13) at r/d=0.5 (circular cylinder) than at r/d=0.472. The difference is probably linked to flow separation angle associated with a circular cylinder. In order to demonstrate

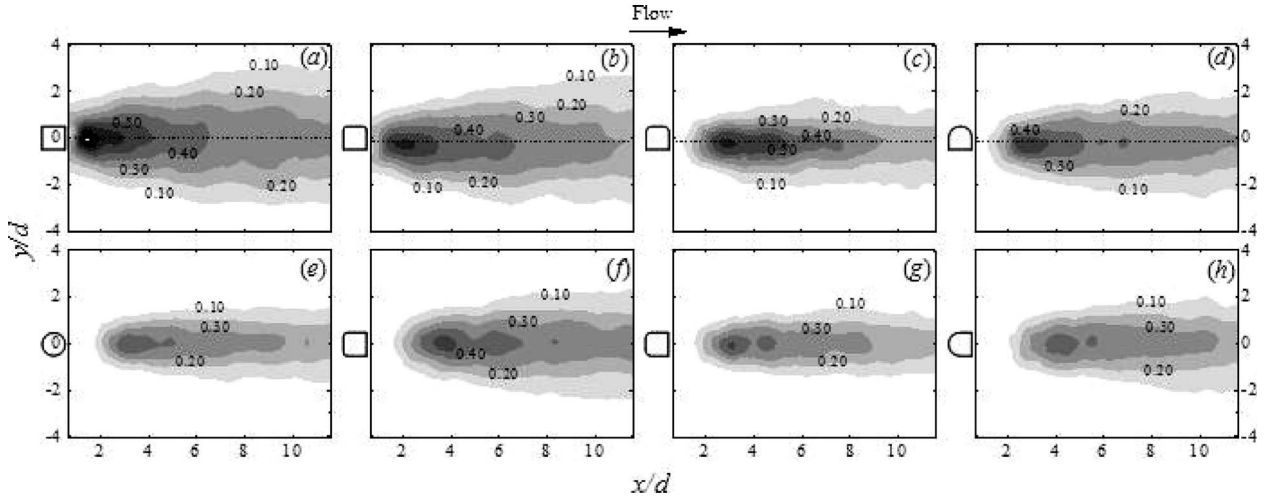

Fig. 12 PIV-measured isocontours of v^*_{rms} at Re=2600. Asymmetric cylinders: (*b*) r/d=0.157, (*c*) 0.236, (*d*) 0.472. Symmetric cylinders: (*a*) r/d=0 (square cylinder), (*e*) 0.5 (circular cylinder), (*f*) 0.157, (*g*) 0.236, (*h*) 0.472. Cutoff value v^*_{rms}=0.1, contour increment=0.1. The dashed lines denote the wake centerline.

Downloaded 03 Jun 2010 to 171.66.16.158. Redistribution subject to ASME license or copyright; see http://www.asme.org/terms/Terms_Use.cfm

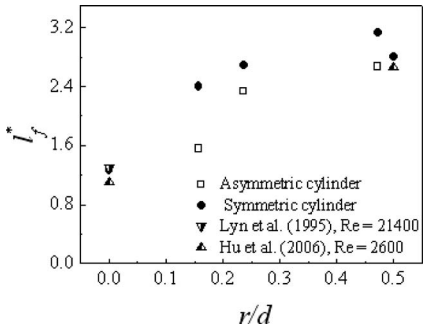

Fig. 13 Dependence of the vortex formation length, l_f^*, on corner radius at Re=2600

the point, flow visualization was conducted in a water tunnel with a square working section of 0.3 m(width)×0.6 m(height). Two cylinders were examined, i.e., a circular acrylic tube of 0.01 m in diameter and a square cylinder of a height of 0.01 m with rounded leading corners (r/d=0.472). Two pinholes of 0.8 mm in diameter were drilled symmetrically at 60 deg clockwise and counterclockwise, respectively, from the leading stagnation point at the midspan of each cylinder. Dye was injected through the pinholes to mark the flow. More details of the flow visualization experiment were provided by Hu et al. [11]. For clarity, the measurement was performed at Re=500, which was below the Re range (2600–8500) presented earlier. Nevertheless, the flow separation is not expected to differ greatly for this relatively small difference in Re [25]. Figure 15 presents typical photographs of flow visualization. For a square cylinder with rounded corners, flow separation tends to occur at the end of the leading corner arc for the present Re (Fig. 15(*a*)). As such, the angle (θ) of flow separation

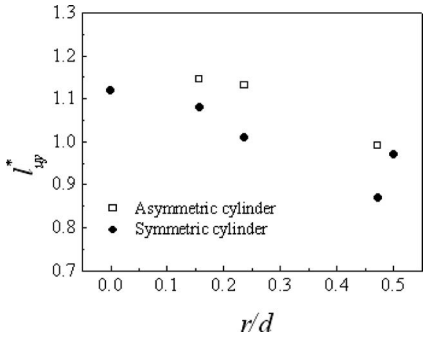

Fig. 14 Dependence of the lateral spacing, l_{uy}^*, between the two peaks of u_{rms}^* on corner radius at Re=2600

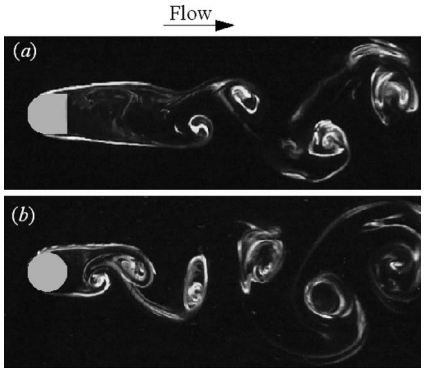

Fig. 15 Typical photographs of flow visualization behind (*a*) r/d=0.472 (symmetric) and (*b*) r/d=0.5 (circular cylinder); Re =500

from square cylinders with rounded leading corners increases progressively from 45 deg at r/d=0 to 87 deg at r/d=0.472 [35]. However, the photograph in Fig. 15(*b*) suggests that θ is about 80 deg at r/d=0.5, which is consistent with the data in literature [25]. This difference in θ implies a lower base pressure at r/d=0.5, as supported by the higher C_d at r/d=0.5 than at r/d=0.472 (Fig. 2). In addition, the sharp trailing corners (Fig. 15(*a*)) may also impede the separated shear layers to move toward the centerline, compared with a circular cylinder. Consequently, l_c and l_f are longer than their counterparts of the circular cylinder. For the same token, St (Fig. 4) and U_1 (Fig. 7(*a*)) are larger at r/d =0.472 than at r/d=0.5 and L_0 is smaller (Fig. 7(*b*)).

6 Conclusions

The characteristics of the cross-flow around asymmetric and symmetric square cylinders of different corner radii are experimentally studied at Re=2600–8500. The work leads to following conclusions.

1. The aerodynamic and near-wake characteristics for the bluff bodies of various cross sections are systematically measured and compared, including the mean and fluctuating velocities and various characteristic lengths such as the recirculation region length, the vortex formation length, and wake width, providing an experimental database for numerical modeling. It has been found that with increasing r/d, l_c expands, l_f elongates, St climbs, and C_{pb} rises; meanwhile, C_d, C_d', and C_L' drop, accompanied by shrinking Γ_0, U_1, $u_{\mathrm{rms,max}}$, $v_{\mathrm{rms,max}}$, L_0, and l_{uy}.
2. The behaviors of the shear layers separating from the two sides of a bluff body depend strongly on each other. As such a modification on one side of a square cylinder alters almost equally vortex shedding from both sides. Given the same leading corner radius, the asymmetry (i.e., one squared and one rounded leading corner) of a cylinder enhances C_d, C_L, C_d', and C_L' compared with its symmetric counterpart (with both leading corners rounded).
3. Asymmetric cross section of cylinders causes the wake centerline to shift laterally to the sharp corner side of the bluff body, and a larger corner radius corresponds to a larger shift. However, the wake remains approximately symmetric about the shifted centerline. Furthermore, an asymmetric cylinder produces a nonzero mean lift, which grows with increasing r/d, reaching about 0.4 at r/d=0.472.
4. C_d St is presently a constant, about 0.25, irrespective of the corner radius, the cross section of a bluff body, and Re =6000–8500.

Acknowledgment

Y.Z. wishes to acknowledge support given to him by the Research Grants Council of the Government of the HKSAR through Grant No. PolyU 5334/06E.

References

[1] Gad el Hak, M., 2000, *Flow Control: Passive, Active and Reactive Flow*, Cambridge University Press, Cambridge, England.
[2] Delany, N. K. and Sorensen, N. E. 1953 "Low-Speed Drag of Cylinder of Various Shapes," NACA Technical Report No. TN-3038.
[3] Naudascher, E., Weask, J. R., and Fey, B., 1981, "Exploratory Study on Damping of Galloping Vibrations," J. Wind. Eng. Ind. Aerodyn., **8**, pp. 211–222.
[4] Kwok, K. C. S., Wilhelm, P. A., and Wilkie, B. G., 1988, "Effect of Edge Configuration on Wind-Induced Response of a Tall Building," Eng. Struct., **10**, pp. 135–140.
[5] Okamoto, S., and Uemura, N., 1991, "Effect of Rounding Side-Corners on Aerodynamic Forces and Turbulent Wake of a Cube Placed on a Ground Plane," Exp. Fluids, **11**, pp. 58–64.
[6] Tamura, T., Miyagi, T., and Kitagishi, T., 1998, "Numerical Prediction of Unsteady Pressures on a Square Cylinder With Various Corner Shapes," J. Wind. Eng. Ind. Aerodyn., **74–76**, pp. 531–542.
[7] Tamura, T., and Miyagi, T., 1999, "The Effect of Turbulence on Aerodynamic Forces on a Square Cylinder With Various Corner Shapes," J. Wind. Eng. Ind.

Downloaded 03 Jun 2010 to 171.66.16.158. Redistribution subject to ASME license or copyright; see http://www.asme.org/terms/Terms_Use.cfm

Aerodyn., **83**, pp. 135–145.
[8] Zheng, W., and Dalton, C., 1999, "Numerical Prediction of Force on Rectangular Cylinders in Oscillating Viscous Flow," J. Fluids Struct., **13**, pp. 225–249.
[9] Bearman, P. W., Graham, J. M. R., Obasaju, E. D., and Drossopoulos, G. M., 1984, "The Influence of Corner Radius on the Forces Experienced by Cylindrical Bluff Bodies in Oscillatory Flow," Appl. Ocean. Res., **6**, pp. 83–89.
[10] Dalton, C., and Zheng, W., 2003, "Numerical Solutions of a Viscous Uniform Approach Flow Past Square and Diamond Cylinders," J. Fluids Struct., **18**, pp. 455–565.
[11] Hu, J. C., Zhou, Y., and Dalton, C., 2006, "Effects of the Corner Radius on the Near Wake of a Square Prism," Exp. Fluids, **40**, pp. 106–118.
[12] Huang, J. F., Zhou, Y., and Zhou, T. M., 2006, "Three-Dimensional Wake Structure Measurement Using a Modified PIV Technique," Exp. Fluids, **40**, pp. 884–896.
[13] Norberg, C., 1993, "Flow Around Rectangular Cylinders: Pressure Forces and Wake Frequencies," J. Wind. Eng. Ind. Aerodyn., **49**, pp. 187–196.
[14] Bokaian, A., and Geoola, F., 1984, "Wake-Induced Galloping of Two Interfering Circular Cylinders," J. Fluid Mech., **146**, pp. 383–415.
[15] Igarashi, T., 1981, "Characteristics of the Flow Around Two Circular Cylinders Arranged in Tandem," Bull. JSME, **24**(188), pp. 323–331.
[16] Alam, M. M., 2004 "Aerodynamics Characteristics and Suppression of Fluid Forces Acting on Two Bluff Bodies in Various Arrangements and Multistable Flow Detection by Wavelets," Ph.D. thesis, Kitami Institute of Technology, Japan.
[17] West, G. S., and Apelt, C. J., 1997, "Fluctuating Lift and Drag Forces on Finite Lengths of a Circular Cylinder in the Subcritical Reynolds Number Range," J. Fluids Struct., **11**, pp. 135–158.
[18] Mittal, R., and Balanchandar, S., 1995, "Effect of Three-Dimensionality on the Lift and Drag of Nominally Two-Dimensional Cylinders," Phys. Fluids, **7**, pp. 1841–1865.
[19] Schewe, G., 1983, "On the Force Fluctuations Acting on a Circular Cylinder in Cross-Flow From Subcritical up to Transcritical Reynolds Numbers," J. Fluid Mech., **133**, pp. 265–285.
[20] Surry, D., 1972, "Some Effects of Intense Turbulent on the Aerodynamic of a Circular Cylinder at Subcritical Reynolds Number," J. Fluid Mech., **52**, pp. 543–563.
[21] Laneville, A., Gartshore, I. S., and Parkinson, G. V., 1975 "An Explanation of Some Effects of Turbulence on Bluff Bodies," Proceedings of the Fourth International Conference Wind Effects on Buildings and Structure, Heathrow, England, K75-363, pp. 333–341.
[22] Roshko, A. 1954, "On the Drag and Shedding Frequency of Two-Dimensional Bluff Bodies," NACA Technical Rerport No. TN-3169.
[23] Lyn, D. A., Einav, S., Rodi, W., and Park, J. H., 1995, "A Laser-Doppler Velocimetry Study of Ensemble-Averaged Characteristics of the Turbulent Near Wake of a Square Cylinder," J. Fluid Mech., **304**, pp. 285–319.
[24] Zhou, Y., and Antonia, R. A., 1994, "Effect of Initial Conditions on Structures in a Turbulent Near-Wake," AIAA J., **32**, pp. 1207–1213.
[25] Zdravkovich, M. M., 1997, *Flow Around Circular Cylinders* (Fundamentals Vol. 1), Oxford University Press, New York.
[26] Schewe, G., and Larsen, A., 1998, "Reynolds Number Effects in the Flow Around a Bluff Bridge Deck Cross Section," J. Wind. Eng. Ind. Aerodyn., **74–76**, pp. 829–838.
[27] Ahlborn, B., Seto, L., and Noack, R., 2002, "On Drag, Strouhal Number and Vortex-Street Structure," Fluid Dyn. Res., **30**, pp. 379–399.
[28] Bearman, P. W., 1965, "Investigation of the Flow Behind a Two-Dimensional Model With a Blunt Trailing Edge and Fitted With Splitter Plates," J. Fluid Mech., **31**, pp. 559–563.
[29] Griffin, O. M., 1981, "Universal Similarity in the Wakes of Stationary and Vibrating Bluff Structures," ASME J. Fluids Eng., **103**, pp. 52–58.
[30] Konstantinidis, E., Balabani, S., and Yianneskis, M., 2003, "The Effect of Flow Perturbations on the Near Wake Characteristics of a Circular Cylinder," J. Fluids Struct., **18**, pp. 367–386.
[31] Bloor, S. M., 1964, "The Transition to Turbulence in the Wake of a Circular Cylinder," J. Fluid Mech., **19**, pp. 290–309.
[32] Anderson, E. A., and Szewczyk, A. A., 1996, "A Look at a Universal Parameter for 2D and 3D Bluff Body Flows," J. Fluids Struct., **10**, pp. 543–553.
[33] Griffin, O. M., and Ramberg, S. E., 1974, "The Vortex Street Wakes of a Vibrating Cylinders," J. Fluid Mech., **66**, pp. 553–576.
[34] Ramberg, S. E., 1983, "The Effects of Yaw and Finite Length Upon the Vortex Wakes of Stationary and Vibrating Circular Cylinders," J. Fluid Mech., **128**, pp. 81–107.
[35] Okajima, A., 1982, "Strouhal Numbers of Rectangular Cylinders," J. Fluid Mech., **123**, pp. 379–398.

Downloaded 03 Jun 2010 to 171.66.16.158. Redistribution subject to ASME license or copyright; see http://www.asme.org/terms/Terms_Use.cfm

Assessment of Tandem Venturi on Enhancement of Cavitational Chemical Reaction

Hoseyn Sayyaadi
Faculty of Mechanical Engineering,
K. N. Toosi University of Technology,
P.O. Box 19395-1999,
No. 15-19 Pardis Street,
Mollasadra Avenue,
Vanak Square,
Tehran 1999143344, Iran
e-mail: sayyaadi@kntu.ac.ir
e-mail: hoseynsayyaadi@gmail.com

The collapsing phenomenon of cavitation bubbles generates extremely high local pressures and temperatures that can be utilized for the chemical oxidation process. This process is carried out in cavitation reactors. A Venturi tube is one of the most common forms of hydrodynamic cavitation reactors, which is suitable for industrial scale applications. In this work, the hydraulic performance and efficiency in chemical reaction of a new form of hydrodynamic cavitation reactors, which is called "tandem Venturi," were studied and compared with the conventional type of the single Venturi. The tandem Venturi is used for enhancement of the chemical reaction of hydrodynamic cavitating flow. The reaction enhancement is useful especially for the reaction of aqueous solutions not containing volatile organic compounds (VOCs). The operating pressure, inlet pressure, flow rate, and consequently the cavitation number were controlled and systematically varied for both single and tandem Venturis. Moreover, a specified amount of H_2O_2 was injected into the flow as required. The effects of operating pressure and the cavitation number on cavitating flow characteristics for single and tandem Venturis were experimentally observed and the results were compared. In addition, the performance of the tandem-Venturi reactor for degradation of non-VOC contaminants (2-chlorophenol) was studied. Its performance was compared with the performance of a conventional Venturi reactor. Two different categories were conducted for the experiments. In the first category, the effect of the net cavitating flow on degradation of non-VOC for the single and tandem Venturis was compared. In the second category, the effect of H_2O_2 injection into the cavitating flow on degradation of non-VOC ("cavitation-oxidation" process) was studied. The performance of the single and tandem Venturis for the cavitation-oxidation process was compared. Further investigation was performed to assess the advantage of utilizing the tandem Venturi from the viewpoint of efficiency of the oxidation process. The results of the energy efficiency were compared with the corresponding efficiency of the single Venturi. Finally, the relationship between the main parameters of cavitation reaction flow with the chemical performance was discussed. [DOI: 10.1115/1.3026731]

Keywords: water treatment, cavitation reaction, tandem Venturi, extent of the cavitation zone, cavitation-oxidation, non-VOC

1 Introduction

Cavitation as a source of energy input for chemical processing is increasingly being studied due to its capability of generating high local pressures and temperatures required for oxidation processing of chemicals. This oxidation capability of cavitation could be utilized in cavitation reactors. These reactors might be used in water treatment plants or can be used for chemical reaction of aqueous solutions. The possibility of exploitation stems from the fact that millions of cavities grow and collapse simultaneously at different locations. Indeed, the term cavitation refers to formation, growth, and collapse of small gas bubbles. When flow pressure reaches a specific critical value, rupture occurs and these nuclei grow explosively. When the flow enters a region in which the bulk liquid pressure is sufficiently high, the cavitating bubbles will collapse drastically. This phenomenon takes place very rapidly and almost adiabatically, and subsequently high temperatures and pressures (hot spots) are generated at the final stage of collapsing. Utilizing the destructive power of cavitation in water treatment and chemical reaction enhancement has been studied by many researchers over the years [1–12]. Although ultrasonic reactors are the most popular means of generating cavitation in the laboratory scale, these reactors suffer from several shortcomings on industrial scale applications [6,8,10]. Over the past few years, hydrodynamic cavitation has been explored as an alternative for acoustic cavitation. In hydrodynamic cavitation, cavities are generated by the flow of liquid under controlled conditions through simple Venturi or orifice geometries. When the flow pressure drops to the vapor pressure, cavitation forms and subsequently the cavities are collapsed with recovery of pressure downstream of the mechanical constriction. It should be pointed out that cavitation reactors, especially the hydrodynamic type, have difficulty in non-VOC chemical reactions. This difficulty comes from the fact that unlike VOC contaminants, the reaction site of non-VOC chemicals is in the bulk liquid or in a liquid interfacial shell around the bubble [1,2,13]. The reaction site of weak solutions is in the bulk liquid. However, for concentrated solutions, the reaction site is in the interfacial shell around the bubbles. Therefore, in this case, the treatment rate depends on migration of hydroxyl radicals into the bulk liquid [1,2,13,14]. On the other hand, existence of these radicals in the bulk liquid depends on the relative lifetime of radicals ($\approx 10^{-6}$ s [15]) compared with the collapsing time of bubbles (4×10^{-7}–4×10^{-5} s [14]). Therefore, it is required to augment the violence of cavitation and/or increase the number of cavitation events in order to increase the number of generated hydroxyl radicals. More generated hydroxyl radicals can result in significant cavitational chemical reaction effect. The tandem Venturi as an

Contributed by the Fluids Engineering Division of ASME for publication in the JOURNAL OF FLUIDS ENGINEERING. Manuscript received January 28, 2008; final manuscript received September 13, 2008; published online November 26, 2008. Assoc. Editor: Timothy J. O'Hern.

 Copyright © 2009 by ASME

Downloaded 03 Jun 2010 to 171.66.16.158. Redistribution subject to ASME license or copyright; see http://www.asme.org/terms/Terms_Use.cfm

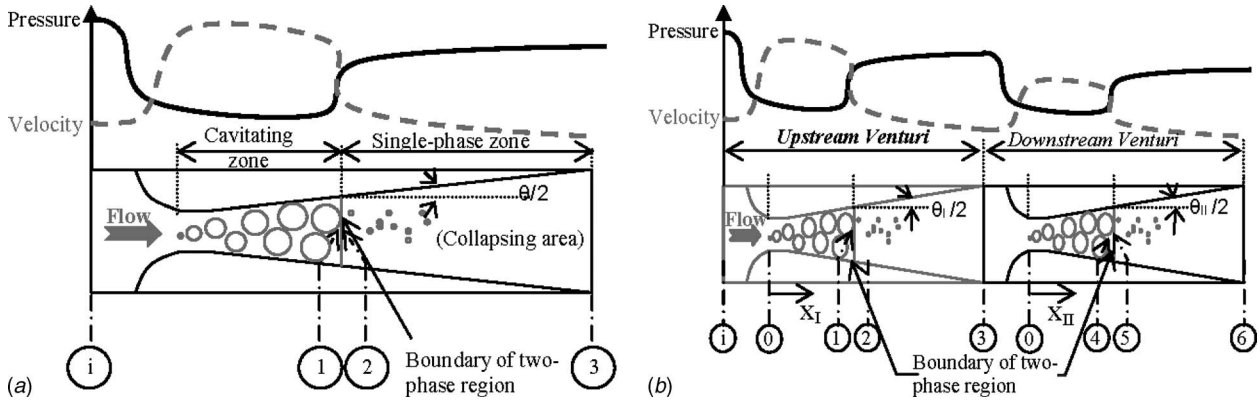

Fig. 1 Schematic of the cavitating flow in the (*a*) single Venturi and (*b*) tandem-Venturi (conditions that are marked with numbers are explained in the Nomenclature)

option to observe this effect is examined in the following work. The new type of a reactor has been constructed by installation of two conventional Venturis in series. The single collapsing region of a conventional Venturi is replaced with two collapsing regions in this new type of the Venturi. In addition, the number of cavitation events is increased for the tandem Venturi. Hence, one may expect a higher cavitation reaction effect for the tandem Venturi compared with the single Venturi. Figure 1 schematically shows the cavitation flow in the tandem Venturi. The idea of using Venturis in series is developed here for the augmentation of the reaction effect for a given water flow rate. The series configuration is considered here instead of other possible arrangement such as parallel Venturis. For a given flow rate of water to be treated, in the case of parallel Venturis, flow is divided between two single Venturis unlike the case of Venturis in series, which the entire flow rate passes through both Venturis and therefore experiences two regions of cavitation. In the case of parallel Venturis, only a half part of the flow that must be treated passes through each single Venturi with only one cavitation region. Other configurations such as three Venturis in series are not considered in this research. Nevertheless, the author believes that for the case of Venturis in series, since the collapsing of cavitation in the last Venturi is milder than the upstream Venturi [1], using more than two Venturis in series might not be an economical idea due to the higher pumping cost (system pressure drop increases as the number of Venturis in series is increased). In other words, the tandem Venturi is developed as a way to generate higher numbers of cavitation events and hence a higher generation rate of the hydroxyl radical. The performance of the single and tandem Venturis for degradation of a 2-chlorophenol solution (representative of non-VOCs) and the efficiency of reaction have been studied and compared. Furthermore, the effect of different experimental parameters on cavitation flow regime and the extent of the cavitation zone have been observed and the results have been compared for both Venturis.

1.1 Chemical Reaction Agents. The cavitation reaction effect is defined as the possibility that components react by a mechanism in which reactive intermediates are directly generated by the cavitation events. Such intermediates should be *radicals* or *radical ions*. Then, these radicals or radical ions contribute to subsequent chemical reaction in the gas-vapor phase, liquid interfacial shell, or bulk liquid depending on the volatility and concentration of the chemicals [5,14].

Regardless of solute reaction zones, the vapor reaction always takes place in the gas phase. This reaction is *pyrolysis* dissociation of the water molecules to a hydrogen atom ($\dot{H}$) and a hydroxyl radical ($\dot{OH}$). The pyrolysis reaction in the gas-vapor phase is

$$H_2O \leftrightarrow \dot{OH} + \dot{H} \tag{1}$$

Most of the subsequent reactions are the result of oxidation of solute molecules with hydroxyl radicals. Since the lifetime of this radical is short, the subsequent reaction depends on the collapsing time of the bubble compared with the lifetime of the radical.

The lifetime of this radical is estimated to be approximately 10^{-6} s [15]. If the relative collapsing time of bubbles is less than 10^{-6} s, the generated radicals have enough time to migrate from the gas-vapor phase of the collapsing bubble to the thin liquid shell around the bubble, or to the bulk liquid to allow a chemical reaction. These radicals react with solute molecules in the liquid phase or undergo mutual recombination to give other species such as water or hydrogen peroxide (H_2O_2). If the collapsing times of bubbles are relatively larger than the lifetimes of radical, the radicals do not have enough time to escape from the collapsing bubble into the liquid phase. It can be predicted that for the case in which bubbles have longer collapsing time, a lower chemical reaction effect might be observed.

2 Definition of Terms

Cavitation number. The dimensionless parameter that characterizes cavitation flow regime is cavitation number, σ,

$$\sigma = \frac{P_b - P_v}{(1/2)\rho_l v_0^2} \tag{2}$$

where P_b is the Venturi backpressure. The value of P_b is equal to P_3 and P_6 for upstream and downstream Venturis of tandem arrangement, respectively (see Fig. 1(*b*)). Therefore, the cavitation number for each upstream or downstream Venturi (σ_{I} and σ_{II}) can be defined according to Eq. (2) with corresponding values of P_b and v_0 ($v_{0\mathrm{I}}$ and $v_{0\mathrm{II}}$) separately. $v_{0\mathrm{I}}$ and $v_{0\mathrm{II}}$ are the throat velocities in upstream and downstream Venturis, respectively (Fig. 1(*b*)).

3 Experimental Apparatus

A schematic of the experimental setup and geometric specifications of the single Venturi and tandem Venturi are provided in Figs. 2(*a*)–2(*c*), respectively. The chemical reaction yield of 2-chlorophenol is evaluated based on the decomposition of reactant using gas chromatography. The system with a total capacity of 20 l (including pipeline capacity) is constructed from stainless steel in order to prevent undesirable chemical reaction. Flow is recirculated using an EBARA in-line pump model LPS 6.75A (stainless steel). Flow rate was measured using a vortex type flow meter. Pressure and temperature were measured at specified locations, which are shown in Fig. 2(*a*).

The Venturi inlet pressure and flow rate can be controlled by changing the rotation speed of the pump using an inverter. Subsequently the cavitation number will be controlled. The solution

Downloaded 03 Jun 2010 to 171.66.16.158. Redistribution subject to ASME license or copyright; see http://www.asme.org/terms/Terms_Use.cfm

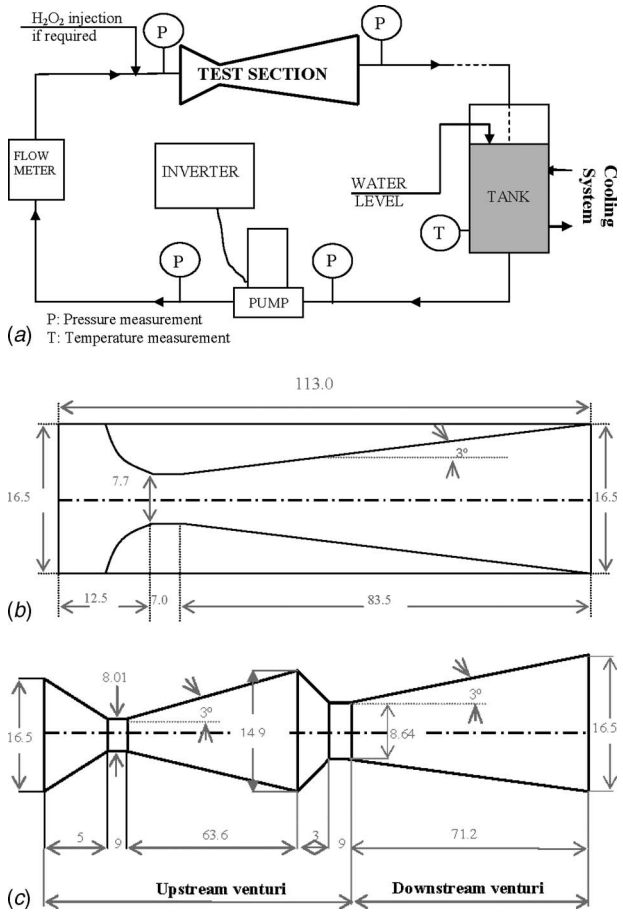

Fig. 2 (*a*) Schematics of the experimental setup, (*b*) geometrical specification of the single Venturi, and (*c*) geometrical specification of the tandem Venturi (all dimensions are in millimeters)

temperature is kept constant in order to control the rate of reaction. A cooling system integrated with a reservoir is utilized to control the temperature of the solution. This cooling system is illustrated in Fig. 2(*a*). Four capillary tubes (0.71 mm inside diameter) are designed and mounted upstream of the test section. These capillary tubes inject the required amount of H_2O_2 in flow.

3.1 Measurement Techniques and Procedure. 2-chlorophenol in crystalline form was used. This crystalline form was mixed with distilled water prior to the experiment. The dissolved oxygen content of the solution was measured using a dissolved oxygen (DO) meter prior to the experiment. A degasser unit was used to maintain the oxygen content of water. The concentration of 2-chlorophenol was measured using a gas chromatograph, which was calibrated against known concentration of 2-chlorophenol. During the experiment, the samples were withdrawn from the reservoir. Particulate contaminants were removed from the samples through filtering. Finally, the samples were injected into the gas chromatograph column.

3.2 Uncertainty Estimates. The estimated uncertainties in the measured quantities are flow rates of ± 1 l/min, pressure of ± 10 kPa, concentration of ± 0.1 mg/l, temperature of ± 0.1°C, and dissolved oxygen content of solution of ± 0.1 ppm.

Based on the above-mentioned estimated values, the uncertainties of nondimensional concentration, degradation efficiency (Eq. (10)), and cavitation number (Eq. (2)) can be evaluated as $\pm 0.95\%$, ± 1.4 mg/kJ, and $\pm 3.9\%$, respectively.

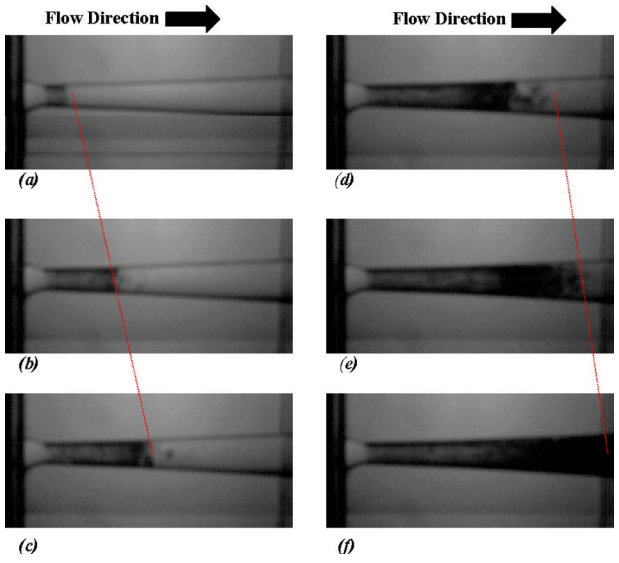

Fig. 3 Cavitation flow regime in the single Venturi under various experimental conditions and 100 kPa operating pressure (experimental conditions are summarized in Table 1)

4 Results and Discussions

4.1 Comparison of Cavitation Flow Regimes. In this section, various cavitation flow regimes under the effects of different experimental conditions are explained, and subsequently, the behavior of single and tandem Venturis is compared. Furthermore, the effect of inlet pressures, flow rates, and cavitation numbers (as flow parameters) on cavitation flow regime, especially on the extent of the cavitation zone (number of cavitation events), is reviewed. The cavitation flow is observed using KODAK SCR-500 high speed charge coupled device (CCD) camera with 500 frames/s speed and 1/20,000 s exposure time.

4.1.1 Cavitation Flow Regimes in Single Venturi. Figure 3 shows the effect of inlet pressure when the total backpressure is kept constant at 100 kPa. The experimental conditions are listed in Table 1 for six different cases. As shown in Fig. 3, the cavitation zone extends further into the single Venturi in proceeding from cases (a) to (f), where both the flow rate and the inlet pressure increase. The increasing flow rate and inlet pressure lead to the decreasing cavitation number. In other words, the extent of the cavitation zone is larger for smaller cavitation numbers.

4.1.2 Cavitation Flow Regimes in Tandem Venturi. Figure 4 shows the cavitation flow regime for tandem arrangement at various flow rates and various inlet conditions. The experimental conditions are listed in Table 2. Figure 4 indicates that when the flow rate increases, the extent of the cavitation zone, and the cavitation number in the upstream Venturi, remained constant. The result shows that the variations in the extent of the cavitation zone with the variation in the cavitation number for the downstream Venturi

Table 1 General experimental conditions of the single Venturi (initial oxygen content=8.2 ppm and temperature=24°C)

Case	Flow rate (l/min)	Venturi inlet pressure (kPa)	Venturi outlet pressure (kPa)	σ
a	120	120	100	0.83
b	135	130	100	0.77
c	150	160	100	0.63
d	165	180	100	0.56
e	180	210	100	0.48
f	210	280	100	0.36

Downloaded 03 Jun 2010 to 171.66.16.158. Redistribution subject to ASME license or copyright; see http://www.asme.org/terms/Terms_Use.cfm

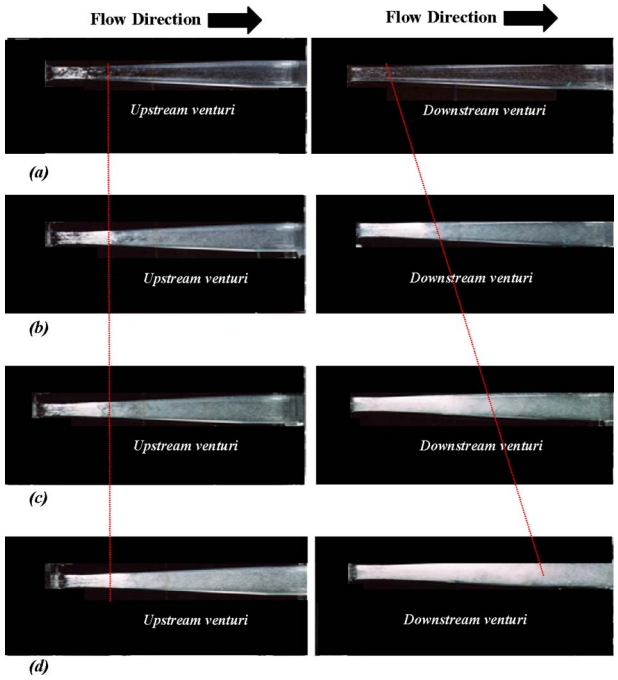

Fig. 4 Cavitation flow regime in the tandem Venturi under various experimental conditions and 100 kPa operating pressure (experimental conditions are summarized in Table 2)

are similar to those observed in the single Venturi. The extent of the cavitation zone is related to the ratio of the inlet pressure to the backpressure (cavitation number). This ratio remains constant for various inlet pressures for the upstream Venturi. Therefore, when the inlet pressure increases, the outlet pressure of the upstream Venturi increases proportionally in a way that the ratio of the inlet to outlet pressure remains unchanged. The aforementioned statement can be simply explained according to the following hydraulics evaluations.

4.1.2.1 Continuity equation. The expressions for the continuity equation between the Venturi inlets and throats (sections "in" and "0_I" of upstream Venturi and sections "3" and "0_{II}" of the downstream Venturi, as shown in Fig. 1(*b*)) for the upstream and downstream are as follows.

For upstream Venturi,

$$\rho v_{\text{in}} A_{\text{in}} = \rho v_{0\text{I}} A_{0\text{I}} \tag{3}$$

For downstream Venturi,

$$\rho_{l_3} v_3 A_{i3} = \rho v_{0\text{II}} A_{0\text{II}} \tag{4}$$

4.1.2.2 Momentum equation. The expressions for the momentum equation between the Venturi inlets and throats for the upstream and downstream Venturis can be simplified to the statement of the Bernoulli equation as follows.

For upstream Venturi,

$$p_{\text{in}} + \frac{\rho_l}{2} v_{\text{in}}^2 = p_v + \frac{\rho_l}{2} v_{0\text{I}}^2 \tag{5}$$

For downstream Venturi,

$$p_3 + \frac{\rho_l}{2} v_3^2 = p_v + \frac{\rho_l}{2} v_{0\text{II}}^2 \tag{6}$$

By elimination of the common terms in Eqs. (3)–(6), the following expression is obtained for the choked velocities (the velocity in which the cavitation forms and the flow becomes choked) of the upstream and downstream Venturis:

$$v_{0\text{I}} = \left\{ \frac{2}{\rho_l} \frac{p_{\text{in}} - p_v}{(1 - \beta_{\text{in}}^2)} \right\}^{1/2} \tag{7a}$$

$$v_{0\text{II}} = \left\{ \frac{2}{\rho_l} \frac{p_3 - p_v}{(1 - \beta_{\text{inII}}^2)} \right\}^{1/2} \tag{7b}$$

in which β_{inI} and β_{inII} are the ratios of the throat cross-sectional area to the inlet cross-sectional area for the upstream and downstream Venturis, respectively.

The continuity equation between throats of the upstream and downstream Venturis (sections 0_I and 0_{II}) is

$$\rho_l v_{0\text{I}} A_{0\text{I}} = \rho_l v_{0\text{II}} A_{0\text{II}} \tag{8}$$

Substitution of $v_{0\text{II}}$ from Eq. (7*b*) into Eq. (8) yields the following expression:

$$\frac{p_3 - p_v}{\rho_l / 2 v_{0\text{I}}^2} = (1 - \beta_{\text{inII}}^2) \left(\frac{A_{0\text{II}}}{A_{0\text{I}}} \right)^2 = \text{const} \tag{9}$$

The right-hand side of Eq. (9) is a constant value for a specific geometry of the tandem Venturi (all parameters are geometrical terms). In addition, the left-hand side of Eq. (9) is the definition of the cavitation number in the upstream Venturi (σ_I) based on Eq. (2). Hence, the cavitation number and consequently the extent of the cavitation zone (cavitation size) in the upstream Venturi remain constant for the various inlet pressures or the various flow rates for the tandem arrangement.

It should be noted that Eqs. (3)–(6), (7*a*), (7*b*), (8), and (9) are developed in order to simply interpret why the extent of cavitation observed in the downstream Venturi is fixed. A more sophisticated analysis would solve equations of coupled bubble dynamics and cavitating flow to predict the exact behavior of the cavitating flow [4,7]. Indeed, the extent of the cavitation zone for each Venturi oscillates over a small range due to the unsteady behavior of the cavitating flow [1]. However, it was found that the model that is presented here could predict the average of the extent of the cavitation zone with reasonable accuracy [1].

4.2 The Comparison of the Operation of Various Venturis on Cavitation Reaction. The effect of various types of Venturis on decomposition of non-VOC solutions is investigated in this study. It should be mentioned that the cavitation reaction is generally affected by several parameters including the initial size of bubbles, the content of dissolved gas, and the solution temperature. The initial size of bubbles can affect the intensity of collapsing, the content of dissolved gas can affect the intensity of cavi-

Table 2 General experimental conditions of the tandem Venturi (initial oxygen content =8.1 ppm and temperature=24°C)

Case	Flow rate (l/min)	Upstream Venturi inlet pressure (kPa)	Upstream Venturi outlet pressure (kPa)	Downstream Venturi outlet pressure (kPa)	σ_I	σ_{II}
a	160	156	120	100	0.80	0.83
b	190	200	160	120	0.80	0.75
c	210	260	200	120	0.80	0.60
d	250	350	280	120	0.80	0.42

Downloaded 03 Jun 2010 to 171.66.16.158. Redistribution subject to ASME license or copyright; see http://www.asme.org/terms/Terms_Use.cfm

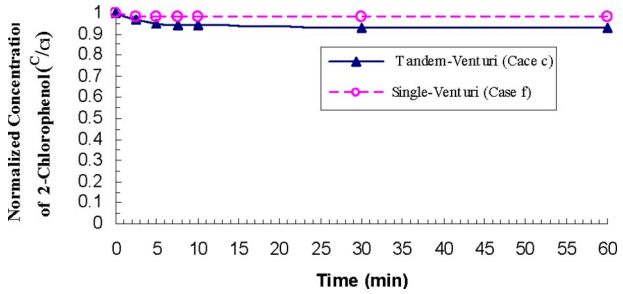

Fig. 5 Comparison of the 2-chlorophenol decomposition effect by cavitating flow in the tandem Venturi and single Venturi (operating pressure=100 kPa, initial concentration of 2-chlorophenol=14 ppm, flow rate=210 l/min, and *p*H≈8.10; other experimental conditions are indicated in Tables 1 and 2)

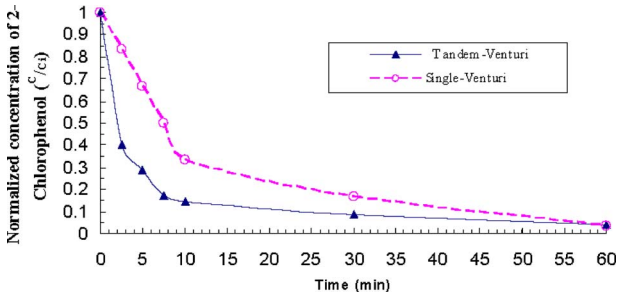

Fig. 6 Comparison of the 2-chlorophenol decomposition effect by cavitation-oxidation process in the tandem Venturi and single Venturi (operating pressure=100 kPa, initial concentration of 2-chlorophenol=15 ppm, flow rate=210 l/min, injected amount of H_2O_2=1000 ppm, and *p*H≈8.07; other experimental conditions are indicated in Tables 1 and 2)

tation, and solution temperature affects the chemical reaction rate. However, investigation of the effect of these parameters is beyond the scope of this paper. Therefore, these parameters are maintained at relatively similar values for experimental investigation in both the tandem- and single-Venturi cases. The content of dissolved gas, which is measured, using the DO meter, at the early stage of the experiment is almost the same (about 8 ppm) for both cases. The temperature is kept almost constant during each experiment as well. There is no attempt to measure the initial nuclei size in this work, and it is assumed that the average sizes of the nuclei for both cases are almost the same. Therefore, it can be assumed that the results are only affected by the type of the Venturi reactor used.

Figure 5 compares the effect of cavitation reaction for the tandem-Venturi reactor with the single Venturi for dissociation of a 2-chlorophenol aqueous solution. Figure 5 shows that the reaction rates for both cases are slow; however, the tandem-Venturi reaction rate is a little higher than for the single Venturi. It is reported that for the non-VOC contaminants, the reaction zone is outside the collapsing bubble [1,2,13]. Therefore, there is usually no significant migration of hydroxyl radicals into the bulk liquid due to the relatively longer collapsing time of bubbles to the lifetime of hydroxyl radicals (10^{-6} s) [7,14]. The main role of the tandem Venturi is to increase the number of cavitation events and to increase the collapsing regions from one in the single Venturi to two (see Fig. 1). Increasing the number of cavitation events has only a small effect on increasing the reaction rate of the tandem Venturi compared with the single Venturi as is clear from Fig. 5. Therefore, implementation of the new form of the Venturi does not successfully decompose the non-VOC solution. It is required to find a method to shorten the collapsing time of bubbles for augmentation of the non-VOC reaction by hydrodynamic cavitation or to increase the lifetime of hydroxyl radicals (to migrate into the bulk liquid). In other words, utilizing the tandem Venturi does not lead to any change in the collapsing time of bubbles or the lifetime of hydroxyl radicals. It only affects the number of cavitation events and collapsing regions. To shorten the collapsing time of bubbles, the cavitation number can be decreased. A smaller value for the cavitation number leads to the following events.

1. A higher generation rate of hydroxyl radicals because of the higher temperature of gas phase inside the bubbles at the final stage of the collapsing process.
2. More violent collapsing permits migration of some hydroxyl radicals at low cavitation number due to shorter collapsing time.

Since utilizing the cavitation flow at low cavitation numbers requires very high flow rate and hence very high pumping energy [1], the implementation of cavitation alone in single and tandem Venturis is not an efficient method for treating non-VOC solutions. This leads to a lower energy efficiency of the reaction [1]. Therefore, no advantage from utilizing of tandem Venturi will be obtained in this regard. The implementation of other hydrodynamic cavitation reactor such as submerged orifice [5] confirms the very slow decomposition rate of non-VOC (P-NitroPhenol (PNP) solution [5]). It is reported [5] that the complete decomposition needs very long experiment times, on the order of 8–10 hours at very low cavitation number with high pumping energy. This shortcoming of hydrodynamic cavitation requires an alternative method with higher efficiency, which provides a higher decomposition rate in order to save time and energy. Cavitation in the presence of oxidant agents might be an option for the non-VOC reaction.

4.3 The Comparison of the Operation of Various Venturis on Cavitation-Oxidation Reaction. Chemical reaction of non-VOC solutes is related to the release of hydroxyl radical (oxidizer agent) into the liquid media. One alternative for increasing the number of generated hydroxyls is to inject hydrogen peroxide into the cavitating flow. Therefore, the destructive power of cavitation can be used for dissociation of H_2O_2 molecules into hydroxyl radicals. Then these radicals migrate into the bulk liquid and oxidize the molecules of contaminants. In this section, the tandem Venturi is compared with the single Venturi from the viewpoint of 2-chlorophenol (non-VOC) decomposition in a cavitation-oxidation process.

Figure 6 shows a comparison between performance of the tandem Venturi and single Venturi on cavitation-oxidation decomposition of 2-chlorophenol at 100 kPa operating pressure. The flow rate is 210 l/min and 1000 ppm of H_2O_2 is injected. Other experimental conditions are listed in Tables 1 and 2 for the single and tandem Venturis, respectively. It is shown in Fig. 6 that there are some advantages of the tandem Venturi for decomposition of non-VOC aqueous solution over the single Venturi in the cavitation-oxidation process. The tandem Venturi increases the number of cavitation events and the number of collapsing regions in the cavitation-oxidation process. These two effects accelerate the rate of reaction by the tandem Venturi (Fig. 6).

Figure 7 shows the effect of magnitude of H_2O_2 injection on cavitation flow regime. It is observed from the figure that H_2O_2 injection has the following effects on cavitation flow and its chemical reaction performance.

1. Switching the flow regime from attached (sheet) cavitation into traveling cavitation.
2. Increasing the number of cavitation events.

Moreover, it is obvious that it has the following additional effects.

3. Increasing the number of generated oxidizer agents since

Downloaded 03 Jun 2010 to 171.66.16.158. Redistribution subject to ASME license or copyright; see http://www.asme.org/terms/Terms_Use.cfm

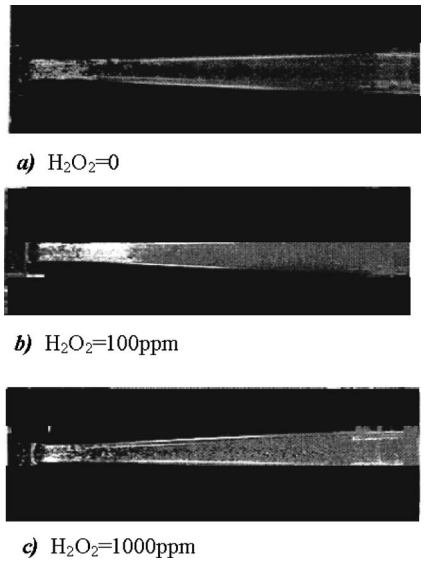

Fig. 7 The effect of H_2O_2 injection on cavitation regime (Q =165 l/min and 100 kPa operating pressure)

each molecule of H_2O_2 generates two hydroxyl radicals rather than one hydroxyl radical generated from dissociation of a water molecule.

4. Increasing the lifetime of hydroxyl radicals and providing more possibility for migration of these radicals into the bulk liquid. The longer lifetime of hydroxyl radical is due to the fact that in this case two hydroxyl radicals are generated from dissociation of one H_2O_2 molecule, unlike the case of water molecule, in which a hydroxyl and a hydrogen atom are generated. Therefore, hydroxyl radicals that are generated with H_2O_2 injection have lower vicinity with $\overset{+}{H}$ atoms and hence a longer lifetime than cavitation with no H_2O_2 injection.

It is useful to mention that the tandem Venturi itself does not play any role in above-mentioned effects 1, 3, and 4. It only plays a similar role as the injection of oxidizer plays in increasing the cavitation events. Therefore, both tandem arrangement and the injection of H_2O_2 help to increase the number of cavitation events.

It is required to mention that all data, which are presented for comparison of the cavitation reaction for the two cases of single and tandem Venturis (Figs. 5 and 6), are obtained at a constant flow rate. Flow rate affects both the cavitation number and the number of water circulation for a given volume of water that is stored in the storage tank (see Fig. 2(*a*)). In order to have the same conditions for the single and tandem Venturis, experiment was conducted at the constant flow rate.

4.4 The Efficiency of Reaction. It is helpful to review the chemical reaction efficiency of both Venturis briefly. In this regard, our attention is focused on energy consumption of a specific amount of decomposition. This energy is the electrical power consumed by the pump.

Oxidation (or chemical reaction) efficiency is defined as follows [5]:

$$\eta_{\text{chem}}(t) = \frac{(C_i - C(t)) \cdot V}{t \cdot P_{\text{pump}}} \tag{10}$$

where C_i is the initial concentration of the target substance, $C(t)$ is the concentration at time t, V is the total liquid volume (20 l), and P_{pump} is the power consumed by the pump in kilowatts. The consumed power of the pump can be obtained from the pump performance curves provided by its manufacturer. The performance curves are utilized using the experimental results and flow rate that are indicated in Tables 1 and 2 for the single and tandem Venturis, respectively.

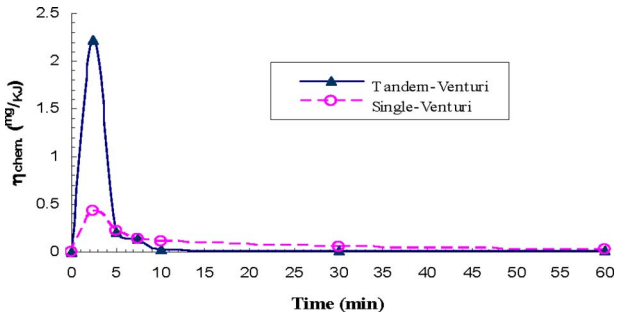

Fig. 8 Comparison of decomposition efficiency of the tandem Venturi and single Venturi in the cavitation-oxidation decomposition of 2-chlorophenol (operating pressure=100 kPa, initial concentration of 2-chlorophenol=15 ppm, flow rate =210 l/min, and injected amount of H_2O_2=1000 ppm)

Figure 8 shows chemical decomposition efficiency of single and tandem Venturis. Both single and tandem Venturis are implemented on similar conditions (same flow rate). As is clear from Fig. 8, the decomposition efficiency of the tandem Venturi is much higher than the single Venturi for the first 5 min of the experiment. This higher value is due to the very fast decomposition rate of the tandem Venturi compared with the single Venturi (Fig. 6). After the first 5 min of the experiment, the reaction efficiency of the single Venturi is slightly higher than the tandem Venturi. This is due to the very high decomposition rate of the tandem Venturi at the early stage of the experiment. However, it is clear that the overall decomposition efficiency of the tandem Venturi is much better than the single one. Moreover, Fig. 8 indicates that the decomposition efficiency for both types of reactors is highest at the early stage of the experiment while it reduces as the experiment progresses. The higher efficiency at the early stage of the experiment is due to the fact that the decomposition rate decreases as the experiment progresses. While the input energy remains constant at a specific time interval.

Consequently, from Fig. 8 it is found that the implementation of the tandem Venturi has an advantage over the single Venturi in the cavitation-oxidation process due to the higher decomposition rate and the higher efficiency in the decomposition of non-VOC.

At the end, it should be pointed out that the presence of the hydrogen peroxide is essential in order to achieve the higher decomposition efficiency either in the case of single Venturi or in the case of the tandem Venturi. In the absence of the hydrogen peroxide, the oxidation efficiency of non-VOC is much lower. For example, in the decomposition of the PNP solution using the submerged cavitation nozzle, the maximum efficiency was about 0.005 mg/kJ [5], whereas when the hydrogen peroxide is injected, the maximum decomposition efficiency increases to the range of 0.5 mg/kJ for the single Venturi and 2.3 mg/kJ for the tandem Venturi.

5 Conclusion

The cavitation reaction site for non-VOC contaminants is on the outside of the collapsing bubbles. Therefore, in this case, the treatment rate depends on the migration of the hydroxyl radicals generated by cavitation into the bulk liquid or in the interfacial liquid shell around the bubbles. Utilizing the tandem Venturi is considered as an alternative for increasing the number of cavitation events and for increasing the number of collapsing regions in a reactor. It was found that the implementation of the tandem Venturi provides a higher number of cavitation events and collapsing regions. It was experimentally verified for the single Venturi

Downloaded 03 Jun 2010 to 171.66.16.158. Redistribution subject to ASME license or copyright; see http://www.asme.org/terms/Terms_Use.cfm

that the extent of the cavitation zone increases when the inlet pressure and the flow rate are increased. The increase in the inlet pressure and the flow rate decreases the cavitation number. In the case of the tandem Venturi, the extent of the cavitation zone and cavitation number for the upstream Venturi remained constant as the inlet pressure and flow rate varied. This result was also verified analytically. The extent of the cavitation zone and cavitation number of the downstream Venturi changed similar to the case of the single Venturi while the inlet pressure and flow rate (cavitation number) are changed. It was observed that the cavitation flow has no significant effect on the degradation rate of non-VOC chemicals for both single and tandem Venturis. That is simply because the tandem Venturi cannot play any role in decreasing the collapsing time of the bubbles or increasing the lifetime of the radicals. Only a small increase in the reaction was observed for the tandem Venturi in degradation of 2-chlorophenol compared with the single Venturi for only cavitation flow due to the higher number of cavitation events and collapsing regions in the tandem Venturi than the single Venturi. Instead, the injection of H_2O_2 as an alternative for increasing the lifetime and the number of generated radicals was considered. The experiment concluded that the contribution of cavitation and injection of H_2O_2 (the cavitation-oxidation reaction) properly treated non-VOC aqueous solutions. Furthermore, the decomposition rate of non-VOC takes place faster with higher energy efficiency in the tandem Venturi. The existence of the hydroxyl radicals in the bulk liquid, which is related to the relative collapsing time and the lifetime of the radicals, is the most important parameter in the cavitational reaction of non-VOC. In the absence of hydroxyl radicals, the cavitation reactors could not efficiently decompose non-VOC solutions.

Acknowledgment

This work has been carried out in collaboration with the Fluid Engineering Laboratory of the Mechanical Engineering Department, The University of Tokyo.

Nomenclature

A = flow area
C = concentration of chemicals (ppm)
E_p = energy consumption of the pump (kJ)
P = pressure (kPa)
P_v = vapor pressure (kPa)
Q = flow rate (l/min)
V = total capacity of the experimental setup (l)
t = time (s)
v = flow velocity (m/s)

Greek Symbols

ρ = density (kg/m^3)
σ = cavitation number
θ = divergence angle of the Venturi
β_{in} = inlet area ratio ($=A_0/A_{in}$)
η_{chem} = decomposition efficiency (mg/kJ)

Subscripts

i = initial condition
in = inlet condition of the Venturi
b = outlet condition of the Venturi
ℓ = liquid state
I = upstream Venturi of the tandem arrangement
II = downstream Venturi of the tandem arrangement
0 = condition at the Venturi throat
1 = shock upstream or shock upstream of the upstream Venturi of the tandem arrangement
2 = shock downstream or shock downstream of the upstream Venturi of the tandem arrangement
3 = outlet condition or outlet condition of the upstream Venturi of the tandem arrangement
4 = shock upstream of the downstream Venturi of the tandem arrangement
5 = shock downstream of the downstream Venturi of the tandem arrangement
6 = outlet condition of the downstream Venturi in the tandem arrangement

References

[1] Sayyaadi, H., 2003, "Water Treatment Using Cavitating Flow," Ph.D. thesis, The University of Tokyo, Tokyo, Japan.
[2] Sayyaadi, H., 2006, "Cavitation Reactor for Water Reclamation From VOC and Non-VOC Contaminants," *Proceedings of the Fourth IWA International Conference on Oxidation Technology*, Goslar, Germany, Paper Code: 307, pp. 727–733.
[3] Environmental Protection Agency (EPA), 1994, Report No. EPA/540/AR-93/520, CAV-OX Cavitation Oxidation Process Magnum Water Technology, Inc., http://www.epa.gov/ord/SITE/reports/540ar93520/540ar93520.pdf.
[4] Lertnuwat, B., 2003, "Numerical Simulation of Cavitation Flows," Ph.D. thesis, The University of Tokyo, Tokyo, Japan.
[5] Kalumuck, K. M., and Chahine, G. L., 2000, "The Use of Cavitating Jets to Oxidize Organic Compound in Water," ASME J. Fluids Eng., **122**, pp. 465–470.
[6] Senthil Kumar, P. S., and Pandit, A. B., 1999, "Modeling of Hydrodynamic Cavitation," Chem. Eng. Technol., **22**(12), pp. 1017–1027.
[7] Moholkar, V. S., and Pandit, A. B., 2001, "Numerical Investigations in the Behavior of One-Dimensional Bubbly Flow in Hydrodynamic Cavitation," Chem. Eng. Sci., **56**, pp. 1411–1418.
[8] Moholkar, V. S., and Pandit, A. B., 2001, "Modeling of Hydrodynamic Cavitation: A Unified Approach," Chem. Eng. Sci., **56**, pp. 6295–6302.
[9] Moholkar, V. S., and Pandit, A. B., 1997, "Bubble Behavior in Hydrodynamic Cavitation: Effect of Turbulence," AIChE J., **43**(6), pp. 1641–1648.
[10] Senthil Kumar, P., and Pandit, A. B., 2000, "Experimental Quantification of Chemical Effects of Hydrodynamic Cavitation," Chem. Eng. Sci., **55**, pp. 1633–1639.
[11] Moholkar, V. S., and Pandit, A. B., 2001, "Numerical Investigations in the Behavior of One-Dimensional Bubbly Flow in Hydrodynamic Cavitation," Chem. Eng. Sci., **56**, pp. 1411–1418.
[12] Henglein, A., 1993, "Contribution to Various Aspects of Cavitation Chemistry," *Advances in Sonochemistry*, Vol. 3, JAI, Greenwich, CT, pp. 17–83.
[13] Riesz, P., 1991, "Free Radical Generation by Ultrasound in Aqueous Solutions of Volatile and Non-Volatile Solutes," *Advances in Sonochemistry*, Vol. 2, T. Mason, ed., JAI, Greenwich, CT, pp. 23–64.
[14] Shah, Y. T., Pandit, A. B., and Moholkar, V. S., 1999, *Cavitation Reaction Engineering*, Kluwer Academic/Plenum, New York.
[15] Margulis, M. A., and Mal'tsev, A. N., 1968, "The Effect of Ultrasound on Water in the Presence of Dissolved Gases," Zh. Fiz. Khim., **42**, pp. 1441–1451.

Downloaded 03 Jun 2010 to 171.66.16.158. Redistribution subject to ASME license or copyright; see http://www.asme.org/terms/Terms_Use.cfm

Modeling of Pressure Drop During Condensation in Circular and Noncircular Microchannels

Akhil Agarwal
Shell Global Solutions, Inc.,
Houston, TX 77082-3101

Srinivas Garimella[1]
George W. Woodruff School of Mechanical Engineering,
Georgia Institute of Technology,
Atlanta, GA 30332-0405
e-mail: srinivas.garimella@me.gatech.edu

*This paper presents a multiple flow-regime model for pressure drop during condensation of refrigerant R134a in horizontal microchannels. Condensation pressure drops measured in two circular and six noncircular channels ranging in hydraulic diameter from 0.42 mm to 0.8 mm are considered here. For each tube under consideration, pressure drop measurements were taken over the entire range of qualities from 100% vapor to 100% liquid for five different refrigerant mass fluxes between 150 kg/m^2 s and 750 kg/m^2 s. Results from previous work by the authors on condensation flow mechanisms in microchannel geometries were used to assign the applicable flow regime to the data points. Garimella et al. (2005, "Condensation Pressure Drop in Circular Microchannels," Heat Transfer Eng., **26**(3) pp. 1–8) reported a comprehensive model for circular tubes that addresses the progression of the condensation process from the vapor phase to the liquid phase by modifying and combining the pressure drop models for intermittent (Garimella et al., 2002, "An Experimentally Validated Model for Two-Phase Pressure Drop in the Intermittent Flow Regime for Circular Microchannels," ASME J. Fluids Eng., **124**(1), pp. 205–214) and annular (Garimella et al., 2003, "Two-Phase Pressure Drops in the Annular Flow Regime in Circular Microchannels," 21st IIR International Congress of Refrigeration, International Institute of Refrigeration, p. ICR0360) flows reported earlier by them. This paper presents new condensation pressure drop data on six noncircular channels over the same flow conditions as the previous work on circular channels. In addition, a multiple flow-regime model similar to that developed earlier by Garimella et al. for circular microchannels is developed here for these new cross sections. This combined model accurately predicts condensation pressure drops in the annular, disperse-wave, mist, discrete-wave, and intermittent flow regimes for both circular and noncircular microchannels of similar hydraulic diameters. Overlap and transition regions between the respective regimes are also addressed to yield relatively smooth transitions between the predicted pressure drops. The resulting model predicts 80% of the data within ±25%. The effect of tube shape on pressure drop is also demonstrated.* [DOI: 10.1115/1.3026582]

1 Introduction

Microchannel tubes are increasingly being used for the fabrication of condensers in vapor-compression systems for a wide variety of applications due to the high heat transfer coefficients that these geometries offer. Heat transfer coefficients and pressure drop in phase-change processes are a strong function of the local vapor quality. For air-water flow [1] as well as condensation of refrigerants [2,3], it has been demonstrated that flow regimes and transitions in small diameter circular and noncircular geometries are different from those observed in larger diameter circular tubes. Because two-phase pressure drops depend on the corresponding flow patterns, it is reasonable to expect that condensation pressure drop in small diameter channels may not be predicted adequately by the existing correlations for larger diameter tubes. Much of literature on two-phase pressure drops addresses tubes with diameter greater than 8 mm. Examples include the classical correlations for large diameter tubes developed by Lockhart and Martinelli [4], Chisholm [5], and Friedel [6,7]. Garimella et al. [8] demonstrated that these models are not able to predict pressure drops during condensation in circular microchannels of diameters 0.506–4.91 mm. Limited research has been conducted on addressing the effect of tube shape at small hydraulic diameters on pressure drop and heat transfer coefficients during condensation. The relatively few studies on two-phase flow in small diameter round tubes have primarily used isothermal air-water mixtures.

In the recent past, a few researchers [9–12] have developed pressure drop models for small diameter tubes by modifying the classical pressure drop correlations mentioned above. For example, Tran et al. [10] modified the Chisholm [5] correlation to apply it to pressure drop in boiling flow of three refrigerants including R-134a in small diameter tubes. Similarly, the correlations by Kawahara et al. [12], Mishima and Hibiki [11], and Lee and Lee [9] represent modifications to the original Lockhart–Martinelli [4] correlation. However, Garimella et al. [13] showed that these models are not very successful in accurately predicting pressure drops during condensation of refrigerants in annular flow through microchannel geometries.

Garimella et al. [8] developed a condensation pressure drop model for circular tubes ranging in diameter from 0.506 mm to 4.91 mm based on submodels for intermittent-flow [14], and disperse-wave-, annular-, and mist-flow regimes [13]. The present study reports a considerable amount of new measurements and data on six new noncircular microchannels of similar D_h and an extended model to enable prediction of condensation pressure drop in a variety of shapes. The tube shapes under consideration are shown in Fig 1. Two circular tubes of comparable diameters are also included in the analysis to serve as a baseline.

[1]Corresponding author.

Contributed by the Fluids Engineering Division of ASME for publication in the JOURNAL OF FLUIDS ENGINEERING. Manuscript received February 26, 2007; final manuscript received April 1, 2008; published online December 2, 2008. Assoc. Editor: Joseph Katz. Paper presented at the 2006 ASME International Mechanical Engineering Congress (IMECE2006), Chicago, IL, November 5–10, 2006.

 Copyright © 2009 by ASME

Downloaded 03 Jun 2010 to 171.66.16.158. Redistribution subject to ASME license or copyright; see http://www.asme.org/terms/Terms_Use.cfm

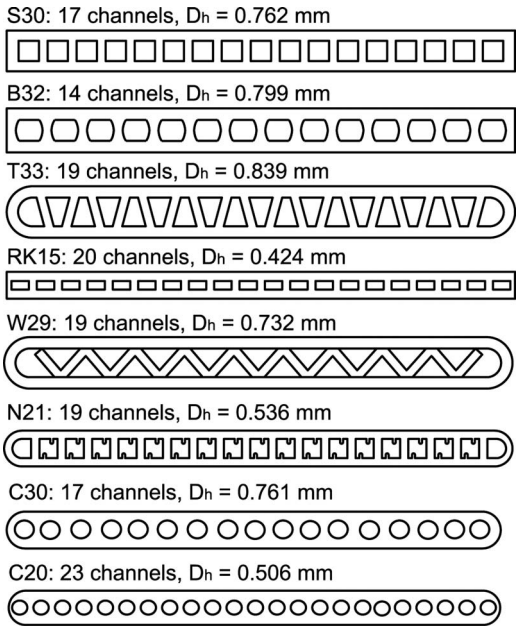

Fig. 1 Tube shapes and hydraulic diameters

2 Experimental Approach

The test facility used for the pressure drop measurements reported here was first developed to observe condensation flow mechanisms in small D_h channels. The insights from these observations are used here for the development of flow-mechanism-based pressure drop models. The facility enables visualization of the actual condensation process (not simulations using air-water mixtures). Subcooled liquid refrigerant is boiled and superheated by a tube-in-tube evaporator. The superheated vapor enters one of two water-cooled precondensers to partially condense the vapor. The measured conditions at the superheated state, the heat duty of the precondenser, and the measured pressure at the precondenser outlet determine the thermodynamic state at the inlet to the test section. The outlet state of the test section was calculated in an analogous, but independent, manner starting from the measured subcooled state at the postcondenser outlet and the heat duty to completely condense and subcool the refrigerant. For flow visualization, two-phase refrigerant of the desired inlet quality was supplied to a glass test section with the cross section under consideration. The glass section was enclosed in an outer Plexiglas annulus through which compressed air flowed. The compressed air decreased the differential pressure to be withstood by the glass channel while also serving as a coolant for condensation. Air temperatures and flow rates were adjusted to allow a small amount of condensation ($0.05 < \Delta x < 0.10$) in the test section. Condensation flow mechanisms were recorded using video photography across the entire vapor-liquid dome in small increments of vapor quality. A detailed description of the techniques for flow visualization as well as the effects of tube shape on these flow patterns was reported by Coleman and Garimella [3]. The effect of tube miniaturization on the flow mechanisms for $1 < D_h < 4$ mm, $0 < x < 1$, and $150 < G < 750$ kg/m^2 s was also investigated [2].

Pressure drop measurements were also conducted on this facility. The glass test section was replaced with aluminum tubes of the desired cross section. The circular and noncircular geometries relevant to this paper are shown in Fig. 1. The test sections were fabricated as flat tubes with multiple extruded parallel channels with the exception of the W29 tubes, which were formed by brazing a W-shaped insert inside a flattened tube. The designations for each tube are based on the shape of the extruded channel and its nominal hydraulic diameter in British units; for instance, S30 has square channels with $D_h = 0.030$ in (0.762 mm). Similarly, B32 is "barrel shaped," N21 is "N shaped," RK15 is rectangular, T33 is triangular, and W29 has a "W-shaped" insert, which forms roughly triangular channels. For all test sections, the outer tubes carrying the coolant had 16 rectangular channels of 0.986 mm hydraulic diameter. This method of using multiple parallel channels ensured that the refrigerant flow rates used were large enough to be adequately controlled and measured, with accurate heat balances around the test loop. Three such tubes were brazed together, with refrigerant flowing through the center tube and coolant (air) flowing in counterflow through the top and bottom tubes. The low thermal capacity and heat transfer coefficients of air maintained low condensation rates and small changes in quality in the test section, which in turn enabled the measurement of the pressure drop variation as a function of quality with high resolution. This small quality change across the test section minimized the likelihood of flow-regime transitions within the test section for any data point. The measured pressure drop in the test section is characteristic of the average quality and mass flux in the test section. These measurements were conducted at a nominal saturation pressure of 1396 kPa, which corresponds to a saturation temperature of 52.3 °C; the saturation temperature was within ±3 °C of this for all the data points. Refrigerant flow rates were measured using Coriolis mass flow meters (±0.15% uncertainty). Absolute pressure transducers with uncertainties of ±0.25% of the span were used to measure pressures of the refrigerant at various locations. Pressure drops across the test section were measured using a bank of three selectable differential pressure transducers, with maximum ΔP values of 6.22 kPa, 62.2 kPa, and 248.2 kPa, respectively, and an accuracy of ±0.25% of the span. As the geometry, mass flux, and quality were varied, the pressure drop for a particular data point was measured using the most accurate of the three transducers. Other instrumentation details for thermocouples, resistance temperature detectors (RTDs), cooling water flow rates, etc., are available in Ref. [14]. Representative uncertainties for the range of mass flux and qualities studied are as follows:

$$G = 150 \text{ kg/m}^2 \text{ s}:$$

$$x_{\text{avg}} = 0.13 \pm 0.032, \quad x_{\text{avg}} = 0.50 \pm 0.027, \quad x_{\text{avg}} = 0.91 \pm 0.021$$

$$G = 450 \text{ kg/m}^2 \text{ s}:$$

$$x_{\text{avg}} = 0.12 \pm 0.045, \quad x_{\text{avg}} = 0.48 \pm 0.014, \quad x_{\text{avg}} = 0.88 \pm 0.026$$

$$G = 750 \text{ kg/m}^2 \text{ s}:$$

$$x_{\text{avg}} = 0.11 \pm 0.039, \quad x_{\text{avg}} = 0.51 \pm 0.022, \quad x_{\text{avg}} = 0.74 \pm 0.035$$

For each of the test sections investigated, single-phase liquid and vapor tests were first conducted to calculate friction factors over the laminar, transition, and turbulent regimes, and compared with literature. Contraction and expansion losses at the inlet and outlet were subtracted from the total measured pressure drop using the appropriate loss coefficients. The residual frictional component of the pressure drop was compared with the values predicted by the Churchill [15] correlation. In every case, the relative roughness values needed to match the Churchill [15] correlation values were well within the range of roughnesses for such tubes. The excellent agreement between the single-phase data and this correlation validates the test procedures.

The measured pressure drops included expansion and contraction losses due to the headers at both ends of the test section and the pressure change due to deceleration caused by the changing vapor fraction as condensation takes place. The portion of the total pressure drop (change) attributable to deceleration of the fluid was estimated from void fraction and momentum change analyses; contraction/expansion losses at the inlet and outlet of the test section were estimated using two-phase "minor loss" models avail-

Downloaded 03 Jun 2010 to 171.66.16.158. Redistribution subject to ASME license or copyright; see http://www.asme.org/terms/Terms_Use.cfm

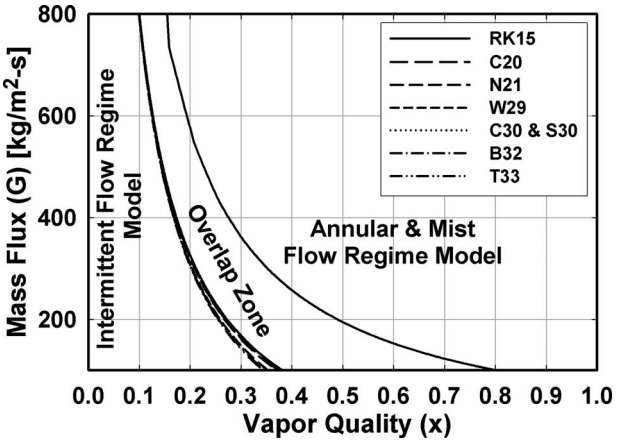

Fig. 2 Flow-regime assignment

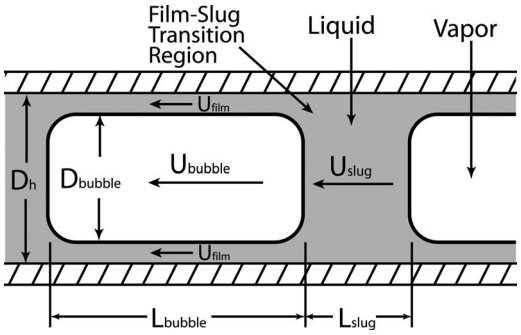

Fig. 3 Schematic of intermittent flow

able in literature. This process is described in detail by Garimella et al. [14]. These estimates were validated using pressure drop measurements on a "near-zero" length test section and tests conducted with and without condensation in the test section as described by Garimella et al. [14]. Excellent agreement was obtained between these data and the models. The residual frictional component of the pressure drop was used for developing pressure drop models for the respective flow regimes.

3 Flow Regime Assignment

Flow visualization results of Coleman and Garimella [1,2] and the transition criteria developed by Garimella et al. [14] from these results were used to assign each of the pressure drop data points to the respective flow regimes. According to these criteria, transition from the intermittent to the other flow regimes occurs as follows:

$$x \leq \frac{a}{G+b} \tag{1}$$

where G is the total mass flux expressed in $\mathrm{kg/m^2\,s}$ and a and b are geometry dependent constants given by

$$a = 69.57 + 22.60 \exp(0.259 \cdot D_h) \tag{2}$$

$$b = -59.99 + 176.8 \exp(0.383 \cdot D_h) \tag{3}$$

where D_h is the hydraulic diameter of the tubes in millimeters. On a mass-flux versus quality map, these transition lines appear in the lower left corner, as shown in Fig. 2. Since the hydraulic diameters of all the tubes under consideration in the current study are very close to each other, the transition lines are not distinguishable. For the purpose of pressure drop model development, the primary flow regimes depicted here are the intermittent regime and the annular film/mist/disperse patterns of the annular-flow regime. The work of Coleman and Garimella [2,3,16] identified several other regimes and patterns; however, for pressure drop model development, it will be shown that this broad categorization suffices. Since all the tubes under consideration in the current study have $D_h < 1$ mm, the wavy-flow regime is not seen in Fig. 2.

As reported previously [8], the intermittent-flow model for circular tubes developed by Garimella et al. [14], with subsequent modifications to encompass data from a larger range of geometries [17], can be applied to the data points to the left of the corresponding transition lines shown in Fig. 2. The preliminary annular-flow model reported by Garimella et al. [13] is used as the other starting point and extended to the mist- and disperse-flow regions [8] that occur at high mass fluxes and vapor qualities. For all the tubes under consideration in the current study, the hydraulic diameters are less than 1 mm. In the absence of other valid transition criteria, the transition criteria for 1 mm square channels proposed by Coleman and Garimella [2] are assumed to be valid for all tubes. It should be noted that the transitions between these various regimes do not occur abruptly at unique combinations of mass flux and quality, but rather across overlap zones in which the flow could switch back and forth between the respective regimes. This overlap region is also shown in Fig. 2, and appropriate interpolation techniques for the pressure drops calculated from the individual models are also recommended in Secs. 4–6.

The data set considered here consists of a total of 1194 points. Of these, 173 points lie in the intermittent regime, 809 points are in the disperse-annular-mist-flow regime, and the remaining 212 points are in the overlap zone between these two regimes. Pressure drop models for these regimes are described below.

4 Model Development and Results

4.1 Intermittent and Discrete-Wave Flow. Models for intermittent flow in circular [14] and noncircular [17] channels were presented in earlier work, and are used as one of the starting points for this paper. From the flow visualization studies, it can be inferred that in the intermittent regime, the vapor phase travels as long solitary bubbles surrounded by an annular liquid film and separated by liquid slugs. As the tube size decreases, surface tension forces at the bubble interface begin to dominate the gravitational forces and the bubble tends to a cylindrical shape. The corresponding "unit cell" used for the development of the model is shown in Fig. 3. In general, the bubble travels faster than the liquid slug, which implies that there is a continual uptake of liquid from the film into the front of the slug. These phenomena were accounted for in the model. In addition, based on the recorded flow patterns, it was assumed that the bubble is cylindrical and that there is no entrainment of vapor in slug, or liquid in bubble. Furthermore for any given condition, it was assumed that the length/frequency/speed of bubbles/slugs is constant, with no bubble coalescence, and a smooth bubble/film interface. Unlike other work in the literature, here the pressure drop in the bubble/film region was not neglected.

The total pressure drop for this flow pattern includes contributions from the liquid slug, the vapor bubble, and the flow of liquid between the film and slug as follows:

$$\Delta P_{\text{total}} = \Delta P_{\text{slug}} + \Delta P_{f/b} + \Delta P_{\text{film-slug transitions}} \tag{4}$$

A simple control volume analysis [14,17] similar to that performed by Suo and Griffith [18] showed that the velocity in the liquid slug can be directly calculated given the overall mass flux and quality. The results of several investigations [18–20] suggested that the bubble velocity for these conditions was 1.2 times the slug velocity. With this assumption, the diameter of the bubble, velocity within the film, and relative length of bubble and slug can all be calculated from a system of simultaneous equations including a shear balance at the bubble-film interface. Thus, the Reynolds number in the liquid slug and vapor bubble (based on the relative velocity at the interface between the bubble and the surrounding film) could be directly determined. The Churchill

Downloaded 03 Jun 2010 to 171.66.16.158. Redistribution subject to ASME license or copyright; see http://www.asme.org/terms/Terms_Use.cfm

[15] correlation was then used to calculate the friction factor and thus the pressure gradient at the respective Reynolds numbers in the liquid slug and bubble/film regions. A relationship from literature for the pressure loss associated with the mixing that occurs in the uptake of liquid from the film to the slug was used to estimate the pressure loss due to each of these transitions. These components of the total pressure drop are shown below:

$$\frac{\Delta P}{L} = \left(\frac{dP}{dx}\right)_{\substack{\text{film}\\\text{bubble}}} \left(\frac{L_{\text{bubble}}}{L_{\text{UC}}}\right) + \left(\frac{dP}{dx}\right)_{\text{slug}} \left(\frac{L_{\text{slug}}}{L_{\text{UC}}}\right) + \Delta P_{\text{one transition}} \left(\frac{N_{\text{UC}}}{L}\right) \tag{5}$$

For the solution of the above equation, the number of unit cells per unit length is required and can be determined from the slug frequency (which yields the unit cell length). Several models from literature for slug frequency were considered; however, because these models were based primarily on studies of gas-liquid (instead of vapor-liquid) flows in large (>10 mm) diameter tubes, they did not yield satisfactory results. Instead, the following correlation for slug frequency (nondimensional unit-cell length, or unit cells/length) based on slug Re and D_h was developed:

$$a(\text{Re}_{\text{slug}})^b = \omega \frac{D_h}{U_{\text{bubble}}} = D_h \left(\frac{N_{\text{UC}}}{L_{\text{tube}}}\right) = \left(\frac{D_h}{L_{\text{UC}}}\right) \tag{6}$$

The coefficients a and b were fitted using the difference between the measured pressure drop and the pressure drop calculated as described above for the slug and bubble/film regions, i.e., the net pressure drop due to transitions. The correlation yielded $a=2.437$ and $b=-0.560$ for both circular and noncircular (except triangular) channels. For circular channels (0.5–4.91 mm), the predicted pressure drops are on average within ±13.5% of the measured values, with 90% of the predicted results being within ±27% of the measured values.

Garimella et al. [8] extended this model to the discrete-wave flow region. Progressing from the intermittent toward the annular regime, the length of the solitary bubbles increases and the number of slugs decreases. This results in a decrease in the number of unit cells per unit length. Traversing from the intermittent-flow boundary toward the annular-flow boundary, the bubbles disappear completely, and the number of unit cells per unit length approaches zero. Based on this, the slug frequency model developed by Garimella et al. [14,17] for intermittent flow was modified to include data from the overlap zone, resulting in the following combined model for the two regions:

$$N_{\text{UC}} \left(\frac{D_h}{L_{\text{tube}}}\right) = \left(\frac{D_h}{L_{\text{UC}}}\right) = 1.573(\text{Re}_{\text{slug}})^{-0.507} \tag{7}$$

Although the above model was originally proposed by the authors only for circular tubes, it is found to predict the data for the noncircular (except triangular) tubes equally well. For the triangular shape tubes, i.e., T33 and W29, Garimella et al. [17] proposed the following correlation to predict N_{UC}:

$$N_{\text{UC}} \left(\frac{D_h}{L_{\text{tube}}}\right) = \left(\frac{D_h}{L_{\text{UC}}}\right) = 0.9965 \exp(-8.33 \times 10^{-4} \text{Re}_{\text{slug}}) \tag{8}$$

These slug frequency equations (Eqs. (7) and (8)) based on the new data from the present study were used to compute the pressure drops in the intermittent-flow regime for the noncircular tubes shown in Fig. 1.

4.2 Annular/Mist/Disperse Flow. A preliminary model for pressure drops in the annular-flow regime for the circular tubes under consideration here was reported by Garimella et al. [13], with subsequent modifications reported by Garimella et al. [8] to extend its applicability to the mist- and disperse-flow regions. A schematic of the flow pattern used to represent annular flow is shown in Fig. 4. For the development of this model, the following

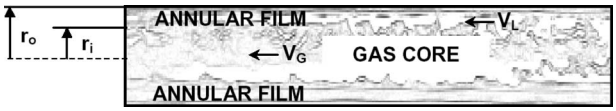

Fig. 4 Annular film flow pattern

assumptions were made: steady flow, equal pressure gradients in the liquid and gas core across the cross section, uniform thickness of the liquid film, and no entrainment of the liquid in the gas core. The measured pressure drops were used to compute the Darcy form of the interfacial friction factor to represent the interfacial shear stress as follows:

$$\frac{\Delta P}{L} = \frac{1}{2} \cdot f_i \rho_v V_v^2 \cdot \frac{1}{D_i} \tag{9}$$

The above equation uses the interface diameter, D_i. This same expression can be represented in terms of the more convenient tube diameter, D, through the use of a void fraction model [21] as follows:

$$\frac{\Delta P}{L} = \frac{1}{2} \cdot f_i \frac{G^2 \cdot x^2}{\rho_v \cdot \alpha^{2.5}} \cdot \frac{1}{D} \tag{10}$$

The ratio of this interfacial friction factor obtained from the experimental data to the corresponding liquid-phase Darcy friction factor computed using the Churchill [15] equation was then computed and correlated as follows:

$$\frac{f_i}{f_l} = A \cdot X^a \, \text{Re}_l^b \, \psi^c \tag{11}$$

Here the Martinelli parameter X is given by

$$X = \left[\frac{(dP/dz)_l}{(dP/dz)_v}\right]^{1/2} \tag{12}$$

The following nondimensional parameter that accounts for the effects of surface tension was introduced by Lee and Lee [9]:

$$\psi = \frac{j_L \mu_L}{\sigma} \tag{13}$$

where $j_L = G(1-x)/\rho_l(1-\alpha)$ is the liquid superficial velocity.

For this model, the liquid-phase Reynolds number required in Eq. (11) above, which is also needed to compute the liquid-phase pressure drop in the Martinelli parameter, was defined in terms of the annular-flow area occupied by the liquid phase as follows:

$$\text{Re}_l = \frac{GD(1-x)}{(1+\sqrt{\alpha}) \cdot \mu_l} \tag{14}$$

Similarly, the gas-phase Reynolds number, required for the calculation of the pressure drop through the gas core in the Martinelli parameter, was calculated as follows:

$$\text{Re}_g = \frac{GxD}{\mu_g \sqrt{\alpha}} \tag{15}$$

Regression analysis on the data grouped into two regions based on the liquid-phase Reynolds number yielded the following values for the respective parameters in Eq. (11):

Laminar region ($\text{Re}_l < 2100$):

$$A = 1.308 \times 10^{-3}, \quad a = 0.427, \quad b = 0.930, \quad c = -0.121$$

Turbulent region ($\text{Re}_l > 3400$):

$$A = 25.64, \quad a = 0.532, \quad b = -0.327, \quad c = 0.021$$

For the transition region data, the pressure drop is first independently calculated using the laminar and turbulent constants shown above at the low and high values of the mass flux and quality representing the boundaries of the laminar and turbulent regions.

Downloaded 03 Jun 2010 to 171.66.16.158. Redistribution subject to ASME license or copyright; see http://www.asme.org/terms/Terms_Use.cfm

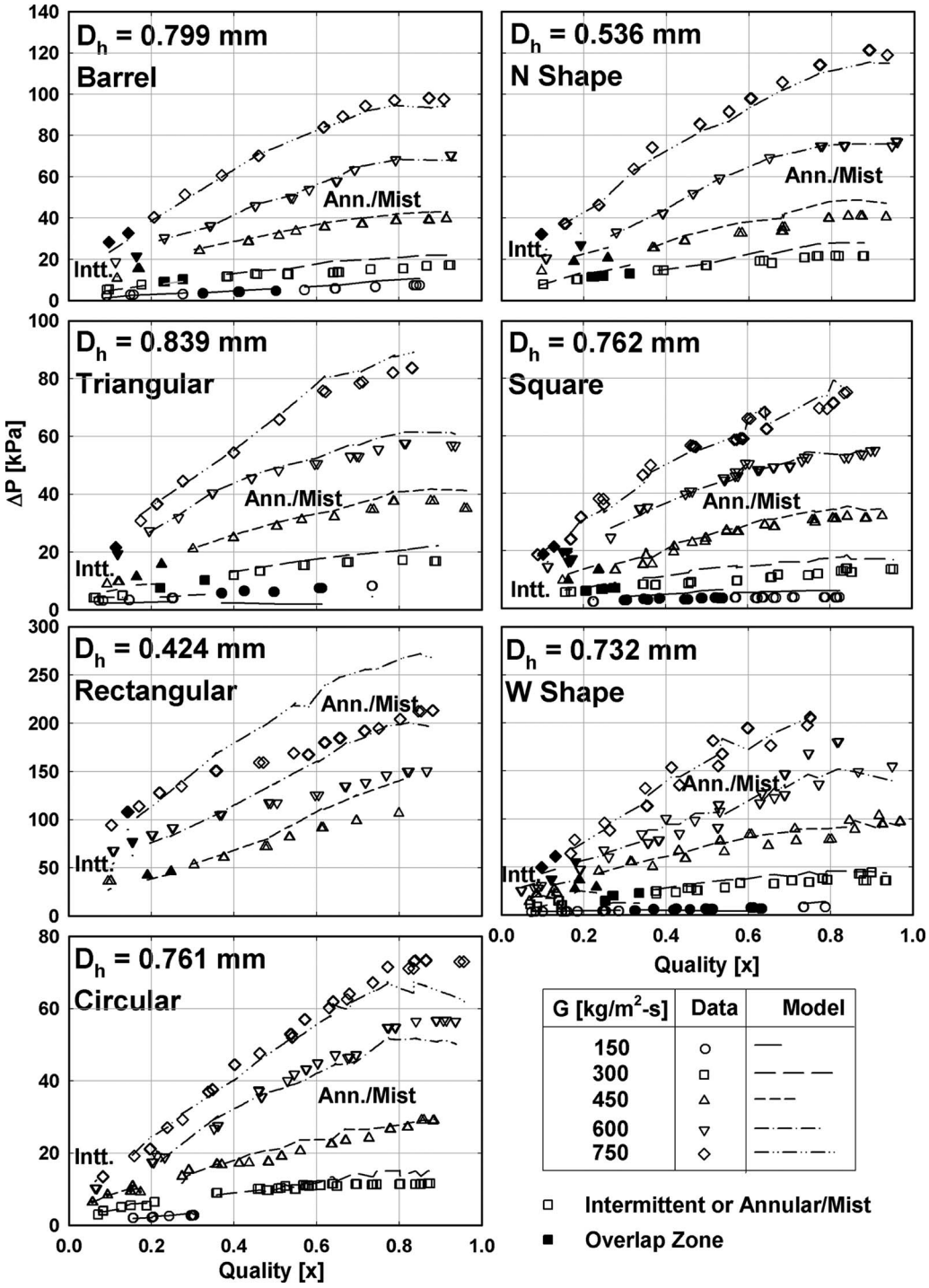

Fig. 5 Predicted and experimental ΔP versus x

Linear interpolation between these bounding values is then conducted separately based on the quality and the mass flux under consideration. The average of these two pressure drops resulting from the interpolation based on G and x represents the two-phase pressure drop for the transition region data point.

This model [8] predicted 87% of the circular tube data within $\pm 20\%$. It should be noted that these predictions include not only the annular-flow region but also the mist- and disperse-flow data, whereas the previous model of Garimella et al. [13] applied only to the annular-flow regime. The model described above distinguishes the data based on whether the liquid phase is laminar or turbulent. The gas core was consistently turbulent for all the data points under consideration in the mist-, annular-, and disperse-flow regimes. Thus the model is not valid for cases with a laminar gas core; however, in such an instance, it is unlikely that the flow will be in one of these regimes.

4.3 Modifications for Noncircular Tubes. The pressure drop model for circular tubes described above, when applied to the noncircular tubes correctly predicts the trends, but with considerable differences between the predicted and measured pressure drop values. This is primarily because of the effect of tube shape. To account for this effect, the constant A in Eq. (11) was determined for each individual tube by regression analysis, while keep-

Downloaded 03 Jun 2010 to 171.66.16.158. Redistribution subject to ASME license or copyright; see http://www.asme.org/terms/Terms_Use.cfm

Table 1 Values of the constant *A* determined for each of the tubes by individual regression

Tube	D_h (mm)	Roughness	Const. A (Eq. (11))	Avg. abs. deviation (%)
RK15	0.424	0.0390	2.576×10^{-3}	21
C20	0.506	0.0003	1.325×10^{-3}	14
N21	0.536	0.0030	1.304×10^{-3}	12
W29	0.732	0.1000	3.667×10^{-3}	15
C30	0.761	0.0005	1.258×10^{-3}	9
S30	0.762	0.0009	1.470×10^{-3}	20
B32	0.799	0.0070	1.911×10^{-3}	12
T33	0.839	0.0065	1.984×10^{-3}	18

ing exponents a, b, and c the same. Table 1 summarizes the values of A determined for each tube in this manner. The relative roughnesses of the tubes (reported originally by Coleman [22] and Garimella et al. [17]), required for the evaluation of the corresponding single-phase friction factor using the Churchill [15] correlation, are also shown. Also, it should be noted that since all the tubes under consideration in the current study have $D_h < 1$ mm, the liquid film is not in the turbulent region for any of the data points. Therefore, only the values of the exponents a, b, and c shown above for the laminar regime apply for the tubes considered in the present study.

The values of the constant A reported here are more strongly influenced by tube shape rather than hydraulic diameter. Comparing, for instance, the two circular tubes in Table 1, it can be seen that, even though the hydraulic diameter changes by approximately 40%, the change in the value of A obtained from regression is just 2%. This is to be expected because Garimella et al. [8] were able to predict the pressure drop for all circular tubes in the 0.506–4.91 mm diameter range using a single value for A, 1.308×10^{-3}, which lies between the values of the constants obtained here for tubes C20 and C30 individually.

The development above uses a physical model where the liquid forms an annular film around a gas core; however, the resulting correlation is also recommended for the mist-flow region. This applicability may be explained as follows. The flow visualization work of Coleman and Garimella [2] considered tubes only as small as those with $D_h=1$ mm, whereas the pressure drop measurements reported here include tubes with D_h as small as 0.424 mm. It is known from Coleman and Garimella's work that the extent of the annular-flow regime increases as the tube size decreases, as evidenced by the major portion of the flow-regime map for $D_h=1$ mm being in the annular-flow regime. Using this rationale, the annular-flow regime is expected to be larger for the $D_h<1$ mm tubes for which pressure drops are reported in this paper. In the absence of actual flow visualization data for these latter tubes, and keeping the uncertainties of extrapolation of the transition criteria in mind, the $D_h=1$ mm transition criteria were directly applied to the smaller tubes also in the present work. It is therefore to be expected that several of the data classified here as mist-flow points using the $D_h=1$ mm transition criteria could, in fact, be in the annular-flow regime. This phenomenon explains the applicability of the model developed using an annular-flow mechanism also to the neighboring flow regimes.

5 Model Implementation and Discussion

A comparison of the measured pressure drops and those calculated using the above two models is shown in Fig. 5 for each tube shape considered in this study. In the overlap zone (Fig. 2), the flow exhibits both the adjoining mechanisms (intermittent and annular/disperse-wave/mist flow). Therefore, for calculating the pressure drops in the overlap zones in Fig. 5, an interpolation technique similar to that described by Garimella et al. [8] in connection with the transition between laminar and turbulent data was applied to the pressure drops calculated using the intermittent- and annular-/disperse-wave-/mist-flow models. Figure 6 shows the predicted pressure drop versus the experimentally measured values for the entire set of data considered in this study: 80% of the data are predicted within ±25%. The applicable flow regimes for each data point are also shown in Fig. 5 and demonstrate that the model effectively captures the trends in the data based on the underlying physical phenomena: the variation in pressure drop with quality, mass flux, and tube diameter is well represented by the model.

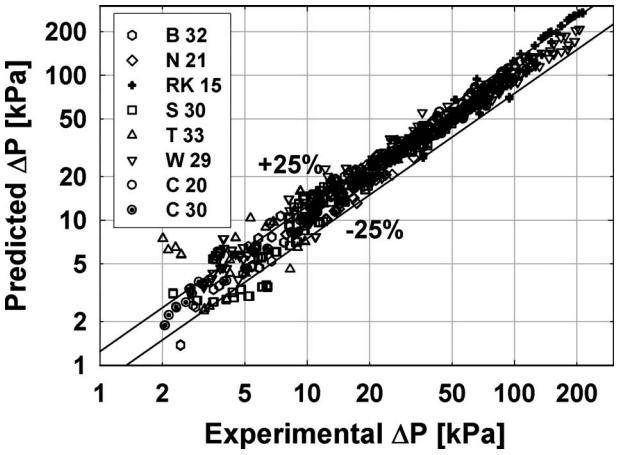

Fig. 6 Pressure drop model predictions

To further see the effect of the variation in tube shape on pressure drop, the pressure drop was plotted for each tube versus quality with a constant $L/D_{h,\text{nominal}}=500$ in Fig. 7. The length of all the tubes was fixed to 0.375 m and D_h was determined such that the flow cross-sectional area is the same as that of a circular tube of diameter 0.75 mm. The relative surface roughness for each tube was kept the same as in the case of the original tube. The pressure drop predicted by the intermittent- and the annular-/mist-flow-regime models exhibits the same trend in the variation with tube shape. The pressure drop increases with mass flux and quality as expected. The model predicts a decrease in pressure drop toward single-phase gas flow pressure drops as the quality approaches 1, as evidenced by the maxima in the graphs around $x \cong 0.9$. The slight changes in slope at the interfaces of the respective flow regimes reflect the different flow mechanisms across these interfaces. This graph shows that the W-insert tube has the highest pressure drop, which is to be expected because this is the only tube that does not have extruded channels. Among the other tubes, the rectangular channel (with an aspect ratio of 2) has high pressure drops, followed by triangular, N-shaped, square, and circular channels in decreasing order of pressure drop. The difference between the pressure drops for the square and rectangular tubes in Fig. 7 indicates that a change in aspect ratio by a factor of 2 causes an appreciable change in pressure drop. It is once again emphasized that the hydraulic diameters of these tubes (and therefore L/D_h) are not the same; rather the channel length and the flow area are the same. The D_h values required to keep the constant cross-sectional area are shown in Fig. 7 and do exhibit a range from 0.521 mm to 0.75 mm. A plot keeping L/D_h constant would show different trends; however, it would represent different mass flow conditions.

6 Conclusions

A multiple flow regime pressure drop model for condensing flow of refrigerant R134a in horizontal circular and noncircular tubes with $D<1$ mm was developed. Prior flow visualization studies by the authors were used to determine the applicable flow regimes for the pressure drop data, and individual pressure drop

Downloaded 03 Jun 2010 to 171.66.16.158. Redistribution subject to ASME license or copyright; see http://www.asme.org/terms/Terms_Use.cfm

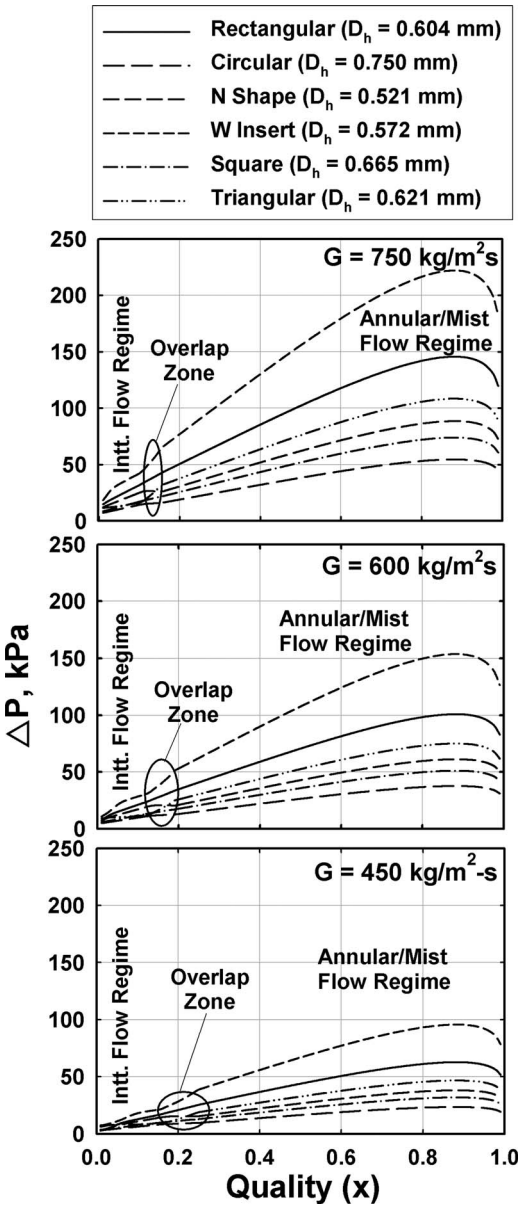

Fig. 7 Effect of tube shape on condensation pressure drop

models for each major flow regime were developed. The intermittent-flow pressure drop model (also shown to apply to overlap zone) treats the overall pressure drop as a combination of the contributions due to the liquid slug, the film-bubble interface region, and the transitions between the slug and the bubble. A slug frequency model was used to provide closure to the intermittent-flow model. In the annular-flow pressure drop model (also shown to apply to disperse-wave and mist flows), the interfacial friction factor derived from the measured pressure drops was correlated in terms of the corresponding liquid-phase Reynolds number and friction factor, the Martinelli parameter, and a surface tension-related parameter. Appropriate interpolation techniques were specified to address the regions of overlap and transition between the different regimes. The resulting combined model predicted 80% of the data for this wide range of flow conditions and tube shapes within ±25%.

Nomenclature

D = diameter (m or mm as noted)
ΔP = pressure drop (kPa)
f = friction factor (Darcy)
G = mass flux (kg/m^2 s)
L = tube length (m)
Re = Reynolds number
N = number
X = Martinelli parameter
x = vapor quality
α = void fraction
μ = dynamic viscosity (kg/m s)
ρ = density (kg/m^3)
σ = surface tension (N/m)
V = velocity (m/s)

Subscripts

avg = average
f = friction
h = hydraulic
I = gas-liquid interface
l = liquid
UC = unit cell
v = vapor

References

[1] Coleman, J. W., and Garimella, S., 1999, "Characterization of Two-Phase Flow Patterns in Small Diameter Round and Rectangular Tubes," Int. J. Heat Mass Transfer, **42**(15), pp. 2869–2881.
[2] Coleman, J. W., and Garimella, S., 2000, "Two-Phase Flow Regime Transitions in Microchannel Tubes: The Effect of Hydraulic Diameter," *American Society of Mechanical Engineers, Heat Transfer Division*, Vol. HTD-366, American Society of Mechanical Engineers, New York, pp. 71–83.
[3] Coleman, J. W., and Garimella, S., 2003, "Two-Phase Flow Regimes in Round, Square and Rectangular Tubes During Condensation of Refrigerant R134a," Int. J. Refrig., **26**(1), pp. 117–128.
[4] Lockhart, R. W., and Martinelli, R. C., 1949, "Proposed Correlation of Data for Isothermal Two-Phase, Two-Component Flow in Pipes," Chem. Eng. Prog., **45**(1), pp. 39–45.
[5] Chisholm, D., 1973, "Pressure Gradients Due to Friction During the Flow of Evaporating Two-Phase Mixtures in Smooth Tubes and Channels," Int. J. Heat Mass Transfer, **16**(2), pp. 347–358.
[6] Friedel, L., 1980, "Pressure Drop During Gas/Vapor-Liquid Flow in Pipes," Int. Chem. Eng., **20**(3), pp. 352–367.
[7] Friedel, L., 1979, "Improved Friction Pressure Drop Correlations for Horizontal and Vertical Two Phase Pipe Flow," *European Two Phase Flow Group Meeting*, Ispra, Italy, paper No. E2.
[8] Garimella, S., Agarwal, A., and Killion, J. D., 2005, "Condensation Pressure Drop in Circular Microchannels," Heat Transfer Eng., **26**(3), pp. 1–8.
[9] Lee, H. J., and Lee, S. Y., 2001, "Pressure Drop Correlations for Two-Phase Flow Within Horizontal Rectangular Channels With Small Heights," Int. J. Multiphase Flow, **27**(5), pp. 783–796.
[10] Tran, T. N., Chyu, M.-C., Wambsganss, M. W., and France, D. M., 2000, "Two-Phase Pressure Drop of Refrigerants During Flow Boiling in Small Channels, An Experimental Investigation and Correlation Development," Int. J. Multiphase Flow, **26**(11), pp. 1739–1754.
[11] Mishima, K., and Hibiki, T., 1996, "Some Characteristics of Air-Water Two-Phase Flow in Small Diameter Vertical Tubes," Int. J. Multiphase Flow, **22**(4), pp. 703–712.
[12] Kawahara, A., Chung, P. M.-Y., and Kawaji, M., 2002, "Investigation of Two-Phase Flow Pattern, Void Fraction and Pressure Drop in a Microchannel," Int. J. Multiphase Flow, **28**(9), pp. 1411–1435.
[13] Garimella, S., Agarwal, A., and Coleman, J. W., 2003, "Two-Phase Pressure Drops in the Annular Flow Regime in Circular Microchannels," *21st IIR International Congress of Refrigeration*, International Institute of Refrigeration, p. ICR0360.
[14] Garimella, S., Killion, J. D., and Coleman, J. W., 2002, "An Experimentally Validated Model for Two-Phase Pressure Drop in the Intermittent Flow Regime for Circular Microchannels," ASME J. Fluids Eng., **124**(1), pp. 205–214.
[15] Churchill, S. W., 1977, "Friction-Factor Equation Spans All Fluid-Flow Regimes," Chem. Eng. Prog., **84**(24), pp. 91–92.
[16] Coleman, J. W., and Garimella, S., 2000, "Visualization of Two-Phase Refrigerant Flow During Phase Change," *Proceedings of the 34th National Heat Transfer Conference*, ASME, Vol. NHTC 2000-12115.
[17] Garimella, S., Killion, J. D., and Coleman, J. W., 2003, "An Experimentally Validated Model for Two-Phase Pressure Drop in the Intermittent Flow Regime for Noncircular Microchannels," ASME J. Fluids Eng., **125**(5), pp. 887–894.
[18] Suo, M., and Griffith, P., 1964, "Two-Phase Flow in Capillary Tubes," ASME J. Basic Eng., **86**, pp. 576–582.
[19] Dukler, A. E., and Hubbard, M. G., 1975, "A Model for Gas-Liquid Slug Flow

Downloaded 03 Jun 2010 to 171.66.16.158. Redistribution subject to ASME license or copyright; see http://www.asme.org/terms/Terms_Use.cfm

in Horizontal and Near Horizontal Tubes," Ind. Eng. Chem. Fundam., **14**(4), pp. 337–347.
[20] Fukano, T., Kariyasaki, A., and Kagawa, M., 1989, "Flow Patterns and Pressure Drop in Isothermal Gas-Liquid Concurrent Flow in a Horizontal Capillary Tube," *Proceedings of the 1989 ANS National Heat Transfer Conference*, Vol. 4, pp. 153–161.
[21] Baroczy, C. J., 1965, "Correlation of Liquid Fraction in Two-Phase Flow With Applications to Liquid Metals," Chem. Eng. Prog., Symp. Ser., **61**(57), pp. 179–191.
[22] Coleman, J. W., 2000, "Flow Visualization and Pressure Drop in Small Hydraulic Diameter Geometries During Phase Change of Refrigerants," Ph.D. thesis, Iowa State University, Ames, IA.

Downloaded 03 Jun 2010 to 171.66.16.158. Redistribution subject to ASME license or copyright; see http://www.asme.org/terms/Terms_Use.cfm

Liquid Taylor Bubbles Rising in a Vertical Column of a Heavier Liquid: An Approximate Analysis

T. K. Mandal
Department of Chemical Engineering,
National Institute of Technology,
Durgapur WB-713209, India
e-mail: tapasmn@gmail.com

G. Das[1]
Department of Chemical Engineering,
Indian Institute of Technology,
Kharagpur WB-721302, India
e-mail: gargi@che.iitkgp.ernet.in

P. K. Das
Department of Mechanical Engineering,
Indian Institute of Technology,
Kharagpur WB-721302, India
e-mail: pkd@mech.iitkgp.ernet.in

It has been noted that a volume of lighter liquid when injected into a stationary column of a heavier liquid, it rises up as a simple elongated Taylor bubble. In the present study, experimental and theoretical analyses have been performed to understand the rise of liquid Taylor bubbles. The experiments have been performed with different liquid pairs with their viscosities ranging from 0.71 mPa s to 1.75 mPa s and conduit sizes ranging from 0.012 m to 0.0461 m. The bubble shape has been predicted using a potential flow analysis and validated from photographic measurements. This analysis has been further modified to predict the rise velocity. The modified analysis accounts for the density difference between the two liquids, viscosity effects of the primary liquid, and interfacial tension of two fluids. A semi-empirical equation has been developed, which gives satisfactory results for most of the cases. [DOI: 10.1115/1.3026730]

Keywords: liquid Taylor bubble, shape, rise velocity, mathematical modeling, viscous potential flow

1 Introduction

Taylor bubbles (TBs) are typical elongated gas bubbles, which occupy almost the entire cross section of a liquid filled conduit and move along its axis. In a circular tube they are characterized by an axisymmetric bullet shaped nose, a cylindrical body, and a flat or jagged tail (Fig. 1). However, the shape of the Taylor bubble depends to a larger extent on the cross section [1–3] and inclination of the conduit and to a smaller extent on the properties of the fluid pair. The shape is also sensitive to the size of the conduit. For example, Taylor bubbles observed in narrow circular tubes have a dome shaped nose and tail [4,5], while in a wider conduit, these are characterized by a hemispherical nose and a flat tail. Taylor bubbles are observed in a myriad of gas-liquid two-phase systems. During the drainage of the liquid from a liquid filled vertical tube whose top end is closed, the rising gas finger assumes the characteristic shape of a Taylor bubble. In slug flow, Taylor bubbles and liquid slugs follow one another in rapid succession.

Over the years, the hydrodynamics of Taylor bubbles have attracted the attention of a number of researchers. In their pioneering works Dumitrescu [6] and Davies and Taylor [7] theoretically analyzed the motion of elongated gas bubbles rising through a vertical tube filled with an ideal fluid. Later the same problem was investigated comprehensively using theoretical [8–13], experimental [1,14–20], and numerical [21–25] techniques. In addition, studies have been performed to investigate the effect of liquid properties such as surface tension [26–30] and viscosity [31–36], liquid velocity, conduit geometry [4,37,38], and inclination [1,15,16] on the dynamics of Taylor bubbles. Nevertheless, the complexity of the problem could not be resolved completely as one can appreciate from the large number of correlations proposed in literature [39–41]. Recently Viana et al. [42] considered a voluminous data bank of experimental results and proposed a universal correlation for the rise velocity of Taylor bubbles through circular tubes.

When a lighter liquid is introduced in a tube filled with another immiscible and heavier liquid, it rises up as a single elongated drop, which is similar in shape to that of a Taylor bubble, as shown in Fig. 1. The dynamics of such liquid Taylor bubbles (LTBs) play an important role in the transport of liquid-liquid two-phase mixtures through conduits. However, the motion of a LTB has rarely been investigated except for a few brief mentions [1]. Brauner and Ullmann [43,44] studied gas entrainment from a Taylor bubble for moving and stationary bubbles. In the present work the motion of LTB through vertical tubes has been studied experimentally for different liquid-liquid systems and tube diameters. The theoretical models available in literature for gas-liquid systems have been modified to predict the shape and rise velocity of the LTBs. No such study has to date been reported on the rise of a liquid Taylor bubble to the best of the author's knowledge.

2 Experiments

The schematic of the experimental facility is shown in Fig. 2. The main component of the setup is a 1.5 m long borosilicate glass tube G pivoted to a frame F to facilitate free rotation. The tube is closed at both ends. Near the ends two small side tubes N_1 and N_2 are provided with valve connections. They are used for filling up and emptying the tube with the test liquids. Experiments have been conducted in tubes of different internal diameters ranging from 0.012 m to 0.0461 m. The liquids used and their measured properties are listed in Table 1. The viscosity, surface tension, and specific gravity of the individual liquids are measured using an Ostwald viscometer, stalagmometer, and electronic balance, respectively, while the interfacial tension between different liquid pairs is estimated using a ring tensiometer. The liquid properties are measured several times and the average values are taken to minimize experimental errors.

As the hydrodynamics of the bubble is sensitive to any trace of impurity, the tubes are thoroughly cleaned before using a particular pair of liquids. They are washed with detergent solution and distilled water to remove any dirt or grease. Then they are rinsed with acetone and dried. The tube is first completely filled up with the heavier liquid (henceforth referred to as the primary liquid). The lighter liquid designated as the secondary liquid is slowly introduced through the side tube N_1 keeping G in the vertical position. During this process, an identical volume of primary liq-

[1]Corresponding author.

Contributed by the Fluids Engineering Division of ASME for publication in the JOURNAL OF FLUIDS ENGINEERING. Manuscript received December 9, 2007; final manuscript received September 3, 2008; published online December 2, 2008. Assoc. Editor: Theodore Heindel.

 Copyright © 2009 by ASME

Downloaded 03 Jun 2010 to 171.66.16.158. Redistribution subject to ASME license or copyright; see http://www.asme.org/terms/Terms_Use.cfm

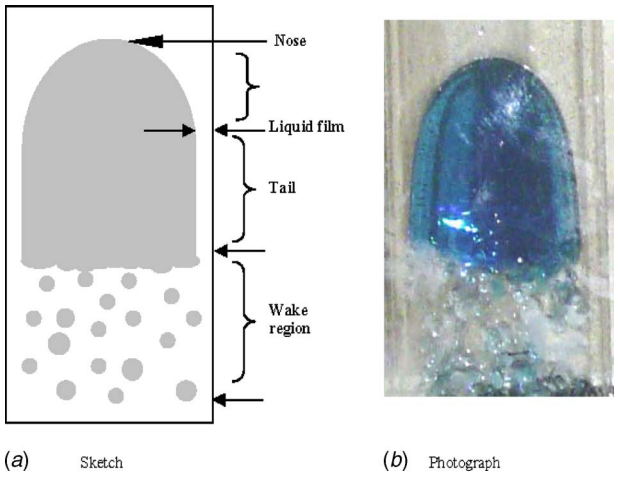

Fig. 1 Kerosene Taylor bubble rising in water: (*a*) sketch and (*b*) photograph

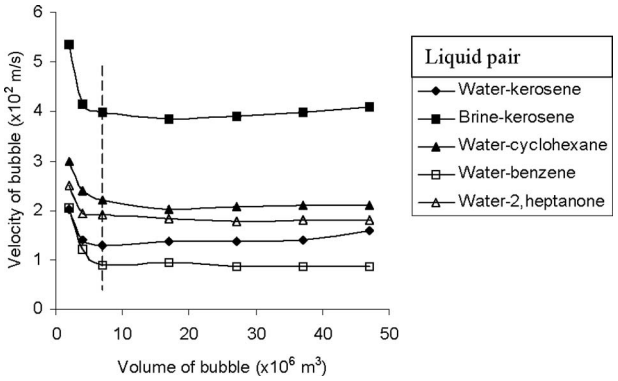

Fig. 3 Experimental values of the bubble velocity as a function of the bubble volume for the different pairs of liquids studied

uid is discharged through tube N_2. Both valves are closed once a required amount of secondary liquid is introduced into the tube. Extreme care is taken to ensure that no air bubble gets entrapped inside the tube during the process of filling up since visual observations reveal that the small air bubbles get attached to the tip of the LTB. This renders the tip pointed and increases the rise velocity substantially.

For studying the rise of LTB, the tube is inverted so that the secondary liquid occupies the bottommost position. The secondary fluid assumes the typical shape of a Taylor bubble and rises by downward displacement of the heaver fluid. Its rise velocity is estimated by noting the time of travel between two markings (P_1 and P_2) at a known distance (0.5 m apart). The markings are made at a distance 0.5 m from each end of the tube. These markings are made away from the entry and exit of the tube to avoid end effects, if any. In order to ensure that the LTB acquires its terminal rise velocity before reaching the first marking, several velocity measurements have been made over different length intervals at various positions of the tube. It is noted that the velocity thus obtained remains constant over different distances after about 0.45 m from the entry section. Therefore a distance of 0.5 m has been selected from the entry and exit sections for the experiments, and the velocity has been measured from the time taken by the LTB to traverse a distance of 0.5 m. A number of typical bubbles are photographed using a digital camera (Sony, DSC F717), near the marking P_2. During photography we used a rectangular glass view box (VB) (in Fig. 2) to minimize the effects of reflection and refraction at the curved tube surface. The rise velocities for a given volume of LTB are measured at least five times and the average value is registered. The velocity has also been measured using the optical probe technique described by Jana et al. [45] as an additional check. The uncertainties in measurements have been obtained as $\pm 0.5\%$.

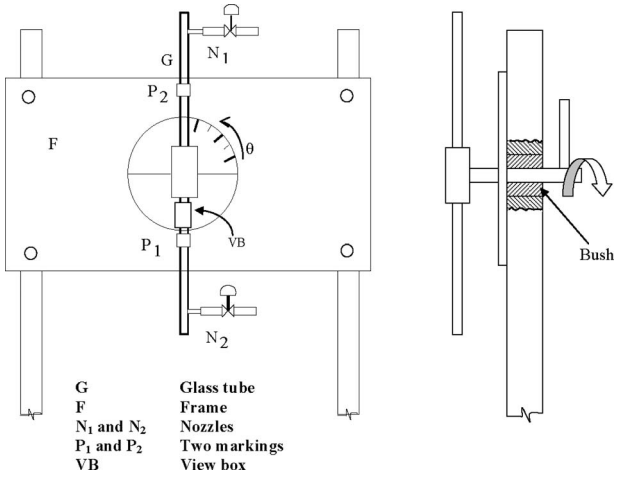

Fig. 2 Schematic of the experimental facility

Table 1 Physical properties of test liquids

Fluid	Density (kg/m^3)	Viscosity (mPa s)	Interfacial tension with water (N/m)
Water	1000	1	—
Kerosene	787	1.2	0.0385
Benzene	879	0.73	0.0356
Cyclohexane	775	0.96	0.0585
2,heptanone	810	0.71	0.0208
Brine solution	1200	1.75	0.0378 (With kerosene)

3 Results and Discussions

A typical curve representing the variation of rise velocity with bubble volume has been plotted in Fig. 3. The figure shows that rise velocity decreases sharply with an increase in bubble volume for all the cases and finally attains an asymptotic value. The visual observations reveal that at a small volume, bubbles are of spheroidal shape. With increase in volume, they gradually enlarge to form spherical cap bubbles and a large amount of the lighter liquid produces Taylor bubbles. Once Taylor bubbles are formed, the rise velocity remains constant.

To understand the effect of fluid properties on the rise velocity, the variation in the Froude number (Fr) with the Eötvös number (Eo) is plotted in Fig. 4. For all the liquid pairs, Fr increases sharply with Eo until it gradually reaches an asymptotic value. However, the different curves for different liquid pairs indicate the importance of fluid properties other than those included in Eo. It is interesting to note that White and Beardmore [15] performed experiments on gas-liquid systems using a wide variety of liquids and obtained a trend similar to that observed for the different liquid pairs in Fig. 4. This indicates a striking similarity between the rise of Taylor bubbles in both gas-liquid and liquid-liquid systems.

With this consideration, a simple model has been proposed to predict the shape and velocity of a LTB rising through a heavier liquid.

Downloaded 03 Jun 2010 to 171.66.16.158. Redistribution subject to ASME license or copyright; see http://www.asme.org/terms/Terms_Use.cfm

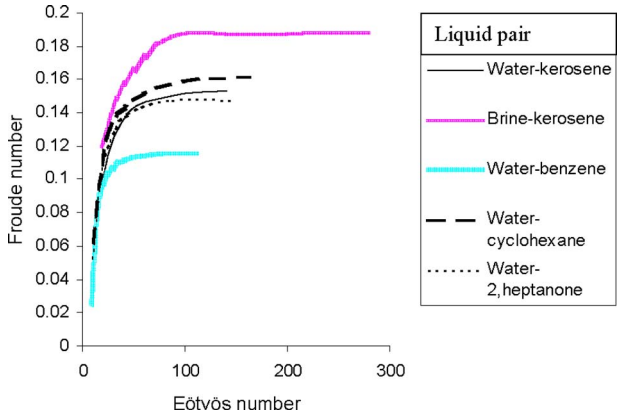

Fig. 4 Experimental Froude number as a function of the Eötvös number for the different pairs of liquids studied

4 Prediction of the Shape of LTB

A close observation of the photographs has revealed that the nose of the bubble once formed does not change with length. It is independent of bubble size and is a function of tube dimensions only. This is in agreement with the observations made for gas bubbles through stationary liquid columns. On this basis, the shape of the Taylor bubble is obtained from a potential flow analysis of the situation. The underlying assumptions of the model are as follows.

(1) Both the fluids are incompressible.
(2) The effect of viscosity is negligible.
(3) Flow is unidirectional.
(4) The origin of the frame of reference lies at the tip of the bubble nose and rises with the bubble at its rise velocity. Accordingly, the bubble appears stationary with respect to the reference frame and the primary liquid flows toward the bubble at its rise velocity (U), as shown in Fig. 5.

Following the methodology of Batchelor [8], the mass balance of the heavier liquid between AA at infinite distance from the bubble and BB at the intersection of the nose and tail region (Fig. 5) yields

$$\pi U R^2 = \pi(U + U_F)(R^2 - R_c^2) \tag{1}$$

where R is the tube radius, R_c is the equilibrium radius at the tail of the Taylor bubble (Fig. 5), U is the bubble rise velocity in the stationary liquid, and U_F is the terminal film velocity relative to the tube wall at section BB.

Rearranging Eq. (1) we get

$$U R_c^2 = U_F(R^2 - R_c^2) \tag{2}$$

Following the methodology of Dumitrescu [6], the plug flow has been assumed in the film. The asymptotic film profile in the nose region can thus be approximated as

$$R^2 U = \{R^2 - (R - \delta)^2\} U_i \tag{3}$$

where U_i, the tangential velocity at the interface, is $U+U_F$, δ, the film thickness, is $(R-r_i)$, and r_i is the radial coordinate of the interface.

For the flow of the primary liquid along the bubble surface between point 0 (stagnation point) and point 1 in Fig. 5, we apply Bernoulli's equation and obtain

$$P_0 + h_1 \rho_p g = P_1 + \tfrac{1}{2}\rho_p U_i^2 + h_2 \rho_p g \tag{4}$$

where ρ_p is the density of the primary liquid, P_0 is the pressure at point 0, the tip of the bubble nose, and P_1 is the pressure at point 1. h_1 and h_2, as denoted in Fig. 5, are the respective distances of points 0 and 1 from a reference plane.

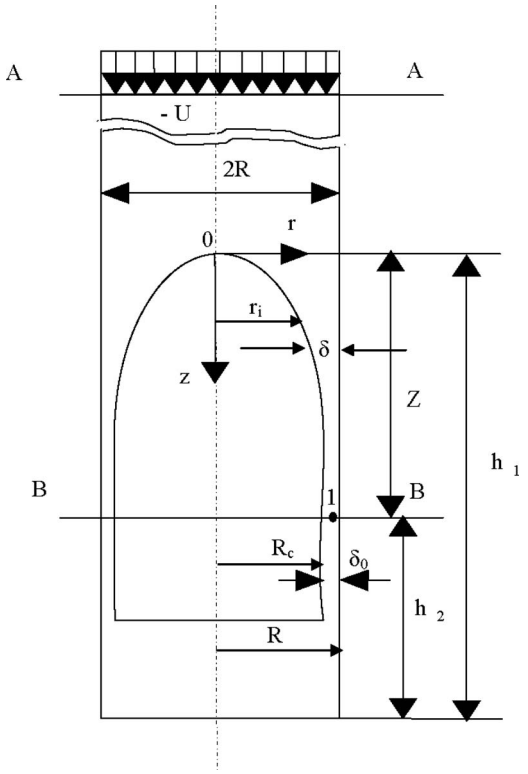

Fig. 5 Coordinate axis to predict the shape of the liquid Taylor bubble

From assumption (4), the bubble is assumed stationary with respect to the frame of reference. This gives the pressure difference $(P_1 - P_0)$ as

$$P_1 = P_0 + Z\rho_s g \tag{5}$$

where ρ_s is the density of the secondary liquid and Z, the axial distance from the bubble tip, is $(h_1 - h_2)$.

From Eqs. (4) and (5) one gets

$$P_0 + (h_1 - h_2)\rho_p g = P_0 + Z\rho_s g + \tfrac{1}{2}\rho_p U_i^2 \tag{6}$$

or

$$U_i = \left[2Zg\frac{(\rho_p - \rho_s)}{\rho_p} \right]^{1/2} \tag{7}$$

Combining Eqs. (3) and (7) we get

$$U = \left\{ 1 - \left(1 - \frac{\delta}{R} \right)^2 \right\} \left[2gZ\left(\frac{\rho_p - \rho_s}{\rho_p} \right) \right]^{1/2} \tag{8}$$

Substituting the dimensionless bubble radius as $r^* = (1 - (\delta/R))$ in Eq. (8), the final expression becomes

$$r^* = \left[1 - \mathrm{Fr}\left(\frac{R}{Z} \right)^{1/2} \right]^{1/2} \tag{9}$$

where

$$\mathrm{Fr} = \frac{U\sqrt{\rho_p}}{\sqrt{\Delta\rho g D}}$$

$\Delta\rho = \rho_p - \rho_s$ and D is the tube diameter.

The above expression shows that the bubble shape is a function of the Froude number (Fr) and the tube dimension. It does not depend on the bubble dimension, as has also been noted from photographs. The bubble shape can thus be predicted from Eq. (9) for different tube diameters and liquid pairs.

Downloaded 03 Jun 2010 to 171.66.16.158. Redistribution subject to ASME license or copyright; see http://www.asme.org/terms/Terms_Use.cfm

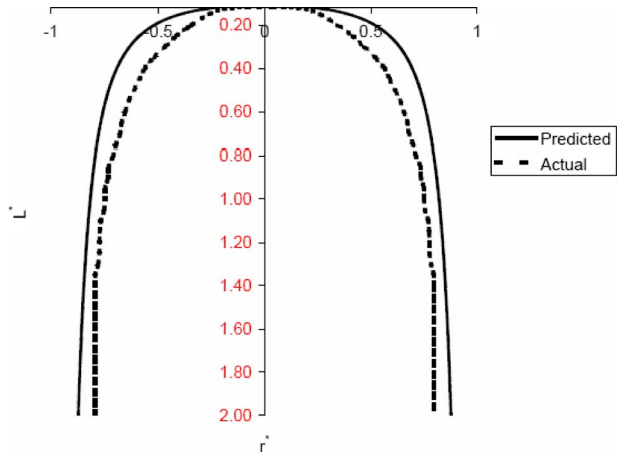

Fig. 6 Comparison between the prediction of Eq. (9) and the experimental shape of a kerosene bubble rising in a 0.0461 m i.d. tube filled with water

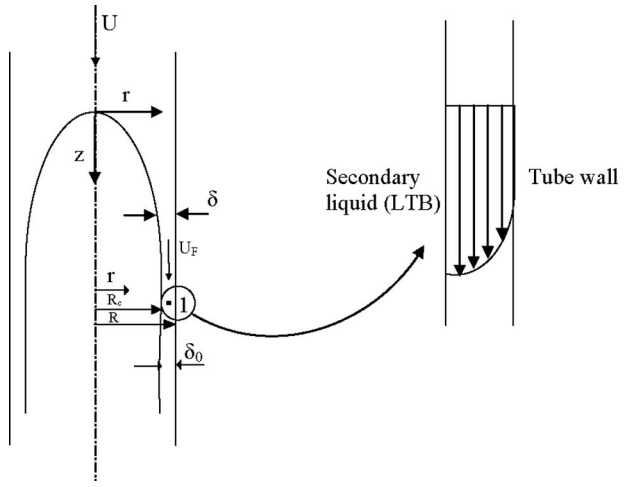

Fig. 7 The flow of primary liquid around the liquid Taylor bubble

The actual shape of the LTB has also been obtained from photographs with the help of the software IMAGE PRO-PLUS Version 5.1. A comparison between the shapes estimated from experiments and analysis is made by superimposing the two on a plot of dimensionless bubble length ($L^*=Z/R$) against the dimensionless bubble radius (r^*). One representative case for the kerosene-water pair in a 0.0461 m i.d. tube is presented in Fig. 6. The slight mismatch in the figure can be attributed to the simplifying assumptions of the model, which does not account for the effect of viscosity and surface tension.

5 Prediction of the Rise Velocity of LTB

The rise velocity is predicted from a modified form of the potential flow analysis. The model modifies the analysis by Brown [33] and incorporates the density correction as well as the effect of viscosity in the tail region of the Taylor bubble while considering the inviscid flow at the nose due to the flat velocity profile in the approach field. The assumptions underlying the model include viscous potential flow, laminar flow in the film, zero interfacial shear stress, and negligible pressure gradient along the film. With these considerations, the liquid flow in the film and nose regions has been considered in more detail with a view to obtain the rise velocity of the bubble.

6 The Film Region

Following the methodology of Brown [33] the film region has been divided into two distinct sections; one in which a portion of the liquid is accelerating freely, and the remaining portion is supported by wall shear and another in which the entire film is in steady laminar flow and supported by wall shear. The analysis of the flow in the transition region is more complex as compared with the analysis of the equilibrium laminar film.

The flow of the liquid in the equilibrium annular film of a LTB is shown in Fig. 7. The force balance on an element of the film (say at point 1) for a vertical tube gives

$$\frac{1}{r}\frac{\partial(\tau r)}{\partial r} - \rho_p g + \frac{\partial P}{\partial Z} = 0 \tag{10}$$

Now considering that $\partial P/\partial Z$ arises due to static pressure difference inside the bubble,

$$\frac{\partial P}{\partial Z} = \rho_s g$$

$$\left[\because \Delta P = Z\rho_s g, \frac{\partial P}{\partial Z} = \rho_s g\right] \tag{11}$$

Therefore Eq. (10) becomes

$$\frac{1}{r}\frac{\partial(\tau r)}{\partial r} - (\rho_p - \rho_s)g = 0 \tag{12}$$

or

$$d(\tau r) = (\rho_p - \rho_s)g r dr \tag{13}$$

where r is the radial position and τ is the shear stress.

Integrating Eq. (13) from the bubble interface to any point in the film region gives

$$\tau r = (\rho_p - \rho_s)g\frac{r^2 - R_c^2}{2} \tag{14}$$

where R_c is the equilibrium radius at the tail of the Taylor bubble.

If the primary liquid is Newtonian, then

$$\tau = \mu_p \frac{du}{dr} \tag{15}$$

where μ_p is the viscosity of the primary liquid, u is the axial component of velocity, and r is the radial position.

Substituting Eq. (15) in Eq. (14) we get

$$du = (\rho_p - \rho_s)g\frac{r^2 - R_c^2}{2\mu_p r}dr \tag{16}$$

The velocity distribution in the film is obtained by integrating Eq. (16) from r (any radial position) to R (tube radius) as follows:

$$-u = \left(\frac{\rho_p - \rho_s}{2\mu_p}\right)g\left[\frac{R^2 - r^2}{2} - R_c^2 \ln\frac{R}{r}\right] \tag{17}$$

This gives the average velocity of the liquid in the film from a balance of the volumetric flow rates as

$$\pi U_F(R^2 - R_c^2) = 2\pi\int_{R_c}^{R} u r dr \tag{18}$$

Combining Eqs. (17) and (18) we get

Downloaded 03 Jun 2010 to 171.66.16.158. Redistribution subject to ASME license or copyright; see http://www.asme.org/terms/Terms_Use.cfm

$$U_F = \frac{\rho_p - \rho_s}{\mu_p} g \left[\frac{R_c^4}{2(R^2 - R_c^2)} \ln \frac{R_c}{R} + \frac{3R_c^2}{8} - \frac{R^2}{8} \right] \tag{19}$$

From Eqs. (2) and (19) we get

$$U = \frac{\rho_p - \rho_s}{\mu_p} g \frac{R^2}{\left(1 - \frac{\delta}{R}\right)^2} \left[\frac{2}{3} \left(\frac{\delta}{R}\right)^3 \left(1 - \frac{\delta}{R}\right) + \frac{1}{10} \left(\frac{\delta}{R}\right)^5 + \frac{1}{60} \left(\frac{\delta}{R}\right)^6 + \cdots \right] \tag{20}$$

The above equation can be expressed in terms of relative film thickness $\xi_0(\delta_0/R)$ as

$$U = \frac{\rho_p - \rho_s}{\mu_p} g \frac{R^2}{(1 - \xi_0)^2} \left[\frac{2}{3} \xi_0^3 (1 - \xi_0) + \frac{1}{10} \xi_0^5 + \frac{1}{60} \xi_0^6 + \cdots \right] \tag{21}$$

where δ_0 is the terminal film thickness in the tail region of the LTB beyond line BB in Fig. 5 and R is the tube radius.

Neglecting the higher order term greater than 4, the equation reduces to

$$U = \frac{2}{3} \frac{\rho_p - \rho_s}{\mu_p} g R^2 \frac{\xi_0^3}{1 - \xi_0} \tag{22}$$

7 Nose Region

From the potential flow analysis at the nose region, as mentioned by Brown [33], the velocity of the Taylor bubbles are well correlated by the equation

$$U = 0.496 \sqrt{g R_c} \tag{23}$$

Upon introducing the density correction term the above equation becomes

$$U = 0.496 \sqrt{\frac{\rho_p - \rho_s}{\rho_p} g R_c} \tag{24}$$

A simultaneous solution of Eqs. (22) and (24) gives the equilibrium film thickness as

$$\delta_0 = \frac{-1 + \sqrt{1 + 4NR}}{2N} \tag{25}$$

where

$$N = \left[1.81 \frac{(\rho_p - \rho_s)\rho_p}{\mu_p^2} g \right]^{1/3} \tag{26}$$

Expressing R_c in terms of N,

$$R_c = R - \delta_0 = R \left(1 - \frac{-1 + \sqrt{1 + 4NR}}{2NR} \right) \tag{27}$$

and combining Eqs. (24) and (27), we get

$$U = 0.496 \sqrt{\frac{\rho_p - \rho_s}{\rho_p} g R} \sqrt{1 - \frac{-1 + \sqrt{1 + 4NR}}{2NR}} \tag{28}$$

Equation (28) can be used to predict the rise velocity of a Taylor bubble by accounting for the density and viscosity effects. An attempt has next been made to incorporate the effect of surface tension in the expression.

A survey of the past literature shows that in gas-liquid systems the different correlations for the rise of TBs generally account for the influence of surface tension by using the Eötvös number $[g(\rho_p - \rho_s)D^2/\sigma]$. Different researchers [29,38,40] proposed different expressions including Eo in their correlations. For large buoyancy Reynolds number ($\mathrm{Re}_b > 200$), Wallis [40] considered the effect of interfacial tension using the following function of the Eötvös number:

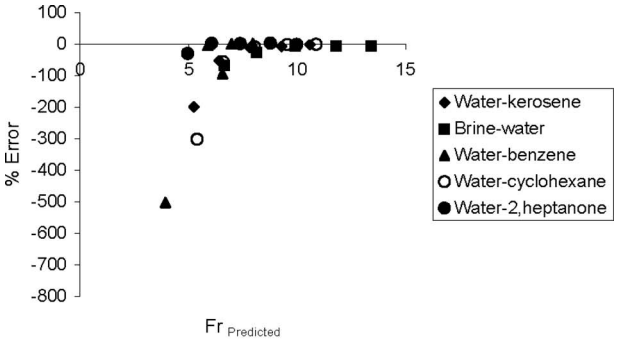

(*a*) % Error in prediction of Eq. (28)

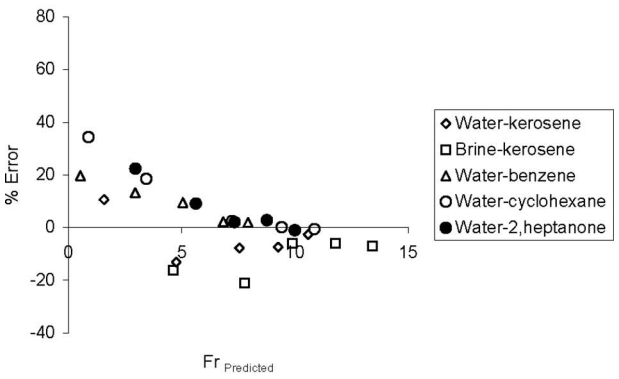

(*b*) % Error in prediction of Eq. (29)

Fig. 8 Percentage error in prediction of rise velocity of a liquid Taylor bubble

$$\frac{1}{\left(1 + \frac{3805}{\mathrm{Eo}^{3.06}}\right)^{0.58}}$$

Incorporating the same factor in Eq. (28), the final expression of the rise velocity is obtained as

$$U = 0.496 \sqrt{\frac{\rho_p - \rho_s}{\rho_p} g R} \sqrt{1 - \frac{-1 + \sqrt{1 + 4NR}}{2NR}} \frac{1}{\left(1 + \frac{3805}{\mathrm{Eo}^{3.06}}\right)^{0.58}} \tag{29}$$

The above analysis yields a semi-empirical equation, which accounts for the effects of surface tension, viscous effects, and density difference between the two liquids. The predictions of the equation have been validated with the experimental results for different tube diameters and liquid properties. These validations are presented in Fig. 8 and Table 2. In Fig. 8 the percentage error is plotted against the predicted Froude number where the percentage error is calculated based on the experimental value. The figure shows the improvement in prediction of Eq. (29) as compared with Eq. (28). Moreover predictions are better for some liquid pairs, namely, water-kerosene, brine-kerosene, and water-benzene.

The results are also listed in Table 2 along with the buoyancy Reynolds number ($\mathrm{Re}_b = [D^3 g(\rho_p - \rho_s)\rho_p]^{1/2}/\mu_p$) for each case to show the diameter effect on the predicted results. The table shows that the theoretical values are close to the experimental results for pipes of larger diameters while the deviation is consistently higher for tubes of 0.012 m and 0.0176 m diameter. It is felt that this discrepancy arises because the present analysis does not consider the effect of the viscosity of the secondary liquid. This may be justifiable in the analysis of rising gas bubbles, as the viscosity of

Downloaded 03 Jun 2010 to 171.66.16.158. Redistribution subject to ASME license or copyright; see http://www.asme.org/terms/Terms_Use.cfm

Table 2 Comparison of predicted results with experimental results

Sl. No.	Liq. Pair	$D\times10^2$ (m)	$\mathrm{Re}_b\times10^{-3}$	$U_{expt}\times10^2$ (m/s)	$U_{predicted}$ from Eq. (28) $\times10^2$ (m/s)	Deviation (%)	$U_{predicted}$ from Eq. (29)$\times10^2$ (m/s)	Deviation (%)
1	Kerosene bubble in water	1.2	1.90	1.75	5.24	−199.6	1.56	10.6
		1.76	3.38	4.21	6.42	−52.61	4.76	−13.1
		2.57	5.96	6.99	7.82	−11.9	7.54	−7.8
		3.58	9.79	8.6	9.29	−7.93	9.25	−7.4
		4.61	14.31	10.3	10.6	−2.73	10.58	−2.6
2	Kerosene bubble in brine	1.2	2.90	3.96	6.4	−67.7	4.61	−16.36
		1.76	5.15	6.4	8.1	−26.9	7.76	−21.12
		2.57	9.08	9.3	9.9	−6.45	9.88	−5.95
		3.58	14.94	11.1	11.8	−6.2	11.78	−6.13
		4.61	21.82	12.55	13.4	−7.06	13.43	−7.05
3	Benzene bubble in water	1.2	1.43	0.65	3.93	−502.8	0.52	19.7
		1.76	2.54	3.39	6.56	−93.8	2.94	13.3
		2.57	4.49	5.58	5.87	−5.2	5.05	9.5
		3.58	7.38	6.98	6.98	0.023	6.83	2.2
		4.61	10.78	8.08	7.96	1.5	7.92	1.97
4	Cyclohexane bubble in water	1.2	1.95	1.3	5.4	−302.3	0.88	34.3
		1.76	3.47	4.2	6.6	−56.8	3.43	18.5
		2.57	6.12	7.4	8.04	−8.69	7.22	2.5
		3.58	10.06	9.4	9.55	−1.42	9.4	0.14
		4.61	14.71	10.8	10.88	−0.96	10.85	−0.62
5	2,heptanone bubble in water	1.2	1.79	3.81	4.95	−29.97	2.95	22.4
		1.76	3.18	6.18	6.06	2.03	5.62	9.1
		2.57	5.61	7.48	7.38	1.3	7.3	2.07
		3.58	9.22	9.01	8.77	2.65	8.76	2.75
		4.61	13.48	9.89	9.99	−1.07	9.99	−1.05

gas is substantially lower than the viscosity of the surrounding liquid. On the contrary, the viscosities of the primary and secondary fluids are of comparable orders of magnitude in the present case.

8 Conclusions

Based on potential flow theory, a model has been proposed to predict the shape of a liquid Taylor bubble. The slight deviations between the predicted and actual shapes suggest the limitations of the theory. Accordingly, it has been modified to predict the rise velocity of the LTBs. The modified analysis incorporates the effect of viscosity of the primary fluid, density difference between the two liquids, and surface tension effects. The analysis by Brown [33] has been considered for this purpose and the laminar film solution at the tail region is coupled with the potential flow theory at the nose region. The effect of surface tension has been considered from the correlation proposed by Wallis [40]. The predictions of the analysis are in close agreement with experimental data on rise velocity for most of the cases. The only exceptions are at small pipe diameters. This probably arises due to the limitations of the semi-empirical approach.

The complex hydrodynamics of a liquid Taylor bubble can be explained from a rigorous analysis starting from the basic physics of the flow situation. Computational techniques may be adopted for this purpose. Extensive experiments are required to study the effect of viscosity of the secondary fluid on the rise velocity of the Taylor bubble and to incorporate this effect in the theoretical analysis.

Nomenclature

Eo = Eötvös number$=(\rho_p-\rho_s)gD^2/\sigma$
Fr = Froude number$=U\sqrt{\rho_p}/\sqrt{\Delta\rho gD}$
Re_b = buoyancy Reynolds number$=[D^3g(\rho_p-\rho_s)\rho_p]^{1/2}/\mu_p$
h_1, h_2 = respective distances of points 0 and 1 from a reference plane in Fig. 5 (m)
L^* = dimensionless bubble length$=Z/R$
r^* = dimensionless bubble radius$=(1-\delta/R)$
D = tube diameter (m)
N = dimensional parameter (m^{-1})
P_0 = pressure at the tip of the bubble nose (Pa)
P_1 = pressure at point 1 (Pa)
R = tube radius (m)
R_c = equilibrium radius at the tail of the Taylor bubble (m)
U = bubble rise velocity in stationary liquid (m/s)
U_F = average liquid velocity in the film relative to the tube wall (m/s)
U_i = tangential velocity at the interface (m/s)
g = gravitational acceleration (m/s^2)
r = radial position (m)
r_i = radial coordinate of the interface
u = axial component of velocity (m/s)
Z = axial distance from the bubble tip (m)

Greek Letters

δ = film thickness at any radial position as shown in Fig. 5 $=R-r_i$ (m)
δ_0 = terminal film thickness in tail region as shown in Fig. 5 $=R-R_c$ (m)
ρ_p = density of the primary liquid (kg/m^3)
ρ_s = density of the secondary liquid (kg/m^3)
$\Delta\rho$ = $(\rho_p-\rho_s)$ (kg/m^3)
τ = shear stress (N/m^2)
ξ_0 = dimensionless terminal film thickness$=\delta_0/R$

Downloaded 03 Jun 2010 to 171.66.16.158. Redistribution subject to ASME license or copyright; see http://www.asme.org/terms/Terms_Use.cfm

μ_p = viscosity of primary liquid (mPa s)
σ = interfacial tension (N/m)

References

[1] Zukoski, E. E., 1966, "Influence of Viscosity, Surface Tension, and Inclination Angle on Motion of Long Bubbles in Closed Tubes," J. Fluid Mech., **25**, pp. 821–837.

[2] Couet, B., and Strumolo, G. S., 1987, "The Effects of Surface Tension and Tube Inclination on a Two-Dimensional Rising Bubble," J. Fluid Mech., **184**, pp. 1–14.

[3] Fagundes Netto, J. R., Fabre, J., and Peresson, L., 1999, "Shape of Long Bubbles in Horizontal Slug Flow," Int. J. Multiphase Flow, **25**, pp. 1129–1160.

[4] Bi, C. Q., and Zhao, T. S., 2001, "Taylor Bubbles in Miniaturized Circular and Noncircular Channels," Int. J. Multiphase Flow, **27**, pp. 561–570.

[5] Wallis, G. B., 1969, *One-Dimensional Two-Phase Flow*, McGraw-Hill, New York.

[6] Dumitrescu, D. T., 1943, "Stromung and Einer Luftbluse in Senkrechten rohr," Z. Angew. Math. Mech., **23**, pp. 139–149.

[7] Davies, R. M., and Taylor, G., 1950, "The Mechanics of Large Bubbles Rising Through Extended Liquids and Through Liquids in Tubes," Proc. R. Soc. London, Ser. A, **200**, pp. 375–390.

[8] Batchelor, G. K., 1967, *An Introduction to Fluid Dynamics*, Cambridge University, Cambridge, England.

[9] Collins, R., De Moraes, F. F., Davidson, J. F., and Harrison, D., 1978, "The Motion of the Large Gas Bubble Rising Through Liquid Flowing in a Tube," J. Fluid Mech., **89**, pp. 497–514.

[10] Bendiksen, K. H., 1985, "On the Motion of Long Bubbles in Vertical Tubes," Int. J. Multiphase Flow, **11**, pp. 797–812.

[11] Batchelor, G. K., 1987, "The Stability of a Large Gas Bubble Rising Through Liquid," J. Fluid Mech., **184**, pp. 399–442.

[12] Reinelt, D. A., 1987, "The Rate at Which a Long Bubble Rises in Vertical Tube," J. Fluid Mech., **175**, pp. 557–565.

[13] Funada, T., Joseph, D. D., Maehara, T., and Yamashita, S., 2005, "Ellipsoidal Model of the Rise of a Taylor Bubble in a Round Tube," Int. J. Multiphase Flow, **31**, pp. 473–491.

[14] Harmathy, T. Z., 1960, "Velocity of Large Drops and Bubbles in Media of Infinite or Restricted Extent," AIChE J., **6**, pp. 281–288.

[15] White, E. T., and Beardmore, R. H., 1962, "The Velocity of Rise of Single Cylindrical Air Bubbles Through Liquids Contained in Vertical Tubes," Chem. Eng. Sci., **17**, pp. 351–361.

[16] Maneri, C. C., and Zuber, N., 1974, "An Experimental Study of Plane Bubbles Rising Inclination," Int. J. Multiphase Flow, **1**, pp. 623–645.

[17] Bhaga, T., and Weber, M., 1981, "Bubbles in Viscous Liquids: Shapes, Wakes and Velocities," J. Fluid Mech., **105**, pp. 61–85.

[18] Nigmatulin, T. R., and Bonetto, F. J., 1997, "Shape of Taylor Bubbles in Vertical Tubes," Int. Commun. Heat Mass Transfer, **24**, pp. 1177–1185.

[19] Salman, W., Gavriilidis, A., and Angeli, P., 2006, "On the Formation of Taylor Bubbles in Small Tubes," Chem. Eng. Sci., **61**, pp. 6653–6666.

[20] Nogueira, S., Riethmuler, M. L., Campos, J. B. L. M., and Pinto, A. M. F. R., 2006, "Flow in the Nose Region and Annular Film Around a Taylor Bubble Rising Through Vertical Columns of Stagnant and Flowing Newtonian Liquids," Chem. Eng. Sci., **61**, pp. 845–857.

[21] Birkhoff, G., and Carter, D., 1957, "Rising Plane Bubbles," J. Math. Mech., **6**, pp. 769–779.

[22] Miksis, M. J., Vanden-Broeck, J.-M., and Keller, J. B., 1982, "Rising Bubbles," J. Fluid Mech., **123**, pp. 31–41.

[23] Mao, Z., and Dukler, A. E., 1990, "The Motion of Taylor Bubbles in Vertical Tubes. I. A Numerical Simulation for the Shape and Rise Velocity of Taylor Bubbles in Stagnant and Flowing Liquids," J. Comput. Phys., **91**, pp. 132–160.

[24] Bugg, J. D., Mack, K., and Rezkallah, K. S., 1998, "A Numerical Model of Taylor Bubbles Rising Through Stagnant Liquids in Vertical Tubes," Int. J. Multiphase Flow, **24**, pp. 271–281.

[25] Daripa, P., 2000, "A Computational Study of Rising Plane Taylor Bubbles," J. Comput. Phys., **157**, pp. 120–142.

[26] Bretherton, F. P., 1961, "The Motion of Long Bubbles in Tubes," J. Fluid Mech., **10**, pp. 166–188.

[27] Tung, K. W., and Parlange, J. Y., 1976, "Note on the Motion of Long Bubbles in Closed Tubes-Influence of Surface Tension," Acta Mech., **24**, pp. 313–317.

[28] Vanden-Broeck, J.-M., 1984, "Rising Bubbles in a Two-Dimensional Tube With Surface Tension," Phys. Fluids, **27**, pp. 2604–2607.

[29] Nickens, H. V., and Yannitell, D. W., 1987, "The Effects of Surface Tension and Viscosity on the Rise Velocity of a Large Gas Bubble in a Closed Vertical Liquid-Liquid Tube," Int. J. Multiphase Flow, **13**, pp. 57–69.

[30] Couet, B., Strumolo, G. S., and Dukler, A. E., 1986, "Modeling of Two-Dimensional Bubbles in a Rectangular Channel of Finite Width," Phys. Fluids, **29**, pp. 2367–2372.

[31] Garabedian, P. R., 1957, "On Steady-State Bubbles Generated by Taylor Instability," Proc. R. Soc. London, Ser. A, **241**, pp. 423–431.

[32] Goldsmith, H. L., and Mason, S. G., 1962, "The Motion of Single Large Bubbles in Closed Vertical Tubes," J. Fluid Mech., **14**, pp. 42–58.

[33] Brown, R. A. S., 1965, "The Mechanics of Large Gas Bubbles in Tubes. I. Bubble Velocities in Stagnant Liquids," Can. J. Chem. Eng., **Q2**, pp. 217–223.

[34] Pinto, A. M. F. R., and Campos, J. B. L. M., 1996, "Coalescence of Two Gas Slugs Rising in a Vertical Column of Liquid Pinto and Campos," Chem. Eng. Sci., **51**, pp. 45–54.

[35] Nogueira, S., Riethmuler, M. L., Campos, J. B. L. M., and Pinto, A. M. F. R., 2006, "Flow in the Nose Region and Annular Film Around a Taylor Bubble Rising Through Vertical Columns of Stagnant and Flowing Newtonian Liquids," Chem. Eng. Sci., **61**, pp. 845–857.

[36] Nogueira, S., Riethmuler, M. L., Campos, J. B. L. M., and Pinto, A. M. F. R., 2006, "Flow Patterns in the Wake of a Taylor Bubble Rising Through Vertical Columns of Stagnant and Flowing Newtonian Liquids: An Experimental Study," Chem. Eng. Sci., **61**, pp. 7199–7212.

[37] Liao, Q., and Zhao, T. S., 2003, "Modeling of Taylor Bubble Rising in a Vertical Mini Noncircular Channel Filled With a Stagnant Liquid," Int. J. Multiphase Flow, **29**, pp. 411–434.

[38] Clanet, C., Heraud, P., and Searby, G., 2004, "On the Motion of Bubbles in Vertical Tubes of Arbitrary Cross-Sections: Some Complements to the Dumitrescu–Taylor Problem," J. Fluid Mech., **519**, pp. 359–376.

[39] Clift, R., Grace, J. R., and Weber, M. E., 1978, *Bubbles, Drops, and Particles*, Academic, New York.

[40] Wallis, G. B., 1962, "General Correlations for the Rise Velocity of Cylindrical Bubbles in Vertical Tubes," General Engineering Laboratory, General Electric Co., Report No. 62GL130.

[41] Tomiyama, A., Nakahara, Y., Adachi, Y., and Hosokawa, S., 2003, "Shapes and Rising Velocities of Single Bubbles Rising Through an Inner Subchannel," J. Nucl. Sci. Technol., **40**, pp. 136–142.

[42] Viana, F., Pardo, R., Yanez, R., Trallero, J. L., and Joseph, D. D., 2003, "Universal Correlation for the Rise Velocity of Long Bubbles in Round Pipes," J. Fluid Mech., **494**, pp. 379–398.

[43] Brauner, N., and Ullmann, A., 2004, "Modeling of Gas Entrainment From Taylor Bubbles: Part A: Slug Flow," Int. J. Multiphase Flow, **30**, pp. 239–272.

[44] Brauner, N., and Ullmann, A., 2004, "Modeling of Gas Entrainment From Taylor Bubbles: Part B: A Stationary Bubble," Int. J. Multiphase Flow, **30**, pp. 273–290.

[45] Jana, A. K., Das, G., and Das, P. K., 2006, "A Novel Technique to Identify Flow Patterns During Liquid-Liquid Two-Phase Upflow Through a Vertical Pipe," Ind. Eng. Chem. Res., **45**, pp. 2381–2393.

Downloaded 03 Jun 2010 to 171.66.16.158. Redistribution subject to ASME license or copyright; see http://www.asme.org/terms/Terms_Use.cfm

A Simplified Approach for Predicting the Intermittent Behavior of Gas-Liquid Mixtures in Pipes

M. Fossa

A. Marchitto[1]
e-mail: anna@ditec.unige.it

Dipartimento di Ingegneria della Produzione,
Termoenergetica e Modelli Matematici (DIPTEM),
Università degli Studi di Genova,
Via all'Opera Pia 15a,
16145 Genova, Italy

A new approach to the classical slug flow model is here proposed based on an original correlation for the minimum liquid level in the stratified regions of intermittent horizontal flows. This correlation is obtained by fitting experimental data obtained from a statistical analysis of void fraction signals from ring impedance probes. The new procedure improves the original model in terms of computing time reduction and algorithm simplification. In addition, it is demonstrated that the new closure relationship can be derived with more consistent experimental results, with respect to the slug length, which is employed in the original approach. The predictions of the main flow parameters are presented with reference to the classical and new approach, and all the results are critically compared with literature experimental data. It is demonstrated that the simplified procedure is able to predict the pressure drops and average void fraction values in good agreement with experimental measurements, while only the slug frequency and slug length predictions are affected by poor reliability. [DOI: 10.1115/1.2953296]

Keywords: two-phase slug flow, void fraction, pressure multiplier, liquid film level

1 Introduction

In the pipe flow of gas-liquid mixtures, slug or intermittent flow conditions are frequently encountered in the whole range of pipe inclinations and for a wide range of gas and liquid flow rates.

Slug regime is characterized by a sequence of liquid slugs separated by large gas bubbles. It is a highly complex phenomenon with an unsteady nature and large time fluctuations in flow parameters, such as the pressure and velocities, and phase concentration. Processes involving heat and mass transfer are also unsteady with substantial fluctuations in temperature and concentration.

Due to the complexity of the unsteady problem, an exact solution of the continuum and momentum equations is available only for a limited set of flow conditions or under given simplified assumptions.

Therefore a variety of approximate methods have been proposed for predicting the flow behavior, in order to obtain reliable estimations on pressure drop and phase distribution.

A mechanistic model of intermittent flow was proposed by Duckler and Hubbard [1] and tested with data taken in small diameter horizontal pipes. Nicholson et al. [2] modified this model without introducing substantial changes in the original set of equations proposed by Duckler and Hubbard.

Other models in literature were proposed by Stanislav et al. [3], Taitel and Barnea [4], Fabre and Linè [5], and Andreussi et al. [6] for horizontal flow; Fernandes et al. [7], Orell and Rembrand [8], Sylvester [9], and Taitel and Barnea [4] for vertical flow; and Bonnacaze et al. [10] for inclined flow.

These models are all based on a one dimensional steady-state approach applied to a slug flow model. The main assumption in such models is that slug flow can be represented by a sequence of identical slug units traveling along the pipe at a constant translational velocity. The slug unit is constituted by a liquid slug followed by a gas pocket with a liquid film at the pipe wall. The slug models consider representative slug units, and the flow is assumed to consist of a sequence of similar slug units. Moreover the analysis is restricted to the case of constant liquid properties and the gas compressibility is ignored.

The procedure is based on a set of proper closure relationships of empirical and semiempirical origin in order to solve the conservation equations for both the liquid and gas phases.

These relationships concern the evaluation of such flow parameters as the gas fraction in the liquid slug, the translational velocity of the slug, the dispersed bubble velocity, and the slug length (or the slug frequency). These parameters are then considered auxiliary variables, given in terms of proper closure relations.

Among these flow parameters, the authors' attention has been focused on the relationships for the slug length. Common experimental observations for air-water systems (Duckler and Hubbard [1]; Nicholson et al. [2]) suggest that the stable slug length is relatively insensitive to the gas and liquid flow rates but show large time fluctuations of such parameter, with typical scatter of values from the average one around 50% and even more.

The authors' experimental data have confirmed the above assertion and have pointed out another experimental observation: the minimum liquid level values in the stratified region could be measured with higher degrees of confidence (maximum scatter from the average value around 20%). The authors performed the experimental procedure (described by Fossa et al. [11]), which is based on the statistical analysis of the instantaneous cross sectional averaged void fraction obtained by means of ring impedance probes.

The conclusion from the experimental work of the authors is that a proper choice of closure relationships for the mass and momentum balances should be oriented to flow parameters that could be measured with lower uncertainty.

The aim of this study is hence to propose a simplified procedure to infer the main parameters of the horizontal gas-liquid intermittent flow, with respect to the classical slug flow model by Duckler and Taitel. In the new simplified model, the core closure equation refers to the minimum liquid height in the stratified regions under the gas pockets, and it replaces the original closure equation on

[1]Corresponding author.

Contributed by the Fluids Engineering Division of ASME for publication in the JOURNAL OF FLUIDS ENGINEERING. Manuscript received August 27, 2007; final manuscript received March 26, 2008; published online December 8, 2008. Assoc. Editor: Theodore Heindel.

Downloaded 03 Jun 2010 to 171.66.16.158. Redistribution subject to ASME license or copyright; see http://www.asme.org/terms/Terms_Use.cfm

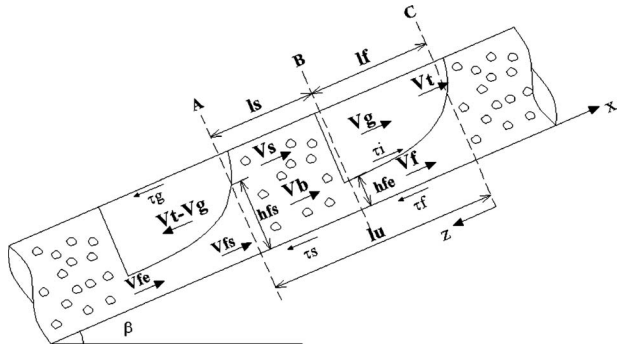

Fig. 1 Slug flow geometry

liquid slug length. In such a way great mathematical simplifications and processing time reductions can be achieved.

In this paper comparisons between the classical and new slug flow models are performed from the point of view of the analytical expressions, and the predictions from both methods are critically compared to experimental data from the open literature and those obtained by the present authors.

2 Analytical Models

2.1 Steady-State Slug Flow Model. The classical slug flow model (Duckler and Hubbard [1]; Nicholson et al. [2]) is based on the flow pattern showed schematically in Fig. 1. The slug unit is subdivided into two volumes: the liquid slug having length equal to l_s and the film zone (length l_f). The liquid slug may contain small gas bubbles that are assumed to be uniformly distributed over the liquid volume itself, with bulk concentration α_s. The average liquid slug velocity is indicated as V_s and the dispersed bubble velocity as V_b.

The film zone consists of a liquid film and an elongated gas bubble. For horizontal and near horizontal pipes, the elongated bubble occupies the upper part of the flow channel. The elongated bubble propagates downstream at a translational velocity V_t. The liquid film velocity is designated as V_f and the gas velocity in the stratified region as V_g. Note that the liquid and gas velocities in the film zone vary along the pipe due to the variation of the film thickness $h_f(z)$ behind the liquid slug.

Assuming that both the liquid and gas phases are incompressible, the two-phase mass balances over the slug unit can be written as follows:

$$V_m = V_{SL} + V_{SG} = V_s H_{Ls} + V_b \alpha_s \tag{1}$$

where V_m is the mixture velocity, and V_{SL} and V_{SG} are the liquid and gas superficial velocities, respectively.

The momentum equations for the two phases in the stratified region, with reference to a coordinate system moving backward along the pipe at a velocity V_t, can be written as follows:

$$\rho_l (V_t - V_f)\frac{\partial (V_t - V_f)}{\partial z} = -\frac{\partial P}{\partial z} + \frac{\tau_f S_f}{A_f} - \frac{\tau_i S_i}{A_f} + \rho_l g \sin\beta - \rho_l g \cos\beta \frac{\partial h_f}{\partial z} \tag{2}$$

$$\rho_g (V_t - V_g)\frac{\partial (V_t - V_g)}{\partial z} = -\frac{\partial P}{\partial z} + \frac{\tau_g S_g}{A_g} + \frac{\tau_i S_i}{A_g} + \rho_g g \sin\beta - \rho_g g \cos\beta \frac{\partial h_f}{\partial z} \tag{3}$$

where τ_f, τ_g, and τ_i are the shear stresses between liquid and wall, gas and wall, and liquid and gas, respectively, while S_f, S_g, and S_i are the corresponding contact surfaces.

The shear stresses τ_f, τ_g, and τ_i are in turn expressed as a function of their corresponding friction factors (f_f, f_g, and f_i), calculated with single-phase flow correlations.

Combining Eqs. (1)–(3), a differential equation for the liquid film height h_f as a function of backstream coordinate z can be obtained,

$$\frac{dh_f}{dz} = \frac{\dfrac{\tau_f S_f}{A_f} - \dfrac{\tau_g S_g}{A_g} - \tau_i S_i\left(\dfrac{1}{A_f} + \dfrac{1}{A_g}\right) + (\rho_l - \rho_g) g \sin\beta}{(\rho_l - \rho_g) g \cos\beta - \rho_l (V_t - V_f)\dfrac{(V_t - V_s) H_{Ls}}{H_{Lf}^2}\dfrac{dH_{Lf}}{dh_f} - \rho_g (V_t - V_g)\dfrac{(V_t - V_b)(1 - H_{Ls})}{(1 - H_{Lf})^2}\dfrac{dH_{Lf}}{dh_f}} \tag{4}$$

where

$$\frac{dH_{Lf}}{dh_f} = \frac{4}{\pi D}\sqrt{1 - \left(2\frac{h_f}{D} - 1\right)^2} \tag{5}$$

$H_{Ls} = 1 - \alpha_s$ is the liquid holdup in the slug and H_{Lf} is the local liquid holdup in the stratified region.

Equation (4) contains some unknown variables, such as the translational velocity V_t, the dispersed bubble velocity V_b, the liquid holdup in the slug H_{Ls}, and the liquid slug length l_s. These parameters need to be expressed in terms of proper empirical correlations in order to solve Eq. (4) for $h_f(z)$.

The integration of Eq. (4) needs, in the original slug flow model, an iterative procedure by changing the liquid slug length l_f up to convergence on guessed and recalculated slug lengths.

To solve the mass and momentum equations, a set of closure relationships is required. They refer to the quantities V_t, V_b, H_{Ls}, and l_s. The closure relationships allow the other flow parameters to be calculated. The corresponding film velocity V_f can be found using a mass balance for liquid phase. Pressure drop, average void fraction, slug length, and slug frequency can therefore be estimated over the slug unit.

The pressure drop for a slug unit can be calculated using a global force balance along a slug unit between cuts A-A and C-C (see Fig. 1). The balance of the momentum fluxes in and out the control volume yields the following pressure drop:

$$\Delta P_u = \rho_u g \sin\beta l_u + \frac{\tau_s \pi D}{A} l_s + \int_0^{l_f} \frac{\tau_f S_f + \tau_g S_g}{A} dz \tag{6}$$

where ρ_u is the average density of a slug unit,

$$\rho_u = \alpha_u \rho_g + (1 - \alpha_u)\rho_l \tag{7}$$

and α_u is the average void fraction of a slug unit

$$\alpha_u = \frac{(-V_{SL} + V_s H_{Ls} + V_t \alpha_s)}{V_t} \tag{8}$$

Downloaded 03 Jun 2010 to 171.66.16.158. Redistribution subject to ASME license or copyright; see http://www.asme.org/terms/Terms_Use.cfm

The first term of the right-hand side of Eq. (6) is the gravitational contribution to the pressure drop; the second and third terms are the frictional contributions in the slug and film zones.

Alternatively, the pressure drop can be calculated neglecting the contribution of the film zone and considering only the control volume between the plane cuts A-A and B-B (see Fig. 1). In this case a mixing pressure drop due to the near-wake region behind the long bubble has to be taken into account.

2.2 Simplified Approach to the Slug Flow Model. The present approach to the modeling of slug flow is still based on the steady-state slug flow analysis, but it differs from the classical procedure previously presented in the way of solving the mass and momentum equations and on the choice of the closure relationships to be employed.

Experimental observations for air-water systems suggest that the stable slug length is relatively insensitive to the gas and liquid flow rates but due to time fluctuations, the experimental values of this parameter are usually affected by a standard deviation from the mean value often over 50% (Andreussi et al. [12]).

On the other hand, the minimum liquid level in the stratified region could be evaluated with higher degrees of confidence ($\pm 20\%$) by means of experimental techniques like those adopted by Ruder et al. [13] and Fossa et al. [11]. According to these observations, the classical procedure is modified by replacing the slug length relationship with a proper original correlation proposed by Fossa et al. [11], which provides the minimum liquid level in the stratified region as a function of gas volume fraction,

$$\frac{h_{\min}}{D} = 0.16 + 0.33(1 - X_v) \tag{9}$$

This apparently minor modification has two main advantages: first it introduces a physical quantity that is affected by a much smaller experimental uncertainty; second it allows the solving procedure to be improved by a faster and reliable algorithm, which does not require iterative routines.

The other closure relationships needed by our model were selected from a set of reference studies on the argument (Nicholson et al. [2], Fernandes et al. [7], Bendiksen [14]). Based on a preliminary validation analysis, the algorithm developed in this paper considers the following closure equations:

(1) *Bendiksen* [14]:

$$V_t = c_0 V_m + v_0$$

$$c_0 = 1.05 + 0.15 \sin^2(\beta)$$

$$v_0 = [0.351 \sin(\beta) + 0.542 \cos(\beta)]\sqrt{gD} \tag{10}$$

$$\frac{V_m}{\sqrt{gD}} \leqslant 3.5$$

$$c_0 = 1.2, \quad v_0 = 0.351 \sin(\beta)\sqrt{gD}, \quad \frac{V_m}{\sqrt{gD}} > 3.5$$

(2) *Fernandes* et al. [7]:

$$V_b = V_s + v_0, \quad v_0 = 1.54[\sigma g(\rho_l - \rho_g)/\rho_l^2]^{1/4}(1 - \alpha_s)^{0.5} \tag{11}$$

(3) *Nicholson* et al. [2]:

$$H_{Ls} = \frac{1}{1 + \left(\frac{V_m}{8.66}\right)^{1.39}} \tag{12}$$

It is worthwhile to note that in the Nicholson paper (and in other ones of the open literature), a further closure relationship is given to calculate the length of the slug unit. In that case, the proposed correlation was

$$l_s = 30D \tag{13}$$

The friction factors f_f and f_g are calculated with the correlations proposed by Taitel and Barnea [4], while the f_i values are calculated according to the formula suggested by Shoham and Taitel [15].

The new procedure requires, as input data, the operating conditions, such as the phase superficial velocities and densities and the diameter and inclination of the pipe.

The procedure then calculates the flow parameters required: the minimum liquid level $h_{\min}$ in the stratified region, the translational velocity V_t, the dispersed bubble velocity V_b, and the liquid holdup in the slug H_{Ls} (Eqs. (10)–(12)).

Equation (4) has now given integration extremes: the film height in the start section is obtained from the liquid holdup, and it is assumed to be equal to H_{Ls}; the final liquid level height is directly available from the new closure relationship (Eq. (9)).

The numerical integration of Eq. (4) is therefore performed once, and it allows the evaluation of the film length l_f. The slug length l_s can be evaluated by means of the conservation equation for the liquid phase.

The slug unit pressure drop and average void fraction can be calculated in the same way as the classical procedure, through a global force balance along the slug unit (Eqs. (6) and (8)).

3 Experimental Evaluation of the Minimum Film Level

3.1 Experimental Apparatus. The experimental apparatus consists of a horizontal test section where air and water can be mixed to generate the two-phase flow under bubble, stratified, and intermittent flow regimes. The test section is about 12 m long and allows pressure and void fraction measurements to be performed. A complete description of the plant is available in Guglielmini and Soressi [16]. The investigation refers to air-water horizontal flows in 60 mm and 40 mm i.d. pipes. The operating conditions cover the V_{SG}=0.3–4.0 m/s and V_{SL}=0.6–3.0 m/s gas and liquid superficial velocity ranges, respectively (reference pressures of 1.1–1.4 bars, as measured 5 m downstream the phase mixer). Intermittent flows (plug and slug) were observed.

The void fraction sensors adopted in this investigation consist of ring electrode pairs placed on the internal wall of the cylindrical test duct, flushed to the pipe surface. A complete description of the metering device is available in Fossa [17]. Three probes were employed in the 60 mm pipe, located at z/D=33, 100, and 160, respectively, from the phase mixer. The 40 mm test pipe was equipped with four probes at z/D=95, 148, 151, and 255, respectively. The void fraction sensors and related electronics are able to pick up the instantaneous cross sectional average value and to allow 100 Hz sampling time series to be collected and stored. The void fraction time series are elaborated according to the procedure described in detail in Fossa et al. [11], which allows the time-average void fraction, the slug length, the slug frequency, and the minimum film level values to be inferred.

In what follows, all the experimental data reported for comparison with predictions are obtained according to the analysis described in Fossa et al. [11].

The test pipe was also equipped with 15 pressure taps to measure the pressure profile along the pipe: details on the procedure are given in Guglielmini and Soressi [16].

3.2 Experimental Minimum Film Level Evaluation. The procedure to infer the minimum liquid level is based on the statistical analysis of the void fraction records, which allows the time-average cross sectional void fraction α and the void prob-

Downloaded 03 Jun 2010 to 171.66.16.158. Redistribution subject to ASME license or copyright; see http://www.asme.org/terms/Terms_Use.cfm

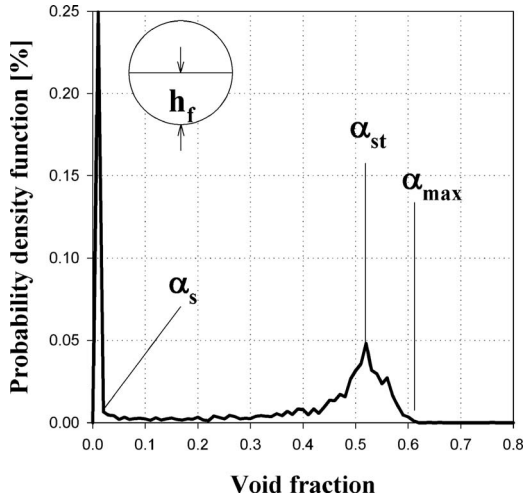

Fig. 2 Void fraction PDF for flow parameter evaluation

ability density function (PDF) to be inferred (Fig. 2). As it is well known, the intermittent flow is associated with a twin-peaked PDF, where the low void fraction peak is pertinent to slug passage and the high void fraction peak is associated with the stratified phase regions.

From, PDF analysis, the following parameters can be determined (Fig. 2): α_s, which corresponds to the low void fraction peak; α_{st}, at which the maximum of the right peak occurs; and α_{max}, where the PDF goes to zero. The average liquid film height (h) and minimum liquid level (h_{min}) in the stratified regions have been calculated from α_{st} and α_{max} values, respectively, by means of simple trigonometric considerations and by neglecting the presence of gas inside the liquid layer. Figure 3 refers to the minimum liquid level in the stratified region between slugs as measured either in the 40 mm pipe or the 60 mm one. Data were made dimensionless through the pipe inner diameter D and correlated by us with the empirical formula (Eq. (9)), which holds in the 0.6–3.0 m/s and 0.3–4.0 m/s liquid and gas superficial velocity ranges, respectively.

The figure inspection reveals that the formula fits quite well

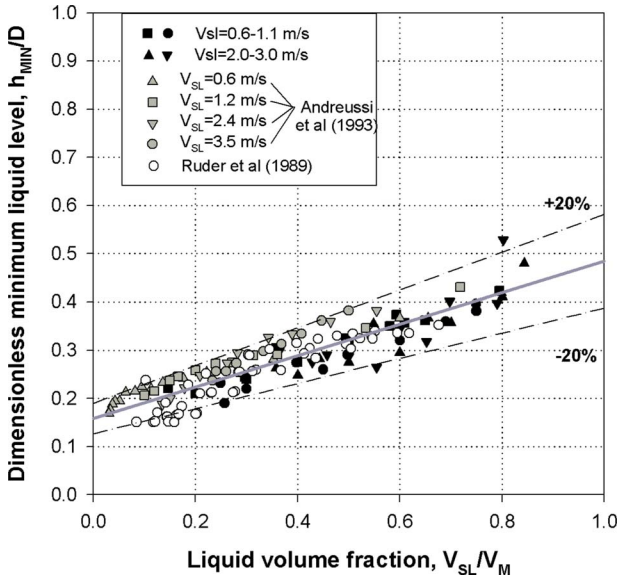

Fig. 3 Predicted and measured minimum liquid levels (D =40 mm) and comparison with literature data

(within 20% confidence bounds) either our data or those of literature collected by Ruder et al. [13] and by Andreussi et al. [6], as deduced from their liquid holdup values.

3.3 Measurement Uncertainty. Regarding the void fraction evaluation, a repeatability investigation was performed over 50 test runs and different probes: the standard deviation of the void fraction measurements was found to be 1.5%. The calibration of the probes, with respect to the dispersed and stratified flow patterns, was performed according the procedure described in Ref. [17]. The overall uncertainty on void fraction measurements (void meter accuracy and random errors) turned out to be around 3%. Concerning the two-phase pressure multiplier evaluation, 15 pressure taps were employed to measure the pressure profiles along the test pipes and to compare them with the experimental ones obtained during the single-phase flow. The analysis of available data (more than 300 experiments by the authors) showed that random errors prevail over the errors introduced by the instrumentation (flow meters and pressure transducers, 2% accuracy of the readings). Random errors yield data scatter around the regression line that describes the pressure profile. According to Moffats recommendations [18] on the computerized analysis of errors, experimental values of residuals in the regression lines were employed to calculate the uncertainties in estimating the single- and two-phase pressure drops. It was found that in single-phase flows the 95% uncertainty is about 3%, while during the two-phase flow the uncertainty is about 8%. As a consequence the two-phase multiplier is affected by an overall uncertainty of about 9%.

4 Model Results and Discussion

The classical and simplified procedures have been compared in terms of prediction capability concerning the pressure drop, the average void fraction, the minimum liquid level in the stratified region, and the slug frequency (or slug length).

The operating conditions considered for simulations cover the 0.6–3.0 m/s and 0.3–4.0 m/s liquid and gas superficial velocity ranges, respectively. The test sections investigated are horizontal (β=0) 40 mm and 60 mm inner diameter pipes.

The predictions obtained through the classical and simplified procedures have been compared with experimental void fraction and pressure drop data. In order to test the present model predictions on a wider range of operative conditions and fluid characteristics (such as liquid viscosity or density), the procedure has been extended to two different simulations: in the first one the ratio between liquid and gas densities has been selected in the range of 100–1000 in the second one the liquid viscosity has been varied from 0.001 kg/ms to 0.3 kg/ms. The results and the procedure comparison are presented in terms of pressure multiplier and average void fraction values.

4.1 Pressure Drop Estimation. Both procedures have proven to be able to reconstruct pressure drops in the slug unit in good agreement with experimental measurements. Figures 4(a) and 4(b) show the pressure drop in terms of pressure multiplier ϕ_{l0}^2, plotted versus the gas volume fraction, for V_{SL}=1.1 m/s and 2.0 m/s, respectively, and for both the diameters. Experimental data refer to the measurements collected at z/D=255 for the 40 mm inner diameter pipe and z/D=160 for the 60 mm one.

The expression "cla" refers to data obtained with classical procedure, and "new" to data obtained with new simplified procedure. Figure 4 also shows some values obtained from the well known correlation proposed by Lockhart and Martinelli [19].

The algorithms show a good agreement with experimental data in the superficial liquid velocity range of 0.6–1.1 m/s; for higher velocities both the algorithms seem to underestimate the experimental values.

The mean deviation between the predictions provided by the two procedures assumes values within 5% (V_{SL}=0.6 m/s) and 2%

Downloaded 03 Jun 2010 to 171.66.16.158. Redistribution subject to ASME license or copyright; see http://www.asme.org/terms/Terms_Use.cfm

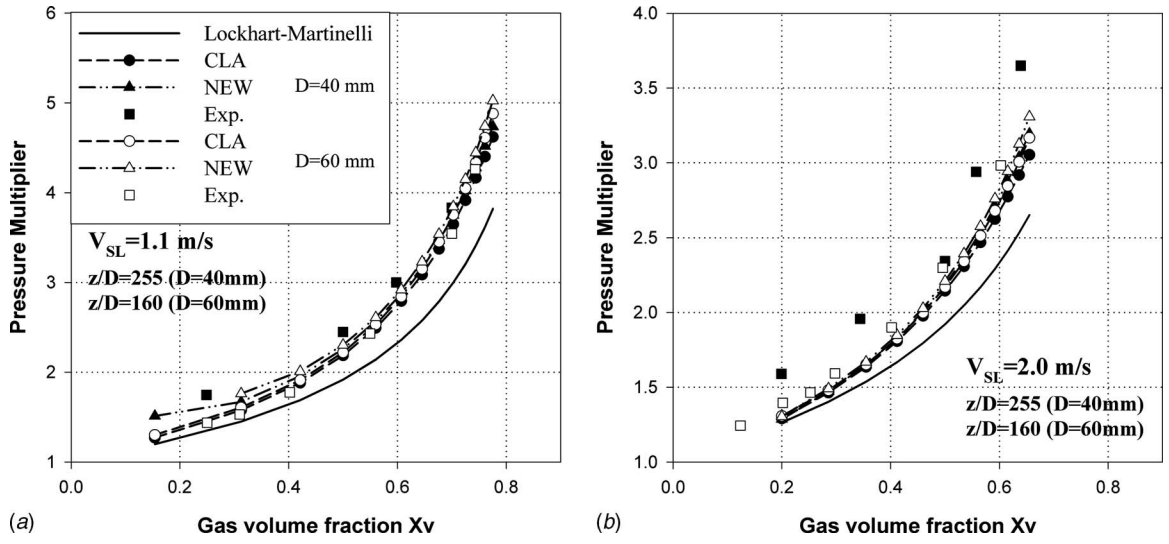

Fig. 4 Pressure multiplier versus gas volume fraction; (*a*) V_{SL}=1.1 m/s; (*b*) V_{SL}=2.0 m/s

(V_{SL}=2.0–3.0 m/s). The mean deviation between the classical procedure and the Lockhart–Martinelli model is even greater, and it reaches 36% for V_{SL}=0.6 m/s.

4.2 Average Void Fraction. Figures 5(*a*) and 5(*b*) show the average void fraction plotted in terms of gas volume fraction for both 40 mm and 60 mm diameter pipes, obtained by the two procedures and experimentally measured at z/D=255 (40 mm pipe) and at z/D=160 (60 mm inner diameter pipe).

The figure also shows some values obtained with the correlation proposed by Armand and Treshchev [20].

The void fraction values evaluated with the two procedures are almost coincident (in the figure the results superposed). The agreement with experimental data is good, with a slight tendency to overestimate the measurements for D=40 mm.

Trends of void fraction reconstruction seem to show a weak dependence on liquid superficial velocity: when V_{SL} increases, an increase of void fraction can be observed. Both the procedures give predictions in good agreement with the Armand and Treshchev model (mean deviation about 4%).

4.3 Minimum Liquid Level. Figure 6 shows the comparison between minimum liquid level values calculated by the classical procedure and those from Eq. (9) employed in the present model. Experimental data refer to our measurements collected at z/D=255 for the 40 mm pipe and at z/D=160 for the 60 mm pipe according to the procedures and the operating conditions described in Secs. 4.1 and 4.2.

The poor agreement between the predictions of the classical procedure and the experimental data is apparent from the figure inspection the gap increases with the liquid superficial velocity and the greatest deviations correspond to V_{SL}=3.0 m/s. It is worth noting that Eq. (9), on which the present model is based, fits with great accuracy this experimental set of data, being the correlation coefficient R and the standard error of the proposed correlation equal to 0.974 and to 0.014, respectively.

4.4 Slug Frequency and Slug Length. In terms of slug frequency, the classical procedure is shown to be in reasonable agreement with experimental data only for superficial gas velocities higher than 1.5 m/s. On the other hand, data obtained by the simplified procedure are strongly different from experimental results: the mean deviation between theoretical and experimental data is sometimes higher than 100%.

Slug frequency can be related to slug length by means of the translational velocity. As clearly reported in literature (Duckler and Hubbard [1]; Nicholson et al. [2]), experimental slug length values are almost independent of fluid flow rates. Furthermore slug length values show scatters having standard deviations up to

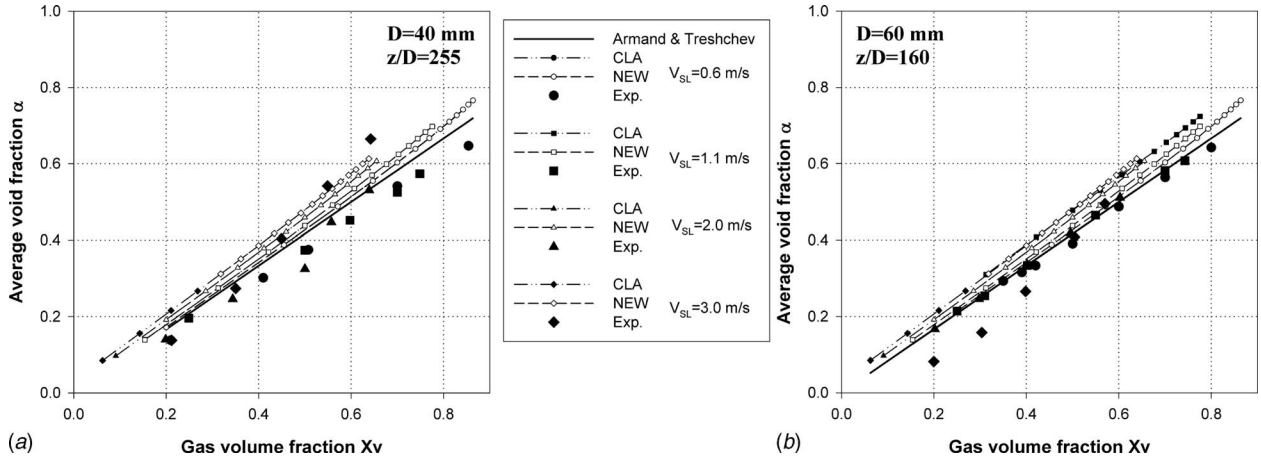

Fig. 5 Average void fraction versus gas volume fraction; (*a*) *D*=40 mm; (*b*) *D*=60 mm

Downloaded 03 Jun 2010 to 171.66.16.158. Redistribution subject to ASME license or copyright; see http://www.asme.org/terms/Terms_Use.cfm

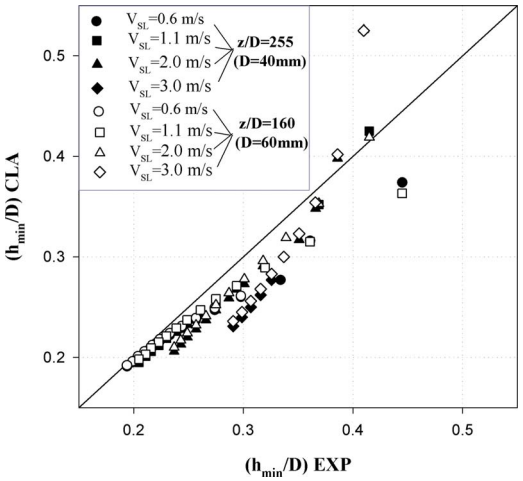

Fig. 6 Minimum film level measured values versus the predictions by the classical procedure (cla). Filled symbols, *D* =40 mm; open symbols, *D*=60 mm

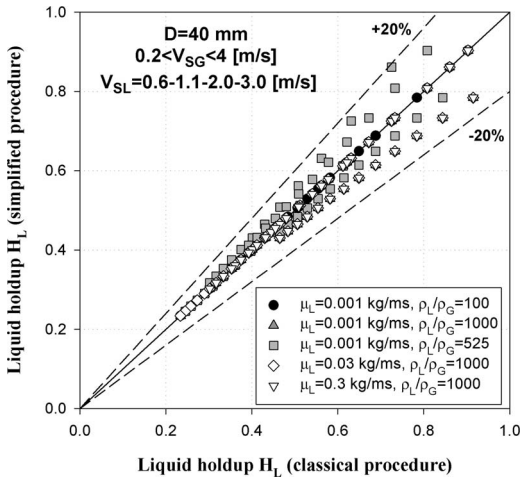

Fig. 8 Average liquid holdup values determined with classical and modified procedures for phase density ratios in the range of 100–1000 and liquid viscosities in the range of 0.001–0.3 kg/ms

60% of the average value. Data obtained by the simplified procedure seem to have a strong dependence by operative conditions. Therefore the simplified algorithm has proven to be unreliable in slug length prediction.

4.5 Effect of Density and Viscosity Ratios on Predictions. Figures 7 and 8 show the comparison of results given by the two procedures in terms of pressure multiplier and average liquid holdup, respectively, for phase density ratio selected in the range of 100–1000 and liquid viscosity in the range of 0.001–0.3 kg/ms.

The two procedures, classical one (abscissa) and new one (ordinate), show a good agreement in the liquid holdup evaluation, for all the conditions tested: mean deviation is always lower than 20% (see Fig. 8).

Regarding the pressure drop prediction, the mean deviation between predicted values reaches 39%, but only for a low pressure multiplier (1–3, see Figure 7); for higher values of pressure multiplier the two procedures are in good agreement, with mean deviation always lower than 15%.

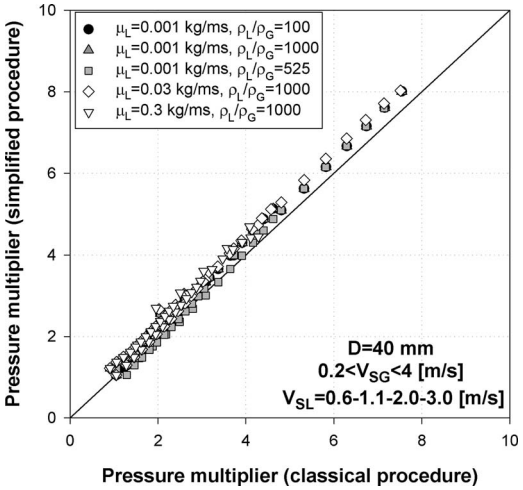

Fig. 7 Pressure multiplier values determined with classical and modified procedures for phase density ratios in the range of 100–1000 and liquid viscosities in the range of 0.001–0.3 kg/ms

5 Conclusions

A new procedure has been proposed to predict the behavior of intermittent horizontal flows. The procedure is an evolution of the classical slug flow model originally proposed by Taitel and Duckler. The new model introduces a different set of closure relationships, including a correlation by the authors on liquid film height that allows the slug unit momentum equation to be solved in a more efficient and straightforward way. This relationship considers the minimum film level in the stratified region, and it was obtained by the authors from the statistical analysis of their own experimental data on instantaneous void fraction. The new correlation proved to give accurate predictions of minimum film level, also with respect to literature data, with deviations in the range of ±20%. The proposed model predictions have been compared with experimental results and with the predictions by the classical model. The simplified model is reliable to infer a reliable estimation of the fundamental flow parameters such as the pressure drop and the average void fraction, while the classical model seems to be preferable to infer estimations on the slug frequency and slug lengths.

Nomenclature

D = pipe diameter (m)
f = friction factor (−)
$h_f(z)$ = film thickness (m)
h = average liquid film height (m)
h_{min} = minimum liquid film height (m)
H_{Lf} = liquid holdup in the stratified region (=1−α_f) (−)
H_{Ls} = liquid holdup in the slug (=1−α_s) (−)
l = length (m)
V = fluid velocity (m/s)
V_t = translational slug velocity (m/s)
X_v = gas volume fraction (−)

Greek Letters

α = time-average cross sectional void fraction (−)
α_{max} = void fraction at which the PDF goes to zero (−)
α_{st} = low void fraction peak (−)
β = pipe inclination (deg)
ρ_l = density (kg/m^3)
σ = interfacial tension [Pa m]
τ = shear stress, [Pa]

Downloaded 03 Jun 2010 to 171.66.16.158. Redistribution subject to ASME license or copyright; see http://www.asme.org/terms/Terms_Use.cfm

Subscripts

f = liquid film
g = gas phase
i = at the interface liquid-gas
m = mixture
s = of the liquid slug
SG = gas superficial
SL = liquid superficial
u = of the slug unit

References

[1] Duckler, A., and Hubbard, M. G., 1975, "A Model for Gas—Liquid Slug Flow in Horizontal and Near Horizontal Tubes," Ind. Eng. Chem. Fundam., **14**, pp. 337–347.

[2] Nicholson, M. K., Aziz, K., and Gregory, G. A., 1978, "Intermittent Two Phase Flow in Horizontal Pipes: Predictive Models," Can. J. Chem. Eng., **56**, pp. 653–663.

[3] Stanislav, J. F., Kokal, S., and Nicholson, M. K., 1986, "Intermittent Gas-Liquid Flow in Upward Inclined Pipes," Int. J. Multiphase Flow, **12**, pp. 325–335.

[4] Taitel, Y., and Barnea, D., 1990, "A Consistent Approach for Calculating Pressure Drop in Inclinated Slug Flow," Chem. Eng. Sci., **45**(5), pp. 1199–1206.

[5] Fabre, J., and Line, A., 1992, "Modelling of Two-Phase Slug Flow," Annu. Rev. Fluid Mech., **24**, pp. 21–46.

[6] Andreussi, P., Minervini, A., and Paglianti, A., 1993, "Mechanistic Model of Slug Flow in Near-Horizontal Pipes," AIChE J., **39**(5), pp. 1281–1291.

[7] Fernandes, R. C., Semiat, R., and Duckler, A., 1983, "Hydrodynamic Model for Gas-Liquid Slug Flow in Vertical Tubes," AIChE J., **29**, pp. 981–989.

[8] Orell, A., and Rembrand, R., 1986, "A Model for Gas-Liquid Slug Flow in a Vertical Tube," Ind. Eng. Chem. Fundam., **25**, pp. 196–206.

[9] Sylvester, N. D., 1987, "A Mechanistic Model for Two Phase Vertical Slug Flow in Pipes," ASME J. Energy Resour. Technol., **109**, pp. 206–213.

[10] Bonnecaze, R. H., Eriskine, W. Jr., and Greskovich, E. J., 1971, "Holdup and Pressure Drop for Two-Phase Slug Flow in Inclined Pipelines," AIChE J., **17**, pp. 1109–1113.

[11] Fossa, M., Guglielmini, G., and Marchitto, A., 2003, "Intermittent Flow Parameters From Void Fraction Analysis," Flow Meas. Instrum., **14**(4–5), pp. 61–68.

[12] Andreussi, P., Bendiksen, K. H., and Nydal, O. J., 1993, "Void Distribution in Slug Flow," Int. J. Multiphase Flow, **19**, pp. 817–828.

[13] Ruder, Z., Hanratty, P. J., and Hanratty, T. J., 1989, "Necessary Conditions for the Existence of Stable Slugs," Int. J. Multiphase Flow, **15**(2) pp. 209–226.

[14] Bendiksen, K. H., 1984, "An Experimental Investigation of the Motion of Long Bubbles in Inclined Tubes," Int. J. Multiphase Flow, **6**, pp. 467–483.

[15] Shoham, O., and Taitel, Y., 1984, "Stratified Turbolent-Turbolent Gas Liquid Flow in Horizontal and Inclined Pipes," AIChE J., **30**, pp. 377–385.

[16] Guglielmini, G., and Soressi, E., 1996, "Experimental Data of Two-Phase Pressure Drop Across Sudden Area Contractions in Horizontal Flow," *Proceeding of the Fifth International Conference on Multiphase Flow in Industrial Plants*, Amalfi, Italy, pp. 54–62.

[17] Fossa, M., 1998, "Design and Performance of a Conductance Probe for Measuring the Liquid Fraction in Two-Phase Gas-Liquid Flows," Flow Meas. Instrum., **9**, pp. 103–109.

[18] Moffat, R. J., 1988, "Describing the Uncertainties in Experimental Results," Exp. Therm. Fluid Sci., **1**, pp. 3–17.

[19] Lockhart, R. W., and Martinelli, R. C., 1949, "Proposed Correlation of Data for Isothermal Two-Phase Flow in Pipes," Chem. Eng. Prog., **45**(1), pp. 39–48.

[20] Armand, A., and Treshchev, G., 1959, "Investigation of the Resistance During the Movement of Steam-Water Mixtures in Heated Pipe at High Pressure," Report No. AERE Lib/Trans 81.

Downloaded 03 Jun 2010 to 171.66.16.158. Redistribution subject to ASME license or copyright; see http://www.asme.org/terms/Terms_Use.cfm

A Hybrid Model to Predict the Onset of Gas Entrainment With Surface Tension Effects

W. Saleh

R. C. Bowden

I. G. Hassan[1]
e-mail: IbrahimH@alcor.concordia.ca

L. Kadem

Department of Mechanical and Industrial Engineering,
Concordia University,
Montreal, QC, H3G 2W1, Canada

The onset of gas entrainment in a single downward discharge, from a stratified gas-liquid region, was modeled. The discharge was modeled as a point-sink and Kelvin–Laplace's equation was used to incorporate surface tension effects. Consequently, a criterion to characterize the dip radius of curvature, at the onset of gas entrainment, was required. The dip geometry was experimentally investigated and a correlation was developed relating the dip radius of curvature to the discharge Froude number. The correlation was used in conjunction with the theoretical model. It was found that the predicted critical height demonstrated good agreement with experimental data with the three-dimensional point-sink approach, while poor agreement using the two-dimensional finite-branch approach was found. The inclusion of surface tension improved the model's capability to predict the critical height, particularly at discharge Froude numbers below 1.
[DOI: 10.1115/1.2969465]

Keywords: onset of gas entrainment, surface tension, critical height, header-feeder

1 Introduction

Recent loss-of-coolant accident (LOCA) research has been motivated by safety and accident analysis codes. Codes, such as CATHENA, use experimentally or analytically derived thermohydraulic models in their predictions. These models are used to simulate, for example, a pressurized reservoir under two-phase conditions, with an exiting bottom or side oriented discharge. An example of an industrial application is the Canada deuterium and uranium (CANDU) nuclear reactor, which incorporates a fluid distribution system where coolant flows from a large reservoir (known as the header) through a network of pipes (known as feeders) to the reactor fuel channels. A break in the distribution network, or a pump failure, can cause a two-phase environment to occur within the header. This, in turn, can lead to the gas phase entraining into the feeder branches, where liquid flows under normal operation, resulting in a two-phase mixture to flow into the fuel channels. Two-phase flow impacts the designed cooling effectiveness and can lead to an increase in the reactor core temperature. Elevated core temperatures above design limits can pose serious safety concerns.

With a stratified gas-liquid environment and a single side or bottom discharge Zuber [1] found that if the gas-liquid interface was located above the discharging branch inlet, the gas phase could be entrained at a critical height called the onset of gas entrainment (OGE) by either vortex-induced or vortex-free mechanisms, with the later causing a significant impact to the flow quality. If the interface was below the discharge inlet, liquid was entrained into the discharge flow at a critical liquid height, called the onset of liquid entrainment (OLE). Following this, a variety of independent studies were done in an effort to understand the phenomena (OGE and OLE) and, in particular, predict its behavior under a variety of conditions. Of those studies, a few have focused on a single downward discharge from a stratified two-phase environment and are summarized below. A few researchers later experimentally investigated the critical height at the onset of gas entrainment by the vortex-free mechanism in a single downward oriented discharging branch. The experiments were performed with stratified two-phase flow in the main duct at various operating pressures, discharge branch diameters, and fluids. The authors provided empirical correlations of the critical height as a function of the discharge Froude number, from a circular pipe [2,3] and a square duct [4]. The traditional Froude number, which is a ratio of the inertial to gravitational forces, was modified in these studies to include the density ratio of both fluid phases, following Ref. [1].

Several authors experimentally investigated the critical height at the onset of vortex-free gas entrainment in multiple discharges on a flat vertical wall [5–8]. These studies demonstrated the effects of the branch location relative to one another, which could be oriented in the same vertical plane, horizontal plane, or inclined plane. These studies maintained a symmetrical inflow at the discharge inlet by locating the discharge on one end of a large reservoir. The large reservoir was supplied with a controllable source of both air and water, which enabled the liquid height to be well controlled. The discharge diameter that they selected was 6.35 mm and the reservoir was operated at pressures ranging from 300 kPa to 500 kPa. The critical height was presented as a function of the discharge Froude number, similar to the previous works. Later, Ahmad and Hassan [9] experimentally investigated the critical height at the onset of vortex-free gas entrainment in single, dual, and triple discharge cases with three 6.35 mm orifices located on a curved wall at 0 deg, 45 deg, and 90 deg from horizontal. The data were not correlated but notably the critical height was also presented as a function of the discharge Froude number. They also used a test facility where the test section was mounted at the end of a large reservoir. This ensured a symmetrical inflow and a smooth-stratified two-phase environment with a controllable liquid and gas supply.

There have been a handful of relevant analytical studies done since 1990 that deal with the onset of liquid and gas entrainments in either single or multiple discharges. These studies have been done to emulate the situation of a symmetrical inflow toward the discharge. The onset of liquid entrainment was investigated for a single discharging side slot of finite width [10] and finite diameter [11]. Following, Armstrong et al. [12] provided an analytical model for the onset of liquid entrainment for two simultaneous side discharges. They found that the discharges could be accurately represented as point-sinks, which resulted in relatively good

[1]Corresponding author.

Contributed by the Fluids Engineering Division of ASME for publication in the JOURNAL OF FLUIDS ENGINEERING. Manuscript received November 5, 2007; final manuscript received May 30, 2008; published online December 9, 2008. Assoc. Editor: Theodore Heindel.

 Copyright © 2009 by ASME

Downloaded 03 Jun 2010 to 171.66.16.158. Redistribution subject to ASME license or copyright; see http://www.asme.org/terms/Terms_Use.cfm

agreement with their experimental data. Hassan et al. [13], and later Maier et al. [14], improved the dual discharge models for various geometries—for inclined walls and discharges, respectively—by considering the discharges to have a finite diameter. These researchers were able to get better agreement with experimental data by demonstrating their model to more appropriately predict the physical limits.

More recently, Ahmed et al. [15] modeled the onset of gas entrainment in a single discharging side branch, installed on a flat vertical wall, from a smooth-stratified gas-liquid environment. Two models were proposed by the authors, first a simplified model that treated the discharge as a three-dimensional point-sink, and second a more complex model that assumed the discharge to have a finite diameter. They treated each fluid phase independently and assumed both to be incompressible, inviscid, irrotational, and quasisteady with negligible surface tension. These assumptions directed the authors to a potential flow problem and considered the gas-liquid interface to be the link between both phases. To that end, they used a balance of Bernoulli's equation along the interface applied between two convenient points in the flow field. To predict the onset of gas entrainment phenomena they used a criterion based on the work of Taylor [16], who investigated the onset of instability of inviscid liquid surfaces accelerated vertically. It was stated that a liquid surface would become unstable if accelerated at a rate greater than that of gravity. With the onset of gas entrainment criterion being established, along with Bernoulli's equation, the velocity field needed to be defined. To do this the authors first assumed the discharge to be a point-sink. Using a known potential function to define the velocity field the authors found a relationship in the form of

$$\frac{H_{\mathrm{OGE}}}{d} = 0.625\mathrm{Fr}^{0.4} \tag{1}$$

where

$$\mathrm{Fr} = \frac{4\dot{m}}{\pi\sqrt{gd^5\rho_L(\rho_L - \rho_G)}} \tag{2}$$

The critical height (H_{OGE}) at the onset of gas entrainment is shown to be a function of the Froude number. The Froude number is a function of the discharge liquid mass flow rate ($\dot{m}$), the discharge diameter (d), the gravitational acceleration (g), and the fluid densities (ρ_L—liquid and ρ_G—gas). For the second finite-branch model, the authors accounted for the branch diameter by solving Laplace's three-dimensional equation. This was a result of applying a potential function to the continuity equation with the appropriate boundary conditions. This second model was found to be more representative of the physical limits with the discharge Froude number less than approximately 10. At this point the difference between both the point-sink and finite-branch models was approximately 5%. With the Froude decreased to approximately 1, the difference between the predictions of both models increased to nearly 20%. Following this, Andaleeb et al. [17] used a similar point-sink approach to model discharges on a curved surface. The model accounted for the effect of wall curvature and they found relatively good agreement with experimental data provided in Ref. [9].

To further the modeling of gas entrainment the effects of surface tension on the critical height are considered in this study. One of the main elements of the analytical approach is to consider that a dip forms in the heavier liquid surface, followed by a sudden collapse of the surface equilibrium—resulting in gas entrainment. It is well known from experimental studies that the dip forms prior to gas entrainment [9]. It is believed that surface tension plays an important role in the dip formation and the size and shape of the dip, as well as effects of flow conditions, are of particular interest. This study will provide a hybrid theoretical analysis of the effects of surface tension based on the dip formation assumption. The theoretical model will use experimental evidence to quantify the effects of surface tension on the critical height at the onset of gas entrainment. A single discharge installed at the bottom of a circular pipe will be considered based on the scaling relationships from a typical CANDU header-feeder bank. Reasoning for the inclusion of surface tension effects will become clear from dimensional analysis. A single feeder bank of a CANDU header was used as the prototype since its geometry has salient features that could be common to other systems. This study is not intended to directly model or simulate the CANDU header-feeder system since additional considerations are needed, which are beyond the scope of the investigation.

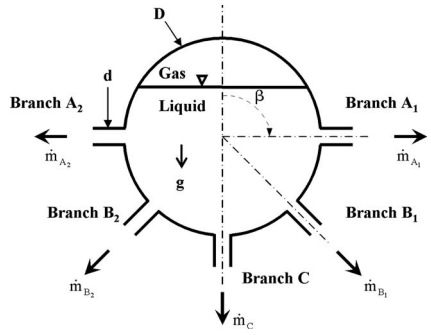

Fig. 1 A typical header-feeder bank geometry with stratified two-phase conditions

2 Problem Description

Consider an example of a typical CANDU header-feeder bank arrangement under stratified two-phase conditions, as shown in Fig. 1. A typical header has a circular cross section and measures approximately 6 m in length, and between 0.356 m and 0.406 m inside diameter (i.d.), and is closed on both ends. Flow enters the top of the header through two turrets located at either end of the header and exits through a network of feeder branches. Each feeder bank contains five 50.8 mm diameter orifices located radially at β=90 deg, 135 deg, 180 deg, 225 deg, and 270 deg. The feeders are physically connected to the fuel channels by pipes of near equal hydraulic resistance, which sets equal flow rates in all branches. In the general case, the flow rate in any channel can vary. The following analysis considers only a single discharging bottom branch (β=180 deg), referred to as branch C, and neglects the effects of the turrets.

2.1 Dimensional Analysis

2.1.1 Geometry. The relevant geometric parameters are also shown in Fig. 1. The header has a circular cross section of diameter D and branch C has a diameter, d. The effects of additional discharges, such as branches A_1, A_2, B_1, and B_2, are not considered in the present analysis.

2.1.2 Fluid Transport Properties. The two fluid phases are represented in Fig. 1 as "Gas" and "Liquid" and each has a set of independent variables that is relevant to the problem. Considering first the gas phase as ideal, the pressure and temperature are related by the density (ρ_G) from the ideal gas law and its dynamic viscosity is (μ_G). The liquid density (ρ_L) and its viscosity (μ_L) are relevant, as is the surface tension (σ) at the gas-liquid interface. For stratified flows the gravitational acceleration (g) is an important parameter. It was suggested that it should be incorporated with the density ratio to address buoyancy as $g(\rho_L - \rho_G)/\rho_L$ [18]. The single phase liquid mass flow rate in branch C is $\dot{m}_C$.

2.1.3 Two-Phase Phenomena. With the required independent geometrical and fluid properties established, some comments about the phenomena are needed to establish the dependent variables. The flow through branch C is single phase prior to OGE.

Downloaded 03 Jun 2010 to 171.66.16.158. Redistribution subject to ASME license or copyright; see http://www.asme.org/terms/Terms_Use.cfm

Table 1 Saturation properties of heavy-water at 300°C and 8.6 MPa

	Saturated liquid	Saturated vapor
Density (kg/m^3)	784.87	52.64
Viscosity ($N\,s/m^2$)	9.36×10^{-5}	1.97×10^{-5}
Surface tension (N/m)	1.39×10^{-2}	

Onset of gas entrainment occurs when the branch flow is no longer a single phase liquid but rather a mixture of the gas and liquid phases. The onset of entrainment has been characterized previously by the vertical distance, or height H, between the branch inlet and the gas-liquid interface. With the gas-liquid interface above the branch centerline—initially liquid only flow in the branch—a critical value of H will exist at which the gas phase will entrain into the branch at H_{OGE} [1]. The critical height is expected to be a function of the independent parameters discussed above, which include the single phase liquid properties, mass flow rate, and geometry. For onset of gas entrainment in branch C the functional relationship is expected to be

$$H_{OGE,C} = f\left(d, D, \frac{g\Delta\rho}{\rho_L}, \mu_L, \rho_L, \sigma, \dot{m}_C\right) \tag{3}$$

2.1.4 Reduction in Variables: Pi Theorem. In the simplest case of a single discharging branch there are at most five dimensionless groups using three basic dimension of mass, length, and time. Dimensional analysis was performed using the branch diameter, single phase liquid density, and liquid mass flow rate as repeating variables. The resulting relationship for the critical height ($H_{OGE,C}$) was found to be

$$\frac{H_{OGE,C}}{d} = f\left(\frac{D}{d}, \mathrm{Fr}_C, \mathrm{Re}_C, \mathrm{We}_C\right) \tag{4}$$

where

$$\mathrm{Fr}_C = \frac{\dot{m}_C^2}{g d^5 \rho_L(\rho_L - \rho_G)} \tag{5}$$

$$\mathrm{Re}_C = \frac{\dot{m}_C}{\mu_L d} \tag{6}$$

$$\mathrm{We}_C = \frac{\dot{m}_C^2}{\sigma \cdot d^3 \rho_L} \tag{7}$$

The discharge Froude number (Fr_C) is the ratio of inertial and gravitational forces, the discharge Reynolds number (Re_C) is a ratio of inertial and viscous forces, and the Weber number (We_C) is a ratio of inertial and surface tension forces. The shape of the discharge was not included in the definition of the Froude number, so Eq. (5) does not include the $(4/\pi)^2$ term, which would be expected when comparing it with Eq. (2). The discharge liquid velocity (v_C) through branch C can be defined using the liquid mass flow rate ($\dot{m}_C$) and discharge cross-section area ($0.25\pi d^2$) as $v_C = (4\dot{m}_C)/\rho_L(\pi d^2)$.

Consider now a typical CANDU header that operates with heavy-water (D_2O) nominally at temperatures and pressures in the range of 300°C and 10 MPa [19]. During a postulated small break LOCA the pressure within the header can decrease, causing the heavy-water to vaporize. At 300°C the saturation pressure is approximately 8.6 MPa and the saturated liquid and vapor properties are listed in Table 1. The saturation properties are used here as an estimate to determine the properties of the vapor phase.

Using the saturation properties the variations of the idealized liquid Froude, Reynolds, and Weber numbers were evaluated, using $d=50.8$ mm, and presented in Fig. 2. The gravitational force is shown to be dominant when compared to the viscous (Reynolds) and surface tension (Weber) forces, as demonstrated by the Froude number. The Froude number is commonly used in free-surface flows, particularly in geophysical flows such as rivers and oceans. The Weber number shows that surface tension effects are relevant at low values of v_C. Also, with the Froude and Weber numbers below 1 the inertia forces become smaller than the gravitational and surface tension forces. This implies that gravitational and surface tension forces will begin to compete with each other. In this case a new dimensionless group emerges at these low values of liquid velocity, v_C, the Bond (Bo) number, which is a ratio of gravitational to surface tension forces. This concept will be further demonstrated in the theoretical analysis below.

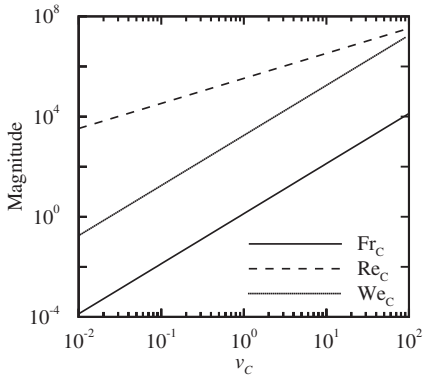

Fig. 2 Estimated dimensionless numbers of liquid flow in a feeder branch

3 Experimental Investigation

An established experimental test facility at Concordia University was used in this study. A brief discussion is presented regarding its components, namely, the test section and flow distribution system. The objectives of this study were to use the facility to estimate the size and shape of the dip in the air-water interface at the onset of gas entrainment.

3.1 Test Section. The test section, modeled from a header-feeder bank's geometry, had a semicircular cross section and a single downward discharge, located at $\beta=180$ deg and was referred to as branch C. A 50.8 mm diameter hole, 50.8 mm in length, was machined into the end of a solid brass rod to form the semicircular surface. Branch C consists of a 6.35 mm hole machined 30.4 mm deep into the semicircular surface and then enlarged to 9.56 mm diameter for the remaining 90.4 mm depth. The test section was installed in the two-phase reservoir, as shown in Fig. 3. Its curved surface was exposed to a smooth-stratified gas-liquid environment.

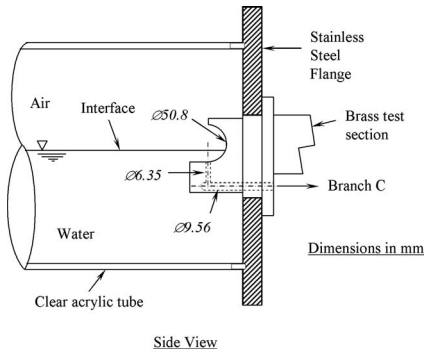

Fig. 3 Test section

Downloaded 03 Jun 2010 to 171.66.16.158. Redistribution subject to ASME license or copyright; see http://www.asme.org/terms/Terms_Use.cfm

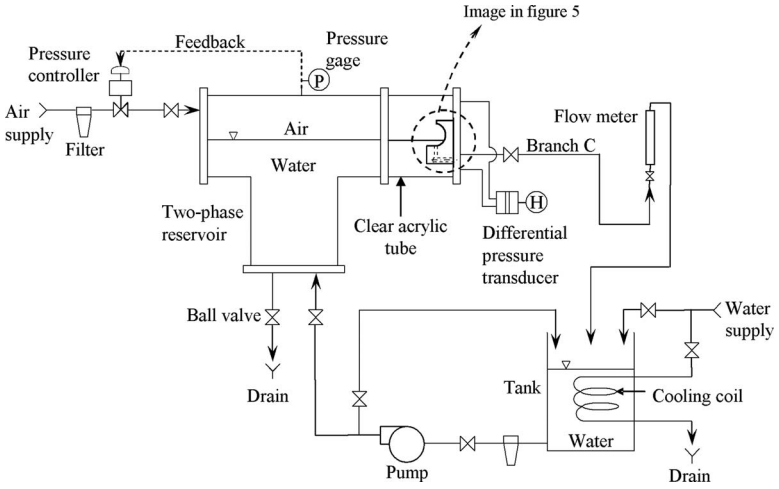

Fig. 4 Test facility

3.2 Test Facility and Instrumentation. The test facility is presented in Fig. 4. The two-phase reservoir was made from two stainless steel pipes welded together in a T-shape. Two of the three ends were capped with blind flanges. On the third end, a clear acrylic tube was installed with its open end capped with a blind flange. The test section was installed in a hole machined at the center of the blind flange. The flow of liquid through branch *C* was controlled by a ball valve and a flow meter was used to regulate and record the liquid flow rate. The flow meter was selected to provide different orders of magnitude of the discharge Froude number ($0.001 \leq Fr_C \leq 60$). The two fluids used in the experiment were water and air and all measurement devices were calibrated by the manufacturer as per component specifications. The maximum uncertainty in the calculation of the Froude number, Fr_C, was estimated to be $\pm 5\%$. The instrument uncertainty in measuring the air static pressure was ± 0.83 kPa whose value was maintained in the range of 308.2 ± 6.8 kPa.

Regulated air was supplied to the two-phase reservoir and the air pressure was monitored by a pressure transducer with a factory calibrated range of 0–830 kPa. Water was stored in a 208 *l* tank and supplied to the two-phase reservoir by a 2.23 kW pump. The discharged water downstream of the flow meter was recirculated back to the tank. The water height was measured by differential pressure transducer with a factory calibrated range of 0–255 mm H_2O.

Measurements were achieved by first filling the two-phase reservoir (by opening the two-phase reservoir inlet valve) so that the air-water interface was well above branch *C* (high enough to not have the dip when the branch was activated). The reservoir was then pressurized to 308.2 kPa and the discharge flow rate through branch C was set to a constant value (a constant Froude number). The air-water interface height, relative to branch *C*'s location, was then slowly decreased by reducing the inlet flow rate until a steady dip was formed in the interface. The dip was formed without gas entrainment occurring. This means that for a certain Froude number, or flow rate, there is one OGE height and one dip shape. This experiment was repeated for a range of discharge Froude numbers.

Images of the dip were recorded using a charge coupled device (CCD) camera with 1344×1024 pixel resolution. The image orientation was aligned with the side of the test section, as demonstrated in Fig. 3. A random sample of the images was then used to measure the size and shape of the dip; the sample size was typically on the order of 20 images. This was found to be sufficient to describe the relatively stable dip formation. A sample image is shown in Fig. 5, with the dip formation prominently displayed above branch *C*. The dip geometry was then recorded by importing the image into software called DIGI-XY. Using the software the spatial resolution was established and points of the dip profile were extracted. For each image an average of 20–30 unique points was selected to describe the surface profile. The process was repeated for a total of seven Froude numbers, ranging from approximately 1 to 30. A sample of the extracted points for three different Froude numbers is presented in Fig. 6. This figure provides an estimate of the size and shape of the dip as the Froude number is varied. It was observed that as the Froude number increased the interface and dip became increasingly unstable as the critical height was approached.

4 Theoretical Analysis

4.1 Point-Sink Analysis. In the point-sink model, the branch will be considered as a point. This means that the branch shape and size will not affect the prediction of onset of gas entrainment. The flow rate is the only parameter that will affect the prediction to this phenomenon and Fig. 7 shows the geometry that will be simulated in the point-sink model. Here, only the bottom branch *C* is used in the analysis. Also, the flow exiting from this branch is liquid only. The liquid level starts from the highest point inside

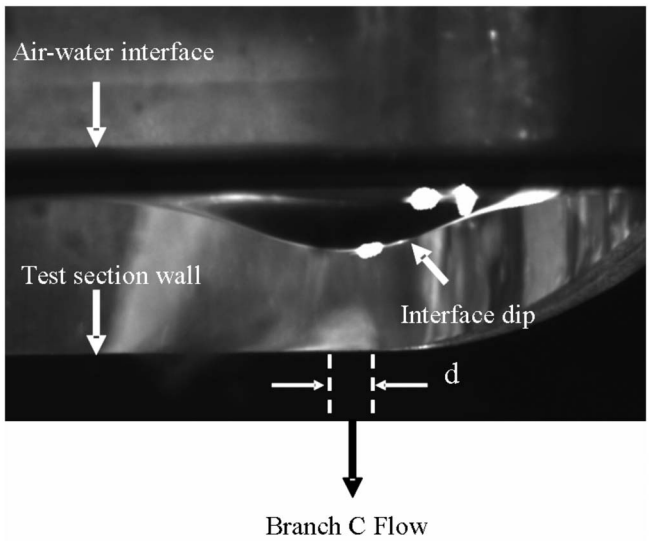

Fig. 5 Sample image of dip formed prior to the onset of gas entrainment

Downloaded 03 Jun 2010 to 171.66.16.158. Redistribution subject to ASME license or copyright; see http://www.asme.org/terms/Terms_Use.cfm

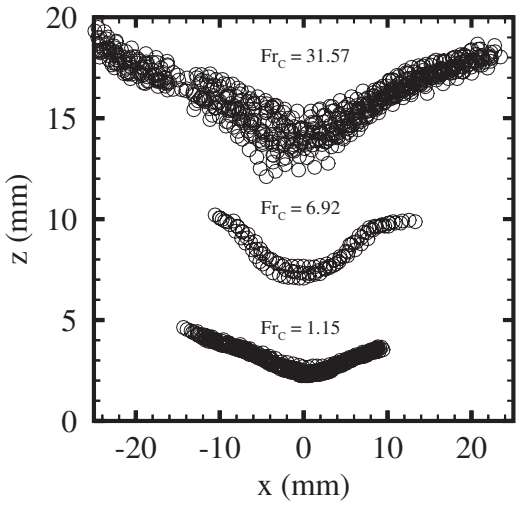

Fig. 6 The dip shape at three discharge Froude numbers in branch *C*

the circular domain called S, and then begins to descend. At a certain instant a dip will appear in the gas-liquid interface due to the vortex-free flow field. By decreasing the liquid level further the dip size will increase and then suddenly collapse, causing both the gas and liquid phases to flow into the branch.

The flow field is considered steady, incompressible, inviscid, and irrotational. These assumptions are characteristic of potential flow and are governed by forces of inertia and gravity. The potential flow assumption allows Bernoulli's equation to be applied between two points within the flow field. Bernoulli's equation will be applied on the interface between points a and b. Consider first the heavier fluid side that results in

$$P_{L,a} + \tfrac{1}{2}\rho_L v_{L,a}^2 + \rho_L g H = P_{L,b} + \tfrac{1}{2}\rho_L v_{L,b}^2 + \rho_L g h \tag{8}$$

Considering $v_{L,a} \ll v_{L,b}$, Eq. (9) becomes

$$P_{L,a} + \rho_L g H = P_{L,b} + \tfrac{1}{2}\rho_L v_{L,b}^2 + \rho_L g h \tag{9}$$

Applying Bernoulli's equation on the lighter fluid side, which is considered as stagnant, results in

$$P_{G,a} + \rho_G g H = P_{G,b} + \rho_G g h \tag{10}$$

The Kelvin–Laplace equation is now introduced to consider the effects of surface tension. The general equation [20] is

$$P_L(x,y,\eta) = P_G - \sigma\left(\frac{1}{R_x} + \frac{1}{R_y}\right) \tag{11}$$

where the pressure on the liquid side is P_L and the pressure on the gas side is P_G. The coordinates x and y are defined in a plane parallel to the gas-liquid interface with η describing the height of the interface above the x-y plane and generally $\eta = \eta(x,y)$. The surface tension coefficient is σ and the radii of curvature in the x and y directions are R_x and R_y, respectively. The shape of the dip is assumed to be represented by a segment of a sphere, which simplifies the general Kelvin–Laplace equation to have $R_x = R_y = \mathrm{ROC}$. Applying this assumption to the general equation at point a results in

$$P_{G,a} = P_{L,a} + \left(\frac{2\sigma}{\mathrm{ROC}_a}\right) \tag{12}$$

Similarly, applying the Kelvin–Laplace equation at point b results in

$$P_{G,b} = P_{L,b} + \left(\frac{2\sigma}{\mathrm{ROC}_b}\right) \tag{13}$$

The radius of curvature at point a (ROC_a) is very large since the gas-liquid interface is considered to be flat, therefore $P_{G,a} \approx P_{L,a}$. From Eqs. (9), (10), and (13), the critical height (H_{OGE}) at the onset of gas entrainment can now be found to be

$$\frac{H_{\mathrm{OGE}}}{d} = \frac{h}{d} + \frac{v_{L,b}^2 \rho_L}{2gd(\rho_L - \rho_G)} - \frac{2\sigma}{\mathrm{ROC}_b g d(\rho_L - \rho_G)} \tag{14}$$

The last term on the right is a ratio of surface tension to gravitational forces and is a modified form of the dimensionless group commonly referred to as the Bond number. The dip radius of curvature figures prominently in Eq. (14) and is variable if fluid properties remain constant. To find the velocity at point b, consider that branch C is assumed to be a point-sink with liquid volumetric flow rate, Q_C. The surface area, S, of the flow field is a hemisphere intersected by a cylinder, and the branch is located at the center of this flow field. The liquid radial velocity (v_r) at any point on the surface S of the flow field is

$$v_r = \frac{\partial \Phi}{\partial r} = \frac{Q_C}{S|_r} \tag{15}$$

where Φ is the potential function, r is the radius of the flow field, and S is given by

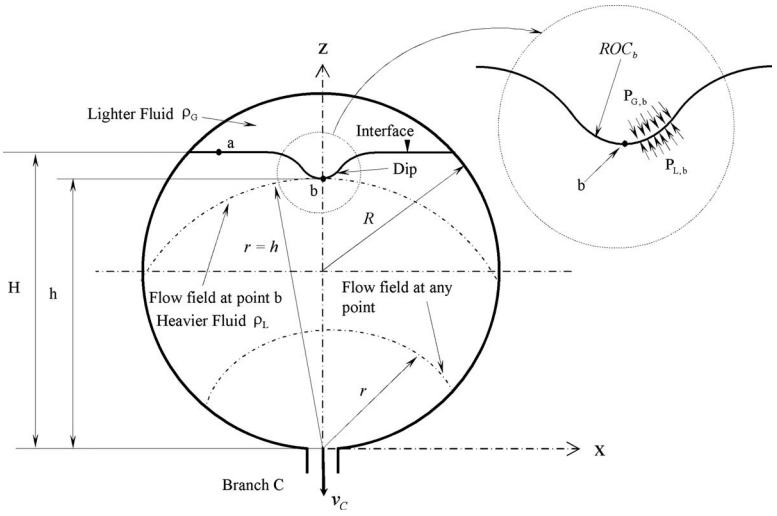

Fig. 7 Geometry used in point-sink analysis

Downloaded 03 Jun 2010 to 171.66.16.158. Redistribution subject to ASME license or copyright; see http://www.asme.org/terms/Terms_Use.cfm

$$S = 2\pi r^2 - 4r\int_0^r \arctan\frac{1}{\sqrt{\frac{4R^2}{r^2 - z^2} - 1}}dz \tag{16}$$

The surface area of the flow field at point b is given by

$$S|_{r=h} = 2\pi h^2 - 4h\int_0^h \arctan\frac{1}{\sqrt{\frac{4R^2}{h^2 - z^2} - 1}}dz \tag{17}$$

The criterion used to predict the onset of gas entrainment is the equality between the acceleration of the liquid above the branch and the acceleration of gravity, g, at point b [16]. The principle (for onset of gas entrainment in a vertical plane) is given as

$$a_b = -g \tag{18}$$

This states that if the liquid acceleration at point b is equal or exceeds the gravitational acceleration then the surface will become unstable, causing the onset of gas entrainment. Using Eqs. (15) and (18) to define the onset criterion yields

$$\left.\frac{\partial\Phi}{\partial r}\right|_{r=h} \cdot \left.\frac{\partial^2\Phi}{\partial r^2}\right|_{r=h} = -g \tag{19}$$

To find $\partial\Phi/\partial r$, Eq. (17) is substituted in Eq. (15), which results in

$$\left.\frac{\partial\Phi}{\partial r}\right|_b = \frac{Q_c}{S|_{r=h}} = \frac{Q_C}{2\pi h^2 - 4h\int_0^h \arctan\frac{1}{\sqrt{\frac{4R^2}{h^2 - z^2} - 1}}dz} \tag{20}$$

The derivative of $\partial\Phi/\partial r$ with respect to r at point b with $r=h$ yields

$$\left.\frac{\partial^2\Phi}{\partial r^2}\right|_b = -Q_C\left(\frac{4\pi h - 4I_1 - 4hI_2}{(2\pi h^2 - 4hI_1)^2}\right) \tag{21}$$

where

$$I_1 = \int_0^h \arctan\frac{1}{\left(\frac{4R^2}{h^2 - z^2} - 1\right)^{1/2}}dz \tag{22}$$

$$I_2 = \int_0^h \frac{4R^2 r}{\left(\frac{4R^2}{h^2 - z^2} - 1\right)^{1.5}(h^2 - z^2)^2\left(1 + \frac{1}{\frac{4R^2}{h^2 - z^2} - 1}\right)}dz \tag{23}$$

We use the definition of Fr_C to be

$$\mathrm{Fr}_C = \frac{v_C}{\sqrt{gd\frac{\Delta\rho}{\rho}}} \tag{24}$$

which is equivalent to the definition in Eq. (2) for a discharge with a circular cross section but using the average velocity instead of the mass flow rate. The volumetric flow rate (Q_C) can then be defined as

$$Q_C = \mathrm{Fr}_C\sqrt{gd\frac{\Delta\rho}{\rho}}\left(\frac{\pi}{4}d^2\right) \tag{25}$$

In summary, Eqs. (14) and (19) form a system of two equations with three unknowns. The unknowns are the critical height H_{OGE}, the height of the dip above the branch inlet h, and the radius of curvature ROC_b of the dip at point b. Without a third equation the system is ill posed. To find the radius of curvature of the surface dip analytically, considering the effects of surface tension as the main cause in a potential flow analysis posed a very serious challenge. The experimentally obtained values for the radius of curvature were therefore used to provide a reasonable alternative.

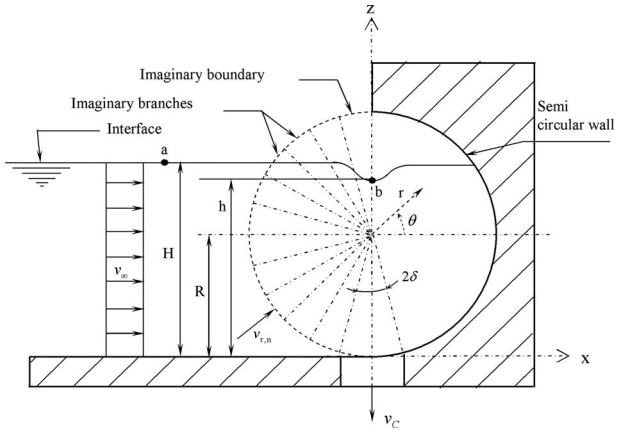

Fig. 8 Configuration for finite-branch analysis

4.2 Two-Dimensional Finite-Branch Analysis. In this analysis a two-dimensional (2D) finite-branch model is considered with a single slot installed on the bottom of a semicircular section, as shown in Fig. 8, with a discharge velocity,v_C. Two fluid phases are present and the lighter fluid is considered stationary while the heavier fluid is considered to be incompressible, homogeneous, and irrotational. These assumptions are characteristic of potential flow and are governed by forces of inertia and gravity. The potential flow assumption allows Bernoulli's equation to be applied between two points within the flow field. Bernoulli's equation will be applied on the interface between points a and b. Reintroducing Eqs. (8)–(10) from above, the Kelvin–Laplace equation, Eq. (11), is now introduced to consider the effects of surface tension in the 2D model. Therefore, the general equation, Eq. (11), becomes

$$P_L(x,\eta) = P_G - \sigma\left(\frac{1}{R_x}\right) \tag{26}$$

The coordinate x is defined as a horizontal line parallel to the gas-liquid interface with η describing the height of the interface above the line and generally $\eta = \eta(x)$. The radius of curvature in the x direction is R_x. The shape of the dip is assumed to be represented by a segment of a cylinder, which simplifies the general Kelvin–Laplace equation to have $R_x = \mathrm{ROC}$. Applying this assumption to the general equation at point a results in

$$P_{G,a} = P_{L,a} + \left(\frac{\sigma}{\mathrm{ROC}_a}\right) \tag{27}$$

Similarly, by applying the Kelvin–Laplace equation at point b results in

$$P_{G,b} = P_{L,b} + \left(\frac{\sigma}{\mathrm{ROC}_b}\right) \tag{28}$$

The radius of curvature at point a (ROC_a) is very large since the gas-liquid interface is considered to be flat and therefore $P_{G,a} \approx P_{L,a}$. From Eqs. (9), (10), and (28), the critical height (H_{OGE}) at the onset of gas entrainment can now be found to be

$$\frac{H_{\mathrm{OGE}}}{d} = \frac{h}{d} + \frac{v_{L,b}^2\rho_L}{2gd(\rho_L - \rho_G)} - \frac{\sigma}{\mathrm{ROC}_b gd(\rho_L - \rho_G)} \tag{29}$$

To find the liquid velocity at point b ($v_{L,b}$), a 2D flow field is considered by applying a potential function to the continuity equation, in cylindrical coordinates, as

Downloaded 03 Jun 2010 to 171.66.16.158. Redistribution subject to ASME license or copyright; see http://www.asme.org/terms/Terms_Use.cfm

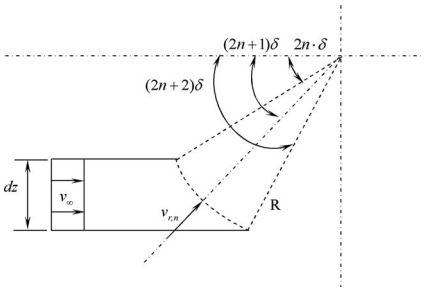

Fig. 9 A balance of the flow across one of the imaginary branches

$$\frac{1}{r}\frac{\partial}{\partial r}\left(r\frac{\partial \Phi}{\partial r}\right)+\frac{1}{r^2}\frac{\partial^2 \Phi}{\partial \theta^2}=0 \tag{30}$$

Assuming that a separable solution exists such that

$$\Phi(r,\theta)=X(r)Y(\theta) \tag{31}$$

and the solution is finite at $r=0$ yields the general solution

$$\Phi(r,\theta)=\alpha_0+\sum_{m=1}^{m=\infty} r^m(\alpha_m \cos(m\theta)+\beta_m \sin(m\theta)) \tag{32}$$

The form of this general solution is defined as the Neumann problem by having

$$\left.\frac{\partial \Phi}{\partial r}\right|_{r=R}=v_r(R,\theta) \tag{33}$$

with v_r being the radial velocity along the circumference at $r=R$. The partial derivative of Φ with respect to r along the circumference is

$$\frac{\partial \Phi}{\partial r}(R,\theta)=\sum_{m=1}^{m=\infty}[(mR^{m-1})(\alpha_m \cos(m\theta)+\beta_m \sin(m\theta))] \tag{34}$$

If $v_r(R,\theta)$ is also represented as a Fourier series as

$$v_r(R,\theta)=\frac{\kappa_0}{2}+\sum_{m=1}^{m=\infty}[\kappa_m \cos(m\theta)+\lambda_m \sin(m\theta)] \tag{35}$$

as indicated by Ref. [21], by comparing these two equations, Eqs. (34) and (35), a necessary condition that must be satisfied to yield a solution is

$$\pi\kappa_0=\int_0^{2\pi} v_r(R,\theta)d\theta=0 \tag{36}$$

Multiplying Eq. (36) by R results in balancing the inlet and outlet flow rates through the boundary. On the inlet side, opposite the slot, the area is divided into several (number n) imaginary branches with an equivalent size as the discharge branch. The purpose is to define the radial velocity component, $v_{r,n}$, in the direction of the domain center and along the semicircular inlet from the freestream velocity v_∞. From Fig. 9 the freestream velocity is defined by

$$v_\infty=v_C\cdot\frac{(2\delta\cdot R)}{H} \tag{37}$$

The number of branches along the imaginary boundary is determined by the height of the heavier fluid in the domain by H. From Fig. 9, a balance of the flow across the imaginary domain for a single imaginary branch gives

$$v_\infty dz=v_{r,n}2\delta R \tag{38}$$

The solution of Φ can now be found and given by Ref. [21] as

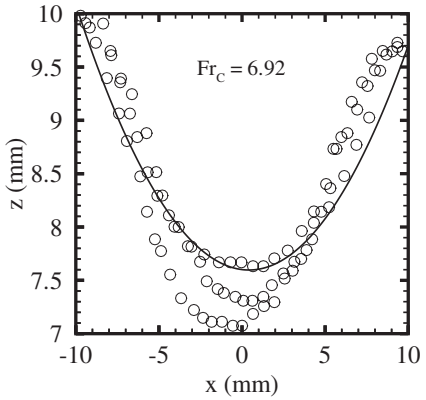

Fig. 10 Example of curve fitting the dip shape

$$\Phi(r,\theta)=\frac{\kappa_0\cdot R}{\pi}-\frac{R}{2\pi}\cdot\int_0^{2\pi} v_r(r,\theta)\log\left\{\frac{(R^2-2Rr\cos(\theta-\theta')+r^2)}{R^2}\right\}d\theta' \tag{39}$$

with the boundary conditions at $r=R$,

$$\frac{3\pi}{2}-\delta<\theta<\frac{3\pi}{2}+\delta,\quad \frac{\partial \Phi}{\partial r}=v_C$$

$$\frac{3\pi}{2}-(2n+2)\delta<\theta<\frac{3\pi}{2}-(2n)\delta,$$

$$v_{r,n}=v_\infty\cos\left(\frac{3\pi}{2}-(2n+1)\delta\right),\quad n=0,1,2\ldots$$

$$\frac{3\pi}{2}+\delta<\theta<\frac{\pi}{2},\quad v_r=0 \tag{40}$$

Each partial derivative in Eq. (19) can be evaluated using the definitions of Φ, r, and θ from the above equations. The values of all integrations in Eqs. (19) and (39) are calculated using numerical integration techniques. To validate the 2D finite-branch analysis model, a comparison was made between an experimental work in Ref. [9] carried out for a circular hole and the present 2D finite-branch analysis model.

4.3 Dip Radius of Curvature. To include the experimental data in the theoretical model a data reduction method was devised so that the radius of curvature could be presented as a function of the Froude number. The objective was to fit the data to a polynomial function for each Froude number tested. With seven Froude numbers, seven different polynomials were produced. The polynomial is of the form $z=C_1x^2+C_2x+C_3$, where C_1-C_3 are the curve fitting constants. A sample of the second order polynomial curve fit is shown in Fig. 10 for $Fr_C=6.92$. In order to adapt this function to the theoretical model the lowest point of the dip should be found, this is point b in Fig. 7 or 8. Conveniently, the lowest point can be found by searching for the location where the slope of the curve is zero. This implies that for the polynomial with $z=f(x)$

$$\left.\frac{dz}{dx}\right|_b=0 \tag{41}$$

The radius of curvature (ROC) of a function of the form $z=f(x)$ can then be found [22] as

Downloaded 03 Jun 2010 to 171.66.16.158. Redistribution subject to ASME license or copyright; see http://www.asme.org/terms/Terms_Use.cfm

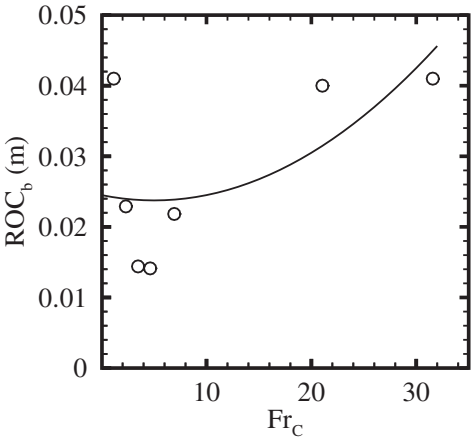

Fig. 11 The dip radius of curvature as a function of the discharge Froude number

$$\mathrm{ROC} = \frac{\left(1 + \left(\frac{dz}{dx}\right)^2\right)^{3/2}}{\left|\frac{d^2z}{dx^2}\right|} \tag{42}$$

and since $dz/dx=0$ at point b, the ROC can be found to be

$$\mathrm{ROC}_b = \left(\left|\frac{d^2z}{dx^2}\right|\right)^{-1} = \frac{1}{2C_1} \tag{43}$$

With a second order polynomial used as the fitting function, Eq. (42) reduces to a function of the fitting coefficient C_1 in Eq. (43). For each of the seven Froude numbers tested the dip radius of curvature was found by this method. The resulting values are shown in Fig. 11.

A second relationship is now required to describe $\mathrm{ROC}_b = f(\mathrm{Fr}_C)$ to complement the theoretical model. A data fit was again used to establish this functional relationship and a second order polynomial was chosen as a suitable fitting function. The polynomial equation that results is

$$\mathrm{ROC}_b = 0.00003 \times (\mathrm{Fr}^2 - 10\mathrm{Fr} + 816.6) \tag{44}$$

The number of images was typically on the order of 20, and approximately 20–30 points were used in each image to record the dip shape and size. The ROC_b was estimated for each image individually and also for the average of all the images combined. The process was repeated for all seven Froude numbers, and the highest deviation in ROC_b, in all cases, was found at $\mathrm{Fr}_C=7$ with a maximum value of $\pm 23\%$ from the polynomial fit in Eq. (43). Following the procedure outlined by Kline and McClintock [23] an estimate of the uncertainty of H_{OGE}/d from Eq. (14) and (29), with the highest deviation of ROC_b, was found to be approximately 2.5%.

The polynomial in Eq. (44) is an estimate of the dip radius of curvature for a single downward discharge installed on a curved surface. Future studies with multiple discharges or different discharge orientations will likely find a different relationship. Future work in this area could provide a more complete picture of the dip formation, size, and dynamics of the problem. A full examination on the dip formation will provide significant insight into the physics of the problem, particularly at high Froude numbers where a transient (fluctuating) dip was observed to occur. A future study to link the dip shape, size, and transients with the three-dimensional velocity fields is also highly desirable and would provide significant insight. Advanced techniques such as particle image velocimetry could serve to develop a correlation between the dip shape and the flow field.

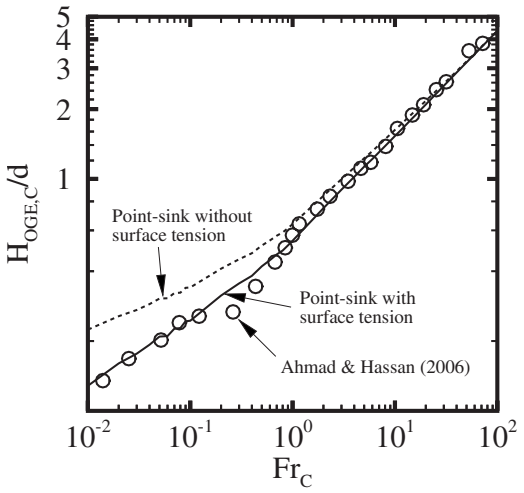

Fig. 12 Predicted values of the critical height with and without surface tension

4.4 The Critical Height. A computer code, written using MAPLE Version 11, was used to solve the system of three equations (Eqs. (14), (19), and (44). The code was used to determine the critical height ($H_{\mathrm{OGE},C}/d$) as a function of the Froude number (Fr_C). The critical height was calculated with and without surface tension effects. The results of the analysis are presented in Fig. 12 and are compared with experiments [9]. The dimensions and fluid used in the theoretical analysis are similar to the experimental study. It can be seen that without surface tension effects, the model overpredicts the critical height and at low Froude numbers the point-sink model begins to diverge from the experimental data. By including the Kelvin–Laplace equation in Bernoulli's equation, on either fluid side, the surface tension effects were included. The character of the new term, the modified Bond number, had a reducing effect on the critical height and demonstrates excellent agreement with the experiments, particularly at low Froude numbers. The three-dimensional point-sink approach, with surface tension effects, is a reasonable method for modeling the onset of gas entrainment in a single downward discharge.

Figure 13 shows the effect of surface tension on the critical height using the 2D finite-branch model. From the figure, it can be seen that the critical height decreases with the addition of surface tension to the model. There are two heights of the water surface at the point of OGE, H, which refers to the free air-water interface

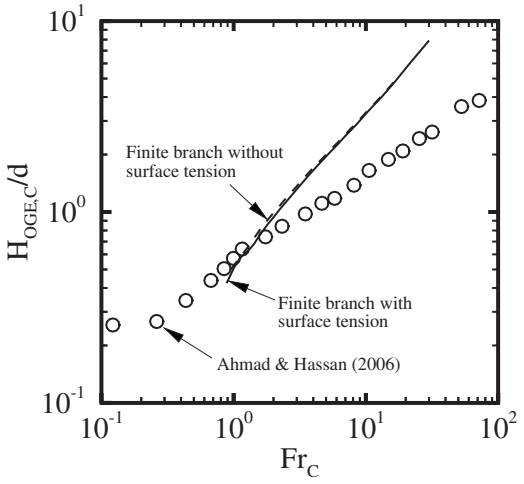

Fig. 13 Predicted values of the critical height with and without surface tension with 2D finite-branch modeling

Downloaded 03 Jun 2010 to 171.66.16.158. Redistribution subject to ASME license or copyright; see http://www.asme.org/terms/Terms_Use.cfm

height and its maximum value is limited by the test section geometry at a physical maximum height of $H \leq 2D$. The height h, which refers to the dip bottom height and its minimum value, is limited by the physical edge of the bottom branch at $h \geq (R - R\cos\delta)$. These two limits were achieved in the present 2D finite-branch model. The analytical model results could not be solved for a Froude number greater than $Fr_C = 30$ or lower than $Fr_C = 0.884$ due to the physical limits. The disagreement between the experimental data and the 2D analytical model is also expected since the modeled 2D flow field is quite different from the experimental flow field, which are inherently three dimensional. Even though there is similarity with the experimental results in the definition of the Froude number, the flow rate and velocity distribution inside the flow field are not the same, hence the disagreement with the experimental data and present 2D finite-branch model.

5 Conclusions

The model presented here is a first look at modeling the onset of gas entrainment with surface tension effects. The Kelvin–Laplace equation served as a useful tool but also caused a new unknown in the model, the dip radius of curvature. By deriving an experimental correlation to describe the dip shape, the radius of curvature was determined. A second order polynomial was used to describe the functional relationship between the discharge Froude number and the dip radius of curvature. In general, the point-sink model overpredicted the critical height when surface tension was neglected. By including surface tension the critical height prediction, at any discharge Froude number, was reduced. The reduction resulted in better agreement with experimental data and was particularly evident at discharge Froude numbers below 1. The finite-branch model did not have good agreement with the experimental data and this was explained to be due to the 2D flow approximation.

The potential flow assumption was found to be valid in modeling the flow field at the onset of vortex-free gas entrainment. By including surface tension an overall improvement in the prediction was found, but with the limitation that the dip geometry needed to be defined. The hybrid theoretical-experimental approach was deemed a useful alternative to a purely theoretical prediction of the dip geometry.

Acknowledgment

Financial support of the Natural Sciences and Engineering Research Council of Canada (NSERC) and the Canada Foundation for Innovation (CFI) is gratefully acknowledged.

Nomenclature

a_b = fluid acceleration at point b (m/s^2)
a = point on the interface
A_1, A_2 = discharge branches at $\beta = 90$ deg and $\beta = 270$ deg
b = point on the interface located at the lowest point of the dip
B_1, B_2 = discharge branches at $\beta = 135$ deg and $\beta = 225$ deg
Bo = Bond number, $\mathrm{Bo} = \sigma/\mathrm{ROC}_b g d(\rho_L - \rho_G)$
C = discharge branch at $\beta = 180$ deg
C_1, C_2, C_3 = radius of curvature data fitting coefficients
d = discharge diameter (m)
D = main pipe or header diameter (m)
Fr = discharge liquid Froude number, $\mathrm{Fr} = 4 \cdot \dot{m}/\pi\sqrt{g \cdot d^5 \cdot \rho_L \cdot \Delta\rho}$
g = acceleration due to gravity (m/s^2)
G = gas phase
h = vertical coordinate of the lowest point of the dip (m)
H = liquid height (m)
H_{OGE} = critical height at the onset of gas entrainment (m)
I_1, I_2 = integral equations, see Eqs. (22) and (23)
L = liquid phase
$\dot{m}$ = mass flow rate (kg/s)
n = imaginary branch number, see Eq. (40)
P = pressure (N/m^2)
Q = flow rate (m^3/s)
r, θ = polar coordinates (m, rad)
R = main pipe radius (m)
Re = discharge liquid Reynolds number, $\mathrm{Re} = \dot{m}/\mu_L d$
R_x, R_y = Surface radius of curvature in the x and y directions (m)
ROC = dip radius of curvature (m)
S = flow field surface area (m^2)
v = fluid velocity (m/s)
v_∞ = freestream velocity, see Eq. (37)
We = discharge liquid Weber number, $\mathrm{We} = \dot{m}^2/\sigma \cdot d^3 \rho_L$
x, y, z = rectangular coordinates (m)
X, Y = separation variables, see Eq. (31)

Greek

α_m, β_m = integration constants in Eq. (34), $0 \leq m \leq \infty$
β = discharge orientation (deg)
δ = angle occupied by half of branch (rad)
κ_m, λ_m = integration constants in Eq. (35), $0 \leq m \leq \infty$
η = interface height above the x-y plane (m)
μ = fluid viscosity ($N\,s/m^2$)
Φ = potential function (m^3/s)
ρ = fluid density (kg/m^3)
$\Delta\rho$ = density difference of fluid phases, $\Delta\rho = \rho_L - \rho_G$ (kg/m^3)
σ = surface tension coefficient (N/m)

References

[1] Zuber, N., 1980, "Problems in Modeling of Small Break LOCA," *Nuclear Regulatory Commission, Report No.* NUREG-0724.
[2] Reimann, J., and Khan, M., 1984, "Flow Through a Small Break at the Bottom of a Large Pipe With Stratified Flow," Nucl. Sci. Eng., **88**, pp. 297–310.
[3] Smoglie, C., and Reimann, J., 1986, "Two-Phase Flow Through Small Branches in a Horizontal Pipe With Stratified Flow," Int. J. Multiphase Flow, **12**, pp. 609–625.
[4] Yonomoto, T., and Tasaka, K., 1991, "Liquid and Gas Entrainment to a Small Break Hole From a Stratified Two-Phase Region," Int. J. Multiphase Flow, **17**, pp. 745–765.
[5] Parrott, S. D., Soliman, H. M., Sims, G. E., and Krishnan, V. S., 1991, "Experiments on the Onset of Gas Pull-Through During Dual Discharge From a Reservoir," Int. J. Multiphase Flow, **17**, pp. 119–129.
[6] Hassan, I. G., Soliman, H. M., Sims, G. E., and Kowalski, J. E., 1996, "Experimental Investigation of the Two-Phase Discharge From a Stratified Region Through Two Side Branches Oriented Vertically," Exp. Therm. Fluid Sci., **13**, pp. 117—128.
[7] Hassan, I. G., Soliman, H. M., Sims, G. E., and Kowalski, J. E., 1996, "Discharge From a Smooth Stratified Two-Phase Region Through Two Horizontal Side Branches Located in the Same Vertical Plane," Int. J. Multiphase Flow, **22**, pp. 1123–1142.
[8] Maier, M. R., Soliman, H. M., and Sims, G. E., 2001, "Onsets of Entrainment During Dual Discharge from a Stratified Two-Phase Region Through Horizontal Branches With Centerlines Falling in an Inclined Plane: Part 2—Experiments on Gas and Liquid Entrainment," Int. J. Multiphase Flow, **27**, pp. 1029–1049.
[9] Ahmad, T., and Hassan, I., 2006, "Experimental Investigation on the Onset of Gas Entrainment From a Stratified Two-Phase Region Through Multiple Branches Mounted on a Curved Surface," ASME J. Fluids Eng., **128**, pp. 726–733.
[10] Soliman, H. M., and Sims, G. E., 1991, "Theoretical Analysis of the Onset of Liquid Entrainment for Slots of Finite Width," Int. J. Heat Fluid Flow, **12**, pp. 360–354.
[11] Soliman, H. M., and Sims, G. E., 1992, "Theoretical Analysis of the Onset of Liquid Entrainment for Orifices of Finite Diameter," Int. J. Multiphase Flow, **18**, pp. 229–235.
[12] Armstrong, K. F., Parrott, S. D., Sims, G. E., Soliman, H. M., and Krishnan, V. S., 1992, "Theoretical and Experimental Study of the Onset of Liquid Entrain-

Downloaded 03 Jun 2010 to 171.66.16.158. Redistribution subject to ASME license or copyright; see http://www.asme.org/terms/Terms_Use.cfm

ment During Dual Discharge From Large Reservoirs," Int. J. Multiphase Flow, **18**, pp. 217–227.
[13] Hassan, I. G., Soliman, H. M., Sims, G. E., and Kowalski, J. E., 1999, "The Onset of Liquid Entrainment During Discharge From Two Branches on an Inclined Wall," Can. J. Chem. Eng., **77**, pp. 433–438.
[14] Maier, M. R., Soliman, H. M., and Sims, G. E., 2001, "Onsets of Entrainment During Dual Discharge From a Stratified Two-Phase Region Through Horizontal Branches With Centerlines Falling in an Inclined Plane: Part 1—Analysis of Liquid Entrainment," Int. J. Multiphase Flow, **27**, pp. 1011–1028.
[15] Ahmed, M., Hassan, I., and Esmail, N., 2003, "Modeling the Onset of Gas Entrainment Through a Finite-Side Branch," ASME J. Fluids Eng., **125**, pp. 902–909.
[16] Taylor, G. I., 1950, "The Instability of Liquid Surfaces When Accelerated in a Direction Perpendicular to the Planes," Proc. R. Soc. London, Ser. A, **201**, pp. 192–196.
[17] Andaleeb, A. F., Hassan, I., Saleh, W., and Ahmad, T., 2006, "Modeling the Onset of Gas Entrainment From a Stratified Two-Phase Region Through Branches on a Curved Surface," ASME J. Fluids Eng., **128**, pp. 717–725.
[18] Craya, A., 1949, "Theoretical Research on the Flow of Nonhomogeneous Fluids," Houille Blanche, **4**, pp. 44–55.
[19] Banerjee, S., and Nieman, Re., 1982, "Fundamental Studies on Heavy Water Reactor Thermal Hydraulics," *Heat Transfer in Nuclear Reactor Safety*, Hemisphere, Washington, DC, 49–86.
[20] White, F. M., 1991, *Viscous Fluid Flow*, McGraw-Hill, New York.
[21] Smith, M. G., 1967, *Introduction to the Theory of Partial Differential Equations*, Van Nostrand, London.
[22] Zwillinger, D., 1996, *Standard Mathematical Tables and Formulae*, 30th ed., CRC, Boca Raton, FL.
[23] Kline, S. J., and McClintock, F. A., 1953, "Describing Uncertainties in Single-Sample Experiments," Mech. Eng. (Am. Soc. Mech. Eng.), **75**, pp. 3–8.

Downloaded 03 Jun 2010 to 171.66.16.158. Redistribution subject to ASME license or copyright; see http://www.asme.org/terms/Terms_Use.cfm

M. Ahmed[1]

N. Ashgriz[2]
e-mail: ashgriz@mie.utoronto.ca

Department of Mechanical and Industrial Engineering,
University of Toronto,
5 King's College Road,
Toronto, ON, M5S 3G8, Canada

H. N. Tran
Department of Chemical Engineering and Applied Chemistry,
University of Toronto,
200 College Street,
Toronto, ON, M5S 3E5, Canada

Break-Up Length and Spreading Angle of Liquid Sheets Formed by Splash Plate Nozzles

An experimental investigation is conducted to determine the effect of liquid viscosity and density, nozzle diameter, and flow velocity on the break-up length and spreading angle of liquid sheets formed by splash plate nozzles. Various mixtures of corn syrup and water were used to obtain viscosities in the range of 1–170 mPa s. Four different splash plate nozzle diameters of 0.5 mm, 0.75 mm, 1 mm, and 2 mm, with a constant plate angle of 55 deg were tested. The liquid sheet angles and the break-up lengths were measured at various operating conditions. An empirical correlation for the sheet spreading angle and a semi-empirical correlation for the sheet break-up lengths are developed.
[DOI: 10.1115/1.3026729]

1 Introduction

Splash plate nozzles are used in a wide variety of industries. In the pulp and paper industry, splash plate nozzles are used to spray black liquor into a Kraft recovery boiler. Black liquor is a by-product of papermaking, which contains up to 90% solids. The boiler performance is intimately related to the spray characteristics produced by the splash plate nozzle. Splash plate nozzles or surface impinging jets also have applications in some auto engines, gas turbines, and liquid-fueled rocket engines as reported by Inamura et al. [1,2].

The sheet break-up length is an important parameter that describes spray properties, such as the droplet size, velocity, and trajectory of droplets. These spray properties determine the combustion time and the location where the reactions take place. If a long uniform liquid sheet is formed by a splash plate nozzle, the spray will be sensitive to the flue gases in the furnace or combustor, which may break up the sheet more rapidly. Furthermore, the heat radiation may affect the liquid viscosity and consequently may have a significant effect on the break-up mechanism, which affects the average droplet size and droplet size distribution.

In a splash plate nozzle, a jet of fluid impinges on a solid surface (the splash plate) and spreads out radially while thinning. The liquid sheet interacts with the surrounding gas and breaks into small droplets. These atomizers have several advantages, such as low injection pressure loss and high controllability of a generated liquid sheet. The atomization characteristics of a splash plate nozzle depends on the characteristics of the liquid sheet (film) produced by the nozzle. For instance, thinner liquid sheets produce smaller droplets; more turbulent sheets produce wider droplet size distributions; and longer sheets allow for more exposure to the hot ambient, resulting in an increased heat and mass transfer [3–5].

The studies on the causes of sheet instability and its breakup have shown that the principal cause of sheet breakup is the interaction of the sheet with the surrounding atmosphere, whereby rapidly growing waves are induced on the sheet. Sheet breakup occurs when the amplitude of these waves reach a critical value. Using a linear instability analysis, the characteristics of these waves have been investigated for inviscid liquid sheets of uniform thickness, as indicated by Hagerty and Shea [6], and for viscous liquid sheets with variation in sheet thickness, as indicated by Dombrowski and co-workers [7,8]. It is found that viscosity retards the growth of perturbations. The predicted growth rate of a disturbance is a function of both wavelength and sheet thickness.

Based on a stationary antisymmetric wave theory, Dombrowski and Hooper [7] developed the following correlation for the break-up length of liquid sheets produced by fan nozzles:

$$L_b = 1.5\left[K\frac{\rho}{\rho_g}\ln\left(\frac{\zeta_o}{\lambda}\right)\left(\frac{\mathrm{We}_h^{0.5}(\mathrm{We}_h-1)}{(\mathrm{We}_h-1)^2}\right)\right]^{0.5} \tag{1}$$

where $\mathrm{We}_L=\rho U^2 h/\sigma$ is the Weber number, U is the velocity of the liquid sheet, K is the thickness parameter for the fan spray nozzle, ρ and ρ_g are the densities of the liquid and the gas, respectively, and ζ_o and λ are the initial disturbance and wave amplitudes, respectively. They concluded that the break-up length increases with increasing shear viscosity and decreases with increasing sheet velocity.

Arai and Hashimoto [9] reported the following correlation for the sheet break-up length of a viscous sheet:

$$\frac{L_b}{h} = \frac{416\ \mathrm{Re}_h^{0.6}}{h^{0.5}\mathrm{We}_h^{0.5}} \tag{2}$$

The linear theories, however, do not properly predict the sheet break-up behavior. They underpredict the break-up length by up to 50%, as reported by Ryan et al. [10]. Furthermore, the linear theories predict a decrease in sheet break-up length with increasing Weber number. However, experimental measurements indicate that the break-up length increases to a maximum, then decreases with increasing Weber number [10,11]. In addition, the break-up length is linearly proportional to the Weber number, and it increases with decreasing impinging angle (more aligned with the impinging surface) and increasing jet velocity, as reported by Ryan et al. [10], Huang [11], Anderson et al. [12], and Li and Ashgriz [13].

In addition to the sheet break-up lengths, other sheet characteristics have also been investigated. These are sheet thickness distribution by Shen and Poulikakos [14] and Choo and Kang [15]; velocity distribution within the sheet by Li and Ashgriz [13] and Speilbauer and Adams [16]; and large scale sheets of high viscosity fluids by Speilbauer and Adams [17], Miikkulainen and co-

[1]Present address: Mechanical Engineering Department, Assiut University, Assiut 71516, Egypt.

[2]Corresponding author.

Contributed by the Fluids Engineering Division of ASME for publication in the JOURNAL OF FLUIDS ENGINEERING. Manuscript received November 12, 2007; final manuscript received August 15, 2008; published online December 11, 2008. Assoc. Editor: Theodore Heindel.

 Copyright © 2009 by ASME

Downloaded 03 Jun 2010 to 171.66.16.158. Redistribution subject to ASME license or copyright; see http://www.asme.org/terms/Terms_Use.cfm

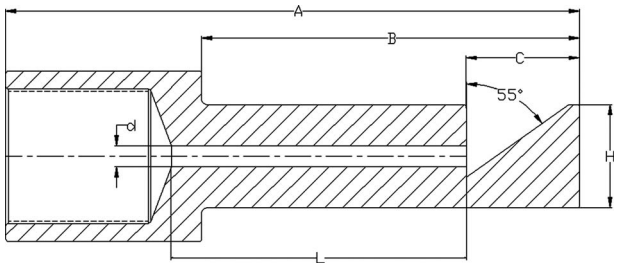

Fig. 1 A sectional view of the splash plate nozzle

workers [18,19], and Ahmed et al. [20]. Results indicate that the sheet thickness is independent of the jet velocity but dependent on the jet angle, jet diameter, and liquid viscosity.

Most recently Ahmed et al. [20] experimentally investigated the break-up mechanism for liquid sheets formed by splash plate nozzles for different liquid viscosities, nozzle diameters, and flow velocities. They reported that the sheet atomization process for the range of parameters studied was governed by two different mechanisms: Rayleigh–Plateau (R-P) and Rayleigh–Taylor (R-T) instabilities. R-P occurs at the rim, and R-T occurs on the thin sheet. The rim instability can be laminar or turbulent, depending on the jet Reynolds number. The R-T instability of the sheet is always observed at the outer edges of the radially spreading sheet, where the sheet is the thinnest. It can also occur inside the sheet, due to the formation of holes and ruptures.

The present study is aimed at developing correlations for the break-up length and spreading angle of liquid sheets produced by the splash plate nozzle. Effects of liquid viscosity, density, and flow velocity and nozzle diameter on the break-up length and spreading angle of liquid sheets formed by splash plate nozzles are presented.

2 Experimental Setup and Procedures

A simple splash plate nozzle design is used in our experiments. The cross-sectional view of this nozzle is shown in Fig. 1. This nozzle is constructed by machining an aluminum rod of length A, such that a pipe with an inner diameter of d is formed (this is the nozzle diameter). The rod is then machined through its cross section at a 55 deg angle to clear the pipe opening. For the nozzle with a pipe diameter of $d=1.0$ mm, the dimensions shown in Fig. 1 are $A=40.3$ mm, $B=21$ mm, $C=8.23$ mm, $H=5.04$ mm, and $L=15.25$ mm. All other nozzles are geometrically scaled by the pipe diameter. Four different nozzle diameters of $d=0.5$ mm, 0.75 mm, 1.0 mm, and 2 mm were used. The splash plate angle was kept constant at 55 deg. Splash plate angle of 55 deg is a commonly used angle in recovery boilers. This angle was found to be the optimum angle in producing the proper boiler performance. In order to keep the number of parameters in the study manageable, the nozzle angle was kept constant at 55 deg for all nozzles. Nozzle angle affects the sheet thickness distribution, and it will be the subject of a future study, along with other nozzle design parameters.

Solutions of corn syrup with water were used to obtain a wide range of viscosities, ranging from 1.0 mPa s to 170 mPa s. Viscosities were measured using a Rheometrics ARES-RFS3 mechanical spectrometer using 50 mm cone and plate geometry. Corn syrup behaves like a Newtonian fluid in the range of parameters studied here. By knowing the density of the corn syrup at room temperature ($\rho=1450$ kg/m^3), densities of the solutions of corn syrup and water were calculated. In addition, the surface tension of the solution was measured using a Kruss K100MK2 tensiometer. A high-speed video camera was used to obtain images of the liquid sheets produced by splash plate nozzles. The flow velocities in the splash plate nozzle ranged from 5 m/s to about 44 m/s. A rotameter was used to measure the flow rate of the liquid from the pressurized tank to the splash plate nozzle. Two rotameters were used to measure flows in the range of 0.1–1.8 l/min, and 2.0–7.0 l/min, respectively. For solutions of water and corn syrup, a graded cylinder and stopwatch were used to measure the flow rate by collecting a certain volume of solution over a known time.

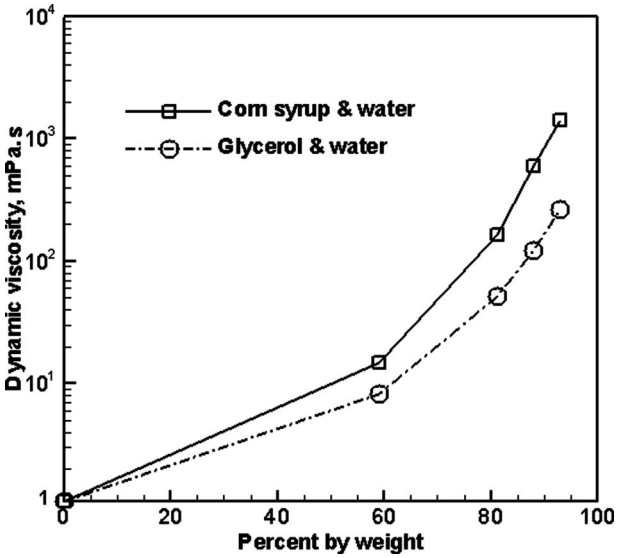

Fig. 2 Variation of viscosity versus percent by weight for two mixtures, corn syrup and water, and glycerol and water

The physical properties of the corn syrup solutions used are provided by Ahmed et al. [20]. The variation of the viscosity versus the weight percentage for two mixtures—corn syrup and water, and glycerol and water—is shown in Fig. 2. The values of viscosity for the mixture of glycerol and water were obtained from the Handbook of Chemistry and Physics [21]. The reasons behind selecting the corn syrup for the current study are that the viscosity of mixture of corn syrup and water at the same weight percent is much higher than that of the mixture of glycerol and water, as shown in Fig. 2.

The overall experimental setup is shown in Fig. 3. The splash plate nozzle is connected to a pressure tank through a flow meter. A constant pressure supply of compressed nitrogen is used, via a pressure regulator, to pressurize a solution of corn syrup and water inside the tank. The break-up length and the sheet angle were directly measured from each image. More than 50 measurements were made to find an average value for each condition.

3 Results and Discussions

The sheet spreading angle and break-up length are measured for a wide range of liquid viscosities, flow velocities, and nozzle diameters. Furthermore, a theoretical model based on the impingement of a liquid jet on a disk is used to develop correlations for the break-up length.

3.1 Sheet Spreading Angle. Sheet spreading angle is obtained by first drawing a tangent to the tip of the splash plate at its centerline and determining the intersection points of this tangent with the edges of the sheet (see Fig. 4). Then, two tangents to the liquid sheet are drawn from the two intersection points. The angle between the two tangent lines to the sheet is defined as the sheet spreading angle (θ). Typical images of liquid sheets produced by a splash plate nozzle at different liquid viscosities are shown in Figs. 5–7. These figures depict the effect of liquid viscosity on the sheet spreading angle for different flow velocities and for the nozzle diameters of 1 mm and 2 mm. The flow velocity is determined based on the measured flow rate and the orifice diameter.

For a liquid viscosity of $\mu=1.0$ mPa s, the sheet spreading

Downloaded 03 Jun 2010 to 171.66.16.158. Redistribution subject to ASME license or copyright; see http://www.asme.org/terms/Terms_Use.cfm

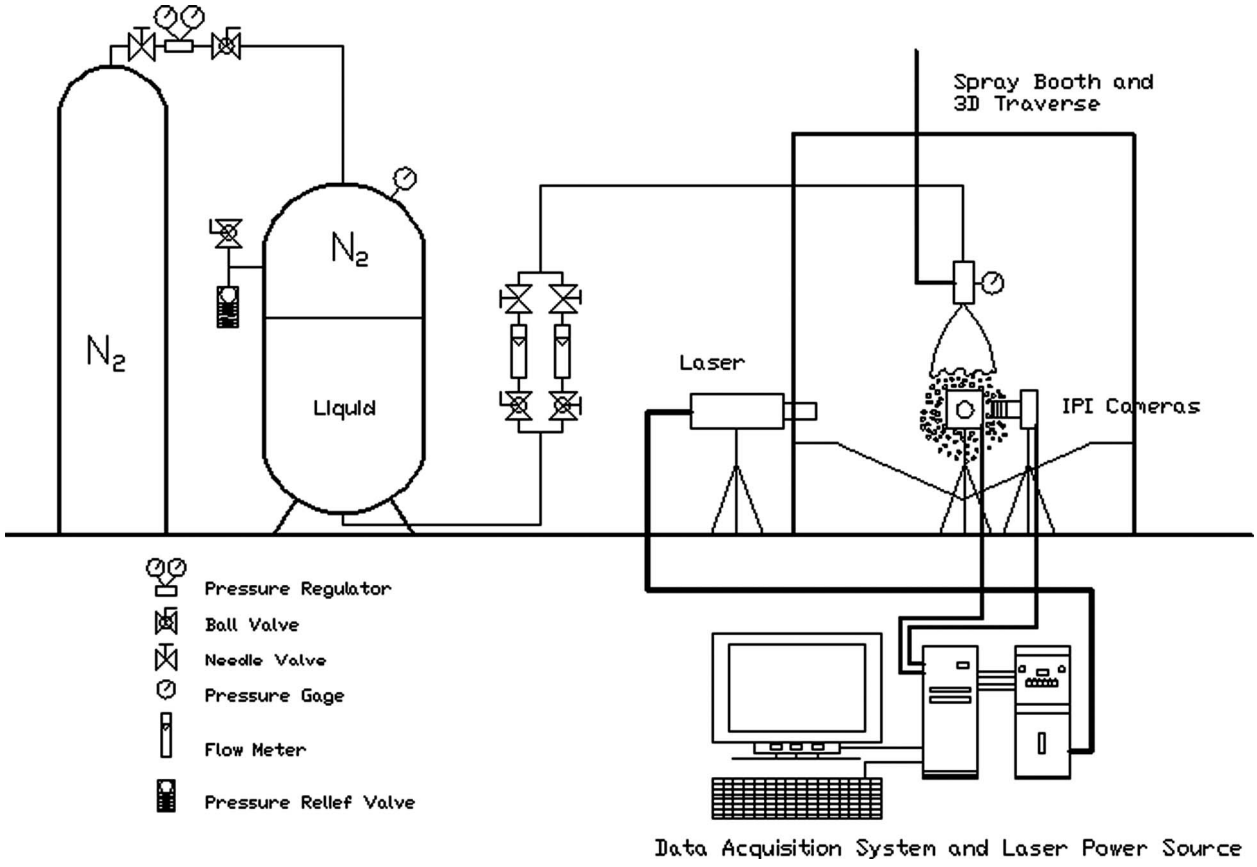

Fig. 3 Schematic of the experimental setup

angle is $\theta=124$ deg, as shown in Fig. 5. By increasing the viscosity to 80 mPa s, the spreading angle decreases to 114 deg. Further increase in viscosity to 170 mPa s decreases the sheet spreading angle to 98 deg. The cause of the decrease in spreading angle with increasing viscosity is due to an increase in surface shear on the plate. Furthermore, increasing the viscosity reduces the nozzle flow Reynolds number. At a low viscosity of $\mu=1.0$ mPa s, the Reynolds number is $\mathrm{Re}_d=24{,}000$ and the flow is turbulent. In this case, the sheet is thin, perturbed, and unstable with significant surface waves. However, increasing the viscosity to 80 mPa s and 170 mPa s, resulting in $\mathrm{Re}=300$ and 140, respectively, the flow becomes laminar. In this case, the sheet is thick and stable. The liquid viscosity damps the surface waves and limits the spreading of the liquid sheet and, consequently, the spreading angle reduces.

Figure 6 shows the effect of the splash plate nozzle flow velocity on the sheet spreading angle at different liquid viscosities of 14 mPa s and 80 mPa s and nozzle diameters of 1 mm and 2 mm. At a nozzle diameter of 2 mm and $\mu=14$ mPa s, increasing the flow velocity V from 8.6 m/s to 17.3 m/s, increases the sheet spreading angle from 108 deg to 119 deg. A similar trend was found at the nozzle diameter of 1 mm and $\mu=80$ mPa s, where increasing the flow velocity from 16 m/s to 35 m/s increases the sheet spreading angle from 94 deg to 128 deg. In general, by increasing the flow velocity, the sheet spreading angle increases due to the increase in applied flow inertia. In addition, the sheet spreading characteristics are mainly dependent on the net resultant driving forces on the impact region. Increasing the flow velocity results in a high impact pressure and, consequently, the sheet spreading angle increases.

The effect of splash plate nozzle diameter on the sheet spreading angle at velocities of 13 m/s and 17 m/s and of liquid viscosities of 1 mPa s and 14 mPa s is shown in Fig. 7. Based on this figure, at a flow velocity of 13 m/s and $\mu=1.0$ mPa s, increasing

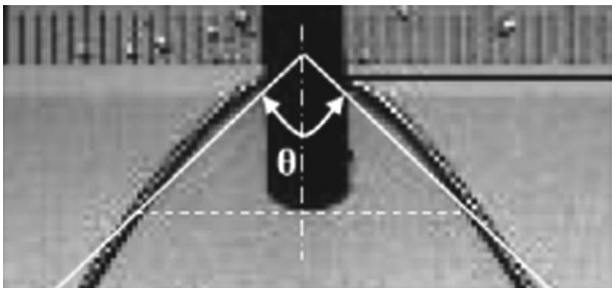

Fig. 4 Definition of spray angle θ

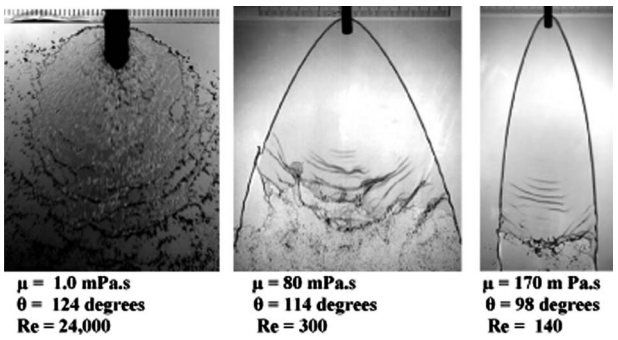

Fig. 5 Effect of liquid viscosity on the sheet spreading angle at a flow velocity of 24 m/s using the splash plate nozzle with a 1.0 mm diameter

Downloaded 03 Jun 2010 to 171.66.16.158. Redistribution subject to ASME license or copyright; see http://www.asme.org/terms/Terms_Use.cfm

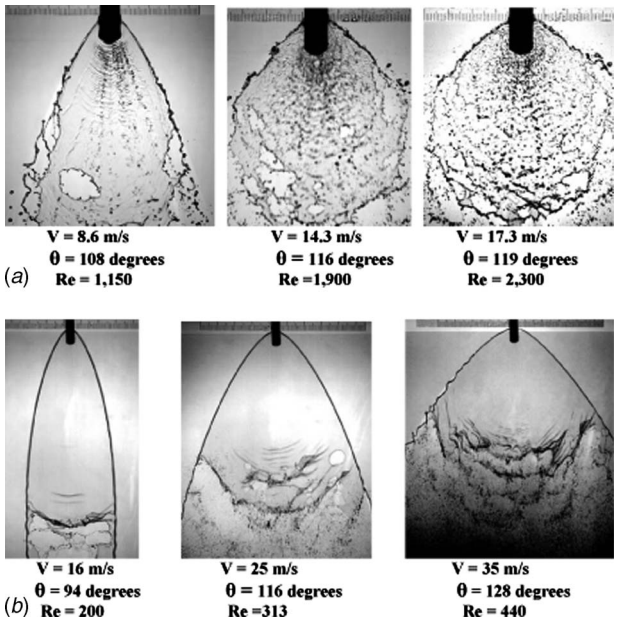

Fig. 6 Effect of the splash plate nozzle flow velocity on the sheet spreading angle at different values of nozzle diameters and liquid viscosities. (*a*) Nozzle diameter=2.0 mm, μ=14.0 mPa s; and (*b*) nozzle diameter=1.0 mm, μ=80.0 mPa s.

the diameter from 1 mm to 2 mm increases the sheet spreading angle from 90 deg to 114 deg. Also, at a flow velocity of 17 m/s and μ=14 mPa s, the spreading angle increases from 110 deg to 118 deg when the nozzle diameter increases from 1 mm to 2 mm. Clearly, increasing the nozzle diameter increases the sheet spreading angle. In conclusion, the sheet spreading characteristics are mainly dependent on the net resultant driving forces on the impact region. Increasing the liquid viscosity tends to increase the wall shear stress and consequently retards the flow. Since the inertia force is constant, this will reduce the sheet spreading angle. However, increasing the flow velocity increases the inertia forces as well as the surface shear. Consequently, the net driving force increases, which increases the sheet spreading angle.

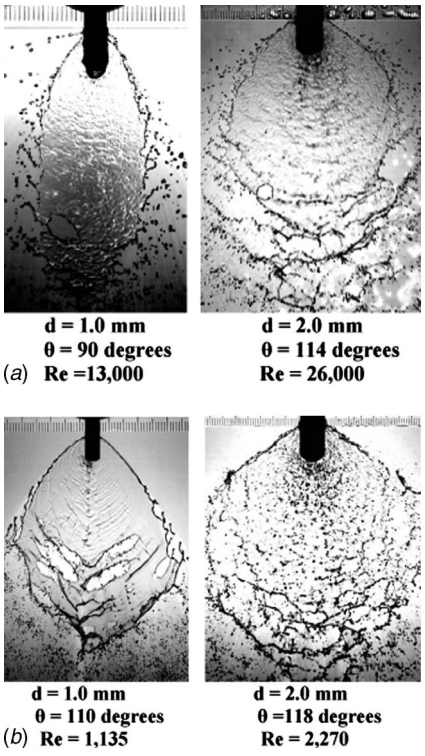

Fig. 7 Effect of the splash plate nozzle diameter on the sheet spreading angle at different values of flow velocities and liquid viscosities. (*a*) Flow velocity=13 m/s, μ=1.00 mPa s; and (*b*) flow velocity=17 m/s, μ=14 mPa s.

The sheet spreading angle is measured for different nozzle diameters (d), liquid viscosities (μ), liquid densities (ρ), and flow velocities (V). All possible regression models that are statistically significant at a level less than 0.01 along with the corresponding values of coefficient of determination (R^2), and the residual mean square (s^2), are reported in Table 1. The residual mean square (s^2) can be defined as

$$S^2 = \frac{\sum_{i=1}^{n} (y_i - y_{pi})^2}{n-2}$$

where y_i is the measured value, y_{pi} is the predicted value, and n is the number of observations. Based on the values of R^2 and s^2, the best regression model was selected and can be defined as follows:

$$\theta = 0.024\rho^{1.23}V^{0.39}d^{0.28}/\mu^{0.08} \tag{3}$$

This correlation has a regression coefficient of R^2=0.75. The comparison between the predicted and measured sheet spreading angles is shown in Fig. 8. Sheet spreading angle increases with jet velocity, jet diameter, and liquid density, but it decreases with liquid viscosity.

3.2 Sheet Break-Up Length. Sheet break-up length is defined as the intact length of the liquid sheet, as described in Fig. 9. The break-up lengths are found based on averaging over 50 images for each case. The manner in which the sheet breaks up into droplets depends on the operating conditions. All possible regression models that are statistically significant at a level less than 0.01 along with the corresponding values of coefficient of determination (R^2), and the residual mean square (s^2), are reported in Tables 2 and 3. The regression model that correlates the break-up length with the primitive variables is shown in Fig. 10, and those that correlate the break-up length with the dimensionless variables are shown in Figs. 11 and 12.

Figure 10 presents the variation of the predicted versus the measured break-up lengths. Two clear trends are observed for the variation of break-up length with flow velocity. At low velocities, the break-up length increases with increasing the flow velocity, as shown in Fig. 10(*a*), and the correlation for this case is

$$L_b = CV^{0.62}d^{1.53}\nu^{0.33} \tag{4a}$$

where C=39,735. At higher velocities the break-up length decreases with increasing the flow velocity, as shown in Fig. 10(*b*), and its correlation is given by

$$L_b = CV^{-0.48}d^{0.87}\nu^{0.24} \tag{4b}$$

where C=1720. The velocity at the transition from the first trend to the second trend can be determined by equating the two correlations. Figure 10(*b*) shows that the correlation does not properly fit the data for the larger orifice diameter of 2 mm. The regression coefficient for this case is R^2=0.85.

Figure 11(*a*) presents the variation of the predicted versus measured break-up lengths based on dimensionless variables, when the break-up length increases with increasing the flow velocity. The correlation for this case is

$$\frac{L_b}{d} = C\frac{\mathrm{We}_d^{0.2}}{\mathrm{Re}_d^{0.25}} \tag{5a}$$

where C=126. Figure 11(*b*) presents the variation of the predicted versus measured break-up lengths when the break-up length de-

Downloaded 03 Jun 2010 to 171.66.16.158. Redistribution subject to ASME license or copyright; see http://www.asme.org/terms/Terms_Use.cfm

Table 1 Regression models of spray angle versus controlling variables in dimensional and nondimensional forms

Variables	Regression model	R^2	S^2
We	$\theta=22.2\mathrm{We}^{0.18}$	0.68	0.0116
Re, We	$\theta=17.2\mathrm{Re}^{0.022}\mathrm{We}^{0.18}$	0.72	0.0103
Re, We, μ/μ_a	$\theta=4.6\mathrm{Re}^{0.156}\mathrm{We}^{0.12}(\mu/\mu_a)^{0.14}$	0.74	0.0096
Re, We, ρ/ρ_a	$\theta=0.0044\mathrm{Re}^{0.1}\mathrm{We}^{0.15}(\rho/\rho_a)^{1.17}$	0.74	0.0097
Re, We, μ/μ_a, ρ/ρ_a	$\theta=0.031\mathrm{Re}^{0.16}\mathrm{We}^{0.11}(\mu/\mu_a)^{0.093}(\rho/\rho_a)^{0.77}$	0.74	0.0095
V, d	$\theta=206.4V^{0.38}d^{0.27}$	0.73	0.01
V, d, ρ, μ	$\theta=0.024V^{0.39}d^{0.28}\rho^{1.23}\mu^{-0.08}$	0.75	0.0095

creases with increasing the flow velocity. The correlations for this case are

$$\frac{L_b}{d}=\frac{C}{\mathrm{We}_d^{0.14}\,\mathrm{Re}_d^{0.22}} \tag{5b}$$

where $C=1340$. These correlations poorly fit the experimental measurements with a very low regression coefficient of $R^2=0.7$ and 0.75, for Figs. 11(*a*) and 11(*b*), respectively.

The above empirical correlations with both primitive and dimensionless variables do not accurately represent the variation of the break-up length over a wide range of parameters. It was found that the data for the 2 mm nozzle diameter did not fit the developed correlation. Inspection of the corresponding images indicated that the break-up regime in this case is the "perforation" type, as shown in Fig. 6(*a*), which occurred at a viscosity of 14 mPa s. However, for water the perforation regime occurs at a much higher Reynolds number, $\mathrm{Re}\geq 24{,}000$.

Therefore, another attempt was made to correlate the data based on a semi-empirical model. In this case, the analytical model for the impingement of a liquid jet on a solid disk is used to determine the sheet velocity and thickness at the tip of the splash plate. The break-up length is then correlated with these variables, rather than the nozzle inlet variables.

The impinging jet theory is used to determine the viscous liquid sheet thickness and its velocity. In general, for normal impingement of a circular jet on a flat surface, the flow quickly spreads out uniformly in all directions, as shown in Fig. 12. The impingement of a liquid jet on a horizontal flat surface using the boundary-layer theory was studied by Watson [22]. His theory provides an analytical expression for the layer thickness and velocity as a function of the radial location in both laminar and turbulent flow regimes.

He found a similarity solution by assuming that the sheet velocity can be written as $u=U(r)f(\eta)$, where $U(r)$ is the velocity at the free surface, and $\eta=z/h(r)$. And

$$f(\eta)=2.73-\frac{3.46}{1+\cos[1.845(1-\eta)]} \tag{6}$$

where "cos" is the cosine integral defined as

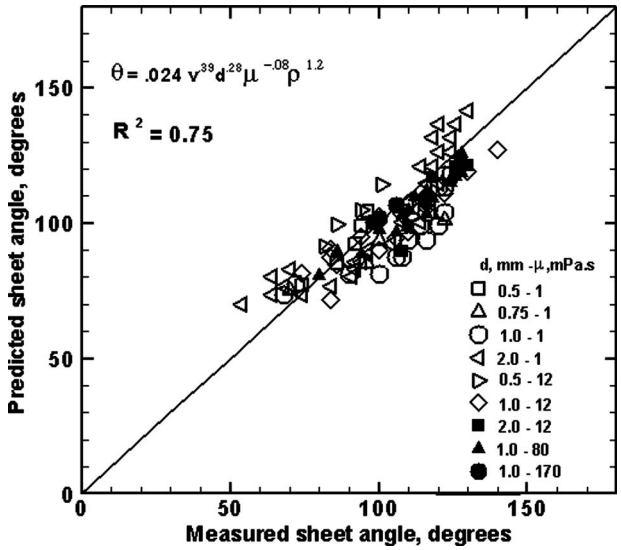

Fig. 8 Variation of the predicted sheet spreading angle versus the measured values

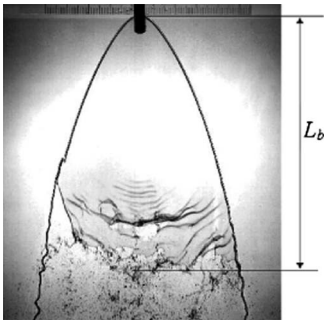

Fig. 9 The definition of the break-up length L_b

Table 2 Regression models of the break-up length versus controlling variables in dimensional and nondimensional forms in the case of decreasing L_b/d with increasing flow velocity

Variables	Regression model	R^2	S^2
Re	$L_b/d=353.2\mathrm{Re}^{0.22}$	0.72	0.0621
Re, We	$L_b/d=1340\mathrm{Re}^{-0.22}\mathrm{We}^{-0.14}$	0.75	0.0538
Re, We, μ/μ_a	$L_b/d=17.5\mathrm{Re}^{0.22}\mathrm{We}^{-0.37}(\mu/\mu_a)^{0.45}$	0.79	0.0462
Re, We, ρ/ρ_a	$L_b/d=21.7\times10^{9}\mathrm{Re}^{-0.37}\mathrm{We}^{-0.073}(\rho/\rho_a)^{-2.35}$	0.76	0.0512
V, d	$L_b=13.7V^{-0.34}d^{0.64}$	0.41	0.1935
V, d, ρ	$L_b=34.3\times10^{-9}V^{-0.42}d^{-0.87}\rho^{3.07}$	0.78	0.0726
V, d, μ	$L_b=302.6V^{-0.48}d^{0.87}\mu^{0.219}$	0.85	0.05
V, d, ν	$L_b=1720V^{-0.48}d^{0.87}\nu^{0.24}$	0.85	0.0487
(h/d), (u_p/V)	$L_b/d=354(h/d)^{0.91}(u_p/V)^{0.44}$	0.82	0.037

Table 3 Regression models of break-up length versus controlling variables in dimensional and nondimensional forms in the case of increasing L_b/d with increasing flow velocity

Variables	Regression model	R^2	S^2
Re	$L_b/d=700\mathrm{Re}^{-0.28}$	0.67	0.0415
Re, We	$L_b/d=126\mathrm{Re}^{-0.25}\mathrm{We}^{0.2}$	0.73	0.036
Re, μ/μ_a	$L_b/d=0.02\mathrm{Re}^{0.5}(\mu/\mu_a)^{0.77}$	0.85	0.0196
V, d, μ	$L_b=3460V^{0.63}d^{1.53}\mu^{0.3}$	0.95	0.0193
V, d, ν	$L_b=39{,}735V^{0.62}d^{1.53}\nu^{0.33}$	0.95	0.0193
(h/d), (u_p/V)	$L_b/d=0.387(h/d)^{-1.91}(u_p/V)^{-2.55}$	0.85	0.019

Downloaded 03 Jun 2010 to 171.66.16.158. Redistribution subject to ASME license or copyright; see http://www.asme.org/terms/Terms_Use.cfm

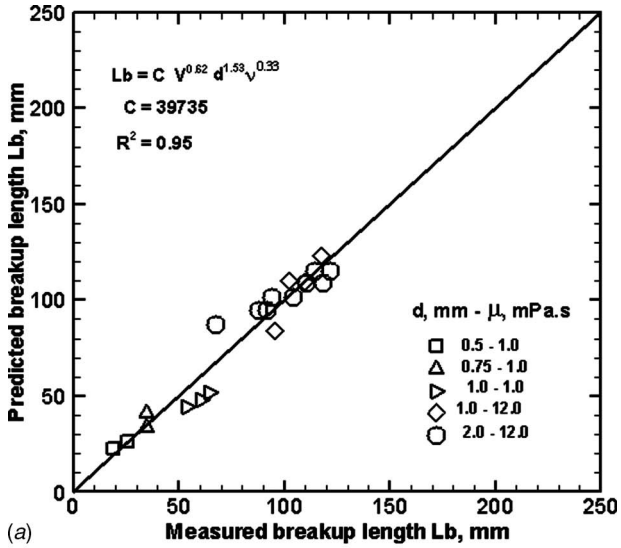

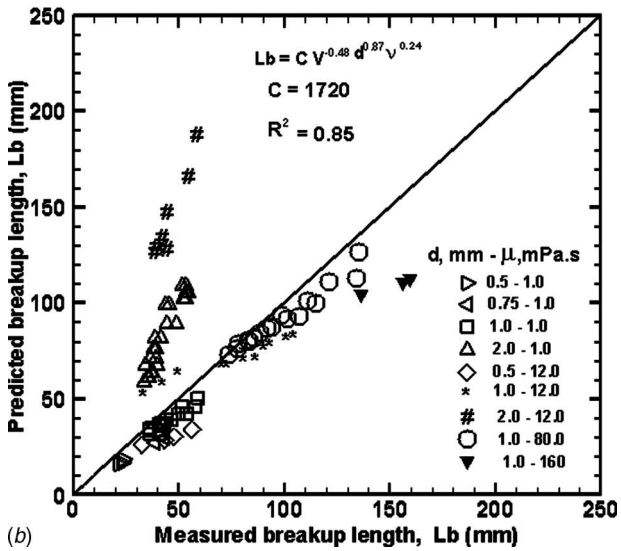

Fig. 10 Variation of the predicted break-up length versus the measured break-up length. (*a*) Breakup increases with increasing flow velocity, and (*b*) breakup decreases with increasing flow velocity.

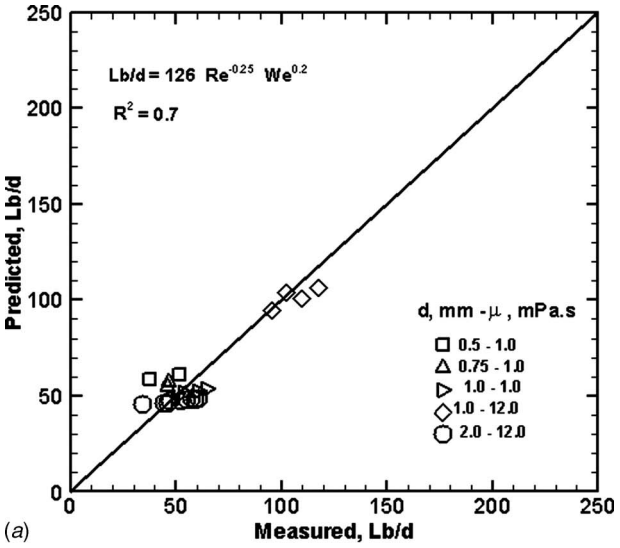

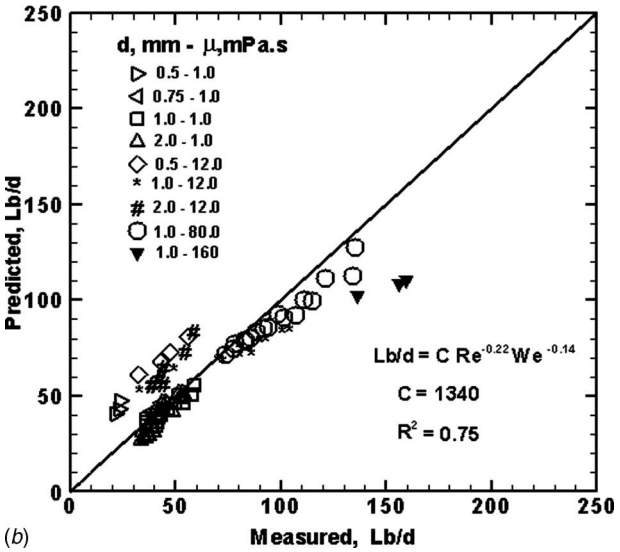

Fig. 11 Variation of the predicted dimensionless break-up length versus the measured values. (*a*) Breakup increases with increasing flow velocity, and (*b*) breakup decreases with increasing flow velocity.

$$\cos(z) = 0.577 + \ln(z) + \sum_{n=1}^{\infty} (-1)^n \frac{z^{2n}}{(2n)\,!\,2n}$$

For the laminar flow, he provided the following general solution:

$$U(r) = \left(\frac{27C^2}{8\pi^4}\right)\left[\frac{Q^2}{\nu(r^3 + l^3)}\right] \tag{7}$$

$$h(r) = \left(\frac{2\pi^2}{3\sqrt{3}}\right)\left(\frac{\nu(r^3 - l^3)}{Qr}\right) \tag{8}$$

where Q is the volume flow rate, l is an arbitrary constant length given as $l = 0.33d\mathrm{Re}^{1/3}$, and $C = 1.402$. And for the turbulent flows,

$$U = 8.22\left[\frac{Q^{5/4}}{\nu^{1/4}(r^{9/4} + l^{9/4})}\right] \tag{9}$$

$$h(r) = 0.0211\left(\frac{\nu}{Q}\right)^{0.25}\left(\frac{r^{2.25} + l^{2.25}}{r}\right) \tag{10}$$

where l is a constant length given as

$$l^{9/4} = 6.065\left(\frac{Q}{\nu}\right)^{1/4} d^2$$

In order to estimate the average thickness and velocity of a liquid sheet at the splash plate tip, only a segment of the axisymmetric flow with a segment angle equal to the splash plate sheet angle is considered. The total flow rate is now modified to con-

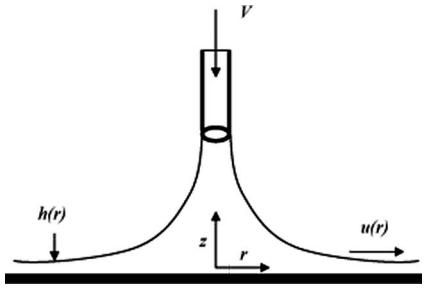

Fig. 12 Liquid jet impact on a horizontal surface

Downloaded 03 Jun 2010 to 171.66.16.158. Redistribution subject to ASME license or copyright; see http://www.asme.org/terms/Terms_Use.cfm

sider the flow through a segment: $Q=Q_n x(2\pi/\theta)$, where Q_n is the nozzle flow rate. V (flow velocity through the splash plate nozzle) is assumed to be the same in both the segment and the full disk cases. Therefore, an equivalent nozzle diameter for a disk case is obtained as $d=d_n\sqrt{2\pi/\theta}$.

Assuming that similar flow conditions occur when $(r/d)_{\text{disk}} = (r/d)_{\text{segment}}$, we get $r=r_n\sqrt{2\pi/\theta}$, where r_n is the radial distance in the case of flow over a full sized disk. The tip radius of the splash plate is $r=r_p$. The final expression for the liquid velocity and the sheet thickness at the nozzle tip of the splash plate for a laminar flow is now written as

$$u_p = \frac{V^2 d^4 \theta^{-2}}{C_1 \nu r_p^3 \theta^{-1.5} + C_2 d^4 V \theta^{-2}} \tag{11}$$

$$h = C_3\left(\frac{\nu r_p^2}{V d^2 \theta^{0.5}}\right) + C_4\left(\frac{d^2}{\theta r_p}\right) \tag{12}$$

And for a turbulent flow,

$$u_p = C_5\left[\frac{V^{1.25} d^{2.5} \nu^{-0.25} \theta^{-1.25}}{C_6 r_p^{2.25} \theta^{-1.125} + C_7 V^{0.25} d^{2.5} \nu^{-.25} \theta^{-1.25}}\right] \tag{13}$$

$$h = C_8\left(\frac{\nu^{0.25}\theta^{-0.75}}{r_p d^{0.5} V^{0.25}}\right)\left\{C_6\left(\frac{r_p^{2.25}}{\theta^{1.125}}\right) + C_7\left(\frac{d^{2.5}V^{.25}}{\nu^{0.25}\theta^{1.25}}\right)\right\} \tag{14}$$

where $C_1=15.75$, $C_2=1.42$, $C_3=12.13$, $C_4=1.1$, $C_5=55.6$, $C_6=7.9$, $C_7=0.64$, $C_8=0.09$, and θ is the sheet angle.

Two different trends have been observed for the variation of the break-up length with jet velocity. In the first case, the break-up length increases with increasing velocity, whereas; in the second case, the break-up length decreases with increasing velocity. Then each regime is correlated individually in terms of the sheet thickness and the velocity at the splash plate tip. The dependence of L_b/d for increasing and decreasing break-up lengths is given as follows. For the first case, where the break-up length increases with the nozzle velocity,

$$\frac{L_b}{d} = 0.387\left(\frac{h}{d}\right)^{-1.9}\left(\frac{u_p}{V}\right)^{-2.6} \quad \text{with} \quad R^2 = 0.85 \tag{15}$$

For the second case, where the break-up length decreases with the nozzle velocity,

$$\frac{L_b}{d} = 354\left(\frac{h}{d}\right)^{0.913}\left(\frac{u_p}{V}\right)^{0.436} \quad \text{with} \quad R^2 = 0.82 \tag{16}$$

Based on the correlations given in Eqs. (15) and (16), the velocity at the transition from the first case to the second case can be determined by equating Eqs. (15) and (16) and solving the resulting equation to obtain the transition velocity in terms of the nozzle diameter, liquid viscosity, and density.

The comparison between experimental measurements with the error bar at 95% confidence level and the predicted break-up length for both cases are shown in Figs. 13(*a*) and 13(*b*). Figure 13(*a*) represents the correlation between the measured and predicted dimensionless break-up lengths in the case of increasing break-up length with flow velocity. In this case, the break-up length increases with decreasing the dimensionless sheet thickness and sheet velocities, as shown by correlation (15). However, in the case of decreasing the break-up length with increasing the flow velocity, as shown in Fig. 13(*b*), the break-up length increases with increasing dimensionless sheet thickness and sheet velocity, as presented by correlation (16).

For a specific nozzle diameter, the break-up length increases with increasing the flow velocity up to a maximum value of V_t. Further increase in the flow velocity, beyond V_t, results in a decrease in the break-up length. This trend is similar to that of a liquid jet. The break-up length of a liquid jet increases with the velocity up to a maximum value, then after, it decreases with the velocity. This trend is attributed to the jet transition from laminar

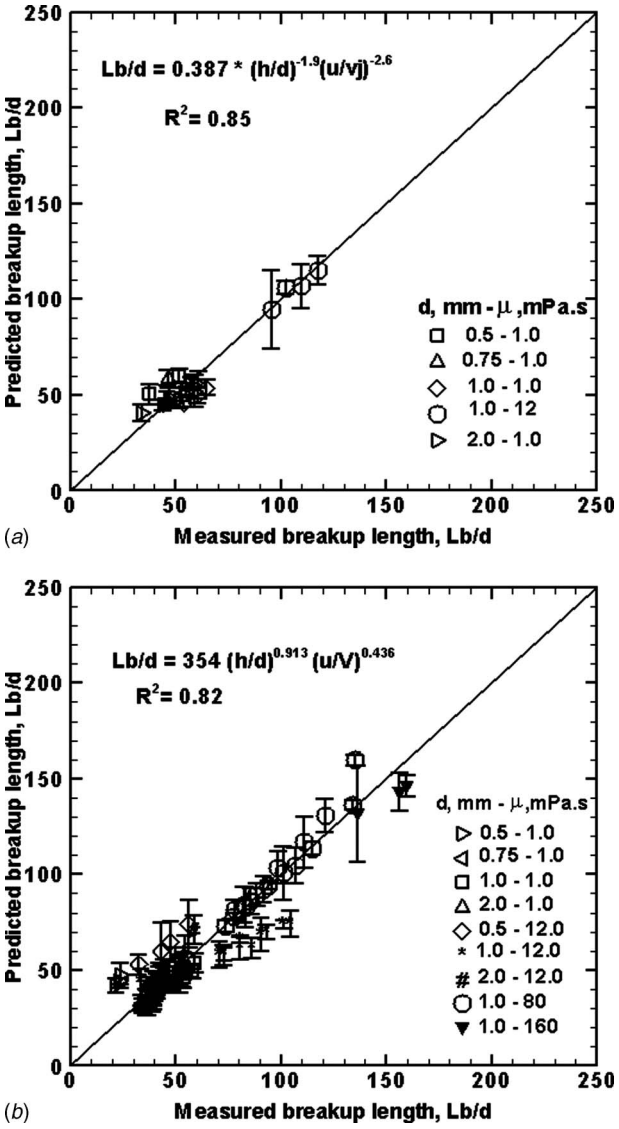

Fig. 13 Variation of the predicted dimensionless break-up length versus the measured values. (*a*) Breakup increases with increasing flow velocity, (*b*) breakup decreases with increasing flow velocity.

to turbulent flow. Similarly, for velocities beyond V_t, a liquid sheet becomes highly turbulent with the formation of tears and perforations. Consequently, the breakup occurs earlier. Similar results are reported for two impinging jets as well [10–12].

In order to determine the transition velocity V_t, substituting the values of $\boldsymbol{u_p}$ and $\boldsymbol{h}$ that are described by Eqs. (11) and (12) in Eqs. (15) and (16). Then equate Eqs. (15) and (16) and let $V=V_t$. The resulting equation represents the mathematical formula to calculate the value of V_t in case of laminar flow. In order to find V_t in case of turbulent flow, repeating the same procedure by substituting the values of u_p and h as described by Eqs. (13) and (14) in Eqs. (15) and (16), and then equating both equations. The resulting equations for laminar and turbulent flows are to be solved in order to determine the transition velocity, V_t, in case of both laminar and turbulent flow. Each equation can be solved by using an iterative technique such as the secant method. For instance, the values of transition velocity (V_t) at $\mu=1.0$ mPa s and different values of nozzle diameters are given in Table 4.

The variation of the break-up length with the velocity of the splash plate nozzle with diameters of 0.5 mm, 0.75 mm, 1 mm,

Downloaded 03 Jun 2010 to 171.66.16.158. Redistribution subject to ASME license or copyright; see http://www.asme.org/terms/Terms_Use.cfm

Table 4 The value of transition velocity (V_t) at liquid viscosity (μ) of 1.0 mPa s

d (mm)	0.5	0.75	1.0	2.0
V_t	23	17	12.5	8

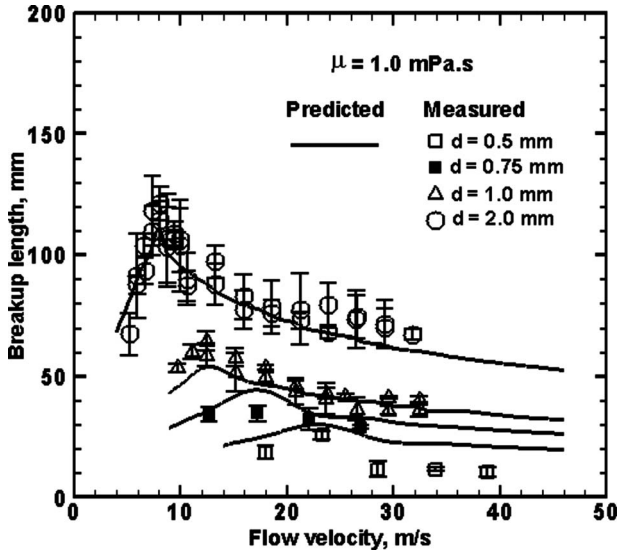

Fig. 14 Variation of the break-up length versus velocity at different values of the splash plate nozzle diameter for water (μ =1 mPa s)

and 2 mm using water is presented in Fig. 14. This figure can be used to explain the uncertainty of the developed correlations where the variation of the break-up length versus the flow velocity is presented. In this figure, the values of the measured break-up length at a 95% confidence level are presented at different values of nozzle diameters (0.5 mm, 0.75 mm, 1 mm, and 2 mm). It was found that the correlation well predicts the break-up length for 1 mm and 2 mm. However, for 0.5 mm and 1 mm, the correlation slightly overpredicts the measured values with a 95% confidence level. Experimental measurements with a 90% confidence level are well predicted by the correlation.

4 Conclusions

An experimental investigation was carried out to determine the effect of liquid viscosity, as well as flow velocity and nozzle diameter, on the sheet spreading angle and the break-up length of the liquid sheet formed by splash plate nozzles. The findings can be summarized as follows.

- The sheet spreading angle at the nozzle tip increases with increasing nozzle diameter, flow velocity, and liquid density, whereas it decreases with increasing liquid viscosity.
- The sheet spreading angle correlation with flow velocity, nozzle diameter, liquid density, and viscosity shows two orders of magnitude in the power differences of various variables. Therefore, it is difficult to develop a correlation based on nondimensional parameters such as the Reynolds number.
- Two different trends for break-up length have been observed. The break-up length first increases with increasing the nozzle flow velocity and then decreases. This trend shown by the sheet break-up process is similar to that found by the jet breakup within a turbulent flow region and fully developed spray region [23].
- In both cases where the break-up length increases and then decreases with the flow velocity, the break-up length was found to be strongly dependent on the sheet thickness. Consequently, it was correlated with the calculated sheet thickness, as well as the velocity at the tip of the splash plate nozzle, where the tip velocity is a function of nozzle diameter, flow velocity, liquid kinematic viscosity, tip radius, and sheet spreading angle.

Acknowledgment

This work is jointly supported by the NSERC and the research consortium on "Increasing Energy and Chemical Recovery Efficiency in the Kraft Process" at the University of Toronto.

Nomenclature

A, B, C, H, and L = splash plate nozzle characteristic dimensions, as defined in Fig. 1

$C1, C2, \ldots,$ $C8$ = constants

cn = cosine integral

d = nozzle diameter

h = liquid sheet thickness

K = thickness parameter for the fan spray

L_b = sheet break-up length

l = constant parameter

Q = equivalent flow rate for the splash plate configuration, m^3/s

Q_n = splash plate nozzle flow rate, m^3/s

r_p = tip radius of the splash plate nozzle

r, z = polar cylindrical coordinate system, as defined in Fig. 11

U = average sheet velocity

u, w = sheet velocity at the r and z directions

V_g = ambient gas velocity

V = liquid velocity through the splash plate nozzle

Re_d = Reynolds number based on the nozzle diameter, $\rho v d/\mu$

Re_h = Reynolds number based on the sheet thickness, $\rho v h/\mu$

We_d = Weber number based on the nozzle diameter, $\rho v^2 d/\sigma$

We_h = Weber number based on the sheet thickness, $\rho v^2 h/\sigma$

Greek Letters

ζ = initial disturbance

λ = wave amplitude

ν = kinematic viscosity

α = splash plate angle

μ = liquid viscosity

μ_g = gas viscosity

θ = sheet angle, as defined in Fig. 4

σ = surface tension, N/m

ρ = liquid density, kg/m^3

ρ_g = gas density, kg/m^3

ε = eddy viscosity

References

[1] Inamura, T., and Tomoda, T., 2004, "Characteristic of Spray Through Wall Impinging Nozzles," Atomization Sprays, **14**, pp. 375–395.

[2] Inamura, T., Yanaoka, H., and Tomoda, T., 2004, "Prediction of Mean Droplet Size of Sprays Issued From Wall Impingement Injector," AIAA J., **42**(3), pp. 614–621.

[3] Bennington, C., and Kerekes, R., 1985, "Effect of Temperature on Drop Size of Black Liquor Sprays," Proceedings of the International Chemical Recovery Conference, TAPPI, New Orleans, LA, pp. 345–354.

[4] Dombrowski, N., and Hooper, P., 1962, "The Effect of Ambient Density on Drop Formation in Sprays," Chem. Eng. Sci., **17**, pp. 291–305.

[5] Obuskovic, N., and Adams, T., 1991, "Fluid Sheet Thickness and Velocity at

Downloaded 03 Jun 2010 to 171.66.16.158. Redistribution subject to ASME license or copyright; see http://www.asme.org/terms/Terms_Use.cfm

the Tip of a Black Liquor Splash Plate Nozzle," Chem. Eng. Commun., **104**, pp. 1–20.
[6] Hagerty, W., and Shea, J., 1955, "A Study of the Stability of Plane Fluid Sheets," ASME J. Appl. Mech., **22**, pp. 509–514.
[7] Dombrowski, N., and Hooper, P., 1964, "A Study of Sprayed Formed by Impinging Jets in Laminar and Turbulent Flow," J. Fluid Mech., **18**, pp. 392–440.
[8] Dombrowski, N., and Johns, W., 1963, "The Aerodynamic Instability and Disintegration of Viscous Liquid Sheets," Chem. Eng. Sci., **18**, pp. 203–213.
[9] Arai, T., and Hashimoto, H., 1986, "Disintegration of a Thin Liquid Sheet in a Concurrent Gas Stream," Int. J. Turbo Jet Engines, **3**, pp. 301–306.
[10] Ryan, H., Anderson, W., Pal, S., and Santoro, R., 1995, "Atomization Characteristics of Impinging Jets," J. Propul. Power, **11**, pp. 135–145.
[11] Huang, J., 1970, "The Break-Up of Axisymmetric Liquid Sheets," J. Fluid Mech., **43**, pp. 305–319.
[12] Anderson, W., Ryan, H., Pal, S., and Santoro, R., 1992, "Fundamental Studies of Impinging Liquid Jets," 30th Aerospace Sciences Meeting and Exhibition, Paper No. AIAA 92–0458.
[13] Li, R., and Ashgriz, N., 2006, "Characteristics of Liquid Sheets Formed by Two Impinging Jets," Phys. Fluids, **18**, pp. 087104.
[14] Shen, Y., and Poulikakos, D., 1998, ""Thickness Variation of Liquid Sheet Formed by Two Impinging Jets Using Holographic Interferometry," ASME J. Fluids Eng., **120**, pp. 482–487.
[15] Choo, Y., and Kang, B., 2001, "Parametric Study on Impinging-Jet Liquid Sheet Thickness Distribution Using an Interferometric Method," Exp. Fluids, **31**, pp. 56–62.
[16] Speilbauer, T., and Adams, T., 1992, "Mechanisms of Liquid Sheet Breakup and the Resulting Drop Size Distributions, Part 1: Types of Spray Nozzles and Mechanisms of Sheet Disintegration," Tappi J., **73**(2), pp. 36–142.
[17] Speilbauer, T., and Adams, T., 1992, "Mechanisms of Liquid Sheet Breakup and the Resulting Drop Size Distributions, Part 2: Strand Breakup and Experimental Observations," Tappi J., **73**(3), pp. 195–200.
[18] Miikkulainen, P., Kankkunen, A., Jarvinen, M., and Fogelholm, C., 2005, "Predicting Droplet Size From Black Liquor Spray Characteristics," Tappi J., **4**(5), pp. 11–17.
[19] Miikkulainen, P., Kankkunen, A., and Jarvinen, M., 2004, "Furnace Endoscope—Measuring Fuel Spray Properties in Hot and Corrosive Environments," Exp. Fluids, **37**, pp. 910–916.
[20] Ahmed, M., Amighi, A., Ashgriz, N., and Tran, H., 2007, "Characteristics of Liquid Sheet Formed by Splash Plate Nozzles," Exp. Fluids, **44**, pp. 125–136.
[21] 1948, *Handbook of Chemistry and Physics*, 20th ed., Chemical Rubber, Cleveland, OH.
[22] Watson, E., 1964, "The Radial Spread of a Liquid Jet Over a Horizontal Plane," J. Fluid Mech., **20**(3), pp. 481–499.
[23] Lefebvre, A. H., 1989, *Atomization and Sprays*, Taylor & Francis, London.

Downloaded 03 Jun 2010 to 171.66.16.158. Redistribution subject to ASME license or copyright; see http://www.asme.org/terms/Terms_Use.cfm

DSMC Simulation: Validation and Application to Low Speed Gas Flows in Microchannels

T. Ewart

J. L. Firpo

I. A. Graur
e-mail: irina.graour@polytech.univ-mrs.fr

P. Perrier

J. G. Méolans

Universite de Provence-Ecole Polytechnique
Universitaire de Marseille,
UMR CNRS 6595,
5 Rue Enrico Fermi,
13453 Marseille, France

A direct simulation Monte Carlo method (DSMC) solver, adapted to the subsonic microflow, is developed under the object-conception language (C++). Some technical details critical in these DSMC computations are provided. The numerical simulations of gas flow in a microchannel are carried out using the developed DSMC solver. Streamwise velocity distributions in the slip flow regime are compared with the analytical solution based on the Navier–Stokes equations with the velocity slip boundary condition. Satisfactory agreements have been achieved. Furthermore, the domain of the validity of this continuum approach is discussed. Simulations are then extended to the transitional flow regime. Streamwise velocity distributions are also compared with the results of the numerical solutions of the linearized Boltzmann equation. We emphasize the influence of the accommodation coefficient on the velocity profiles and on the mass flow rate. The simulation results on the mass flow rate are compared with the experimental data, which allow us to validate the "experimental" technique of the determination of the accommodation coefficient.
[DOI: 10.1115/1.3026733]

1 Introduction

The progress in the fabrication technique during the past ten years lead to the miniaturization of many devices (micropumps, microvalves, microgas detectors, etc.), and lead to the development of the computational methods that allow us to simulate the gas flows inside these devices. Due to the small characteristic sizes of these apparatus comparable to the mean free path of the molecules, the flow regime varies from the continuum to the transitional regime and even to the near free molecular regime. In the transitional and the near free molecular regimes the Monte Carlo simulations [1] are generally considered as the closest approach to the real experimental conditions. During the past decade, several Monte Carlo simulations were performed in gas microflows; the most part of them dealt with supersonic flows [2–5], which are a traditional domain of the DSMC. However, in micro-electro-mechanical systems (MEMS) applications the flow velocity is usually subsonic. Therefore, two main problems appear when one applies the DSMC method to the subsonic gas flow. When the bulk velocity is much slower than the thermal velocity, as is typically the case for gas flows in MEMS, many independent samples are needed to eliminate statistical scatter and to recover the bulk flow properties. The second problem that appears in the subsonic application, provides the correct formulation of the inlet/outlet boundary conditions.

Based on the ideas of Bird [1], we developed our DSMC software using the object oriented language C++. The following ideas are implemented in order to adapt the DSMC technique to the subsonic flow treatment.

- A high number of molecules per cell and also a large sample size are used in order to reduce the statistical fluctuations.
- The number of real molecules represented by each simulated molecule varies according to the cells.
- The developed software is parallelized using message passing interface (MPI) and/or OpenMP application programming interfaces.

The new treatment for the inlet/outlet boundary conditions is proposed.

In order to validate the developed DSMC solver the flow in a rectangular microchannel is simulated. In the transitional regime the computational results are compared with the numerical results obtained for the flow between two parallel plates using the Bhatnagar–Gross–Krook (BGK) kinetic model [6] and with the numerical solution of the linearized Boltzmann equation [7], and in the slip flow regime, with the results of continuum modeling [8].

The accommodation coefficient obtained "experimentally" from mass flow rate measurements in Ref. [9] in the slip regime are injected into the numerical DSMC simulation in the slip and transitional flow regimes. The results of these simulations are compared with the measurements in order to verify the pertinence of the experimental accommodation coefficient for the slip and transitional flow regimes.

2 Algorithm

2.1 Computational Domain. We chose the geometry of the simulation domain close to the experimental geometry [9]: The microchannel is fixed between two tanks (see Fig. 1). The gas flows through the microchannel owing to a pressure difference between the two tanks, where the pressures are maintained constant and equal to p_{in} and p_{out}, respectively. The temperature is supposed to be constant and the same in both tanks and also along the microchannel walls, since we considered here isothermal flows.

2.2 Collisions and Movements. The usual "no time counter" (NTC) method [1] governs the collision pair selections. The collision cross sections are calculated according to the hard sphere (HS) model [10]; this makes it easier to compare our DSMC results with the solution of the linearized Boltzmann equation [7] and the BGK kinetic equation [11], both obtained using HS molecules.

The motion of the simulated molecules during the time step is simple because it is rectilinear. However, these rectilinear trajectories may cross the different types of walls (specular or Maxwellian reflective surfaces) during one time step. We developed an algorithm that solves the problem of molecule-wall collisions in the whole geometry and not cell by cell.

The first advantage of this algorithm, in view of the parallelization, is that the movement of the molecules is calculated in the whole computational domain: A processor will continue to move the molecule within the whole geometry even if the molecule leaves its particular computational domain. The second advantage is the possibility to manage the multireflection of the molecule from the wall, which allows one to calculate correctly the reflection process near a wall junction or in a tube with a small diameter.

Contributed by the Fluids Engineering Division of ASME for publication in the JOURNAL OF FLUIDS ENGINEERING. Manuscript received April 22, 2008; final manuscript received October 3, 2008; published online December 2, 2008. Assoc. Editor: Rajat Mittal.

Downloaded 03 Jun 2010 to 171.66.16.158. Redistribution subject to ASME license or copyright; see http://www.asme.org/terms/Terms_Use.cfm

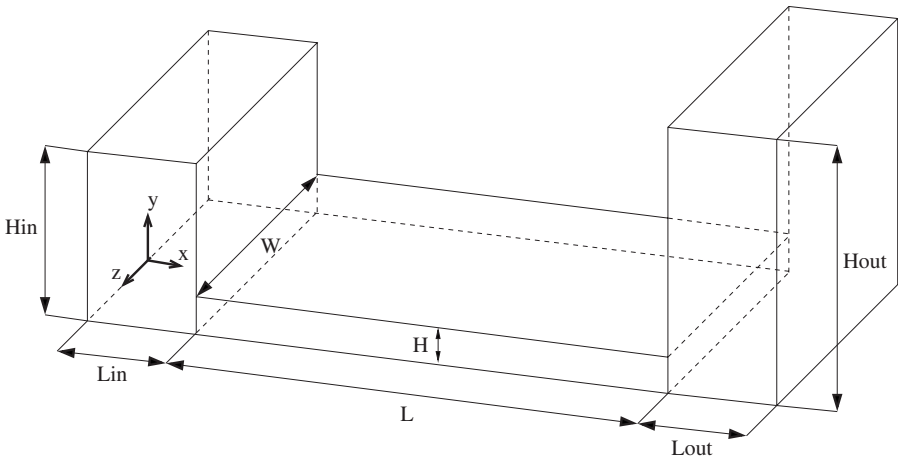

Fig. 1 Schematic view of the channel

2.3 Weighting Factor. Every cell is characterized by a lot of data (position, size, etc.) and one of the most important data is the number of real molecules N_R represented by each simulated molecule. Inside a cell, the number of real molecules in every time step is given through

$$N(t) = N_S(t)N_R \tag{1}$$

where $N_S(t)$ is the number of simulated molecules and $N(t)$ is the number of real molecules in the cell at the time t. At the initial time ($t=0$) N_R is given by

$$N_R = \frac{p(t)V(t)}{kT(t)N_S(t)} \tag{2}$$

where $p(t)$, $T(t)$, and $N_S(t)$ are, respectively, the initialization values ($t=0$) of the pressure, the temperature, and the number of molecules in the cell, and V is the volume of the cell. Usually in DSMC simulations, N_R is the same for all cells [1]. However, a first example of a radial weighting factor was introduced by Bird [1] in axially symmetric flows, where the volume of the cells near the axis is smaller than that far from the axis.

In our simulation we use also a N_R number that varies according to the cells, but as a function of the local density (or pressure) of the gas in the cell, while the volume of the cell remains the same. The main advantage of this concept is that we keep a similar number of simulated molecules N_S in every cell whatever the pressure value. Therefore, in the parallel version of the code the MPI grid is easily determined: Each processor manages the same number of cells and every processor works generally with a similar number of simulated molecules. But this concept also has a shortcoming: It is necessary to follow the molecules when they cross the cells and to correct the number of the simulated molecules. When a simulated molecule leaves cell 1 toward cell 2, it means that N_{R_1} molecules physically enter cell 2. But in cell 2 N_{R_1} real molecules shall be represented by N_{R_1}/N_{R_2} simulated particles, therefore a correction must generally be done. The following three cases are possible.

- $N_{R_1}=N_{R_2}$. We just have to affect the new cell and subcell numbers to the entering simulated molecules.
- $N_{R_1}<N_{R_2}$. Some of the entering simulated molecules have a probability to be destroyed through the rejection procedure.
- $N_{R_1}>N_{R_2}$. All entering molecules fill the subcells of cell 2, and the entering molecules have a probability to be duplicated. Thus, some extra molecules are created in these subcells with the same momentum as the entering molecules.

This kind of correction must be done in each time step. It ensures the conservation of the mean values of the number of real molecules, momentum, and energy when a molecule crosses the cell's boundary [12].

The concept of a variable weighting factor (number of real molecules represented by each simulated molecule N_R) can be used to adapt the splitting of the computational domain in various cells depending on the physical parameter, of which we want to evaluate the mean value. Thus a variable grid structure may be generated, which may become finer and finer, according to the various calculation domains.

2.4 Boundary Conditions

2.4.1 Inlet/Outlet Boundary Conditions (Tanks). As it was mentioned in the Introduction, there are many ways to determine the subsonic constant pressure boundary conditions. Here we simulate the "real" inlet and outlet tanks. The sizes of these tanks are proportional to the characteristic dimensions. When $\mathrm{Kn}>1$, the mean free path is the characteristic dimension and is the one that determines the tank size; when $\mathrm{Kn}<1$, the channel height is the characteristic dimension. Different sizes were tested for the tanks, and finally the minimal optimal size was found as follows. The height and the length of the tanks are equal to ten times the characteristic dimension, when $\mathrm{Kn}<1$, and five times, when $\mathrm{Kn}>1$. Moreover, the width of the tanks is equal to the width of the microchannel.

Steady conditions in the tanks are guaranteed by the following physical features. We suppose that, at the beginning of the numerical simulation, the gas is in the thermodynamic equilibrium state at temperature $T(0)=T$ and is macroscopically at rest. Initially the number of simulated molecules N_S is fixed in both tanks and N_R; the number of real molecules represented by each simulated molecule is obtained from Eq. (2), where $p=(p_{\mathrm{in}}$ or $p_{\mathrm{out}})$ and $V=(V_{\mathrm{in}}$ or $V_{\mathrm{out}})$ are the pressure in the tank and the volume of the tank, respectively. In order to maintain the pressure constant in each tank, we keep the initial number of simulated molecules constant in the tank during the calculation. After each time step we count the number of simulated molecules in the tank. If this number is different from its initial value, we will create or delete the molecules in order to keep the same number of simulated molecules. Creation or destruction is carried out in the first cell of the inlet tank and in the last cell of the outlet tank. The new molecules created in the tank are initialized again with a peculiar velocity equal to the mean quadratic thermal velocity (no macro-

Downloaded 03 Jun 2010 to 171.66.16.158. Redistribution subject to ASME license or copyright; see http://www.asme.org/terms/Terms_Use.cfm

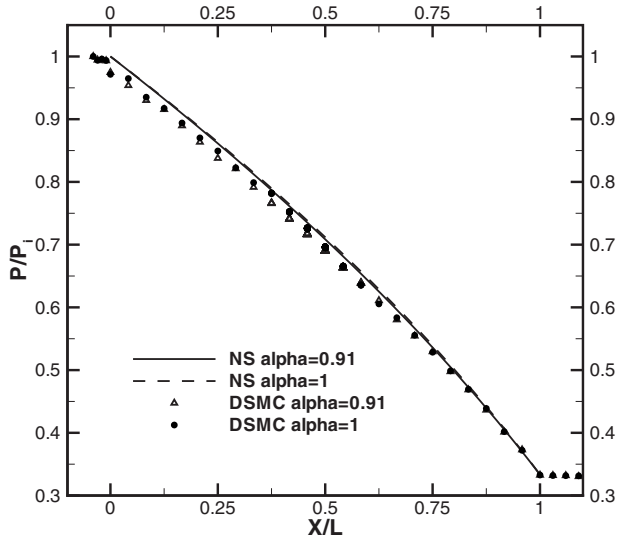

Fig. 2 Streamwise velocity profiles in m/s: the solid line represents the continuum solution [8] with σ_p=1.016, the dash-dotted line is the same continuum solution with $\sigma_p=\sqrt{\pi}/2$, and the DSMC solution (α=1) is presented with the circles

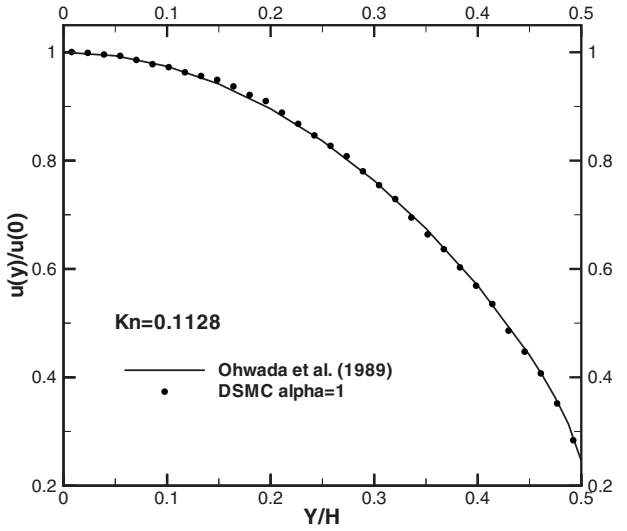

Fig. 3 Streamwise velocity profiles in m/s for Kn=0.1128: the solid line represents the continuum solution [8] with σ_p =1.204, α=0.91, the DSMC solution for α=1 is represented with the circles, and the DSMC solution for α=0.91 is represented with the triangles

scopic velocity). Globally it may be proved that the temperature, pressure, and total energy are maintained in each tank during the time.

2.4.2 Molecules/Wall Interaction. The interaction of the molecules on the wall is described by the specular-diffuse Maxwell scattering kernel, the same as on the wall of the channel. The channel and the tank walls are considered as quasidiffuse, except for the walls perpendicular to the z axis, which are considered as specular walls (in order to simulate a quite large system).

3 Comparisons and Comments

Velocity profiles. First, the streamwise velocity profiles obtained from the present DSMC code are compared with the solutions derived from the linearized Boltzmann equation [7], under the full accommodation assumption, and for a Knudsen number equal to 0.1, which certainly corresponds to the slip regime. Ohwada et al. [7] supposed that the nondimensional pressure gradient $\nu=(H/p)(dp/dx)$ is small compared with 1 and also that the pressure gradient is uniform. But, in fact, in the considered flow regime the pressure gradient is nonuniform (see Fig. 2). According to the continuum modeling, the pressure distribution in the slip regime is proportional to the square root of the distance along the channel [13,8]. Therefore, comparing here the normalized profiles (the velocity profiles are given in Ref. [7] only in nondimensional form $(u/\nu\sqrt{2RT})$) for the same local Knudsen number we test the dependence of the velocity profiles only on the transversal variable y (not at all the pertinence of the DSMC modeling along the channel axis). Figure 3 represents the velocity profiles normalized by the velocity on the channel axis, so the dependence on the pressure gradient is eliminated, and the agreement is very good.

The velocity profiles obtained from the Navier–Stokes equations with the first order boundary condition [8] are plotted in Fig. 4 for the same Knudsen number, Kn=0.1 and for different theoretical values of the velocity slip coefficient calculated under the full accommodation assumption; the velocity slip coefficient obtained by Maxwell [14] $\sigma_p=\sqrt{\pi}/2$ (near 0.886) using a force balance (and thus neglecting the Knudsen layer effect) and the velocity slip coefficient calculated in Ref. [15], σ_p=1.016, taking into account the influence of the Knudsen layer. The continuum dimensional velocities are compared with the results of the DSMC simulation. The Navier–Stokes (NS) velocity profile calculated with the velocity slip coefficient derived from the kinetic theory [15] (σ_p=1.016) gives an excellent agreement with the DSMC simulation anywhere in the channel except in the Knudsen layer zone near the wall of thickness $\sim\lambda/2$. In this zone a direct evaluation of the real slip velocity at the wall was obtained in Ref. [16] by the resolution of the linearized Boltzmann equation for the Kramers problem in the case of the full accommodation. This value of the real slip velocity at the wall (the real gas velocity) may be expressed as a function of the fictitious slip velocity u_s [15], generally used as the boundary condition for the Navier–Stokes equations. In the case where the molecules are completely accommodated in the state of the wall, we have [16] $u_{\text{gas}}=(u_s/\sqrt{2}\sigma_p)\sim 0.696u_s$. Thus, for Kn=0.1, we can estimate the real gas velocity at the wall from the fictitious slip velocity u_s and

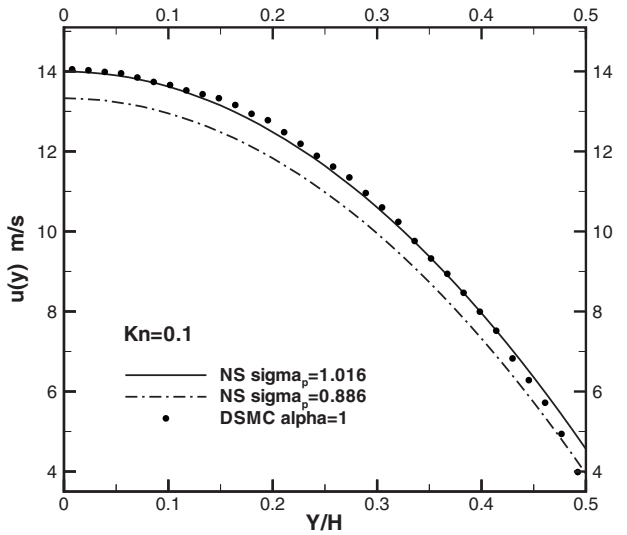

Fig. 4 Streamwise velocity profiles in m/s for Kn=0.2256: the solid line represents the continuum solution [8] with σ_p =1.204, α=0.91, the DSMC solution for α=1 is represented with the circles, and the DSMC solution for α=0.91 is represented with the triangles

Downloaded 03 Jun 2010 to 171.66.16.158. Redistribution subject to ASME license or copyright; see http://www.asme.org/terms/Terms_Use.cfm

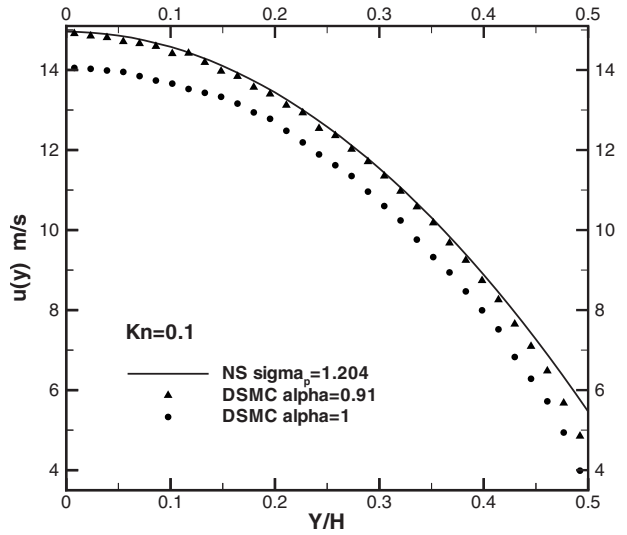

Fig. 5 Streamwise velocity profiles normalized by the velocity on the axis: the solid line represents the solution of the linearized Boltzmann equation [7], and the DSMC solution is represented with the circles

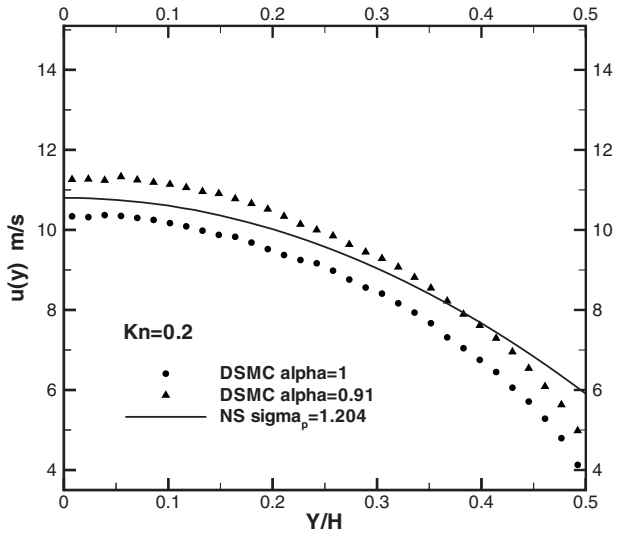

Fig. 6 Streamwise velocity profiles in m/s: the DSMC solution for $\alpha=1$ is presented with the circles, and the DSMC solution for $\alpha=0.91$ is presented with the triangles

obtain $u_{\text{gas}}=3.3$ m/s. The DSMC modeling gives a similar value of gas velocity, i.e., 3.6 m/s. The value of this velocity is important, for example, in order to know the friction factor.

From the mass flow rate measurements and using the analytical expression of the mass flow rate [8] obtained in the frame of the first order continuum modeling, the value of the real velocity slip coefficient $\sigma_p=1.204$ was derived in Ref. [9] for the helium flow in a silicon rectangular channel. However, the notion of the slip coefficient is introduced only in the slip regime, so for the simulation of the flow in transitional or free molecular regimes we need to use directly the accommodation coefficient. Loyalka [6] proposes a very simple relation between the velocity slip and the accommodation coefficients obtained from the numerical solution of the BGK kinetic equation (i.e., taking into account the Knudsen layer effects) using the Maxwellian diffuse-specular scattering kernel at the wall

$$\sigma_p(\alpha)=\frac{2-\alpha}{\alpha}(\sigma_p(\alpha=1)-0.1211(1-\alpha)) \tag{3}$$

From this relation we can also derive the experimental accommodation coefficient, and we found $\alpha=0.91$ for helium [9] and use this value in DSMC simulations. The continuum velocity profile [8] calculated with this experimental velocity slip coefficient $\sigma_p=1.204$ and the results of the DSMC simulation fulfilled for $\alpha=1$ and $\alpha=0.91$ are plotted in Fig. 5. It is to note that the accommodation coefficient influences the whole zone of the channel flow and not only the vicinity of the wall, so when the accommodation coefficient changes the velocity on the symmetry axis changes. Indeed, in Fig. 5 the DSMC curve, plotted for $\alpha=0.91$, and its associated continuum curve plotted for $\sigma_p=1.204$ (indeed the values $\alpha=0.91$ and $\sigma_p=1.204$ are physically consistent [11]) are in perfect agreement. Contrarily, a departure exists with the DSMC full diffusive curve.

Then the same kind of comparison was also carried out for a Knudsen number equal to 0.2. The velocity profile obtained from the continuum modeling using the experimental velocity slip coefficient $\sigma_p=1.204$ is plotted in Fig. 6 and compared with the results of the DSMC simulation corresponding, respectively, to $\alpha=1$ and $\alpha=0.91$. The continuum velocity profile presents a shape slightly but clearly different from the DSMC shape, even when the experimental velocity slip coefficient is used. Finally, the case Kn=0.3 is calculated. The difference between the continuum and the DSMC modeling still increases. Thus, for Kn=0.3, the limit of validity of the continuum modeling is probably reached.

Then the normalized velocity profiles obtained by DSMC calculations in the transitional regime for Kn=1.1 and the solution of the linearized Boltzmann equation [13] are plotted in Fig. 7. The agreement is very good and in this case, the uniformity of the pressure gradient is respected (see Fig. 8). Figure 9 represents the DSMC results for two different values of the accommodation coefficient. From these different figures, the following are observed.

- For the Knudsen numbers under consideration (slip and transitional regimes), when the accommodation coefficient decreases the streamwise velocity increases not only near the wall, but also on the symmetry axis.
- When the Knudsen number increases the slip velocity increases but the velocity on the symmetry axis decreases, and so the velocity profile becomes flatter.

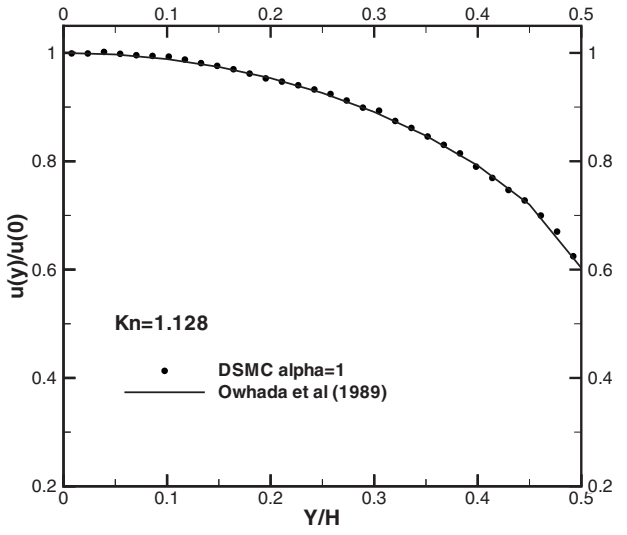

Fig. 7 Pressure profiles (Kn=1.128), normalized with the pressure in the inlet tank: the DSMC solution for $\alpha=1$ is presented with the circles, and the DSMC solution for $\alpha=0.91$ is presented with the triangles

Downloaded 03 Jun 2010 to 171.66.16.158. Redistribution subject to ASME license or copyright; see http://www.asme.org/terms/Terms_Use.cfm

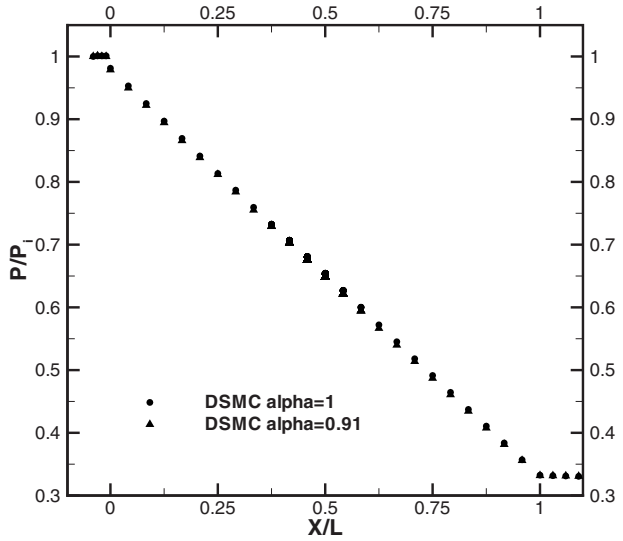

Fig. 8 Streamwise velocity profiles normalized by the velocity on the axis: the solid line represents the solution of the linearized Boltzmann equation [7], and the DSMC solution is presented with the circles

Pressure profiles. We also compared the pressure distribution given by the continuum modeling [8] with the results of the DSMC simulation (see Fig. 2) for a Knudsen number equal to 0.1. The pressure profile is nonlinear as predicted by the continuum approach and depends slightly on the accommodation coefficient. The agreement between the continuum and DSMC results is good. In the transitional flow regime the DSMC pressure distribution becomes linear along the channel and does not depend on the accommodation coefficient (Fig. 8).

It is necessary to add that the proposed inlet and outlet boundary conditions for the DSMC simulation are very convenient: thus the pressures are kept constant in the reservoirs and there is only a small pressure jump (~3%), physically justified [17], between the inlet reservoir and the channel.

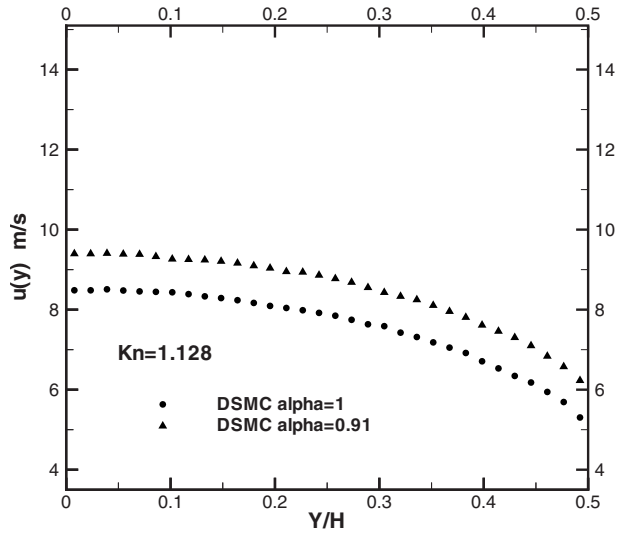

Fig. 9 Pressure profiles (Kn=0.1), normalized with the pressure in the inlet tank: the solid line represents the continuum solution [8] with α=0.91, the dashed line represents the continuum solution [8] with α=1, the DSMC solution for α=1 is presented with the circles, and the DSMC solution for α=0.91 is presented with the triangles

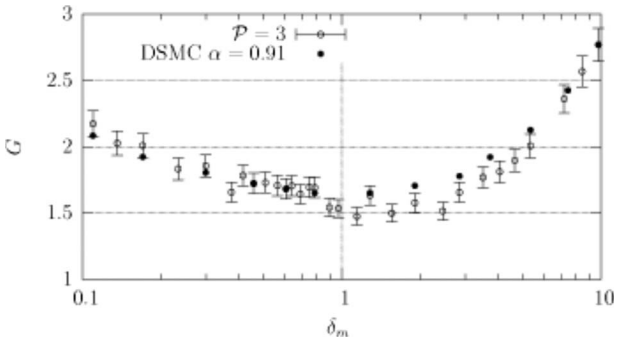

Fig. 10 Experimental and numerical dimensionless mass flow rates in a microchannel using He gas

Mass flow rate. The DSMC calculations are developed for different regimes, slip regime, transitional, and near free molecular regimes, so the rarefaction parameter $\delta=(\sqrt{\pi}/2\mathrm{Kn})$ varies from 0.1 to 10 ($0.088<\mathrm{Kn}<8.86$), which corresponds to experimental conditions from Ref. [9]. We supposed the Maxwellian diffuse-specular reflection of the molecules on the surface and we used the values of the accommodation coefficient α=0.91 obtained from the measurements of the mass flow rate in the hydrodynamic and slip regimes, in the 0.003–0.3 Knudsen number range. The results of the DSMC calculations are presented in Fig. 10 in a nondimensional form G [18] as a function of the rarefaction parameter δ and compared with the experimental points from Ref. [9]. The agreement is very good everywhere except in the zone $1.5<\delta<4.5$. The difference between the DSMC and the experiment is close to the experimental error bar (near $\pm 4.5\%$). Thus, the accommodation coefficient equal to 0.91 may be considered as a good approximation reliable for all regimes, in spite of this small departure observed for $\delta\in[1.5-4.5]$.

We compared our results with the solutions of the BGK kinetic equation associated with the Maxwellian diffuse-specular reflection, calculated in Ref. [11] for different accommodation coefficients α=0.92, 0.96, 1. The mass flow rate given in Ref. [11] are recalculated according to Ref. [19] and presented in Fig. 11. The results of the DSMC simulation obtained with an accommodation coefficient equal to 0.91 are everywhere close to the BGK curve plotted using α=0.96 over all regimes.

Globally, we can consider that the use of the Maxwell diffuse-specular scattering kernel with an accommodation coefficient that is practically constant for the all flow regimes, gives satisfactory results for the mass flow rates derived from the DSMC simulation in all the considered regimes. However, the discrepancy observed for $\delta\in[1.5-4.5]$ or $\mathrm{Kn}\in[0.17-0.5]$ between "almost all" the various models and the experiments is not completely explained. Therefore it will be interesting to implement other scattering kernels in order to try to improve the modeling in this Knudsen zone.

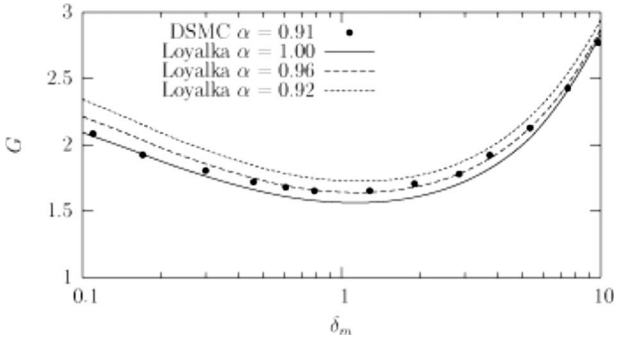

Fig. 11 Experimental and numerical dimensionless mass flow rates in a microchannel using He gas

Downloaded 03 Jun 2010 to 171.66.16.158. Redistribution subject to ASME license or copyright; see http://www.asme.org/terms/Terms_Use.cfm

4 Conclusions

An efficient DSMC solver is developed under the object-conception language (C++). An algorithm for management of the molecular movement and of the molecule-wall collisions working in the whole computational domain and not cell by cell is proposed. Moreover, the concept of a varying N_R, the number of real molecules represented by a simulated molecule, as a function of the local pressure allowed us to keep the same number of the simulated molecules everywhere and to have a very good efficiency when using the parallel version of the developed code.

The results of the DSMC simulation brought a notable contribution for defining the validity domain of the slip regime modeling. The DSMC profiles are in excellent agreement with the continuum profiles for Knudsen numbers of up to 0.1. For Knudsen numbers comprised between 0.2 and 0.3 some disagreements appear between the shapes of the respective modelings. Nevertheless, if disregarding a zone very close to the wall ($\lambda/2$) where the continuum profiles (based on a slip velocity at the wall) are completely fictitious, we observe that the continuum approach underestimates the velocity by about 4.5% for Kn=0.2 and less than 10% for Kn=0.3, which is still a reasonable agreement.

Moreover, the DSMC calculations of the mass flow rates show that the accommodation coefficient extraction method proposed in Ref. [9] is globally justified: the Maxwell diffuse-specular scattering kernel may be used as a boundary condition for the DSMC simulations with an accommodation coefficient value practically the same for all the flow regimes. However, considering the discrepancies observed above for $\mathrm{Kn} \in [0.17-0.5]$, we intend to improve the modeling, introducing other scattering kernels at the wall [20,21].

Acknowledgment

The authors are grateful to the National Center of Scientific Research (CNRS) (Project No. MI2F03-45), the French National Supercomputing Center IDRIS, the Conseil Régional Provence Alpes Côte d'Azur and the RS2N company (Recherche Scientifique et Simulation Numérique, 47 bd Rabatau, F-13008 Marseille) for their financial support. We would also like to acknowledge Yann Jobic and René Occelli for valuable discussions.

References

[1] Bird, G. A., 1994, *Molecular Gas Dynamics and the Direct Simulation of Gas Flows*, Oxford Science, Clarendon Press, Oxford.

[2] Oh, C. K., Oran, E. S., and Sinkovits, R. S., 1997, "Computations of High-Speed, High Knudsen Number Microchannel Flow," J. Thermophys. Heat Transfer, **11**(4), pp. 497–505.

[3] Mavriplis, C., Ahm, J. C., and Goulard, R., 1997, "Heat Transfer and Flowfields in Short Microchannels Using Direct Simulation Monte Carlo," J. Thermophys. Heat Transfer, **11**(4), pp. 489–496.

[4] Liou, W. W., and Fang, Y., 2001, "Heat Transfer in Microchannel Devices Using DSMC," J. Microelectromech. Syst., **10**(2), pp. 274–279.

[5] Le, M., Hassan, I., and Esmail, N., 2007, "The Effect of Outlet Boundary Conditions on Simulating Supersonic Microchannel Flows Using DSMC," Appl. Therm. Eng., **27**, pp. 21–30.

[6] Loyalka, S. K., 1975, "Kinetic Theory of Thermal Transpiration and Mechanocaloric Effects II," J. Chem. Phys., **63**(9), pp. 4054–4960.

[7] Ohwada, T ., Sone, Y., and Aoki, K., 1989, "Numerical Analysis of the Poiseuille and Thermal Transpiration Flows Between Two Parallel Plates on the Basis of the Boltzmann Equation for Hard-Sphere Molecules," Phys. Fluids A, **1**(12), pp. 2042–2049.

[8] Graur, I. A., Méolans, J. G., and Zeitoun, D. E., 2006, "Analytical and Numerical Description for Isothermal Gas Flows in Microchannels," Microfluid. Nanofluid., **2**, pp. 64–77.

[9] Ewart, T., Perrier, P., Graur, I. A., and Méolans, J. G., 2007, "Mass Flow Rate Measurements From Hydrodynamic to Near Free Molecular Regimes," J. Fluid Mech., **584**, pp. 337–356.

[10] Chapman, S., and Cowling, T. G., 1952, *The Mathematical Theory of Non-Uniform Gases*, Cambridge University Press, Cambridge.

[11] Loyalka, S. K., Petrellis, N., and Stvorick, S. T., 1975, "Some Numerical Results for the BGK Model: Thermal Creep and Viscous Slip Problems With Arbitrary Accommodation at the Surface," Phys. Fluids, **18**(9), pp. 1094–1099.

[12] Plimpton, S., and Bartel, T., 1992, "DSMC Simulation of Rarefied Gas Dynamics on a Large Hypercube Supercomputer," AIAA Paper No. AIAA 92–2860.

[13] Arkilic, E. B., Schmidt, M. A., and Breuer, K. S., 1997, "Gaseous Slip Flow in Long Microchannels," J. Microelectromech. Syst., **6**(2), pp. 167–178.

[14] Maxwell, J. C., 1879, "On Stress in Rarefied Gases Arising From Inequalities of Temperature," Philos. Trans. R. Soc. London, **170**, pp. 231–256.

[15] Albertoni, S., Cercignani, C., and Gotusso, L., 1963, "Numerical Evaluation of the Slip Coefficient," Phys. Fluids, **6**, pp. 993–996.

[16] Cercignani, C., 1990, *Mathematical Methods in Kinetic Theory*, Plenum, New York.

[17] Ameurr, D., Croizet, C., Maroteau, F., and Gatignol, R., 2006, "Microfilter Flow Modelling With DSMC Method," Proc. sur CD-ROM du 3éme Congrès Français de Microfluidique SHF, Toulouse, December.

[18] Sharipov, F., and Seleznev, V., 1998, "Data on International Rarefied Gas Flows," J. Phys. Chem. Ref. Data, **27**(3), pp. 657–709.

[19] Sharipov, F., 1999, "Rarefied Gas Flow Through a Long Rectangular Channel," J. Vac. Sci. Technol. A, **17**(5), pp. 3062–3066.

[20] Cercignani, C., and Lampis, M., 1971, "Kinetic Model for Gas-Surface Interaction," Transp. Theory Stat. Phys., **1**, pp. 101–114.

[21] Méolans, J. G., and Dadzie, S. K., 2005, "Scattering Kernel for Polyatomic Molecules," J. Math. Phys., **46**, p. 062101.

Downloaded 03 Jun 2010 to 171.66.16.158. Redistribution subject to ASME license or copyright; see http://www.asme.org/terms/Terms_Use.cfm